Modeling Progressive High-Cycle Fatigue in Polymer Composites

Pieter Hofman

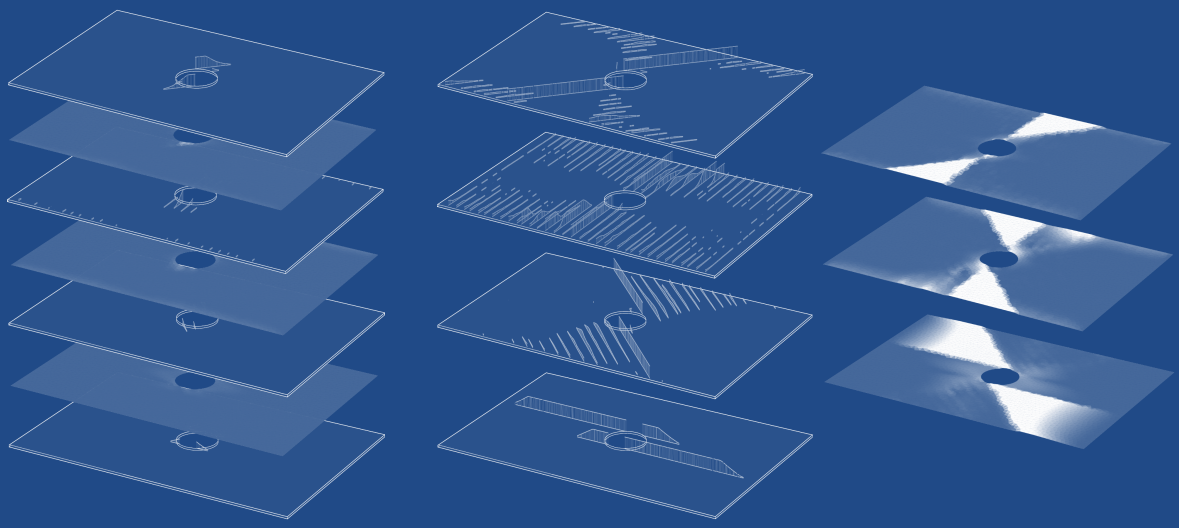

Modeling Progressive High-Cycle Fatigue in Polymer Composites

Modeling Progressive High-Cycle Fatigue in Polymer Composites

Dissertation

for the purpose of obtaining the degree of doctor
at Delft University of Technology
by the authority of the Rector Magnificus,
Prof. dr. ir. H. Bijl,
chair of the Board for Doctorates
to be defended publicly on
Monday 18 May 2026 at 12:30 o'clock

by

Pieter Hofman

This dissertation has been approved by the promotors.

Composition of the doctoral committee:

Rector Magnificus	chairperson
Dr. ir . F. P. van der Meer	Delft University of Technology, promotor
Prof. dr. ir. L. J. Sluijs	Delft University of Technology, promotor

Independent members:

Prof. dr. C. A. Dransfeld	Delft University of Technology
Prof. dr. S. R. Hallett	University of Bristol, United Kingdom
Prof. dr. E. Lindgaard	Aalborg University, Denmark
Prof. dr. ir. R. Akkerman	University of Twente
Dr. B. Chen	Delft University of Technology
Prof. dr. M. Veljkovic	Delft University of Technology, reserve member

This research was carried out as part of the project ENLIGHTEN in the framework of the Partnership Program of the Materials innovation institute M2i and the Netherlands Organization for Scientific Research (NWO).

Keywords: fatigue; polymer composites; progressive failure; cohesive zone modeling; XFEM

Printed by: Ipskamp printing

ISBN 978-94-6518-297-1

An electronic version of this dissertation is available at
http://repository.tudelft.nl/.

Summary

The lack of reliable computer methods for simulating the mechanical response of fiber-reinforced polymer composites is slowing down the industrial uptake of innovative designs and novel manufacturing procedures. Polymer composites are advanced engineering materials, whose microstructure gives rise to a complex interaction and competition between various failure processes on different space and time scales. Consequently, developing accurate, yet efficient and robust simulation tools for predicting the mechanical performance of composites is not straightforward.

Over the past few decades, significant progress has been made towards simulating fatigue in polymer composites. Several modeling approaches have been proposed for propagating initial cracks in elementary specimens. However, the development of reliable failure simulation tools for cases often encountered in practice, where cracks initiate and propagate, plastic deformations interact with fatigue damage and processing effects play a role, is still a challenge.

In this dissertation, new numerical methods are developed for simulating high-cycle fatigue in polymer composites. Firstly, a framework for simulating inter- and intra-laminar damage in multidirectional laminates under cyclic loads is presented, while taking into account the effects of thermal residual stresses as a result of curing. Secondly, the framework is extended to simulate failure in overmolded thermoplastic composites and is used to provide insights into the effect of processing on the mechanical performance.

In Chapter 2, a high-cycle fatigue cohesive zone model covering initiation and propagation is embedded in an XFEM framework for simulating the interactions between transverse matrix cracks and delaminations in multidirectional laminates. For efficient and robust progressive failure simulations, the fatigue cohesive zone model is enhanced with a fully implicit time integration scheme. Furthermore, the model is consistently linearized to achieve fast convergence. With the implicit time integration, adaptive time stepping based on global convergence rates is enabled, further increasing efficiency of the simulations.

To account for varying local stress ratios as a result of thermal residual stresses, the framework is extended in Chapter 3 with an adaptive cycle jump strategy where

local stress ratios are computed during the simulation. The accuracy of the framework is demonstrated through validation against experiments on multidirectional laminates with two different stacking sequences. With the XFEM description for transverse cracking, it is possible to simulate a transition from diffusive damage to localized failure.

To make the step towards failure predictions of overmolded thermoplastic composites, a mesoscopic constitutive model for continuous fiber-reinforced thermoplastic composites is developed in Chapter 4. It is shown that the mesoscopic constitutive model captures the homogenized (transversely isotropic) response of a detailed micromodel with isotropic viscoplastic matrix and elastic fibers under various stress states. For efficient high-cycle fatigue analyses, a two-scale time-homogenized version is derived in Chapter 5, avoiding the need to simulate every cycle individually, thus drastically increasing computational efficiency of simulations.

The final framework (Chapter 5) combines cohesive fatigue with time-homogenized viscoplasticity and is applied to the simulation of a T-section cut from an overmolded rib-stiffened panel. The effects of processing are taken into account by assuming different healing profiles along the overmolded interface. Furthermore, an engineering approach is proposed to obtain a processing-induced geometry and mesh by applying artifical boundary conditions. The simulation outcomes demonstrate that the effects of viscoplasticity and the process-induced mesoscopic geometry of the laminate influence the mechanical response. The effect becomes more pronounced with improved bond quality at the overmolded interface.

The developed numerical methods enable efficient and robust fatigue simulations of polymer composite components under a large number of cycles with interacting and competing failure processes, plastic deformations and processing effects. These tools contribute to more reliable virtual testing and facilitate reaching the full potential of polymer composites.

SAMENVATTING

Het gebrek aan betrouwbare computermodellen voor composieten (vezelversterkte kunststoffen) belemmert de grootschalige toepassing van innovatieve ontwerpen en productieprocessen in de luchtvaart- en automobielindustrie. Composieten zijn geavanceerde technische materialen waarvan de microstructuur leidt tot een complexe wisselwerking tussen verschillende schadeprocessen op meerdere ruimte- en tijdschalen. Het ontwikkelen van nauwkeurige, efficiënte en robuuste simulatiemethoden voor het voorspellen van het mechanische gedrag van composieten is daarom geen eenvoudige opgave.

De afgelopen decennia is aanzienlijke vooruitgang geboekt in het simuleren van vermoeiing (schade door langdurige cyclische belasting) in composieten. Er zijn verschillende modellen ontwikkeld voor het simuleren van scheurgroei in proefstukken met relatief simpele geometriën. Echter, de ontwikkeling van betrouwbare computermodellen voor constructieve elementen die vaak in de praktijk voorkomen, waarbij scheuren eerst ontstaan en zich daarna voortplanten, plastische vervormingen optreden en de effecten van het productieproces een belangrijke rol spelen, is nog steeds een uitdaging.

In dit proefschrift worden nieuwe numerieke methoden ontwikkeld voor het simuleren van vermoeiing in composieten. Eerst wordt een numeriek model gepresenteerd voor het simuleren van inter- en intralaminaire schade in *multidirectional laminates* (laminaten met meerdere vezelrichtingen) onder cyclische belastingen, waarbij rekening wordt gehouden met de effecten van thermische restspanningen als gevolg van uitharding. Vervolgens wordt het model uitgebreid om het schadeproces in *overmolded* (overgoten) thermoplastische composieten te simuleren en wordt het gebruikt om inzicht te verkrijgen in het effect van het productieproces op het mechanische gedrag.

In Hoofdstuk 2 wordt een *cohesive zone model* (een materiaalmodel voor het simuleren van scheuren) voor hoogcyclische vermoeiing ingebed in een XFEM-raamwerk (de *eXtended finite element method*; een geavanceerde numerieke techniek voor het simuleren van scheurvorming). Met dit raamwerk kan de wisselwerking tussen transversale matrixscheuren en delaminaties in *multidirectional laminates* worden gesimuleerd. Voor efficiënte en robuuste simulaties van progressieve schade wordt het *cohesive zone model* verbeterd met een volledig impliciet tijdsintegratieschema.

Bovendien wordt het model consistent gelineariseerd om snelle convergentie te verkrijgen. Met de impliciete tijdsintegratie wordt een adaptief tijdstapschema op basis van globale convergentiesnelheden mogelijk gemaakt, wat de efficiëntie van de simulaties verder verhoogt.

Om rekening te houden met variërende lokale *stress-ratios* (spanningsverhoudingen) als gevolg van thermische restspanningen, wordt het raamwerk in Hoofdstuk 3 uitgebreid met een adaptief tijdstapschema waarbij lokale *stress-ratios* tijdens de simulatie worden berekend. De nauwkeurigheid van het raamwerk wordt aangetoond door validatie aan de hand van experimenten met *multidirectional laminates* met twee verschillende *lay-ups* (stapelvolgordes). Met de XFEM-beschrijving voor transversale matrix scheuren is het mogelijk een overgang van diffuse schade naar gelokaliseerde breuk te simuleren.

Om de stap te zetten naar het simuleren van het schadeproces in *overmolded* thermoplastische composieten, wordt in Hoofdstuk 4 een constitutief model ontwikkeld voor thermoplastische composieten versterkt met continue vezels. Er wordt aangetoond dat het constitutieve model de gehomogeniseerde transversaal isotrope respons van een gedetailleerd micromodel met een isotrope viscoplastische matrix en elastische vezels onder verschillende spanningstoestanden goed beschrijft. Voor efficiënte simulaties van hoogcyclische vermoeiing wordt in Hoofdstuk 5 een tijdgehomogeniseerde versie met twee tijdschalen afgeleid, waardoor het niet nodig is elke cyclus afzonderlijk te simuleren en waarmee de rekenkundige efficiëntie van de simulaties drastisch wordt verhoogd.

Het uiteindelijke raamwerk (Hoofdstuk 5) combineert cohesieve vermoeiingsschade met tijdgehomogeniseerde viscoplasticiteit en wordt toegepast op de simulatie van een T-profiel uit een *overmolded*, ribverstijfd paneel. Er wordt rekening gehouden met de invloed van het productieproces door verschillende hechtingsprofielen langs het nieuwe *overmolded* grensvlak aan te nemen. Verder wordt een ingenieursbenadering voorgesteld om via speciale randvoorwaarden de door het productieproces ontstane geometrie te bepalen. De simulatieresultaten tonen aan dat de effecten van viscoplasticiteit en de door het productieproces veroorzaakte geometrie van het laminaat de mechanische respons beïnvloeden. Dit effect wordt sterker naarmate de hechtkwaliteit aan het *overmolded* grensvlak verbetert.

De ontwikkelde numerieke methoden maken efficiënte en robuuste vermoeiingssimulaties van composieten bij een groot aantal belastingcycli mogelijk. Het model houdt daarbij rekening met wederzijds beïnvloedende schadeprocessen, plastische vervormingen en de invloed van het productieproces. Deze computermodellen dragen bij aan het betrouwbaar virtueel testen en helpen om het volledige potentieel van composieten te benutten.

Acknowledgements

Firstly, I would like to thank my promotors, Frans van der Meer and Bert Sluys. I am grateful to Frans for his mentorship and for introducing me to the field when I was a master's student. His lectures on finite elements first sparked my interest in computational mechanics and laid the foundation for my appreciation of the field.

I would like to thank Bert for his guidance and support throughout my PhD. His encouragement, trust, and critical feedback have been invaluable to my development as a researcher. Our monthly meetings, with the three of us, contributed not only to the research quality but also to the joy of doing it.

My thanks also go to my colleagues Til Gärtner, Sijmen Zwarts, Marina Maia, Leon Riccius, Anne Poot, Winston Lindqwister, Joep Storm, Xinrui Zhang, Martin Lesueur, Sergio Cordeiro, Koert Dingerdis, Renan Barros, Hoessein Alkisaei, Rafid Al-Khoury, Suman Bhattarai, Fanxiang Xu, Lu Ke, Debashis Wadadar and Zhuojun Nan for the pleasant work environment. I enjoyed the time spent together during lunch breaks, dinners outside of work, and conferences in interesting places.

I would especially like to thank Dragan Kovačević, with whom I shared an office for almost two years and co-authored two journal articles. He is not only an excellent academic colleague, but also a friend.

Another special thanks goes to Iuri Rocha for his contagious enthusiasm for computational mechanics and science, and for his helpful advice on navigating the challenges of academia.

I also wish to express my sincere gratitude to Carlos Dávila for answering my emails about his cyclic cohesive zone model, which was used extensively in this thesis, and for our interesting conversations, both in person and online.

My research was carried out as part of the ENLIGHTEN project, and I am grateful to Remko Akkerman, Wouter Grouve, Leon Govaert, Clemens Dransfeld and Boyang Chen as well as others from the consortium who made this possible.

Finally, I would like to thank the people close to me: my parents Peter and Martine, and my uncle Casper and aunt Aya, for their love and support. Special thanks go out to my partner Giovanna, without whom this PhD journey would have been much more difficult.

Pieter Hofman
Amsterdam, March 2026

Contents

1

Introduction

1.1. Background

The transportation sector is a big contributor to CO_2-emissions [1] and it is expected that the demand of air transportation will significantly increase in the next decade [2]. Therefore, to reach the *net-zero* emission target, the transportation sector must become more energy efficient. A way to increase efficiency is making transportation vehicles lighter, which leads to less fuel consumption and consequently a reduction in green-house gas emissions.

Fiber-reinforced polymer composites are well suited for lightweighting, primarily because of their high strength-to-weight ratios and their ability to be tailored to obtain highly specific properties. These composite materials comprise of *short*, *long* or *continuous fibers* (*e.g.* carbon, glass or aramid) and a polymer matrix (*thermoset* or *thermoplastic*) which binds the fibers together.

Since several decades, thermoset composites are used in airplanes, cars, wind turbine blades and bridge decks. However, production times are relatively long due to highly controlled curing processes [3]. In contrast, thermoplastic polymer composites can be easily melted and remelted, allowing for fast and automated manufacturing and enabling high-volume production of composite parts with complex shapes [4, 5]. These features of thermoplastic composites are particularly appealing for lightweighting in the aerospace and automotive industries.

Thermoplastic composites can be easily reshaped and reprocessed several times, offering the possibility to be integrated through innovative manufacturing techniques such as *overmolding*. Overmolding is a manufacturing process where a reinforcing rib is *overinjected* onto a laminate. With this assembly method, no additional material such as adhesives or fasteners are necessary, making the produced

components light and easy to recycle. However, the mechanical performance is strongly affected by the welding process [5, 6]. In particular, the overmolding process results in local wrinkles in the laminate and the quality of the bond between the rib and the laminate is a function of the thermomechanical processing history, which varies along the overmolded interface (see Fig. 1.1). To optimize the production process and the mechanical performance of overmolded composites, a profound understanding of the manufacturing effects on the short-term (quasi-static) and long-term (fatigue) response of the final product is crucial.

The traditional way of assessing the mechanical performance of a new composite design is to perform a large number of experimental tests. Due to the vast number of design parameters and the effects of different processing procedures, a fully experimental approach is extremely time-consuming and costly, and therefore practically infeasible for prototyping. In contrast, computer models allow for *virtual testing* and can replace a substantial part of physical experiments.

Developing reliable computer models for simulating the mechanical response of polymer composites is a challenging task, since failure in composites comprises several interacting and competing damaging processes, such as *fiber fracture*, *fiber-matrix debonding*, *transverse matrix cracking*, *fiber kinking* and *delamination*. In addition, plastic deformations are present in the polymer matrix, especially under shear and compression. These processes interact and, depending on the material system, stacking sequence and ply thickness, lead to a different progression of failure [8–11]. To develop reliable numerical methods, each of these damaging processes must be accurately modeled and their interactions must be properly accounted for. In recent decades, the predictive capabilities of simulation tools for composites have significantly improved [3, 12]. However, there are still several challenges in modeling *progressive failure* in composite components of practical interest.

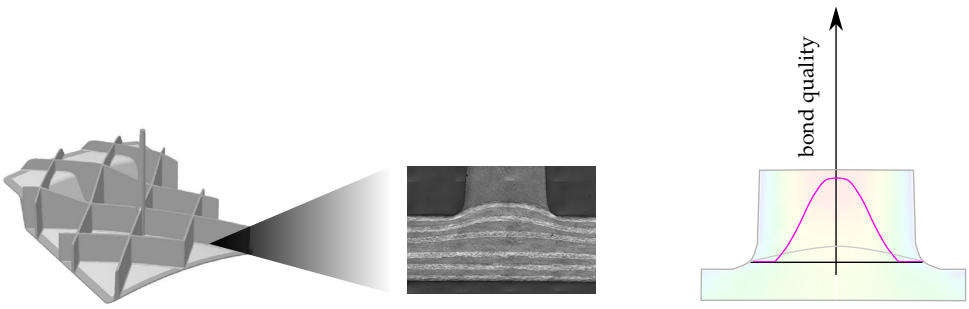

Figure 1.1 Processing effects in an overmolded panel: local wrinkles and non-uniform bond quality of the overmolded interface. First and second picture are adapted from [5] and [7], respectively.

1.2. CHALLENGES

Because of their multiscale nature (see Fig. 1.2), modeling progressive failure in composites is not straightforward: the *macroscale* (*i.e.* the scale of the composite structural component) is often the scale of interest for engineering applications, while most of the material behavior depends on features originating from the *microscale* (*i.e.* the scale of individual fibers and matrix). At the microscale of the material, cracks may initiate and eventually coalesce, at which point a major crack is visible at the mesoscale (*i.e.* the scale of the plies). In theory, these failure processes can be simulated with so-called FE^2 (finite element squared) approaches, where through computational homogenization, sub-scale models—in which the microstructure is explicitly modeled—are coupled to upper-scale integration points and information is exchanged between the two scales. In this approach, the microscopic boundary value problem provides a mesoscopic constitutive relation. Obviously, the success of FE^2 depends on the existence of accurate, yet often simpler, material descriptions at the lower scale. However, even when such descriptions exist, full FE^2 simulations are computationally too expensive for most practical engineering problems beyond simple academic examples. In addition, for predicting failure, it remains challenging to correctly couple the two problems and achieve objective results, in terms of upper-scale mesh size [13, 14], micromodel orientation [15–17], and micromodel size [13, 18].

Because of the high computational cost and the aforementioned challenges associated with multiscale modeling, a *mesoscopic* (ply-level) or *macroscopic* (component-level) approach is still the preferred method for predicting failure in most engineering applications. A challenging aspect for accurate simulations at these scales is adequately taking into account the lower scale features, without explicitly modeling them. For example, in continuous fiber composites, the crack orientation in a ply is dictated by the microstructure: cracks run parallel to the fibers. Furthermore, the polymer matrix behaves viscoplastically while undergoing damage, while the

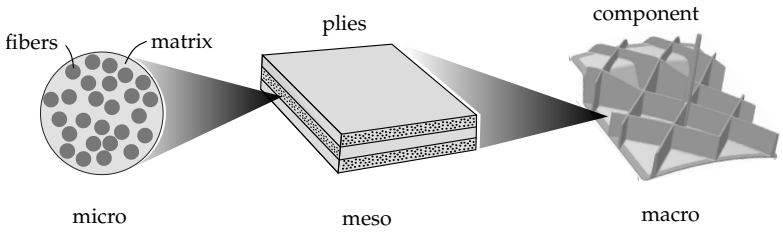

Figure 1.2 Separation of scales for polymer composites (the picture on the right is adapted from [5]).

fibers are mostly elastic until they break. This gives rise to a highly nonlinear anisotropic response on the mesoscale. With regard to overmolded composite parts, the welding process results in non-uniform healing along the overmolded interface and local disturbances in the ply geometries [5, 7]. Ideally, most of these lower-scale phenomena are included, while keeping simulation times manageable.

Apart from the challenges regarding the *spatial* scales, also the *temporal* scales add complexity. In the case of high-cycle fatigue, where the specimen is subjected to thousands or millions of cycles, a single load cycle does not change much in the response, while the effect of multiple cycles can lead to structural failure. Simulating every cycle is computationally infeasible and efficient approaches are required to take into account the effect of the load cycling on the material response, without simulating each load cycle explicitly.

Finally, interacting and competing failure processes generally lead to complex stress histories in the material, increasing the risk of premature abortion of the analyses due to convergence issues. In addition, simulations must run in reasonable amounts of time to become practically relevant for industries. Therefore, besides accuracy of the simulations, robustness and efficiency are equally important aspects in the development of predictive tools.

1.3. RESEARCH GAPS AND OBJECTIVE

In this section, the main research gaps motivating this thesis are outlined, followed by the research objective. In the composite fatigue literature, several modeling approaches have been proposed for simulating fatigue crack propagation in specimens with initial cracks [19–26]. However, for simulating composite components of practical interest, such as *multidirectional laminates* and *overmolded thermoplastic composites*, challenges remain.

Regarding the simulation of fatigue in *multidirectional laminates*, the following topics require further attention:

- **Interacting transverse cracks and delaminations.** In multidirectional laminates, transverse cracks and delaminations can initiate anywhere where stress concentrations are present. Predefined fracture planes can be assigned at locations in the plies where major localization is expected [27–29]. However, without modeling secondary cracks, the transition from distributed damage to localized failure cannot be simulated. This issue has been addressed previously with the eXtended Finite Element Method (XFEM) for simulating mesh-independent transverse cracks under static loads [30, 31]. To extend the framework for cyclic loading, a fatigue cohesive zone model covering

initiation and propagation must be embedded. Furthermore, a proper crack insertion criterion is necessary. For static loading, the strength of the material is a natural choice. Under cyclic loading, fatigue damage already accumulates at stress levels below the static strength and a proper fatigue crack insertion criterion remains yet to be defined.

- **Initiation and propagation**. As mentioned above, a fatigue cohesive zone model for initiation and propagation of transverse cracks and delaminations is necessary. Most fatigue cohesive zone models [19–25, 32] use a Paris relation as input and are therefore only accurate for propagating initial cracks. Recently, a fatigue cohesive zone model that unifies initiation and propagation has been proposed [33, 34]. The model is based on the assumption that Paris-relation and S-N curves are intrinsically related [33, 35]. However, how well this fatigue cohesive zone model can describe transverse cracking and delamination in full-laminate analyses has not been explored.

- **Non-uniform local stress ratio**. The local stress ratio, defined as the ratio of the minimum stress to the maximum stress ($R = \sigma_{\text{min}}/\sigma_{\text{max}}$), is an important parameter in fatigue analyses. Often, in high-cycle fatigue analyses of laminates, it is assumed that local stress ratio is equal to global load ratio. As a result, a load envelope approach, where only the maximum load is applied, can be used to speed up high-cycle fatigue simulations. This no longer holds when nonlinearities are present, such as thermal residual stresses and plastic deformations. In previous progressive fatigue simulations on multidirectional laminates [27, 28, 36–38], the effects of non-uniformly distributed local stress ratios in multidirectional laminates have not been considered.

For simulating failure in *overmolded thermoplastic composites*, a small number of works have focused on static loading [7, 39], while for cyclic loading, no framework exists. To model fatigue in overmolded composites, additional complexities arise that need to be considered in the numerical framework:

- **Viscoplastic deformations**. Viscoplastic deformations in the thermoplastic matrix interact with fatigue cracking and lead to spatially varying local stress ratios. By modeling the matrix and fibers explicitly in a micromechanical framework, anisotropy is explicitly taken into account. For thermoplastic composite carbon/PEEK, this has successfully been done using a physics-based viscoplastic model [40–42] for the matrix, under static [43], creep [44] and fatigue [45] loading. However, for efficient mesoscopic analyses, a continuum

version must be developed, where the transverse isotropy is mathematically described in the constitutive equations.

- **Processing effects**. Processing effects can significantly influence the mechanical response of overmolded composites [5, 6]. For example, crystallinity of the polymer matrix is affected by cooling rates. Furthermore, the performance of the overmolded interface and the mesoscopic geometry of the laminate depend on the processing parameters. For accurate failure analyses, these processing effects must be taken into account. In previous works, simplifying assumptions were made regarding the local fiber orientations [7, 39], where the laminate was considered as a homogenized medium and the non-uniformly distributed local fiber orientations are not taken into account. The effect of accurately accounting for the mesoscopic geometry remains unknown.

The objective of this dissertation is to address the aforementioned research gaps and to contribute to the development of more reliable computational methods for simulating failure in polymer composites under cyclic loads. Firstly, a mesoscale numerical framework for simulating progressive high-cycle fatigue in multidirectional laminates will be presented, taking into account the interactions between transverse cracks and delamination, thermal residual stresses and varying local stress ratios, while remaining robust and computationally efficient. Subsequently, the focus will shift towards simulating fatigue in overmolded thermoplastic composites, considering viscoplastic deformations and processing effects.

1.4. OUTLINE

This dissertation is organized as follows. In Chapter 2, fatigue damage in composite laminates is modeled by embedding a fatigue cohesive zone model for modeling initiation and propagation in a framework for static progressive failure in laminates. The focus is not only on the accuracy of describing transverse cracking and delamination, but also on the efficiency and robustness of the simulations when modeling interacting fatigue damage processes under a large number of cycles.

In Chapter 3, the presented framework is extended and validated against experiments on multidirectional laminates from literature. To apply the framework to laminates often encountered in practice, thermal residual stresses—that develop during curing of the laminates—are taken into account. These residual stresses lead to a non-uniformly distributed local stress ratio, which is captured through a special adaptive stepping scheme and used in the fatigue damage calculations. The performance of the numerical framework is demonstrated through simulations of multidirectional laminates with different stacking sequences under various loading

conditions.

In Chapter 4, a mesoscopic viscoplasticity model for unidirectional thermoplastic composites is presented to account for viscous deformations that develop during long-term loading. The response of the mesomodel is compared to the response of a micromodel with isotropic viscoplasticity for the matrix and with hyperelastic fibers. It is demonstrated that the homogenized response of the micromodel is well-captured by the mesomodel across various stress states and loading rates.

Finally, in Chapter 5, cohesive fatigue and viscoplasticity are combined in a framework for simulating high-cycle fatigue in overmolded specimens. To employ the viscoplasticity model in fatigue simulations in an efficient manner, a two-scale time-homogenized version of the model is developed. Subsequently, the framework is used to simulate fracture and fatigue in an overmolded T-section, accounting for processing effects. In addition, the effects of various modeling assumptions are investigated.

REFERENCES

[1] V. Foster, J. U. Dim, S. Vollmer, F. Zhang, Understanding the challenge of decoupling transport-related CO2 emissions from economic growth in developing countries, *World Development Sustainability* 3 (2023) 100111.

[2] M. Emami Javanmard, Y. Tang, J. A. Martínez-Hernández, Forecasting air transportation demand and its impacts on energy consumption and emission, *Applied Energy* 364 (2024) 123031.

[3] R. Krueger, A. Bergan, Advances in Thermoplastic Composites Over Three Decades – A Literature Review, *NASA/TM–20240005376* (2024).

[4] A. R. Offringa, Thermoplastic composites—rapid processing applications, *Composites Part A: Applied Science and Manufacturing* 27 (4) (1996) 329–336.

[5] R. Akkerman, M. Bouwman, S. Wijskamp, Analysis of the thermoplastic composite overmolding process: Interface strength, *Frontiers in Materials* 7 (2020).

[6] M. A. Valverde, R. Kupfer, T. Wollmann, L. F. Kawashita, M. Gude, S. R. Hallett, Influence of component design on features and properties in thermoplastic overmoulded composites, *Composites Part A: Applied Science and Manufacturing* 132 (2020) 105823.

[7] M. A. Valverde, An Improved Description of the Bonding and Consolidation for Overmoulded Thermoplastic Composite Ribbed Plates, Ph.D. thesis (2021).

[8] F. Aymerich, M. S. Found, Response of notched carbon/PEEK and carbon/epoxy laminates subjected to tension fatigue loading, *Fatigue and Fracture of Engineering Materials and Structures* 23 (8) (2000) 675–683.

[9] O. J. Nixon-Pearson, S. R. Hallett, An investigation into the damage development and residual strengths of open-hole specimens in fatigue, *Composites Part A: Applied Science and Manufacturing* 69 (2015) 266–278.

[10] M. R. Wisnom, S. R. Hallett, The role of delamination in strength, failure mechanism and hole size effect in open hole tensile tests on quasi-isotropic laminates, *Composites Part A: Applied Science and Manufacturing* 40 (4) (2009) 335–342.

[11] J. Cugnoni, R. Amacher, S. Kohler, J. Brunner, E. Kramer, C. Dransfeld, W. Smith, K. Scobbie, L. Sorensen, J. Botsis, Towards aerospace grade thin-ply composites: Effect of ply thickness, fibre, matrix and interlayer toughening on strength and damage tolerance, *Composites Science and Technology* 168 (2018) 467–477.

[12] B. L. Bak, C. Sarrado, A. Turon, J. Costa, Delamination under fatigue loads in composite laminates: A review on the observed phenomenology and computational methods, *Applied Mechanics Reviews* 66 (6) (2014).

[13] J. Oliver, M. Caicedo, E. Roubin, A. Huespe, J. Hernández, Continuum approach to computational multiscale modeling of propagating fracture, *Computer Methods in Applied Mechanics and Engineering* 294 (2015) 384–427.

[14] L. Ke, F. P. van der Meer, A computational homogenization framework with enhanced localization criterion for macroscopic cohesive failure in heterogeneous materials, *Journal of Theoretical, Computational and Applied Mechanics* (2022) 7707.

[15] P. Hofman, L. Ke, F. P. van der Meer, Circular representative volume elements for strain localization problems, *International Journal for Numerical Methods in Engineering* 124 (4) (2023) 784–807.

[16] E. Svenning, M. Fagerström, F. Larsson, Localization aligned weakly periodic boundary conditions, *International Journal for Numerical Methods in Engineering* 111 (5) (2017) 493–500.

[17] E. Coenen, V. Kouznetsova, M. Geers, Novel boundary conditions for strain localization analyses in microstructural volume elements, *International Journal for Numerical Methods in Engineering* 90 (1) (2012) 1–21.

[18] I. Gitman, H. Askes, L. Sluys, Representative volume: Existence and size determination, *Engineering Fracture Mechanics* 74 (16) (2007) 2518–2534.

[19] A. Turon, J. Costa, P. Camanho, C. Dávila, Simulation of delamination in composites under high-cycle fatigue, *Composites Part A: Applied Science and Manufacturing* 38 (11) (2007) 2270–2282.

[20] P. W. Harper, S. R. Hallett, A fatigue degradation law for cohesive interface elements – Development and application to composite materials, *International Journal of Fatigue* 32 (11) (2010) 1774–1787.

[21] B. L. V. Bak, A. Turon, E. Lindgaard, E. Lund, A simulation method for high-cycle fatigue-driven delamination using a cohesive zone model, *International Journal for Numerical Methods in Engineering* 106 (3) (2016) 163–191.

[22] L. F. Kawashita, S. R. Hallett, A crack tip tracking algorithm for cohesive interface element analysis of fatigue delamination propagation in composite materials, *International Journal of Solids and Structures* 49 (21) (2012) 2898–2913.

[23] M. Latifi, F. P. van der Meer, L. J. Sluys, A level set model for simulating fatigue-driven delamination in composites, *International Journal of Fatigue* 80 (2015) 434–442.

[24] A. Amiri-Rad, M. Mashayekhi, F. P. van der Meer, Cohesive zone and level set method for simulation of high cycle fatigue delamination in composite materials, *Composite Structures* 160 (2017) 61–69.

[25] L. Carreras, A. Turon, B. L. Bak, E. Lindgaard, J. Renart, F. Martin de la Escalera, Y. Essa, A simulation method for fatigue-driven delamination in layered structures involving non-negligible fracture process zones and arbitrarily shaped crack fronts, *Composites Part A: Applied Science and Manufacturing* 122 (2019) 107–119.

[26] G. G. Trabal, B. L. V. Bak, B. Chen, L. Carreras, E. Lindgaard, An adaptive floating node based formulation for the analysis of multiple delaminations under high cycle fatigue loading, *Composites Part A: Applied Science and Manufacturing* 160 (2022) 107036.

[27] O. J. Nixon-Pearson, S. R. Hallett, P. W. Harper, L. F. Kawashita, Damage development in open-hole composite specimens in fatigue. Part 2: Numerical modelling, *Composite Structures* 106 (2013) 890–898.

[28] C. Tao, S. Mukhopadhyay, B. Zhang, L. F. Kawashita, J. Qiu, S. R. Hallett, An improved delamination fatigue cohesive interface model for complex three-dimensional multi-interface cases, *Composites Part A: Applied Science and Manufacturing* 107 (2018) 633–646.

[29] V. Maneval, N.-P. Vedvik, A. T. Echtermeyer, Progressive Fatigue Modelling of Open-Hole Glass-Fibre Epoxy Laminates, *Journal of Composites Science* 7 (12) (2023) 516.

[30] F. P. van der Meer, L. J. Sluys, A phantom node formulation with mixed mode cohesive law for splitting in laminates, *International Journal of Fracture* 158 (2) (2009) 107–124.

[31] F. P. van der Meer, L. J. Sluys, Mesh-independent modeling of both distributed and discrete matrix cracking in interaction with delamination in composites, *Engineering Fracture Mechanics* 77 (4) (2010) 719–735.

[32] A. Amiri-Rad, M. Mashayekhi, A Cohesive Zone Approach for Fatigue-Driven Delamination Analysis in Composite Materials, *Applied Composite Materials* 24 (4) (2017) 751–769.

[33] C. G. Dávila, From S-N to the Paris law with a new mixed-mode cohesive fatigue model for delamination in composites, *Theoretical and Applied Fracture Mechanics* 106 (2020) 102499.

[34] C. G. Dávila, C. A. Rose, G. B. Murri, W. C. Jackson, W. M. Johnston, Evaluation of fatigue damage accumulation functions for delamination initiation and propagation, *Nasa/Tp–2020-220584* (2020).

[35] G. Allegri, A unified formulation for fatigue crack onset and growth via cohesive zone modelling, *Journal of the Mechanics and Physics of Solids* 138 (2020) 103900.

[36] E. V. Iarve, K. Hoos, M. Braginsky, E. Zhou, D. H. Mollenhauer, Progressive failure simulation in laminated composites under fatigue loading by using discrete damage modeling, *Journal of Composite Materials* 51 (15) (2016) 2143–2161.

[37] W.-T. Lu, Z. Gao, H. K. Adluru, K. H. Hoos, W. P. Seneviratne, D. H. Mollenhauer, E. V. Iarve, Fatigue damage modeling in laminated composite by using Rx-FEM and strength tracking method, *Composites Part A: Applied Science and Manufacturing* 163 (2022) 107199.

[38] J. Llobet, P. Maimí, A. Turon, B. Bak, E. Lindgaard, L. Carreras, Y. Essa, F. Martin de la Escalera, A continuum damage model for composite laminates: Part IV-Experimental and numerical tests, *Mechanics of Materials* 154 (2021) 103686.

[39] X. Song, F. Daghia, C. Cluzel, Y. Elie, Influence of boundary conditions on the failure behavior of T-joint shaped overmolded composite structures, in: 21st European Conference on Composite Materials, Nantes, France, 2024.

[40] T. A. Tervoort, E. T. J. Klompen, L. E. Govaert, A multi-mode approach to finite, three-dimensional, nonlinear viscoelastic behavior of polymer glasses, *Journal of Rheology* 40 (5) (1996) 779–797.

[41] T. A. Tervoort, R. J. M. Smit, W. A. M. Brekelmans, L. E. Govaert, A Constitutive Equation for the Elasto-Viscoplastic Deformation of Glassy Polymers, *Mechanics of Time-Dependent Materials 1: 269–291, 1998.* 1 (1998) 269–291.

[42] L. C. A. van Breemen, E. T. J. Klompen, L. E. Govaert, H. E. H. Meijer, Extending the EGP constitutive model for polymer glasses to multiple relaxation times, *Journal of the Mechanics and Physics of Solids* 59 (10) (2011) 2191–2207.

[43] D. Kovačević, B. K. Sundararajan, F. P. van der Meer, Microscale modeling of rate-dependent failure in thermoplastic composites under off-axis loading, *Engineering Fracture Mechanics* 276 (2022) 108884.

[44] D. Kovačević, B. K. Sundararajan, F. P. van der Meer, Micromechanical model for off-axis creep rupture in unidirectional composites undergoing finite strains, *Composites Part A: Applied Science and Manufacturing* 176 (2024) 107860.

[45] D. Kovačević, P. Hofman, I. B. C. M. Rocha, F. P. van der Meer, Unifying creep and fatigue modeling of composites: A time-homogenized micromechanical framework with viscoplasticity and cohesive damage, *Journal of the Mechanics and Physics of Solids* 193 (2024) 105904.

2

A NUMERICAL FRAMEWORK FOR PROGRESSIVE FATIGUE IN COMPOSITES

With the exception of minor textual adjustments, this chapter is reproduced from: P. Hofman, F. P. van der Meer, L. J. Sluys, A Numerical Framework for Simulating Progressive Failure in Composite Laminates under High-Cycle Fatigue Loading. *Engineering Fracture Mechanics* 295 (2024) 109786. **doi:10.1016/j.engfracmech.2023.109786**.

ABSTRACT

In this chapter, a recently proposed high-cycle fatigue cohesive zone model, which covers crack initiation and propagation with limited input parameters, is embedded in a robust and efficient numerical framework for simulating progressive failure in composite laminates under fatigue loading. The fatigue cohesive zone model is enhanced with an implicit time integration scheme of the fatigue damage variable which allows for larger cycle increments and more efficient analyses. The method is combined with an adaptive strategy for determining the cycle increment based on global convergence rates. Moreover, a consistent material tangent stiffness matrix has been derived by fully linearizing the underlying mixed-mode quasi-static model and the fatigue damage update. The enhanced fatigue cohesive zone model is used to describe matrix cracking and delamination in laminates. In order to allow for matrix cracks to initiate at arbitrary locations and to avoid complex and costly mesh generation, the phantom node version of the eXtended finite element method (XFEM) is employed. For the insertion of new crack segments, an XFEM fatigue crack insertion criterion is presented, which is consistent with the fatigue cohesive zone formulation. It is shown with numerical examples that the improved fatigue damage update enhances the accuracy, efficiency and robustness of the numerical simulations significantly. The numerical framework is applied to the simulation of progressive fatigue failure in an open-hole $[\pm 45]$-laminate. It is demonstrated that the numerical model is capable of accurately and efficiently simulating the complete failure process from distributed damage to localized failure.

2.1. INTRODUCTION

Fatigue is often a critical failure process in fiber-reinforced polymer laminates. Accurate, efficient and robust numerical prediction tools can help in enhancing the efficiency of the design process of composite laminated structures, reducing manufacturing time, and minimizing the need for extensive testing to ensure the safety of new composite structures.

When fiber-reinforced polymer laminates are subjected to loads, several interacting failure processes take place that make developing reliable prediction tools a challenging endeavor. For example, matrix cracks can initiate and propagate and eventually lead to interface delamination. Finally, fiber breakage can occur leading to overall failure of the laminate. The interaction of these competing processes and the type of final failure depend on the stacking sequence, laminate thickness and the presence of notches [1, 2]. Furthermore, the load character (cyclic or quasi-static) influences the final failure mode [3–5]. In addition, damage accumulation in fiber-reinforced composite materials already takes place at an early stage which results in significant stiffness reduction and stress redistribution. In order to accurately predict the performance of composite laminates, numerical models must take into account the progressive character of failure that covers the initial stage of early damage up to complete failure of the laminate.

In literature, several numerical models have been developed for the quasi-static load case of complex laminates. For example, Jiang et al. [6] modelled splitting and matrix cracks with interface elements at pre-defined locations according to experiments. Hallet et al. [7] used a similar approach for matrix cracks and delamination and included a Weibull statistical criterion for fiber failure. Furthermore, Van der Meer et al. [8, 9] used the *phantom node version* of the *extended finite element method* (XFEM) [10] for modeling matrix cracks to reduce the complexity of meshing and to allow for mesh-independent cracks that can initiate at arbitrary locations with a pre-defined crack spacing. Moreover, Chen et al. [11] used a 3D version of the *floating node method* [12] to model the interaction of a large number of discrete matrix cracks with delaminations and demonstrated that the model was able to accurately predict the sequence of failure processes in notched and unnotched laminates. More modeling approaches of composite laminates subjected to quasi-static loading scenarios can be found in Refs. [13–22]

At present, there are only few progressive failure models that can simulate (high-cycle) fatigue failure in composite laminates. One of the first papers of open-hole fatigue modeling of progressive failure was presented by Nixon-Pearson et al. [23], where pre-inserted interface elements were used to model matrix cracks and a Paris-type cyclic cohesive zone model (CZM) [24, 25] was used for crack

propagation. Iarve et al. [17] developed a model where the *regularized eXtended finite element method* (Rx-FEM) was employed for modeling mesh-independent cracks and a fatigue initiation criterion based on S-N curves was presented. This framework was further extended by Lu et al. [26] to account for high-density crack networks by allowing cracks to appear close to each other. In the work by Tao et al. [27], a similar approach as in Nixon-Pearson et al. [23] was adopted, but extended with a fatigue initiation criterion based on S-N curves, similar as proposed in Ref. [17]. As opposed to the discrete crack modeling approaches for simulating matrix cracking in the previously mentioned approaches, Llobet et al. [28] used a continuum damage modeling approach with fiber-aligned meshes and included a description for fiber damage due to cyclic loading. More recently, Tao et al. [29] developed an enhanced fatigue cohesive zone model where stiffness degradation is described by a Paris-relation-informed neural network and applied it to simulate an open-hole fatigue tension test with good accuracy.

In most of the existing methods, a fatigue cohesive zone model, that requires a Paris-relation [30] as input, is used for modeling delamination and matrix cracking. These cohesive zone models are suitable for describing crack propagation of an initial crack [24, 25, 31–36]. However, in full-laminate analysis, a matrix crack can also initiate under cyclic loading. Upon further applying fatigue load cycles, a fracture process zone develops in the onset phase after which propagation of the crack takes place. In literature, only a few CZMs take these three stages of fatigue crack growth into account [17, 26, 28, 37–40].

Recently, Dávila [37] proposed a cyclic CZM that covers initiation, onset and propagation and is built on Turon's quasi-static mixed-mode CZM [41, 42]. The fatigue CZM relies on S-N curves with simple engineering assumptions and empirical relations to take the dependence of mode-mixity and stress-ratio into account. The method is based on the assumption that an intrinsic relation exists between S-N curves and Paris' relation [43]. The model is capable of simulating complex 3D crack fronts [44] in a reinforced double cantilever beam (DCB) test [45] and can be extended to cases where the *local* stress ratio is not equal to the *global* load ratio, as presented in [46] where the presence of residual stresses was taken into account. In addition, R-curve effects in thermoplastic material systems can be captured with a multi-linear cohesive softening relation which accounts for large-scale fiber bridging [47]. Furthermore, it has been demonstrated that the method can simulate crack migration in a ply-drop specimen [48]. With regard to laminate analyses, the unification of initiation and propagation makes the fatigue CZM suitable for simulating *both* interface delamination and matrix cracking in progressive failure analyses of complex laminates.

Originally, the model presented in Ref. [37] employed an explicit update of the damage variable that evolves with load cycles. Therefore, small cycle increments must be used during simulations to prevent instabilities in the damage evolution and a step size criterion based on the maximum damage experienced in all integration points is required. This approach may become problematic in full-laminate analyses where many integration points, due to stress redistribution and complex loading histories, experience different damage rates throughout the simulation.

In this chapter, an implicit fatigue damage update is presented to make the formulation more suitable for use in full-laminate analyses. The method is combined with efficient cycle jumping based on *global* iterations and a fully consistent tangent matrix has been derived to enhance efficiency and robustness of the simulations. In order to allow for multiple cracks at arbitrary locations, the fatigue CZM is combined with XFEM with a proper fatigue crack insertion criterion that is consistent with the fatigue damage evolution.

The organization of this chapter is as follows. Firstly the improvement to Dávila's fatigue damage formulation is presented and a fully consistent material tangent is derived. Subsequently, the XFEM implementation with a proper fatigue crack insertion criterion is presented. The model is applied to several numerical examples to verify the methods and to show the improved performance. In order to demonstrate the capabilities of the presented numerical framework, an open-hole [±45]-laminate under fatigue loading is simulated.

2.2. FATIGUE COHESIVE ZONE MODEL

The fatigue CZM by Dávila [37, 49] is built on top of the static CZM with mode-dependent dummy stiffness by Turon [41, 42]. In this section, the formulation of the fatigue CZM is given in local coordinate frame with basis vectors $\{\boldsymbol{e}_{\mathrm{n}}, \boldsymbol{e}_{\mathrm{s1}}, \boldsymbol{e}_{\mathrm{s2}}\}$ aligned with the crack plane.

In order to allow for a reduction of elastic stiffness due to fatigue and static loading, a scalar damage variable d is introduced. The traction is computed as

$$\mathbf{t} = (\mathbf{I} - d\mathbf{P})\mathbf{K}[\![\mathbf{u}]\!] \tag{2.1}$$

where $[\![\mathbf{u}]\!]$ is the displacement jump, $\mathbf{K}$ is the dummy stiffness matrix and $\mathbf{P}$ is a selection matrix. The matrices $\mathbf{K}$ and $\mathbf{P}$ are expressed as

$$\mathbf{K} = \begin{bmatrix} K_{\mathrm{n}} & 0 & 0 \\ 0 & K_{\mathrm{sh}} & 0 \\ 0 & 0 & K_{\mathrm{sh}} \end{bmatrix} \tag{2.2}$$

and

$$\mathbf{P} = \begin{bmatrix} \frac{\langle [\![u]\!]_n \rangle}{[\![u]\!]_n} & 0 & 0 \\ 0 & 1 & 0 \\ 0 & 0 & 1 \end{bmatrix} \tag{2.3}$$

In Eq. (2.2), K_n is the normal dummy stiffness and K_{sh} is the shear dummy stiffness. The operator $\langle \bullet \rangle$ is the Macaulay operator, defined as $\max(0, \bullet)$ and makes sure that interfacial penetration is prevented when the normal component of the displacement jump is negative. The damage variable d determines the stiffness reduction and its evolution depends on the mode-mixity such that the energy dissipated matches with the phenomenological mixed-mode fracture energy relation proposed by Benzeggagh and Kenane [50]. It is shown in [42, 51] that the correct energy dissipation under mixed-mode fracture is ensured by relating the ratio between dummy stiffnesses K_n and K_{sh} to the fracture properties with the following equation:

$$K_{sh} = K_n \frac{G_{Ic}}{G_{IIc}} \left(\frac{f_{sh}}{f_n} \right)^2 \tag{2.4}$$

where f_n, f_{sh}, G_{Ic} and G_{IIc} are the tensile strength, shear strength, mode-I and mode-II fracture energies, respectively. The mixed-mode CZM is formulated in the form of an equivalent 1D traction-separation relation:

$$\sigma = (1 - d) K_{\mathcal{B}} \Delta \tag{2.5}$$

where σ is the equivalent stress, $K_{\mathcal{B}}$ is the mode-dependent dummy stiffness and Δ is the equivalent displacement jump. These quantities are defined as

$$\sigma = \sqrt{\langle t_n \rangle^2 + t_{s1}^2 + t_{s2}^2} \tag{2.6}$$

$$K_{\mathcal{B}} = K_n (1 - \mathcal{B}) + \mathcal{B} K_{sh} \tag{2.7}$$

$$\Delta = \frac{K_n \langle [\![u]\!]_n \rangle^2 + K_{sh} [\![u]\!]_{sh}^2}{\sqrt{K_n^2 \langle [\![u]\!]_n \rangle^2 + K_{sh}^2 [\![u]\!]_{sh}^2}} \tag{2.8}$$

where $\mathcal{B}$ is a displacement-based measure of mode-mixity:

$$\mathcal{B} = \frac{K_{sh} [\![u]\!]_{sh}^2}{K_n \langle [\![u]\!]_n \rangle^2 + K_{sh} [\![u]\!]_{sh}^2} \tag{2.9}$$

and $[\![u]\!]_{sh}$ is the Eucledian norm (length) of the shear displacement jump vector:

$$[\![u]\!]_{sh}^2 = [\![u]\!]_{s1}^2 + [\![u]\!]_{s2}^2 \tag{2.10}$$

The equivalent displacement jump at fracture initiation (Δ_0) and complete fracture (Δ_f) of the 1D equivalent traction-separation relation (Eq. (2.5)) are expressed as

$$\Delta_0 = \sqrt{\frac{K_n(\llbracket u \rrbracket_n^0)^2 + \left(K_{sh}(\llbracket u \rrbracket_{sh}^0)^2 - K_n(\llbracket u \rrbracket_n^0)^2\right)\mathcal{B}^{\eta_{BK}}}{K_{\mathcal{B}}}} \tag{2.11}$$

$$\Delta_f = \frac{K_n \llbracket u \rrbracket_n^0 \llbracket u \rrbracket_n^f + \left(K_{sh} \llbracket u \rrbracket_{sh}^0 \llbracket u \rrbracket_{sh}^f - K_n \llbracket u \rrbracket_n^0 \llbracket u \rrbracket_n^f\right)\mathcal{B}^{\eta_{BK}}}{K_{\mathcal{B}}\Delta_0} \tag{2.12}$$

where η_{BK} is the Benzeggagh-Kenane interaction parameter. The pure-mode jump components corresponding to fracture initiation and complete fracture are given by

$$\llbracket u \rrbracket_n^0 = \frac{f_n}{K_n}, \qquad \llbracket u \rrbracket_n^f = \frac{2G_{Ic}}{f_n} \tag{2.13}$$

$$\llbracket u \rrbracket_{sh}^0 = \frac{f_{sh}}{K_{sh}}, \qquad \llbracket u \rrbracket_{sh}^f = \frac{2G_{IIc}}{f_{sh}} \tag{2.14}$$

An energy-based damage variable $\mathcal{D}$ is introduced as the state variable, which is defined as the ratio of dissipated energy G_d over the critical mixed-mode energy release rate G_c:

$$\mathcal{D} \equiv \frac{G_d}{G_c} = \frac{\Delta - \Delta_f}{\Delta_f - \Delta_0} \tag{2.15}$$

and can only increase in *pseudo* time t, such that for time step n ($t = t_n$):

$$\mathcal{D}(t_n) = \max_{0 \le \tau \le t_n} (\mathcal{D}(\tau)) \tag{2.16}$$

The stiffness-based damage variable d in Eq. (2.1) is related to the energy-based damage variable through

$$d = 1 - \frac{(1-\mathcal{D})\Delta_0}{\mathcal{D}\Delta_f + (1-\mathcal{D})\Delta_0} \tag{2.17}$$

2.2.1. DÁVILA'S FATIGUE DAMAGE FORMULATION

In Dávila's fatigue CZM, the number of cycles to failure of a 1D bar with a single crack and cyclic load matches with an S-N curve (see Fig. 2.1). This is achieved by reducing the stiffness at constant applied stress until the traction-separation response reaches the quasi-static softening line, which marks failure of the material point. The evolution of the energy-based damage variable during fatigue $\mathcal{D}_f$ is described with the following (nonlinear) differential equation:

$$\frac{d\mathcal{D}_f}{dN} = f_{\mathcal{D}}(\Delta, \Delta^*, \mathcal{D}) \tag{2.18}$$

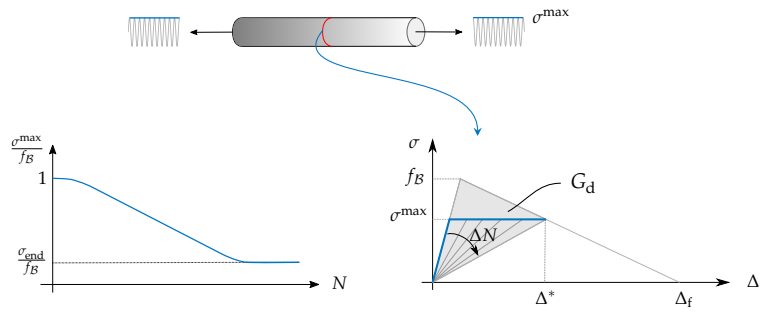

Figure 2.1 Dávila's fatigue cohesive zone model. The evolution of damage variable $\mathcal{D}$ is such that at constant stress and mode-mixity the time to failure N_{fail} matches with an S-N curve.

where Δ^* is the reference displacement, which is the displacement corresponding to the residual traction (see Fig. 2.2) and can be computed as

$$\Delta^* = \mathcal{D}(\Delta_f - \Delta_0) + \Delta_0 \tag{2.19}$$

The quasi-static damage $\mathcal{D}_s$ is computed as

$$\mathcal{D}_s = \frac{\Delta - \Delta_0}{\Delta_f - \Delta_0} \tag{2.20}$$

and the updated damage is determined as the maximum of the static and the fatigue damage

$$\mathcal{D} = \max\left(\mathcal{D}_s, \mathcal{D}_f\right) \tag{2.21}$$

to ensure that the traction-opening response during fatigue loading is inside the quasi-static envelope. In [49], several fatigue damage functions were proposed and compared. It was shown that the so-called CF20 damage function

$$f_{\mathcal{D}}^{\text{CF20}} = \frac{1}{\gamma} \frac{(1-\mathcal{D})^{\beta-p}}{E^{\beta}(p+1)} \left(\frac{\Delta}{\Delta^*}\right)^{\beta} \tag{2.22}$$

gave the most satisfactory results. Here, γ is the number of cycles to failure at the endurance limit (which is usually set to 10^7 cycles), p can be calibrated such that the propagation rates in the simulation match with (available) Paris curves [49] and β is the exponent in the S-N curve, computed as

$$\beta = \frac{-7\eta}{\log E} \tag{2.23}$$

where η is a *brittleness* parameter that can take into account the low-cycle fatigue response in the S-N curve.

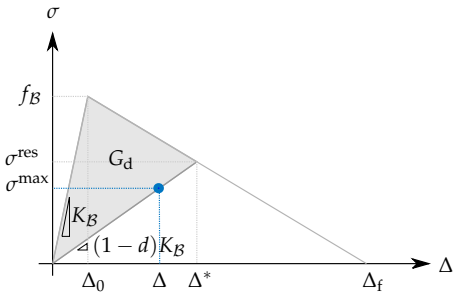

Figure 2.2 Nomenclature of the fatigue CZM. The fatigue traction-separation response (•) is inside the quasi-static envelope.

For a given stress ratio $R \equiv \sigma^{\min}/\sigma^{\max}$, the relative endurance limit E, defined as the ratio of equivalent endurance limit σ_{end} and mode-dependent static strength $f_{\mathcal{B}}$, is computed from the relative endurance limit ϵ (at full load reversal $R = -1$) with the Goodmann diagram:

$$E = \frac{2C\epsilon}{C\epsilon + 1 + R(C\epsilon - 1)} \tag{2.24}$$

where C is an empirical relation which takes into account the effect of mode-mixity [52]:

$$C = 1 - 0.42\mathcal{B} \tag{2.25}$$

In summary, the input fatigue model parameters for CF20 are η, ϵ and p.

2.2.2. IMPLICIT FATIGUE DAMAGE UPDATE

In order to compute the damage at current *pseudo* time t_n, the damage rate function in Eq. (2.18) must be integrated, which is mathematically expressed as

$$\mathcal{D}_{\text{f}}^{t_n} = \mathcal{D}^{t_{n-1}} + \int_{t_{n-1}}^{t_n} f_{\mathcal{D}}(\Delta, \Delta^*, \mathcal{D})\, \mathrm{d}N \tag{2.26}$$

Dávila [37] used an Euler forward (explicit) time integration scheme where the integral is approximated as $\Delta N f_{\mathcal{D}}^{(n-1)}$, with $f_{\mathcal{D}}^{(n-1)}$ representing $f_{\mathcal{D}}$ evaluated at t_{n-1}. In this work, the damage at current time step n (corresponding to time t_n) is computed with the generalized trapezoidal rule:

$$\mathcal{D}_{\text{f}}^{(n)} = \mathcal{D}^{(n-1)} + \Delta N \left[(1-\theta) f_{\mathcal{D}}^{(n-1)} + \theta f_{\mathcal{D}}^{(n)} \right] \tag{2.27}$$

with parameter $\theta \in (0, 1]$.[1] Through Eq. (2.22), $f_{\mathcal{D}}^{(n)}$ requires $\mathcal{D}_{\text{f}}^{(n)}$, making the update with Eq. (2.27) implicit. The resulting nonlinear equation can be solved at

[1] Note that for $\theta = 0$, the formulation reduces to an Euler forward scheme.

local integration point level, *e.g.* with Newton's method by performing iterations until a *local* convergence criterion is met.

Remark 2.1 The right-hand side (RHS) of Eq. (2.27) depends on the step size ΔN. When the step size is too large and a material point completely fails within the time step, no solution exists for Eq. (2.27) (see Fig. 2.3). This issue is circumvented by setting $\mathcal{D}_\mathrm{f} = 1$ when this occurs.

2.2.3. CONSISTENT LINEARIZATION OF THE TRACTION UPDATE

In [37] and [42], a numerical tangent stiffness based on finite differences was used to approximate the tangent of the static cohesive relation and the extension with fatigue damage. However, the accuracy of approximating the tangent and robustness depends on the choice of the perturbation and is case-dependent. In addition, the traction update needs to be performed for each perturbation of the displacement jump component, which may not be computationally efficient.

In order to improve the efficiency and robustness, which is crucial in full-laminate analyses, a consistent tangent stiffness matrix is derived below for the static cohesive zone model [42] and the fatigue damage extension [37], including the improved (implicit) fatigue damage update presented in this work.

The traction at current time n is written as a function of displacement jump $[\![\mathbf{u}]\!]$, current damage $\mathcal{D}$ and cycle jump ΔN:

$$\mathbf{t} = \hat{\mathbf{t}}([\![\mathbf{u}]\!], \mathcal{D}([\![\mathbf{u}]\!], \Delta N)) \tag{2.28}$$

The linearized traction update can be expressed as

$$\delta\mathbf{t} = \underbrace{\left(\frac{\partial \hat{\mathbf{t}}([\![\mathbf{u}]\!], \mathcal{D}([\![\mathbf{u}]\!], \Delta N))}{\partial [\![\mathbf{u}]\!]}\right)_{(n)}}_{\mathbf{D}} \delta[\![\mathbf{u}]\!] \tag{2.29}$$

where it is explicitly indicated that the time n is kept constant. The material tangent $\mathbf{D}$ can be identified in this expression as the linear operator that maps an iterative-increment of the displacement jump to an iterative-increment of the traction vector.

By performing partial differentiation and after some re-arrangement, the expression of the material tangent becomes

$$\mathbf{D} = \underbrace{(\mathbf{I} - d\mathbf{P})\mathbf{K}}_{\text{secant stiffness}} - \mathbf{P}\mathbf{K}[\![\mathbf{u}]\!] \frac{\partial d^\mathrm{T}}{\partial [\![\mathbf{u}]\!]} \tag{2.30}$$

Differentiation of the last term in Eq. (2.30) and applying the chain rule gives

$$\frac{\partial d}{\partial [\![\mathbf{u}]\!]} = \frac{\partial d}{\partial \mathcal{D}} \frac{\partial \mathcal{D}}{\partial [\![\mathbf{u}]\!]} + \frac{\partial d}{\partial \Delta_0} \frac{\partial \Delta_0}{\partial [\![\mathbf{u}]\!]} + \frac{\partial d}{\partial \Delta_\mathrm{f}} \frac{\partial \Delta_\mathrm{f}}{\partial [\![\mathbf{u}]\!]} \tag{2.31}$$

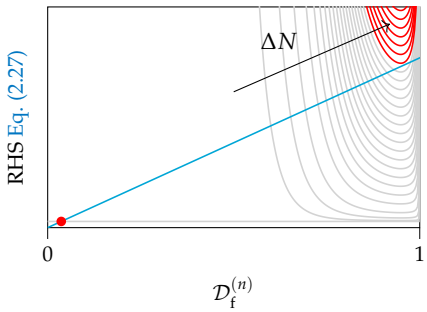

Figure 2.3 Right-hand side of Eq. (2.27) as a function of damage $\mathcal{D}_\mathrm{f}^{(n)}$ (curves in *gray*) at constant equivalent displacement Δ while increasing the cycle increment ΔN starting from $\Delta N = 0$ (horizontal *gray* line). For a given ΔN, the solution of Eq. (2.27) is the intersection with the *blue* line RHS $= \mathcal{D}_\mathrm{f}^{(n)}$. The damage value $\mathcal{D}_0$ of the previous *pseudo* time step n is indicated with •. When the cycle increment is too large, there exists no intersection for $\mathcal{D}_\mathrm{f}^{(n)} \in [\mathcal{D}_0, 1)$ (curves in *red*).

where the partial derivatives $\partial\Delta_0/\partial[\![\mathbf{u}]\!]$ and $\partial\Delta_\mathrm{f}/\partial[\![\mathbf{u}]\!]$ can be further expanded:

$$\frac{\partial\Delta_0}{\partial[\![\mathbf{u}]\!]} = \frac{\partial\Delta_0}{\partial\mathcal{B}}\frac{\partial\mathcal{B}}{\partial[\![\mathbf{u}]\!]} + \frac{\partial\Delta_0}{\partial K_\mathcal{B}}\frac{\partial K_\mathcal{B}}{\partial\mathcal{B}}\frac{\partial\mathcal{B}}{\partial[\![\mathbf{u}]\!]} \tag{2.32}$$

$$\frac{\partial\Delta_\mathrm{f}}{\partial[\![\mathbf{u}]\!]} = \frac{\partial\Delta_\mathrm{f}}{\partial\mathcal{B}}\frac{\partial\mathcal{B}}{\partial[\![\mathbf{u}]\!]} + \frac{\partial\Delta_\mathrm{f}}{\partial K_\mathcal{B}}\frac{\partial K_\mathcal{B}}{\partial\mathcal{B}}\frac{\partial\mathcal{B}}{\partial[\![\mathbf{u}]\!]} + \frac{\partial\Delta_\mathrm{f}}{\partial\Delta_0}\frac{\partial\Delta_0}{\partial[\![\mathbf{u}]\!]} \tag{2.33}$$

The partial derivatives in Eqs. (2.31) to (2.33) can be computed with quantities

already obtained from the traction update algorithm presented before:

$$\frac{\partial d}{\partial \mathcal{D}} = \frac{\Delta_0 \Delta_f}{\left[(\mathcal{D}-1)\Delta_0 - \mathcal{D}\Delta_f\right]^2} \tag{2.34}$$

$$\frac{\partial d}{\partial \Delta_0} = \frac{(\mathcal{D}-1)\mathcal{D}\Delta_f}{\left[(\mathcal{D}-1)\Delta_0 - \mathcal{D}\Delta_f\right]^2} \tag{2.35}$$

$$\frac{\partial d}{\partial \Delta_f} = \frac{(1-\mathcal{D})\mathcal{D}\Delta_0}{\left[(\mathcal{D}-1)\Delta_0 - \mathcal{D}\Delta_f\right]^2} \tag{2.36}$$

$$\frac{\partial \Delta_0}{\partial \mathcal{B}} = \frac{K_{sh}(\llbracket u \rrbracket^0_{sh})^2 - K_n(\llbracket u \rrbracket^0_n)^2}{2\Delta_0 K_{\mathcal{B}}} \mathcal{B}^{\eta_{BK}-1}\eta_{BK} \tag{2.37}$$

$$\frac{\partial \Delta_0}{\partial K_{\mathcal{B}}} = -\frac{\Delta_0}{2K_{\mathcal{B}}} \tag{2.38}$$

$$\frac{\partial \Delta_f}{\partial \mathcal{B}} = \frac{K_{sh}\llbracket u \rrbracket^0_{sh}\llbracket u \rrbracket^f_{sh} - K_n\llbracket u \rrbracket^0_n\llbracket u \rrbracket^f_n}{\Delta_0 K_{\mathcal{B}}} \mathcal{B}^{\eta_{BK}-1}\eta_{BK} \tag{2.39}$$

$$\frac{\partial \Delta_f}{\partial K_{\mathcal{B}}} = -\frac{\Delta_f}{K_{\mathcal{B}}} \tag{2.40}$$

$$\frac{\partial K_{\mathcal{B}}}{\partial \mathcal{B}} = -K_n + K_{sh} \tag{2.41}$$

$$\frac{\partial \mathcal{B}}{\partial \llbracket \mathbf{u} \rrbracket} = \frac{2K_nK_{sh}}{\left(K_n \langle \llbracket u \rrbracket_n \rangle^2 + K_{sh}\llbracket u \rrbracket^2_{sh}\right)^2} \left[-(\llbracket u \rrbracket_{sh})^2 \langle \llbracket u \rrbracket_n \rangle, \llbracket u \rrbracket_{s1} \langle \llbracket u \rrbracket_n \rangle^2, \llbracket u \rrbracket_{s2} \langle \llbracket u \rrbracket_n \rangle^2 \right]^T \tag{2.42}$$

$$\frac{\partial \Delta_f}{\partial \Delta_0} = -\frac{\Delta_f}{\Delta_0} \tag{2.43}$$

During loading, $\partial\mathcal{D}/\partial\llbracket\mathbf{u}\rrbracket$ is non-zero at current time n and global iteration j. Due to the max operator in Eq. (2.21), the term $\partial\mathcal{D}/\partial\llbracket\mathbf{u}\rrbracket$ is not continuous which requires considering each case (static and fatigue loading) separately.

Quasi-static loading When quasi-static damage is larger than fatigue damage, the term $\partial\mathcal{D}/\partial\llbracket\mathbf{u}\rrbracket$ is obtained by partial differentiation of the static damage (Eq. (2.20)):

$$\frac{\partial \mathcal{D}}{\partial \llbracket \mathbf{u} \rrbracket} = \frac{\partial \mathcal{D}_s}{\partial \Delta}\frac{\partial \Delta}{\partial \llbracket \mathbf{u} \rrbracket} + \frac{\partial \mathcal{D}_s}{\partial \Delta_0}\frac{\partial \Delta_0}{\partial \llbracket \mathbf{u} \rrbracket} + \frac{\partial \mathcal{D}_s}{\partial \Delta_f}\frac{\partial \Delta_f}{\partial \llbracket \mathbf{u} \rrbracket} \tag{2.44}$$

with

$$\frac{\partial \Delta}{\partial [\![\mathbf{u}]\!]} = \left(K_{\mathrm{n}}^2 \langle [\![u]\!]_{\mathrm{n}} \rangle^2 + K_{\mathrm{sh}}^2 [\![u]\!]_{\mathrm{sh}}^2\right)^{-3/2} \begin{bmatrix} K_{\mathrm{n}} \langle [\![u]\!]_{\mathrm{n}} \rangle \left[K_{\mathrm{n}}^2 \langle [\![u]\!]_{\mathrm{n}} \rangle^2 + (2K_{\mathrm{sh}}^2 - K_{\mathrm{n}} K_{\mathrm{sh}}) [\![u]\!]_{\mathrm{sh}}^2\right] \\ K_{\mathrm{sh}} [\![u]\!]_{\mathrm{s1}} \left(2K_{\mathrm{n}}^2 \langle [\![u]\!]_{\mathrm{n}} \rangle^2 - K_{\mathrm{n}} K_{\mathrm{sh}} \langle [\![u]\!]_{\mathrm{n}} \rangle^2 + K_{\mathrm{sh}}^2 [\![u]\!]_{\mathrm{sh}}^2\right) \\ K_{\mathrm{sh}} [\![u]\!]_{\mathrm{s2}} \left(2K_{\mathrm{n}}^2 \langle [\![u]\!]_{\mathrm{n}} \rangle^2 - K_{\mathrm{n}} K_{\mathrm{sh}} \langle [\![u]\!]_{\mathrm{n}} \rangle^2 + K_{\mathrm{sh}}^2 [\![u]\!]_{\mathrm{sh}}^2\right) \end{bmatrix} \tag{2.45}$$

$$\frac{\partial \mathcal{D}_{\mathrm{s}}}{\partial \Delta} = \frac{1}{\Delta_{\mathrm{f}} - \Delta_0} \tag{2.46}$$

$$\frac{\partial \mathcal{D}_{\mathrm{s}}}{\partial \Delta_0} = \frac{\Delta - \Delta_{\mathrm{f}}}{(\Delta_{\mathrm{f}} - \Delta_0)^2} \tag{2.47}$$

$$\frac{\partial \mathcal{D}_{\mathrm{s}}}{\partial \Delta_{\mathrm{f}}} = \frac{\Delta_0 - \Delta}{(\Delta_{\mathrm{f}} - \Delta_0)^2} \tag{2.48}$$

Fatigue loading When fatigue damage is larger than quasi-static damage, the term $\partial \mathcal{D} / \partial [\![\mathbf{u}]\!]$ must be determined differently. The implicit damage update in Eq. (2.27) can be recast in residual form as

$$r = \mathcal{D}^{(n)} - \mathcal{D}^{(n-1)} - \Delta N \left[(1-\theta) f_{\mathcal{D}}^{(n-1)} + \theta f_{\mathcal{D}}^{(n)}\right] \tag{2.49}$$

The residual is a function of independent variables $\mathcal{D}$ and $[\![\mathbf{u}]\!]$. Therefore, the variation of the residual is expressed as

$$\delta r = \left(\frac{\partial r}{\partial \mathcal{D}}\right)_{[\![\mathbf{u}]\!]} \delta \mathcal{D} + \left(\frac{\partial r}{\partial [\![\mathbf{u}]\!]}\right)_{\mathcal{D}} \delta [\![\mathbf{u}]\!] \tag{2.50}$$

The *local* damage state at current time n is obtained in every *global* iteration by iteratively solving for the residual to be zero (within a sufficiently small tolerance). Therefore, the variation of the *locally converged* residual does not change between *global* iterations:

$$\delta r = 0 \tag{2.51}$$

which is a consistency condition. Similar to what is done for plasticity models with return mapping algorithms, this consistency condition can be used to obtain a relation between the variation of the displacement jump and the *locally converged* damage variable $\mathcal{D}$ from which the derivative of the damage with respect to displacement jump can be identified:

$$\delta \mathcal{D} = \underbrace{-\frac{\left(\frac{\partial r}{\partial [\![\mathbf{u}]\!]}\right)_{\mathcal{D}}}{\left(\frac{\partial r}{\partial \mathcal{D}}\right)_{[\![\mathbf{u}]\!]}}}_{\frac{\partial \mathcal{D}}{\partial [\![\mathbf{u}]\!]}} \delta [\![\mathbf{u}]\!] \tag{2.52}$$

Applying the chain-rule gives the expressions for the partial derivatives

$$\left(\frac{\partial r}{\partial \mathcal{D}}\right)_{[\![\mathbf{u}]\!]} = \frac{\partial r}{\partial \mathcal{D}} + \frac{\partial r}{\partial \Delta^*}\frac{\partial \Delta^*}{\partial \mathcal{D}} \tag{2.53}$$

$$\left(\frac{\partial r}{\partial [\![\mathbf{u}]\!]}\right)_{\mathcal{D}} = \frac{\partial r}{\partial \Delta}\frac{\partial \Delta}{\partial [\![\mathbf{u}]\!]} + \frac{\partial r}{\partial \Delta^*}\frac{\partial \Delta^*}{\partial [\![\mathbf{u}]\!]} + \sum_{i=1}^{N_\mathcal{P}} \frac{\partial r}{\partial \mathcal{P}_i}\frac{\partial \mathcal{P}_i}{\partial [\![\mathbf{u}]\!]} \tag{2.54}$$

where the last terms after the summation are the partial derivatives of the parameter functions that depend on the displacement jump (for CF20: $\mathcal{P} = \{E, \beta, p\}$). Applying the chain rule to the fourth term in Eq. (2.54) gives

$$\frac{\partial \Delta^*}{\partial [\![\mathbf{u}]\!]} = \frac{\partial \Delta^*}{\partial \Delta_0}\frac{\partial \Delta_0}{\partial [\![\mathbf{u}]\!]} + \frac{\partial \Delta^*}{\partial \Delta_\mathrm{f}}\frac{\partial \Delta_\mathrm{f}}{\partial [\![\mathbf{u}]\!]} \tag{2.55}$$

where $\partial\Delta_0/\partial[\![\mathbf{u}]\!]$ and $\partial\Delta_\mathrm{f}/\partial[\![\mathbf{u}]\!]$ are derived earlier (see Eqs. (2.32) and (2.33)). Performing the differentiation of the other derivatives in Eqs. (2.53) to (2.55) gives

$$\frac{\partial r}{\partial \Delta} = -\Delta N \theta \frac{\partial f_\mathcal{D}}{\partial \Delta} \tag{2.56}$$

$$\frac{\partial r}{\partial \Delta^*} = -\Delta N \theta \frac{\partial f_\mathcal{D}}{\partial \Delta^*} \tag{2.57}$$

$$\frac{\partial r}{\partial \mathcal{D}} = 1 - \Delta N \theta \frac{\partial f_\mathcal{D}}{\partial \mathcal{D}} \tag{2.58}$$

$$\sum_{i=1}^{N_\mathcal{P}} \frac{\partial r}{\partial \mathcal{P}_i}\frac{\partial \mathcal{P}_i}{\partial [\![\mathbf{u}]\!]} = -\Delta N \theta \left[\sum_{i=1}^{N_\mathcal{P}} \frac{\partial f_\mathcal{D}}{\partial \mathcal{P}_i}\frac{\partial \mathcal{P}_i}{\partial \mathcal{B}}\right]\frac{\partial \mathcal{B}}{\partial [\![\mathbf{u}]\!]} \tag{2.59}$$

$$\frac{\partial \Delta^*}{\partial \mathcal{D}} = \Delta_\mathrm{f} - \Delta_0 \tag{2.60}$$

$$\frac{\partial \Delta^*}{\partial \Delta_\mathrm{f}} = \mathcal{D} \tag{2.61}$$

$$\frac{\partial \Delta^*}{\partial \Delta_0} = 1 - \mathcal{D} \tag{2.62}$$

where, for CF20 with $\mathcal{P} = \{E, \beta, p\}$, the term in Eq. (2.59) can be further expanded:

$$\sum_{i=1}^{N_\mathcal{P}} \frac{\partial f_\mathcal{D}}{\partial \mathcal{P}_i}\frac{\partial \mathcal{P}_i}{\partial \mathcal{B}} = \left[\frac{\partial f_\mathcal{D}}{\partial E} + \left(\frac{\partial f_\mathcal{D}}{\partial \beta} + \frac{\partial f_\mathcal{D}}{\partial p}\frac{\partial p}{\partial \beta}\right)\frac{\partial \beta}{\partial E}\right]\frac{\partial E}{\partial C}\frac{\partial C}{\partial \mathcal{B}} \tag{2.63}$$

with

$$\frac{\partial f_{\mathcal{D}}}{\partial \Delta} = \frac{\beta}{\Delta} f_{\mathcal{D}} \tag{2.64}$$

$$\frac{\partial f_{\mathcal{D}}}{\partial \Delta^*} = -\frac{\beta}{\Delta^*} f_{\mathcal{D}} \tag{2.65}$$

$$\frac{\partial f_{\mathcal{D}}}{\partial \mathcal{D}} = \frac{p-\beta}{1-\mathcal{D}} f_{\mathcal{D}} \tag{2.66}$$

$$\frac{\partial f_{\mathcal{D}}}{\partial E} = -\frac{\beta}{E} f_{\mathcal{D}} \tag{2.67}$$

$$\frac{\partial f_{\mathcal{D}}}{\partial \beta} = \left[\ln\left(\frac{\Delta}{\Delta^*}\right) + \ln(1-\mathcal{D}) - \ln(E)\right] f_{\mathcal{D}} \tag{2.68}$$

$$\frac{\partial f_{\mathcal{D}}}{\partial p} = -\frac{f_{\mathcal{D}}}{p+1}\left[1 + (p+1)\ln(1-\mathcal{D})\right] \tag{2.69}$$

$$\frac{\partial E}{\partial C} = \frac{2\epsilon(1-R)}{\left[C\epsilon(R+1) - R + 1\right]^2} \tag{2.70}$$

$$\frac{\partial C}{\partial \mathcal{B}} = -0.42 \tag{2.71}$$

$$\frac{\partial \beta}{\partial E} = \frac{7\eta \ln(10)}{\ln(E)^2 E} \tag{2.72}$$

$$\frac{\partial p}{\partial \beta} = 1 \tag{2.73}$$

2.3. PHANTOM NODE VERSION OF XFEM

The fatigue CZM with the improved damage update is combined with the phantom node version of XFEM [10]. When a certain stress criterion in a bulk integration point is reached, a discontinuity is inserted in the displacement field of the element (see Fig. 2.4). In order to include microstructural information of cracks propagating in the fiber direction, the normal $\mathbf{n}$ of the crack is fixed in the direction perpendicular to the fibers following Van der Meer and Sluys [8].

A discontinuity in the displacement field is achieved by duplicating the original element and expressing the displacement field in terms of the independent displacement fields of the two overlapping sub-elements:

$$\mathbf{u}(\mathbf{x}) = \begin{cases} \mathbf{N}(\mathbf{x})\mathbf{u}_{\mathrm{A}}, \ \mathbf{x} \in \Omega_{\mathrm{A}} \\ \mathbf{N}(\mathbf{x})\mathbf{u}_{\mathrm{B}}, \ \mathbf{x} \in \Omega_{\mathrm{B}} \end{cases} \tag{2.74}$$

where $\mathbf{u}_{\mathrm{A}}$ and $\mathbf{u}_{\mathrm{B}}$ are the vectors containing the nodal DOFs of the sub-elements with original nodes and *phantom nodes*. The connectivity of the sub-elements is

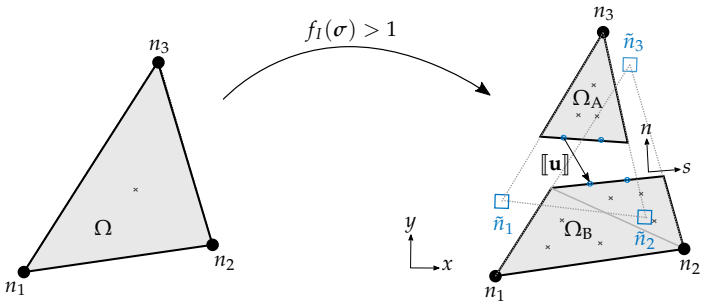

Figure 2.4 Crack insertion in XFEM element. When the stress in a bulk integration point (*left*) satisfies the insertion criterion, a cohesive segment is inserted (*right*).

given as

$$\Omega_A^n = \{\tilde{n}_1, \tilde{n}_2, n_3\} \tag{2.75}$$

$$\Omega_B^n = \{n_1, n_2, \tilde{n}_3\} \tag{2.76}$$

The displacement jump vector along the cohesive segment Γ_d is defined as

$$[\![\mathbf{u}]\!](\mathbf{x}) = \mathbf{N}(\mathbf{x})(\mathbf{u}_A - \mathbf{u}_B),\ \mathbf{x} \in \Gamma_d \tag{2.77}$$

2.3.1. FATIGUE XFEM INSERTION CRITERION

In order to allow for matrix cracks to initiate at arbitrary locations, an XFEM fatigue crack insertion criterion is presented in the following. In the fatigue CZM, fatigue damage already accumulates before the static initiation stress is reached, provided that the stress is above the endurance limit. Therefore, the endurance limit is a natural choice to define as the moment for insertion of cohesive crack segments, which is consistent with the fatigue damage formulation.

The *relative* endurance limit depends on the *local* stress ratio R and mode-mixity $\mathcal{B}$ via Eqs. (2.24) and (2.25). The endurance limit can be computed with the relative endurance limit and the static equivalent strength as

$$\sigma_{\text{end}} = E f_{\mathcal{B}} \tag{2.78}$$

where the static mode-dependent strength $f_{\mathcal{B}}$ is related to the mode-dependent dummy stiffness (Eq. (2.7)) and the equivalent initiation jump (Eq. (2.11)):

$$f_{\mathcal{B}} = K_{\mathcal{B}} \Delta_0 \tag{2.79}$$

Substituting the pure-mode initiation displacement components (Eq. (2.14)) into the expression for the equivalent fracture initiation jump (Eq. (2.11)) and substituting

the result, together with the expression for the mode-dependent dummy stiffness (Eq. (2.7)), into Eq. (2.79) gives

$$f_{\mathcal{B}} = \sqrt{(K_{\mathrm{n}}(1-\mathcal{B}) + \mathcal{B}K_{\mathrm{sh}})\left[f_{\mathrm{n}}^2/K_{\mathrm{n}} + (f_{\mathrm{sh}}^2/K_{\mathrm{sh}} - f_{\mathrm{n}}^2/K_{\mathrm{n}})\mathcal{B}^{\eta_{\mathrm{BK}}}\right]} \tag{2.80}$$

which is an expression in terms of input material model parameters and mode-mixity only. The material model parameters are readily available in a bulk integration point. However, in the absence of a cohesive segment in the XFEM element before crack insertion, Eq. (2.9) cannot be used to compute the displacement-based mode-mixity $\mathcal{B}$. Since the normal $\mathbf{n}$ is fixed in the direction of the fibers and known before crack insertion, the traction in each bulk element can be computed with the bulk stress using $\mathbf{t} = \boldsymbol{\sigma}\mathbf{n}$. By using the fact that before crack insertion damage is zero ($d = 0 \rightarrow t_{\mathrm{n}} = K_{\mathrm{n}}[\![u]\!]_{\mathrm{n}}, t_{\mathrm{sh}} = K_{\mathrm{sh}}[\![u]\!]_{\mathrm{sh}}$), the mode-mixity can be computed in each integration point of a bulk element:

$$\mathcal{B} = \frac{t_{\mathrm{sh}}/K_{\mathrm{sh}}}{\langle t_{\mathrm{n}}\rangle/K_{\mathrm{n}} + t_{\mathrm{sh}}/K_{\mathrm{sh}}} \tag{2.81}$$

from which the endurance limit and the mode-dependent strength can be computed with Eqs. (2.78) to (2.80). The equivalent stress in the bulk integration point is computed with Eq. (2.6). Finally, the XFEM fatigue crack insertion criterion is defined as

$$f_I(\boldsymbol{\sigma}) \equiv \frac{\sigma(\boldsymbol{\sigma})}{\sigma_{\mathrm{end}}(\boldsymbol{\sigma})} > 1.0 \tag{2.82}$$

which represents a surface in stress-space when $f_I(\boldsymbol{\sigma}) = 1.0$ (see Fig. 2.5).

It should be emphasized that at the moment of crack insertion when Eq. (2.82) is satisfied, fatigue damage in the newly inserted cohesive crack segment is zero. Only *after* crack insertion, fatigue damage can accumulate according to the formulation presented in the previous section.

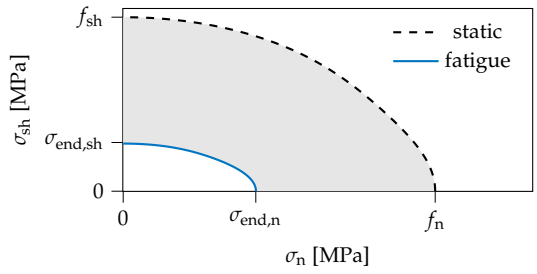

Figure 2.5 Fatigue and static damage initiation surfaces in stress-space.

2.3.2. SHIFTED COHESIVE RELATION

Cohesive XFEM segments are inserted on the fly when the stress criterion is reached. The static initiation stress used in this work is the Benzeggagh-Kenane interpolation of the elastic stored energy [53] before the peak at zero damage (see Eq. (2.79)). For fatigue damage, the fatigue crack insertion criterion presented in the previous section is used.

At the time of insertion, the stress in the material is non-zero. Therefore, following [54], Hille's approach is used [55] where a shift is applied such that the traction for zero opening in the cohesive segment is in equilibrium with the stress in the bulk σ before and after insertion. The shift at the moment of crack insertion is computed as

$$[\![\mathbf{u}]\!]_{\text{shift}} = \mathbf{K}^{-1}\boldsymbol{\sigma}\mathbf{n} \tag{2.83}$$

The updated traction at current time n is computed with Eq. (2.1) where the displacement jump is the sum of the jump passed to the integration point $[\![\mathbf{u}]\!]_{\text{FEM}}$ and the shift $[\![\mathbf{u}]\!]_{\text{shift}}$ (see Fig. 2.6).

2.4. ADAPTIVE CYCLE JUMPING

The cycle increment during fatigue loading is determined with a measure based on the number of *global* Newton-Raphson iterations n_{iter}, following a strategy similar to [56] as previously applied in static loading [8]. The cycle increment ΔN for the next time step $n+1$ is computed from the current (converged) time step n as

$$\Delta N^{(n+1)} = c^{-\left(\frac{n_{\text{iter}} - n_{\text{iter}}^{\text{opt}}}{\xi}\right)} \Delta N^{(n)} \tag{2.84}$$

where c, ξ and $n_{\text{iter}}^{\text{opt}}$ are model parameters. If convergence is not reached within a specified maximum number of iterations $n_{\text{iter}}^{\max}$, the step is cancelled and restarted with a reduced cycle increment $\Delta N^{(n)} \leftarrow c_{\text{red}} \Delta N^{(n)}$.

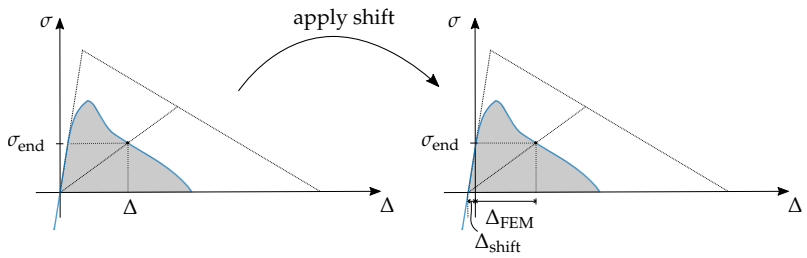

Figure 2.6 Shifted fatigue cohesive zone model.

2.5. SINGLE COHESIVE XFEM ELEMENT TEST

Firstly, a simple case under uniaxial tension is simulated (see Fig. 2.7). The maximum applied stress level is $\sigma^{\max} = 6\,\text{MPa}$. The tensile strength, mode-I fracture energy and dummy stiffness are $f_t = 10\,\text{MPa}$, $G_{Ic} = 0.1\,\text{N mm}^{-1}$ and $K = 10^4\,\text{N mm}^{-3}$. The fatigue model parameters are $p = \beta$, $\eta = 0.8$ and $\epsilon = 0.2$. The XFEM crack is inserted in the middle element when the applied stress $\sigma^{\max} = 0.2 f_t$. For the case of constant tension, the damage evolution can be analytically derived as shown in [49]. The time to failure is given with the following equation:

$$N_{\text{fail}} = \bar{N}(\sigma^{\max}) = \gamma E^{\beta} \left(\frac{\sigma^{\max}}{f_t}\right)^{-\beta} \left[1 - \left(\frac{\sigma^{\max}}{f_t}\right)^{p+1}\right] \tag{2.85}$$

where $\gamma = 10^7$ (see Eq. (2.22)).

In the case of the maximum stress level considered in this example, the damage state at which the material point is considered to have failed is equal to $\mathcal{D}_{\text{fail}} = 1 - \sigma^{\max}/f_t = 0.4$.

The damage evolution as a result of three different time integration parameter values $\theta \in \{0, 0.5, 1\}$ (see Eq. (2.27)), corresponding to Euler forward, trapezoidal rule and Euler backward, is shown in Fig. 2.8. When the step size is sufficiently small, as in the case with $\Delta N = 10$, all three methods show good correspondence with the exact analytical result. When the step size is increased to $\Delta N = 1000$, the trapezoidal rule with $\theta = 0.5$ results in the most accurate response as it is second-order accurate, while Euler forward and Euler backward underestimate and overestimate the damage accumulation, respectively. Also note that with $\Delta N = 1000$, the final damage $\mathcal{D}_{\text{fail}} = 0.4$ is not reached. This is caused by the fact that in the constant stress simulation, no equilibrium solution exists when $\mathcal{D} > \mathcal{D}_{\text{fail}}$.

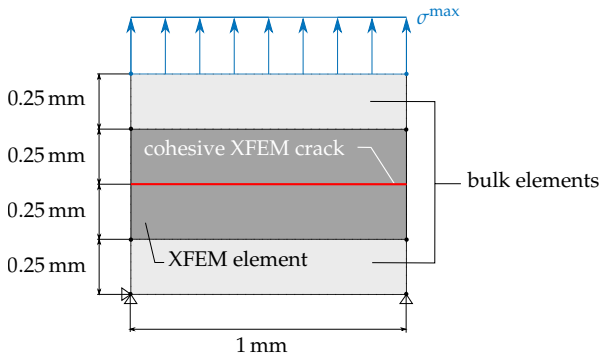

Figure 2.7 Specimen dimensions of single element test.

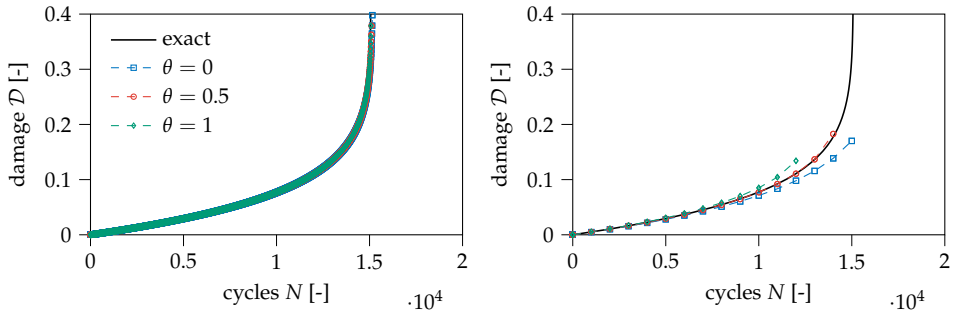

Figure 2.8 Damage evolution with two different constant cycle increments: $\Delta N = 10$ (*left*) and $\Delta N = 1000$ (*right*).

The simulations are also performed with the adaptive cycle jump scheme described in Sec. 2.4, where the cycle increment size ΔN is chosen based on the convergence characteristics from the previous *pseudo* time step. The damage evolution is shown in Fig. 2.9 on the *left*. The number of elapsed cycles in each *pseudo* time step as a result of the accumulation of the (adaptive) cycle increments is shown in Fig. 2.9 on the *right*. It can be observed that the implicit damage update with adaptive stepping based on global convergence behavior is capable of tracing the full evolution of damage with high accuracy and efficient time stepping.

The exercise is repeated with four different stress levels. The corresponding number of cycles to failure is plotted on the underlying S-N curve that serves as input for the model in Fig. 2.10. A good match is obtained with the numerical simulations, which verifies the XFEM implementation with shifted cohesive relation and implicit fatigue damage update.

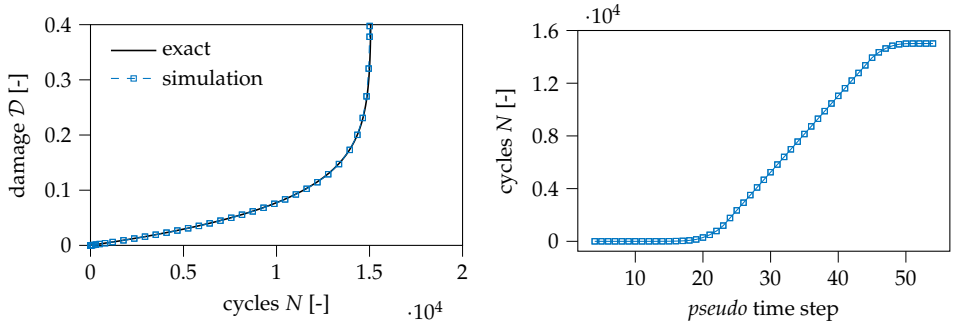

Figure 2.9 Damage evolution (*left*) and elapsed cycles per *pseudo* time step with adaptive cycle increment ΔN (*right*).

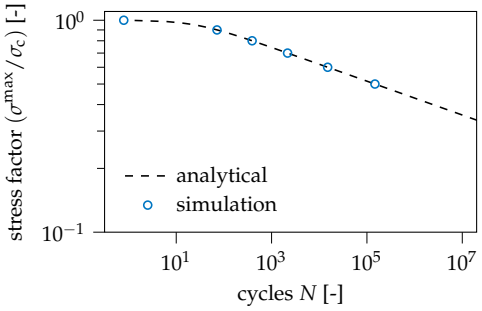

Figure 2.10 Verification of the input at different stress levels.

2.6. DOUBLE CANTILEVER BEAM TEST

The improved performance of the fatigue CZM in simulating fatigue crack growth in a DCB test is compared to the existing formulation in [37]. For this purpose, the case recently studied in [57] with optimal fatigue parameters is used for comparison. The results are compared with the experiments done by Renart et al. [58]. The plies have height $h = 1.472\,\text{mm}$, width 25 mm and an initial crack length $a_0 = 51.2\,\text{mm}$. The computational model is shown in Fig. 2.11.

Each arm of the DCB specimen is modeled with 2D plane strain bilinear quadrilateral elements with unit thickness. The bulk material is orthotropic linear elastic and the static interface material properties and optimal fatigue model parameters determined in [57] are given in Tab. 2.1. Furthermore, normal dummy stiffness $K_n = 2 \times 10^5\,\text{N mm}^{-3}$ is used. In order to drive the fatigue cracking process, displacement control is used with a maximum applied displacement $u_p^{\max} = 5\,\text{mm}$ and *global* load-ratio $R = 0.1$.

2.6.1. COMPARISON OF TIME INTEGRATION SCHEMES

To compare the performance of the implicit damage update with the explicit update, constant cycle increments $\Delta N \in \{10, 20, 50, 100\}$ are used. For the implicit scheme,

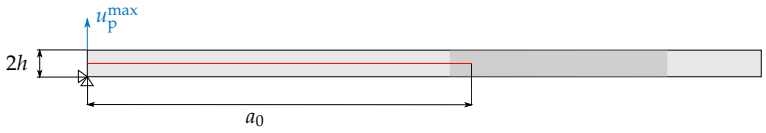

Figure 2.11 Computational model of the DCB specimen. The element width is 0.05 mm in the refined zone (region in dark grey) and 0.25 mm outside this zone (region in light grey). Eight elements are used across the thickness of each arm.

Table 2.1 Ply material properties for the DCB specimen example. Taken from [57].

elastic constants ply		fracture properties interface		fatigue parameters	
E_1	154 GPa	f_n	30 MPa	η	0.8757
$E_2 = E_3$	8.5 GPa	G_{Ic}	0.305 N mm^{-1}	ϵ	0.2628
$G_{12} = G_{13}$	4.2 GPa			p	$\beta + 0.915$
$\nu_{12} = \nu_{13}$	0.35				
ν_{23}	0.4				

the numerical time integration parameter is set to $\theta = 0.5$, which reduces to the trapezoidal rule with second-order accuracy. Fig. 2.12 shows the crack extension Δa as a function of number of cycles N, which clearly indicates the strong influence of the step size for the explicit fatigue damage update, whereas with the implicit scheme, the global response is insensitive to the step size in the investigated range.

Fig. 2.13 shows the traction-opening history of several integration points along the interface for the case with $\Delta N = 50$. With the explicit scheme, numerically unstable damage growth can be observed which is fully removed with the implicit scheme where damage grows during fatigue loading in a continuous fashion. The effect of numerically unstable damage growth is most profound for integration points in the cohesive zone (for which $\mathcal{D} \in (0, 1)$) after the static ramp-up phase, where a sharp drop in stiffness is observed for the first fatigue cycles (see Fig. 2.13).

Under displacement control, the energy release rate (ERR) reduces as the crack extends and the compliance increases. Since the ERR is closely related to the area under the traction-opening relation, points move farther away from the softening line, which in turn decreases the rate of fatigue damage accumulation $\mathrm{d}\mathcal{D}/\mathrm{d}N$ as described by the underlying S-N curve. Consequently, larger step sizes can be used

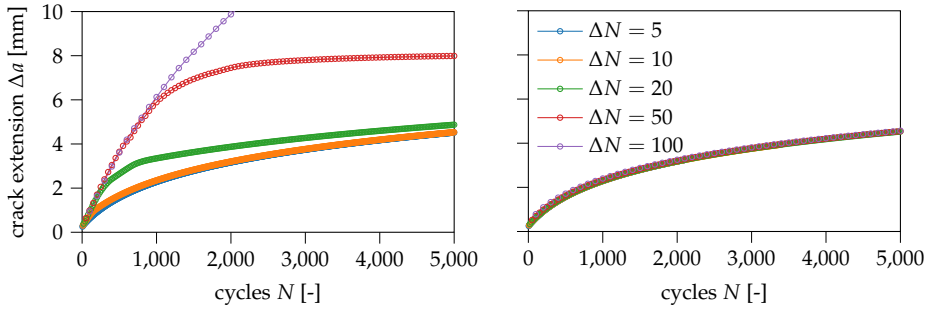

Figure 2.12 Crack extension with number of cycles as a result of explicit (*left*) and implicit (*right*) fatigue damage update.

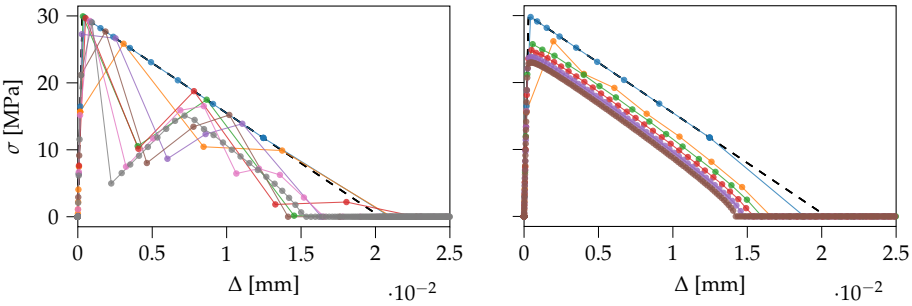

Figure 2.13 Traction-opening histories of several integration points along in the interface as a result of explicit (*left*) and implicit (*right*) fatigue damage update.

as the crack propagates.

2.6.2. SIMULATIONS WITH ADAPTIVE CYCLE JUMPING

Under displacement control, the energy release rate (ERR) reduces and a sweep over several ERR values is performed in a single DCB simulation. Therefore, the crack growth rate can be computed as a function of the ERR at the maximum load level and compared to the response of the experimental Paris relation. The crack length a is computed numerically and is based on the average damage along the interface following [46]:

$$a = a_0 + \sum_{\mathrm{ip}=1}^{N_{\mathrm{ip}}} \mathcal{D}_{\mathrm{ip}} J_{\mathrm{ip}} w_{\mathrm{ip}} \tag{2.86}$$

where $J_{\mathrm{ip}} w_{\mathrm{ip}}$ is the product of the Jacobian and the integration weight. The crack growth rate at time step n is then approximated with Euler backward differentiation:

$$\left.\frac{\mathrm{d}a}{\mathrm{d}N}\right|^{(n)} \approx \frac{a^{(n)} - a^{(n-1)}}{\Delta N} \tag{2.87}$$

The ERR at maximum load $G_{\mathrm{I}}^{\max}$ is computed according to the ASTM D5528 standard [59]:

$$G_{\mathrm{I}}^{\max} = \frac{3 F^{\max} u_{\mathrm{p}}^{\max}}{2b(a + \Delta_{\mathrm{cor}})} \tag{2.88}$$

where $F^{\max}$ is the reaction force at the node where $u_{\mathrm{p}}^{\max}$ is applied (see Fig. 2.11), b is the specimen width and Δ_{cor} takes into account the effect of finite rotations (here $\Delta_{\mathrm{cor}} = 6.2\,\mathrm{mm}$). The computed crack growth rate vs ERR is shown in Fig. 2.14, from which it can be observed that a good match is obtained with the experimental results.

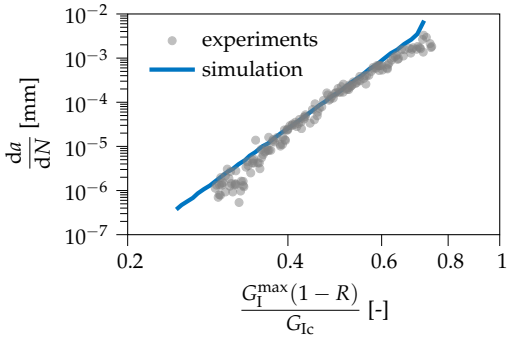

Figure 2.14 Paris relation with simulation and with experimental results from [58].

The complete evolution of the traction is shown in Fig. 2.15, from which three phases can be distinguished. First, the maximum load is applied quasi-statically. When the first load cycles are applied (shown in black), the fracture process continuous to develop into a complete cohesive zone during the *onset phase* (shown in red). When the process zone has fully developed, propagation of the crack takes place (shown in blue).

2.7. OPEN-HOLE $[\pm 45]$-LAMINATE

A $[\pm 45]$-laminate is simulated in order to demonstrate the capabilities of the developed fatigue failure framework to deal with progressive laminate failure. This case was previously studied in the context of static loading in Ref. [9] for the purpose of simulating the interaction between matrix cracking and delamination without fiber fracture. The effect of thermal residual stresses as a result of the curing process [46] is not taken into account. This requires an extension of the framework to capture a varying stress ratio, which will be addressed in Chapter 3.

Modeling preliminaries The laminate has dimensions 38 mm $\times$ 16 mm $\times$ 1 mm and contains a hole in the middle with a diameter of 6.4 mm. The plies have a thickness $t = 0.5$ mm and are modeled with plane stress XFEM elements, whereas delamination between the plies is modeled with zero-thickness interface elements. The constitutive relation of the matrix cohesive segments and interface integration points is described with the improved fatigue CZM presented in Sec. 2.2. The material properties and the fatigue model parameters are given in Tab. 2.2. The dummy stiffness of matrix cracks in normal direction is $K_n = 1.0 \times 10^5\,\mathrm{N\,mm^{-3}}$, whereas K_{sh} is adapted according to Eq. (2.4). The shear stiffness of the interface is related to the shear modulus G_{12} and thickness of the ply ($K_d = G_{12}/\frac{1}{2}t = 22\,000\,\mathrm{N\,mm^{-3}}$)

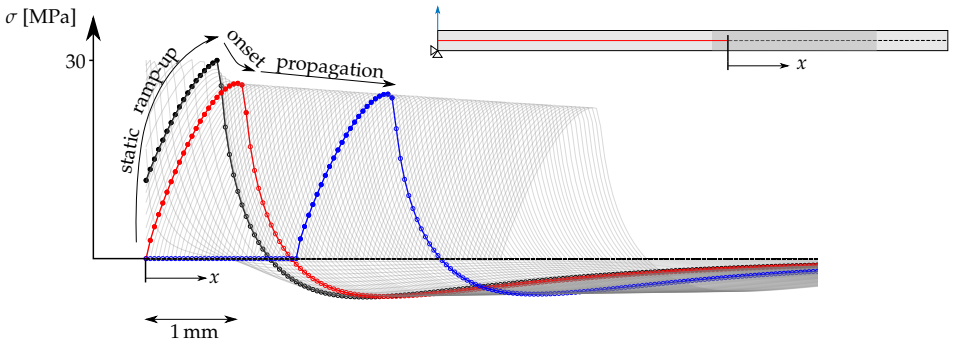

Figure 2.15 Traction profile evolution along the interface at different time steps shown in gray. The stages of the static ramp-up, fatigue crack onset and propagation are indicated with black, red and blue colors respectively.

according to [9], taking into account the effect of out-of-plane ply shear deformation. The computational domain is discretized using linear (constant strain) triangular elements with single-point Gauss integration. Upon crack insertion, a two-point Gauss scheme is employed in the XFEM crack segment. Three-point Newton-Cotes is used for the interface, following [9]. Furthermore, displacement control is used. The maximum applied displacement is $u_{\mathrm{p}}^{\max} = 0.1\,\mathrm{mm}$ with *global* load ratio $R = 0.1$.

Crack segments are inserted when the stress in the bulk integration point reaches the stress endurance limit (see Sec. 2.3.1). The shift is applied in order to ensure traction continuity before and after insertion of the crack, which improves the convergence characteristics. At the end of a converged *pseudo* time step, a maximum of 100 segments can be inserted at a time. After insertion, the *global* Newton-Raphson loop is re-entered to equilibrate the solution with new crack segments [54]. With the XFEM representation, cracks can initiate at arbitrary locations within a predefined crack-spacing width l_{c}.

Eq. (2.84) is used to adapt the cycle increment ΔN throughout the simulations. The used stepping parameters are $c = 2$, $\xi = 2$, $n_{\mathrm{iter}}^{\mathrm{opt}} = 4$, $n_{\mathrm{iter}}^{\max} = 10$ and $c_{\mathrm{red}} = 0.6$.

Table 2.2 Ply material properties for open-hole numerical example.

elastic constants		**fracture properties**		**fatigue parameters**	
E_1	122.7 GPa	f_{n}	80 MPa	η	0.95
E_2	10.1 GPa	f_{sh}	100 MPa	ϵ	0.25
G_{12}	5.5 GPa	G_{Ic}	$0.969\,\mathrm{N\,mm^{-1}}$	p	β
ν_{12}	0.25	G_{IIc}	$1.719\,\mathrm{N\,mm^{-1}}$		
		η_{BK}	2.284		

Global response and damage development Simulations are performed with crack-spacing parameter $l_c = 0.9$. The progressive nature of damage development is depicted in Fig. 2.16, which shows the reduction of *global* stiffness (reaction force over applied displacement at the end) as a function of cycle number N. At the indicated time instances, the damage profiles in the interface and the XFEM matrix cracks are shown. From these figures, several stages of damage development can be distinguished. Firstly, a gradual stiffness reduction takes place due to matrix cracking and delamination of the (small) triangular areas near the hole, followed by a rapid damage development (from (a) to (c)) due to combined matrix cracking and major delamination on one side of the hole. After this phase, a third stage of matrix cracking on the opposite side takes place (from (d) to (f)), leading to delamination with sharp stiffness drops until complete failure of the laminate. The deformed mesh is shown in Fig. 2.17, from which it can be observed that a transition from distributed to localized failure is obtained.

Time-step dependence The influence of the adaptive cycle jumping scheme on the accuracy of the simulation is illustrated in Fig. 2.18, where the stiffness reduction is shown on the top with two different adaptive stepping parameters, corresponding to small and large cycle increments as depicted in Fig. 2.18 on the left. For the small increment simulation, the maximum cycle jump is $\Delta N^{\max} = 1000$. It can be observed that the progression of damage and the time to failure is only slightly affected by the large step sizes, thereby validating the choice to use *global* iterations as a measure for determining the cycle increment ΔN with implicit time integration of the fatigue damage rate function. Moreover, Fig. 2.18 shows that the cycle jumping strategy with consistent tangent and implicit fatigue damage update allows a seamless transition through periods that require small steps and periods that allow for large cycle increments, with minimal influence on the accuracy.

Crack-spacing parameter dependence The exercise is repeated for several crack-spacing parameter values $l_c(\text{mm}) \in \{0.7, 0.9, 1.1, 1.3\}$. Moreover, a case with two cracks per ply at predefined locations is included. The cracks are inserted in each ply in the direction of the fibers and tangential to the hole. The *global* stiffness reduction is shown in Fig. 2.19. An interesting observation is that allowing more than two cracks per ply has a significant positive effect on the fatigue life of the considered laminate. This can be explained by the fact that matrix cracking results in a reduction of stress concentrations in the interface and thus less fatigue damage accumulation. Another observation is that the response varies slightly with different crack-spacing parameter values. However, the discrepancy is not monotonic, in the sense that

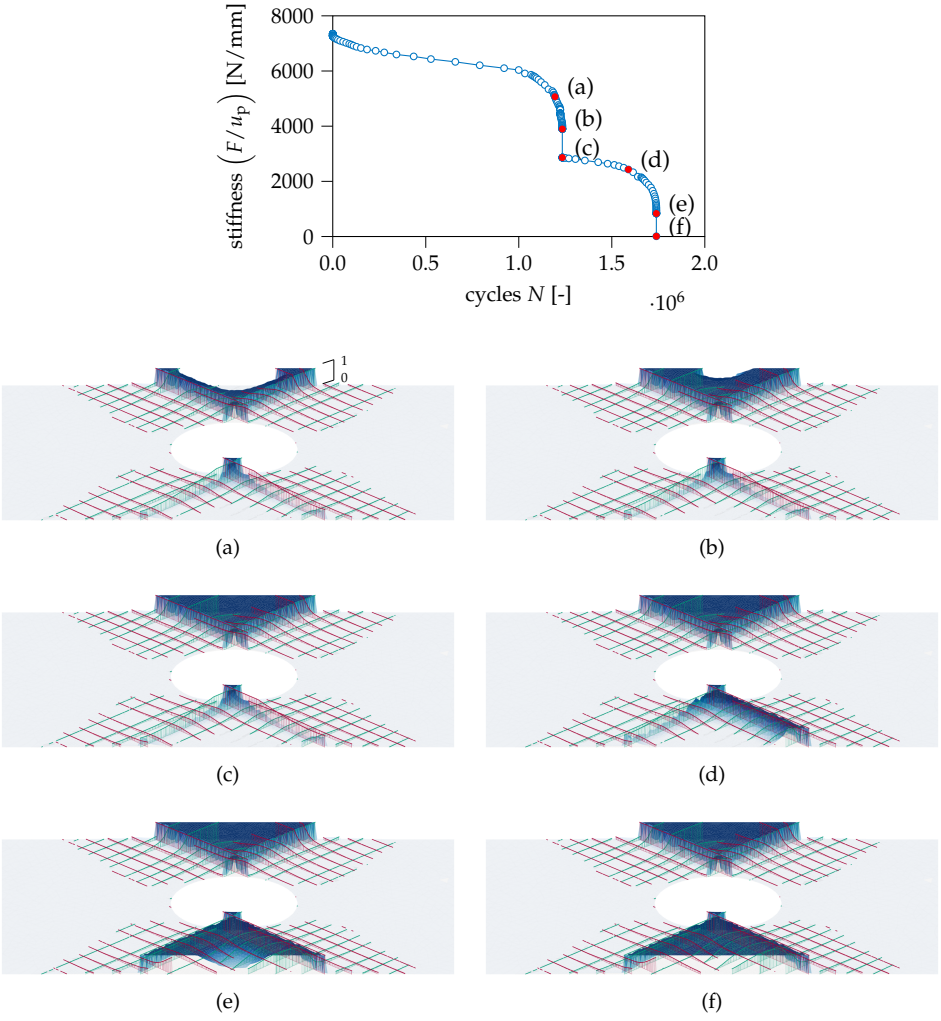

Figure 2.16 Stiffness reduction as a function of number of cycles N (*top*) and damage evolution at indicated time instances in interface (in *blue*) and XFEM matrix cracks in top ply (in *red*) and bottom ply (in *green*).

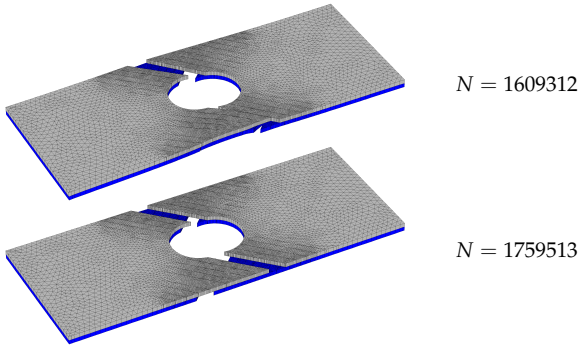

Figure 2.17 Deformations in the laminate showing a transition from distributed to localized failure.

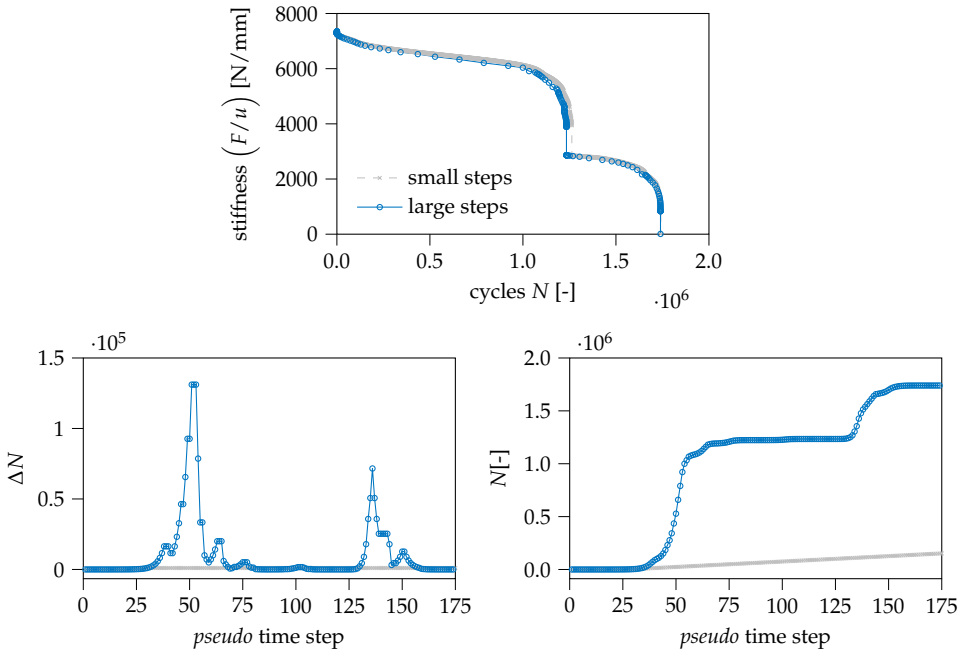

Figure 2.18 Influence of the cycle jump size: stiffness reduction with two different cycle jump parameters corresponding to small and large step sizes (*top*); cycle increments per *pseudo* time step (*left*); accumulation of fatigue cycles throughout the simulation steps (*right*). The simulation with the small step strategy required more than 1500 time steps, whereas with the larger step sizes the simulation finished in 174 time steps.

reducing the spacing does not always lead to an increase in fatigue life. In fact, the difference can be explained by analyzing Fig. 2.20, which depicts the damage in the XFEM matrix cracks in the bottom ply for each spacing parameter value l_c. It can be observed that the crack density and patterns are different, which explains a different progression of stiffness reduction as observed in Fig. 2.19. However, when the response is shown on a log-scale, as is common practice with fatigue analysis, the difference vanishes.

Fig. 2.21 shows the response in four integration points for the case of a crack spacing parameter $l_c = 0.9\,\text{mm}$. As it can be observed, two of the selected points completely separate, while the other integration points unload. This indicates that not necessarily all XFEM cracks that have been inserted accumulate damage until complete material point failure, thereby allowing for simulating the transition from distributed damage to localized failure. Another interesting fact is that the traction-separation response is not parallel to the static softening line, as is the case with the simulated DCB case in the previous section (*cf.* Sec. 2.6.1), indicating the accurate time integration of the damage evolution equation.

2.8. CONCLUSION

A numerical framework for simulating progressive fatigue failure has been presented in this chapter. The recently proposed fatigue cohesive zone model by Dávila, which covers initiation and propagation, has been improved with an implicit time integration scheme and consistent linearization of both the underlying quasi-static and the fatigue cohesive relation. Furthermore, the fatigue cohesive zone model has been combined with XFEM for modeling mesh-independent transverse matrix cracks in full-laminate analyses.

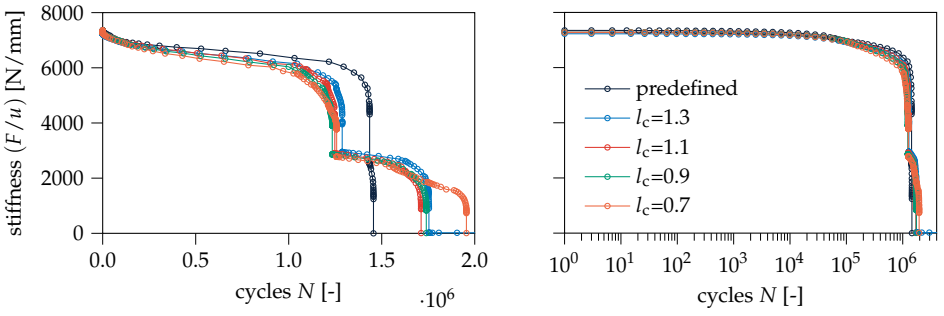

Figure 2.19 Influence of the spacing parameter l_c on the simulation results on two different scales: linear (*left*) and log-scale (*right*).

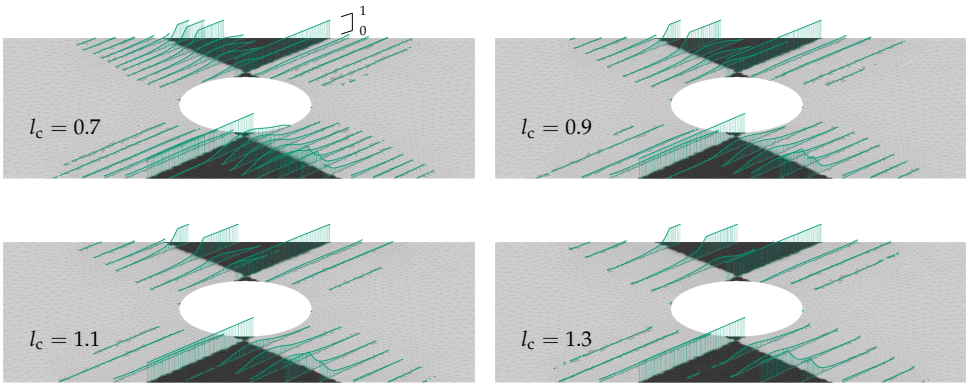

Figure 2.20 Final damage $\mathcal{D}$ in XFEM cracks in bottom ply (shown in *green*) for different crack spacing parameter values l_c. The delaminated area in the interface is shown in *dark gray*.

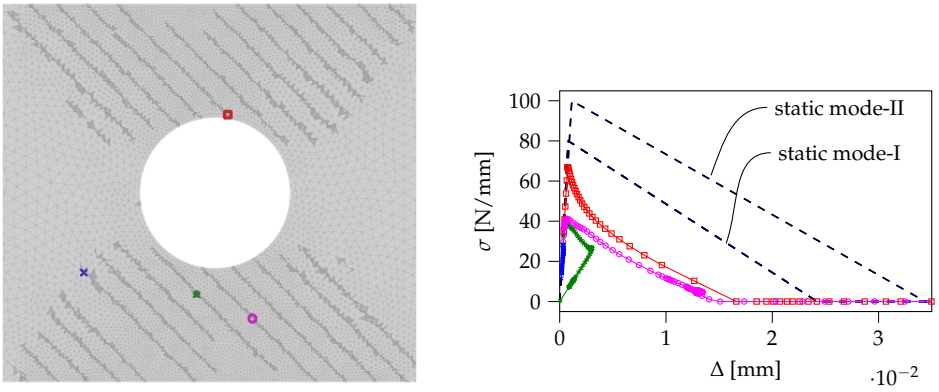

Figure 2.21 Traction-opening histories (*right*) of four XFEM integration points at different crack locations in the ply (*left*).

It has been shown with numerical examples that the improved damage update results in more accurate and efficient analyses. The capabilities of the numerical framework have been demonstrated with the simulation of an open-hole [±45]-laminate under fatigue loading. The numerical model can accurately simulate the interaction of transverse matrix cracking and delamination. A slight sensitivity to the numerical crack-spacing parameter has been observed, although within acceptable range for predicting fatigue life.

REFERENCES

[1] M. R. Wisnom, S. R. Hallett, The role of delamination in strength, failure mechanism and hole size effect in open hole tensile tests on quasi-isotropic laminates, *Composites Part A: Applied Science and Manufacturing* 40 (4) (2009) 335–342.

[2] B. G. Green, M. R. Wisnom, S. R. Hallett, An experimental investigation into the tensile strength scaling of notched composites, *Composites Part A: Applied Science and Manufacturing* 38 (3) (2007) 867–878.

[3] O. J. Nixon-Pearson, S. R. Hallett, P. J. Withers, J. Rouse, Damage development in open-hole composite specimens in fatigue. Part 1: Experimental investigation, *Composite Structures* 106 (2013) 882–889.

[4] F. Aymerich, M. S. Found, Response of notched carbon/PEEK and carbon/epoxy laminates subjected to tension fatigue loading, *Fatigue and Fracture of Engineering Materials and Structures* 23 (8) (2000) 675–683.

[5] B. Aidi, M. K. Philen, S. W. Case, Progressive damage assessment of centrally notched composite specimens in fatigue, *Composites Part A: Applied Science and Manufacturing* 74 (2015) 47–59.

[6] W. G. Jiang, S. R. Hallett, B. G. Green, M. R. Wisnom, A concise interface constitutive law for analysis of delamination and splitting in composite materials and its application to scaled notched tensile specimens, *International Journal for Numerical Methods in Engineering* 69 (9) (2007) 1982–1995.

[7] S. R. Hallett, B. G. Green, W. G. Jiang, M. R. Wisnom, An experimental and numerical investigation into the damage mechanisms in notched composites, *Composites Part A: Applied Science and Manufacturing* 40 (5) (2009) 613–624.

[8] F. P. van der Meer, L. J. Sluys, A phantom node formulation with mixed mode cohesive law for splitting in laminates, *International Journal of Fracture* 158 (2) (2009) 107–124.

[9] F. P. van der Meer, L. J. Sluys, Mesh-independent modeling of both distributed and discrete matrix cracking in interaction with delamination in composites, *Engineering Fracture Mechanics* 77 (4) (2010) 719–735.

[10] A. Hansbo, P. Hansbo, A finite element method for the simulation of strong and weak discontinuities in solid mechanics, *Computer Methods in Applied Mechanics and Engineering* 193 (33-35) (2004) 3523–3540.

[11] B. Y. Chen, T. E. Tay, S. T. Pinho, V. B. Tan, Modelling the tensile failure of composites with the floating node method, *Computer Methods in Applied Mechanics and Engineering* 308 (2016) 414–442.

[12] B. Y. Chen, S. T. Pinho, N. V. De Carvalho, P. M. Baiz, T. E. Tay, A floating node method for the modelling of discontinuities in composites, *Engineering Fracture Mechanics* 127 (2014) 104–134.

[13] M. J. Swindeman, E. V. Iarve, R. A. Brockman, D. H. Mollenhauer, S. R. Hallett, Strength prediction in open hole composite laminates by using discrete damage modeling, *AIAA Journal* 51 (4) (2013) 936–945.

[14] B. Y. Chen, T. E. Tay, P. M. Baiz, S. T. Pinho, Numerical analysis of size effects on open-hole tensile composite laminates, *Composites Part A: Applied Science and Manufacturing* 47 (1) (2013) 52–62.

[15] V. Achard, C. Bouvet, B. Castanié, C. Chirol, Discrete ply modelling of open hole tensile tests, *Composite Structures* 113 (1) (2014) 369–381.

[16] L. F. Kawashita, A. Bedos, S. R. Hallett, Modelling mesh independent transverse cracks in laminated composites with a simplified cohesive segment method, *Computers, Materials and Continua* 32 (2) (2012) 133–158.

[17] E. V. Iarve, K. Hoos, M. Braginsky, E. Zhou, D. H. Mollenhauer, Progressive failure simulation in laminated composites under fatigue loading by using discrete damage modeling, *Journal of Composite Materials* 51 (15) (2016) 2143–2161.

[18] Z. Ma, J. Chen, Q. Yang, Z. Li, X. Su, Progressive fracture analysis of the open-hole composite laminates: Experiment and simulation, *Composite Structures* 262 (2021) 113628.

[19] O. Falcó, R. L. Ávila, B. Tijs, C. S. Lopes, Modelling and simulation methodology for unidirectional composite laminates in a Virtual Test Lab framework, *Composite Structures* 190 (2018) 137–159.

[20] M. Q. Le, H. Bainier, D. Néron, C. Ha-Minh, P. Ladevèze, On matrix cracking and splits modeling in laminated composites, *Composites Part A: Applied Science and Manufacturing* 115 (2018) 294–301.

[21] J. F. Chen, E. V. Morozov, K. Shankar, Simulating progressive failure of composite laminates including in-ply and delamination damage effects, *Composites Part A: Applied Science and Manufacturing* 61 (2014) 185–200.

[22] C. Wang, C. Zhang, Discussions on extension of traditional cohesive element for delamination modeling of laminates used in combination with phantom node intraply elements, *Composite Structures* 261 (2021) 113588.

[23] O. J. Nixon-Pearson, S. R. Hallett, P. W. Harper, L. F. Kawashita, Damage development in open-hole composite specimens in fatigue. Part 2: Numerical modelling, *Composite Structures* 106 (2013) 890–898.

[24] P. W. Harper, S. R. Hallett, A fatigue degradation law for cohesive interface elements – Development and application to composite materials, *International Journal of Fatigue* 32 (11) (2010) 1774–1787.

[25] L. F. Kawashita, S. R. Hallett, A crack tip tracking algorithm for cohesive interface element analysis of fatigue delamination propagation in composite materials, *International Journal of Solids and Structures* 49 (21) (2012) 2898–2913.

[26] W.-T. Lu, Z. Gao, H. K. Adluru, K. H. Hoos, W. P. Seneviratne, D. H. Mollenhauer, E. V. Iarve, Fatigue damage modeling in laminated composite by using Rx-FEM and strength tracking method, *Composites Part A: Applied Science and Manufacturing* 163 (2022) 107199.

[27] C. Tao, S. Mukhopadhyay, B. Zhang, L. F. Kawashita, J. Qiu, S. R. Hallett, An improved delamination fatigue cohesive interface model for complex three-dimensional multi-interface cases, *Composites Part A: Applied Science and Manufacturing* 107 (2018) 633–646.

[28] J. Llobet, P. Maimí, A. Turon, B. Bak, E. Lindgaard, L. Carreras, Y. Essa, F. Martin de la Escalera, A continuum damage model for composite laminates: Part IV-Experimental and numerical tests, *Mechanics of Materials* 154 (2021) 103686.

[29] C. Tao, C. Zhang, H. Ji, J. Qiu, A Paris-law-informed neural fatigue cohesive model and its application to open-hole composite laminates, *International Journal of Solids and Structures* 267 (2023) 112158.

[30] P. Paris, M. Gomes, W. Anderson, A rational analytic theory of fatigue, *Trend Engineering* 388 (1961;13(1):9–14) (1961).

[31] B. L. V. Bak, A. Turon, E. Lindgaard, E. Lund, A simulation method for high-cycle fatigue-driven delamination using a cohesive zone model, *International Journal for Numerical Methods in Engineering* 106 (3) (2016) 163–191.

[32] M. Latifi, F. P. van der Meer, L. J. Sluys, A level set model for simulating fatigue-driven delamination in composites, *International Journal of Fatigue* 80 (2015) 434–442.

[33] A. Turon, J. Costa, P. Camanho, C. Dávila, Simulation of delamination in composites under high-cycle fatigue, *Composites Part A: Applied Science and Manufacturing* 38 (11) (2007) 2270–2282.

[34] L. Carreras, A. Turon, B. L. Bak, E. Lindgaard, J. Renart, F. Martin de la Escalera, Y. Essa, A simulation method for fatigue-driven delamination in layered structures involving non-negligible fracture process zones and arbitrarily shaped crack fronts, *Composites Part A: Applied Science and Manufacturing* 122 (2019) 107–119.

[35] A. Amiri-Rad, M. Mashayekhi, A Cohesive Zone Approach for Fatigue-Driven Delamination Analysis in Composite Materials, *Applied Composite Materials* 24 (4) (2017) 751–769.

[36] A. Amiri-Rad, M. Mashayekhi, F. P. van der Meer, Cohesive zone and level set method for simulation of high cycle fatigue delamination in composite materials, *Composite Structures* 160 (2017) 61–69.

[37] C. G. Dávila, From S-N to the Paris law with a new mixed-mode cohesive fatigue model for delamination in composites, *Theoretical and Applied Fracture Mechanics* 106 (2020) 102499.

[38] M. May, S. R. Hallett, A combined model for initiation and propagation of damage under fatigue loading for cohesive interface elements, *Composites Part A: Applied Science and Manufacturing* 41 (12) (2010) 1787–1796.

[39] M. May, R. Pullin, M. Eaton, C. Featherston, S. R. Hallett, An advanced model for initiation and propagation of damage under fatigue loading - part II: Matrix cracking validation cases, *Composite Structures* 93 (9) (2011) 2350–2357.

[40] S. Nojavan, D. Schesser, Q. D. Yang, An in situ fatigue-CZM for unified crack initiation and propagation in composites under cyclic loading, *Composite Structures* 146 (2016) 34–49.

[41] A. Turon, P. P. Camanho, J. Costa, C. G. Dávila, A damage model for the simulation of delamination in advanced composites under variable-mode loading, *Mechanics of Materials* 38 (11) (2006) 1072–1089.

[42] A. Turon, E. V. González, C. Sarrado, G. Guillamet, P. Maimí, Accurate simulation of delamination under mixed-mode loading using a cohesive model with a mode-dependent penalty stiffness, *Composite Structures* 184 (2018) 506–511.

[43] G. Allegri, A unified formulation for fatigue crack onset and growth via cohesive zone modelling, *Journal of the Mechanics and Physics of Solids* 138 (2020) 103900.

[44] A. Raimondo, C. G. Dávila, C. Bisagni, Cohesive analysis of a 3D benchmark for delamination growth under quasi-static and fatigue loading conditions, *Fatigue and Fracture of Engineering Materials and Structures* (2022).

[45] L. Carreras, J. Renart, A. Turon, J. Costa, B. L. Bak, E. Lindgaard, F. Martin de la Escalera, Y. Essa, A benchmark test for validating 3D simulation methods for delamination growth under quasi-static and fatigue loading, *Composite Structures* 210 (2019) 932–941.

[46] M. W. Joosten, C. G. Dávila, Q. Yang, Predicting fatigue damage in composites subjected to general loading conditions, *Composites Part A: Applied Science and Manufacturing* 156 (2022) 106862.

[47] I. Leciñana, J. Renart, A. Turon, J. Zurbitu, B. Tijs, Characterization and analysis of the mode I interlaminar fatigue behaviour of thermoplastic composites considering R -curve effects, *Engineering Fracture Mechanics* (2023) 109273. .

[48] Y. J. Liang, C. G. Dávila, E. V. Iarve, A reduced-input cohesive zone model with regularized extended finite element method for fatigue analysis of laminated composites in Abaqus, *Composite Structures* 275 (2021) 114494.

[49] C. G. Dávila, C. A. Rose, G. B. Murri, W. C. Jackson, W. M. Johnston, Evaluation of fatigue damage accumulation functions for delamination initiation and propagation, *Nasa/Tp–2020-220584* (2020).

[50] M. L. Benzeggagh, M. Kenane, Measurement of mixed-mode delamination fracture toughness of unidirectional glass/epoxy composites with mixed-mode bending, *Composites Science and Technology* 56 (1996) 439–449.

[51] A. Turon, P. P. Camanho, J. Costa, J. Renart, Accurate simulation of delamination growth under mixed-mode loading using cohesive elements: Definition of interlaminar strengths and elastic stiffness, *Composite Structures* 92 (8) (2010) 1857–1864.

[52] R. C. Juvinall, K. M. Marshek, Fundamentals of Machine Component Design, 5th Edition, John Wiley & Sons, Hoboken, NJ, 2012.

[53] E. V. González, P. Maimí, A. Turon, P. P. Camanho, J. Renart, Simulation of delamination by means of cohesive elements using an explicit finite element code, *Computers, Materials and Continua* 9 (1) (2009) 51–92.

[54] F. P. van der Meer, Mesolevel Modeling of Failure in Composite Laminates: Constitutive, Kinematic and Algorithmic Aspects, *Archives of Computational Methods in Engineering* 19 (3) (2012) 381–425.

[55] T. S. Hille, A. S. Suiker, S. Turteltaub, Microcrack nucleation in thermal barrier coating systems, *Engineering Fracture Mechanics* 76 (6) (2009) 813–825.

[56] C. V. Verhoosel, J. J. C. Remmers, M. A. Gutiérrez, A dissipation-based arc-length method for robust simulation of brittle and ductile failure, *International Journal for Numerical Methods in Engineering* 77 (9) (2009) 1290–1321.

[57] I. Leciñana, J. Zurbitu, J. Renart, A. Turon, A robust fatigue parameter determination method for a local fatigue Cohesive Zone Model, *International Journal of Fatigue* (2023) 107582.

[58] J. Renart, S. Budhe, L. Carreras, J. Mayugo, J. Costa, A new testing device to simultaneously measure the mode I fatigue delamination behavior of a batch of specimens, *International Journal of Fatigue* 116 (2018) 275–283.

[59] ASTM D5528-01, Standard Test Method for Mode I Interlaminar Fracture Toughness of Unidirectional Fiber-Reinforced Polymer Matrix Composites, *Annual Book of ASTM Standards, American Society for Testing and Materials, West Conshohocken, PA* (2002).

3

VALIDATION AGAINST MULTIDIRECTIONAL LAMINATES

With the exception of minor textual adjustments, this chapter is reproduced from: P. Hofman, F. P. van der Meer, L. J. Sluys, Modeling of progressive high-cycle fatigue in composite laminates accounting for local stress ratios. *Composites Part A: Applied Science and Manufacturing* 183 (2024) 108219. **doi:10.1016/j.compositesa.2024.108219**.

ABSTRACT

A numerical framework for simulating progressive failure under high-cycle fatigue loading is validated against experiments of composite quasi-isotropic open-hole laminates. Transverse matrix cracking and delamination are modeled with a mixed-mode fatigue cohesive zone model, covering crack initiation and propagation. Furthermore, XFEM is used for simulating transverse matrix cracks and splits at arbitrary locations. An adaptive cycle jump approach is employed for efficiently simulating high-cycle fatigue while accounting for local stress ratio variations in the presence of thermal residual stresses. The cycle jump scheme is integrated in the XFEM framework, where the local stress ratio is used to determine the insertion of cracks and to propagate fatigue damage. The fatigue cohesive zone model is based on S-N curves and requires static material properties and only a few fatigue parameters, calibrated on simple fracture testing specimens. The simulations demonstrate a good correspondence with experiments in terms of fatigue life and damage evolution.

3.1. INTRODUCTION

Fiber-reinforced polymer (FRP) composites have many advantages over traditional (metallic) engineering materials and are increasingly used in the aerospace and automotive industries. These materials possess high-strength-to-weight ratios, good corrosion resistance and the material can be tailored to meet specific requirements by altering the stacking-sequence, fiber material, matrix material and ply thickness.

In order to speed-up and improve the design and certification process of FRP laminated structures, numerical models must be developed to predict the behavior under critical loading conditions. Cyclic loading is an important loading condition and is often governing for the design of composite structures.

In previous years, many high-cycle fatigue models have been developed, capable of accurately simulating fatigue crack growth in specimens with pre-existing cracks [1–13]. However, there are still challenges in progressive fatigue modeling of multidirectional laminates, where both intra- and inter-laminar cracks can initiate, propagate and interact and the final failure mode is a combination of multiple complex failure processes [14–17].

A few authors have developed a progressive failure modeling methodology to predict fatigue failure in composite laminates [18–25]. In most of the methods, Paris-type fatigue cohesive zone models are used to describe fatigue crack propagation, while fatigue crack initiation is simulated with criteria based on S-N curves. Therefore, these two stages of fatigue damage are treated separately and a large amount of material characterization tests is required to obtain Paris' and S-N curves for different mode-mixities and stress ratios.

Recently, Dávila [26–28] proposed a fatigue cohesive zone model, covering fatigue crack initiation and propagation in a unified formulation. The model requires the static material properties and a limited number of fatigue parameters that can be obtained by calibration with typical fracture characterization tests. The effects of mode-mixity and stress ratio are taken into account in the constitutive equations through empirical relations and engineering assumptions. The fatigue cohesive zone model has been validated against simple fracture tests with thermosets [26–30], tests exhibiting $\mathcal{R}$-curve effects with thermoplastics [31], a *reinforced double cantilever beam* specimen with changing crack front shapes [29, 32] and a *clamped tapered beam* specimen with delamination-migration [33]. Furthermore, the model successfully predicted initiation of transverse matrix cracks in $[0_2/90_4]_s$-laminates with thermal residual stresses [34]. Recently, the model has been used to simulate progressive fatigue failure in an open-hole $[0/90]_s$-laminate with predefined splits [25] and in an open-hole $[\pm 45]_s$-laminate with multiple transverse matrix cracks using XFEM [35]. However, the applicability of the fatigue cohesive zone model to

simulate progressive failure in quasi-isotropic open-hole laminates with a complex interaction of distributed transverse matrix cracks and delamination has not yet been demonstrated.

Moreover, most of the progressive fatigue failure models employ predefined discrete cracks to simulate transverse matrix cracks and splits [18, 20, 23, 25], or a continuum damage mechanics model in combination with fiber-aligned meshes [24]. With XFEM, fiber-aligned meshes are not required and unstructured meshes can be used, thereby reducing meshing efforts. Furthermore, XFEM captures the discrete nature of a transverse (mesoscale) crack and allows for multiple cracks at arbitrary locations, which makes it possible to simulate the complete failure process from distributed cracking to localized failure, including the interaction between discrete matrix cracks and delamination.

This chapter builds on previous work [35] (Chapter 2), where a robust and efficient XFEM-based progressive failure framework for tensile static loading [36, 37] has been extended for simulating high-cycle fatigue. In this framework, both intra- and inter-laminar cracking are modeled with Dávila's mixed-mode fatigue cohesive zone model for simulating fatigue crack initiation and propagation with only a few input parameters. Furthermore, the fatigue cohesive zone model has been enhanced with an implicit time integration scheme of the damage variable and a fully consistent tangent to improve efficiency of the full-laminate analyses. The progressive fatigue failure framework is further extended in this chapter by using an adaptive cycle jump strategy that can capture local stress ratios. This is particularly important in multidirectional laminates, where due to the presence of non-uniform thermal residual stresses after curing, the local stress ratio varies in the laminate. Simulations of two quasi-isotropic open-hole laminates, with different stacking sequences, are performed with various tensile cyclic loadings and results are compared against experimental data from literature.

This chapter is organized as follows. First, the fatigue cohesive zone model with implicit fatigue damage update is summarized, followed by the formulation of XFEM for simulating intra-laminar cracking. Then, the extension with an efficient adaptive cycle jump scheme for simulating high-cycle fatigue, while accounting for local stress ratios, is addressed. Finally, the simulation results of two quasi-isotropic open-hole laminates are presented and discussed.

3.2. PROGRESSIVE FAILURE FRAMEWORK

3.2.1. FATIGUE COHESIVE ZONE MODEL

The high-cycle fatigue cohesive zone model by Dávila [26] builds upon Turon's static mixed-mode cohesive zone model [38–40] and is formulated in terms of an

equivalent 1D traction-separation relation:

$$\sigma = (1 - d)K_{\mathcal{B}}\Delta \tag{3.1}$$

where σ is the equivalent traction, $K_{\mathcal{B}}$ is the mode-dependent dummy stiffness and Δ is the equivalent displacement jump (see Fig. 3.1). The damage variable d is related to an energy-based damage variable $\mathcal{D}$, defined as the ratio of dissipated energy G_{d} over the critical mixed-mode energy release rate G_{c}:

$$\mathcal{D} \equiv \frac{G_{\mathrm{d}}}{G_{\mathrm{c}}} = \frac{\Delta^* - \Delta_0}{\Delta_{\mathrm{f}} - \Delta_0} \tag{3.2}$$

where Δ_0 and Δ_{f} are the initiation and ultimate equivalent displacements, respectively. Furthermore, the reference displacement (corresponding to the displacement at which static damage develops) is defined as

$$\Delta^* = \mathcal{D}(\Delta_{\mathrm{f}} - \Delta_0) + \Delta_0 \tag{3.3}$$

The energy-based damage variable $\mathcal{D}$ is the state variable and can only increase in *pseudo* time t, such that for current time step t_n:

$$\mathcal{D}(t_n) = \max_{0 \le \tau \le t_n} \left(\mathcal{D}(\tau)\right) \tag{3.4}$$

The stiffness-based damage variable d in Eq. (3.1) is related to the energy-based damage variable with the following equation:

$$d = 1 - \frac{(1 - \mathcal{D})\Delta_0}{\mathcal{D}\Delta_{\mathrm{f}} + (1 - \mathcal{D})\Delta_0} \tag{3.5}$$

The evolution of the energy-based damage variable is such that, at constant stress amplitudes and mode-mixities, the number of cycles to failure is described by an S-N curve (see Fig. 3.2). The rate of change of the damage variable $\mathrm{d}\mathcal{D}/\mathrm{d}N$ is described

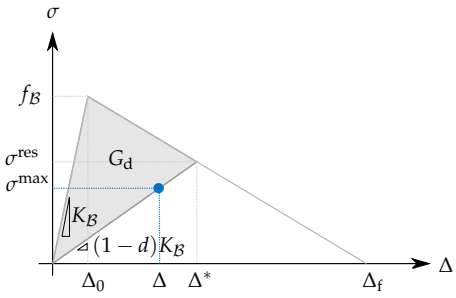

Figure 3.1 Fatigue cohesive zone model: the traction-separation response under fatigue loading (•) is inside the quasi-static envelope.

with a nonlinear differential equation:

$$\frac{\mathrm{d}\mathcal{D}}{\mathrm{d}N} = \frac{1}{\gamma}\frac{(1-\mathcal{D})^{\beta-p}}{E^{\beta}(p+1)}\left(\frac{\Delta}{\Delta^*}\right)^{\beta} \tag{3.6}$$

where the right-hand side is the CF20 damage accumulation function [27]. In this function, γ is the number of cycles to failure at the endurance limit, p can be calibrated to Paris curves and β is the exponent in the S-N curve, expressed as

$$\beta = \frac{-7\eta}{\log E} \tag{3.7}$$

where η is a *brittleness* parameter to account for the low-cycle fatigue response. For a given stress ratio R, the relative endurance limit E, defined as the ratio of equivalent endurance limit σ_{end} and mode-dependent static strength $f_{\mathcal{B}}$, is computed from the endurance limit ϵ at full load reversal ($R = -1$) with the Goodmann diagram:

$$E = \frac{2C\epsilon}{C\epsilon + 1 + R(C\epsilon - 1)} \tag{3.8}$$

In this expression, C is an empirical relation which accounts for the effect of mode-mixity [41]:

$$C = 1 - 0.42\mathcal{B} \tag{3.9}$$

where $\mathcal{B}$ is a displacement-based measure for mode-mixity and is defined as

$$\mathcal{B} = \frac{K_{\text{sh}}[\![u]\!]_{\text{sh}}^2}{K_{\text{n}}\langle[\![u]\!]_{\text{n}}\rangle^2 + K_{\text{sh}}[\![u]\!]_{\text{sh}}^2} \tag{3.10}$$

which is a function of the normal and shear dummy stiffnessess (K_{n} and K_{sh}) and the normal and shear displacement jumps ($[\![u]\!]_{\text{n}}$ and $[\![u]\!]_{\text{sh}}$). Furthermore, the ratio of shear and normal stiffness must satisfy the constraint equation in Ref. [39] to ensure correct energy dissipation during static mixed-mode fracture (see Eq. (2.4)).

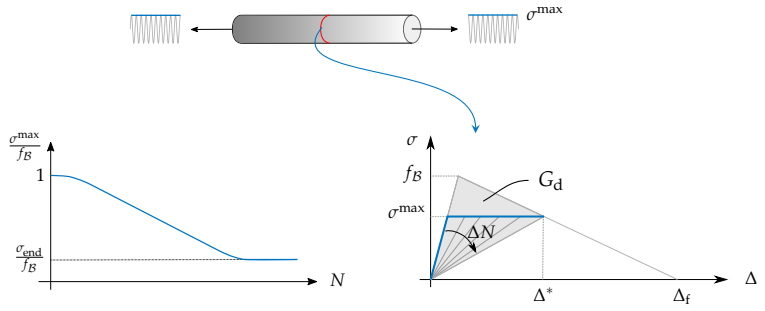

Figure 3.2 S-N-based fatigue cohesive zone model.

Following the previous work [35] (Chapter 2, Sec. 2.2.2), the fatigue damage at current *pseudo* time t_n is computed with an implicit time integration scheme, using the trapezoidal rule:

$$\mathcal{D}_{\mathrm{f}}^{(n)} = \mathcal{D}^{(n-1)} + \frac{\Delta N}{2}\left(\frac{\mathrm{d}\mathcal{D}}{\mathrm{d}N}^{(n-1)} + \frac{\mathrm{d}\mathcal{D}}{\mathrm{d}N}^{(n)}\right) \tag{3.11}$$

where the damage rates $\mathrm{d}\mathcal{D}/\mathrm{d}N^{(n-1)}$ and $\mathrm{d}\mathcal{D}/\mathrm{d}N^{(n)}$ are determined by evaluating Eq. (3.6) with values of the previous and the current *pseudo* time step, respectively. This nonlinear equation is iteratively solved at *local* integration point level with Newton's method. The quasi-static damage $\mathcal{D}_{\mathrm{s}}$ is computed as

$$\mathcal{D}_{\mathrm{s}} = \frac{\Delta - \Delta_0}{\Delta_{\mathrm{f}} - \Delta_0} \tag{3.12}$$

and the updated damage is determined as the maximum of the static and the fatigue damage

$$\mathcal{D} = \max\left(\mathcal{D}_{\mathrm{s}}, \mathcal{D}_{\mathrm{f}}\right) \tag{3.13}$$

The formulation is completed with a consistent tangent stiffness matrix, which is derived and presented in Ref. [35] (Chapter 2, Sec. 2.2.3).

3.2.2. INTRA-LAMINAR CRACKING

The *phantom node version* of XFEM [42] is used for simulating distributed matrix cracks at arbitrary locations [36, 37, 43]. A crack segment is inserted in a continuum element as soon as the stress in the plies $\boldsymbol{\sigma}$ reaches a critical envelope $f_I(\boldsymbol{\sigma}) = 1$. The discontinuity in the displacement field is resolved by duplicating the original element and defining the connectivity of each sub-element Ω_{A} and Ω_{B} (see Fig. 3.3) as

$$\Omega_{\mathrm{A}}^{\mathrm{conn}} = \{\tilde{n}_1, \tilde{n}_2, n_3\} \tag{3.14}$$

$$\Omega_{\mathrm{B}}^{\mathrm{conn}} = \{n_1, n_2, \tilde{n}_3\} \tag{3.15}$$

where $\{n_i\}$ and $\{\tilde{n}_i\}$ are the sets of original and *phantom* nodes, respectively.

The displacement field of the XFEM element is expressed in terms of the independent displacement fields of the two sub-elements that are overlapping:

$$\mathbf{u}(\mathbf{x}) = \begin{cases} \mathbf{N}(\mathbf{x})\mathbf{u}_{\mathrm{A}}, \ \mathbf{x} \in \Omega_{\mathrm{A}} \\ \mathbf{N}(\mathbf{x})\mathbf{u}_{\mathrm{B}}, \ \mathbf{x} \in \Omega_{\mathrm{B}} \end{cases} \tag{3.16}$$

where $\mathbf{u}_{\mathrm{A}}$ and $\mathbf{u}_{\mathrm{B}}$ are the vectors with nodal degrees of freedom of each sub-element and $\mathbf{N}(\mathbf{x})$ is the matrix containing the shape functions. The displacement jump

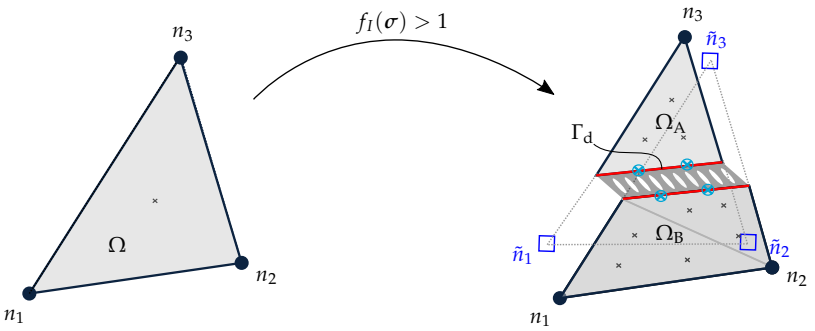

Figure 3.3 XFEM crack insertion. The mixed-mode fatigue cohesive zone model is used in each cohesive integration point (⊗) for describing fatigue damage.

vector along the crack segment Γ_d is defined as

$$[\![\mathbf{u}]\!](\mathbf{x}) = \mathbf{N}(\mathbf{x})(\mathbf{u}_A - \mathbf{u}_B),\ \mathbf{x} \in \Gamma_d \tag{3.17}$$

The crack segment is inserted parallel to the direction of the fibers in the ply to enforce transverse cracks to propagate in fiber direction. The traction-separation relation of the cohesive integration points that are located on the crack segment is described by the fatigue cohesive zone model (Sec. 3.2.1).

In order to retain well-posedness of the problem, a predefined crack-spacing parameter l_c is used [36]. XFEM crack segments can be inserted either at zero orthogonal distance of existing cracks (propagation), or initiate as new cracks at a distance that is at least equal to l_c. The objectivity of the crack-spacing parameter is discussed in earlier publications for static loading [37] and for fatigue loading [35] (Chapter 2, Sec. 2.7).

XFEM crack segments are inserted when a fatigue crack insertion criterion ($f_I(\sigma) > 1.0$) is satisfied. The criterion is based on the endurance limit to maintain consistency with the fatigue damage formulation [35] (Chapter 2, Sec. 2.3.1). The failure index function is defined as the ratio of the equivalent traction σ to the endurance limit σ_{end}:

$$f_I(\sigma) \equiv \frac{\sigma(\sigma)}{\sigma_{\text{end}}(\sigma)} \tag{3.18}$$

with $\sigma_{\text{end}} = E f_{\mathcal{B}}$. The relative endurance limit E is determined from Eqs. (3.8) and (3.9) and the mode-dependent static strength $f_{\mathcal{B}}$ is computed as

$$f_{\mathcal{B}} = \sqrt{(K_n(1-\mathcal{B}) + \mathcal{B}K_{sh})\left[f_n^2/K_n + (f_{sh}^2/K_{sh} - f_n^2/K_n)\mathcal{B}^{\eta_{BK}}\right]} \tag{3.19}$$

where f_n and f_{sh} are the normal and shear static strengths, respectively. During the static ramp-up phase and the control cycles (see Sec. 3.2.3), fatigue damage is

inactive ($R = 1$) and a static criterion is used with failure index function:

$$f_I(\boldsymbol{\sigma}) = \frac{\sigma(\boldsymbol{\sigma})}{f_{\mathcal{B}}} \tag{3.20}$$

3.2.3. CYCLE JUMP SCHEME

A cycle jump approach, which takes into account the effects of the cyclic load in the constitutive relation, is often used in high-cycle fatigue analyses since simulating each cycle explicitly would be computationally intractable. A load envelope approach can be used to apply the loading in a simplified way, for example when a constant amplitude cyclic load is applied and all inelastic behavior is assumed to be of damage-type (with secant unloading), which makes the unloading-reloading a linear problem. Because of this linearity, the *global* load ratio is equal to the *local* stress ratio in each integration point. Consequently, the *local* stress ratio is *a priori* known and can be provided as an input parameter of the constitutive equations. This approach is used by many authors for the simulation of high-cycle fatigue [1–13, 26, 27, 33, 44, 45].

In the presence of multiple unsynchronized load signals, plasticity, geometric nonlinearities or thermal residual stresses, the *local* stress ratio is not equal to the *global* load ratio. However, the load envelope approach does not give access to the *local* stress ratios, even though these should govern the *local* material response.

One approach to overcome this issue is to use a *min-max* technique [46], where two models, one with the minimum and the other with the maximum applied load, are used and information is exchanged between them. Another, more general approach, is a cycle jump strategy with explicit load cycles, also called *control cycles*, before each cycle increment ΔN, as previously applied to composite materials by various authors [34, 47–50]. During these control cycles, the minimum and maximum stresses are monitored such that after the control cycle, the *local* stress ratio can be computed before a cycle jump ΔN is applied. During the cycle jump, the *local* stress ratio is then available for use in the calculation of fatigue damage.

Joosten et al. [34] combined this cycle jump approach with Dávila's fatigue CZM and proposed a *local* stress ratio definition, computed during the control cycles with a projection of the minimum and maximum severities:

$$R \equiv \frac{\mathbf{S}_{\min} \cdot \mathbf{S}_{\max}}{\|\mathbf{S}_{\max}\|^2} \tag{3.21}$$

where $\mathbf{S} = \left[t_{\mathrm{n}}/f_{\mathrm{n}}, t_{\mathrm{sh}}/f_{\mathrm{sh}}\right]^{\mathrm{T}}$ is the stress severity vector. The components of this vector contain the normal (t_{n}) and shear traction (t_{sh}) components, scaled with the pure-mode strengths.

In this work, a similar approach is followed to capture the varying *local* stress ratio in quasi-isotropic laminates with non-uniform thermal residual stresses. Four different loading phases are defined. First, a *thermal load phase* is applied to simulate a temperature drop from the curing temperature T_0 to the cooling temperature T_∞, resulting in a residual stress in every material point due to the mismatch of thermal constants between plies. After the thermal load phase, the *static-ramp-up phase* is simulated to reach the maximum load $F_{\max}$. Subsequently, a *control cycle* is applied in order to determine the *local* stress ratio in every integration point. When the control cycle has finished, a *cycle jump phase* is entered in which fatigue damage accumulates according to the formulation with *local* R in Eq. (3.8). After each cycle jump phase, a control cycle is re-entered to update the stress ratios for the next cycle jump phase. This process is repeated until all fatigue cycles have been simulated. An overview of these phases is shown in Fig. 3.4.

Remark 3.1 It should be mentioned that the use of control cycles to compute the *local* stress ratio in each integration point is an explicit procedure. Since fatigue damage accumulates during cycle jumps, resulting in stress redistribution in the laminate, the *local* stress ratio that is used at the beginning of the step is different from the *local* stress ratio at the end of the step. Although time-step dependence has been strongly reduced with the implicit time integration scheme [35] (Chapter 2, Sec. 2.6.1), a reassessment of the time-step dependence is required. This is carried out in the numerical examples later in this chapter (Sec. 3.3.2).

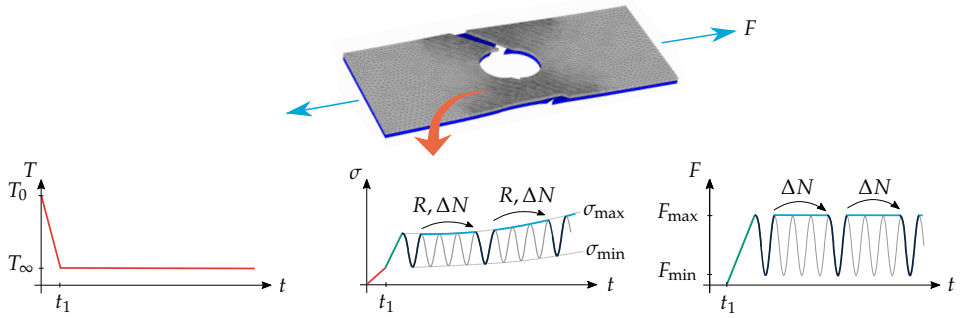

Figure 3.4 Cycle jump scheme with four phases: thermal load phase (in *red*), static ramp-up phase (in *green*), control cycle phase (in *dark blue*) and cycle jump phase (in *light blue*).

3.2.4. MONITORING LOCAL STRESS RATIO IN THE BULK INTEGRATION POINTS

At the end of each cycle jump, the failure index function Eq. (3.18) must be evaluated in every integration point. For this purpose, the *local* stress ratio must be available for computing the endurance limit with Eq. (3.8). The local stress ratio in Eq. (3.21) is defined with traction components in local coordinate frame, aligned with the crack segment. Since crack segments are inserted parallel to the fiber direction, the traction vector $\mathbf{t}$ can be computed from the bulk stress $\boldsymbol{\sigma}$ and the normal vector $\mathbf{n}$, that is perpendicular to the fibers, with $\mathbf{t} = \boldsymbol{\sigma}\mathbf{n}$. The *local* stress ratio can then be computed during control cycles in each bulk integration point, such that it is available when Eq. (3.18) is evaluated.

3.2.5. TRANSFERRING LOCAL STRESS RATIO TO COHESIVE INTEGRATION POINTS

Once new crack segments are inserted, the solution must be re-equilibrated by re-entering the Newton-Raphson solver. Upon insertion of new crack segments, the *local* stress ratio R must be known to evaluate fatigue damage in each new cohesive integration point. To achieve this, the bulk *local* stress ratio is passed to the cohesive integration points on the newly inserted crack segments. With linear (constant stress) elements, this is straightforward. With other types of elements where the stress, and thus the *local* stress ratio, varies across an element, the history transfer approach by Wells and Sluys [51] is a suitable method.

3.2.6. ADAPTIVE STEPPING STRATEGY

Since an implicit time integration scheme is employed for updating the fatigue damage variable during cycle jumps, the cycle increment ΔN can be determined based on *global* convergence behavior [35] (Chapter 2). An adaptive stepping scheme is used during each loading phase of the analysis. The number of iterations n_{iter}, required to reach convergence in the previous time step, is used to determine the next step size:

$$\Delta t^{(n+1)} = c^{-\left(\frac{n_{\text{iter}} - n_{\text{iter}}^{\text{opt}}}{\xi}\right)} \Delta t^{(n)} \tag{3.22}$$

where c, ξ and $n_{\text{iter}}^{\text{opt}}$ are model parameters and Δt is an increment in *pseudo* time which translates to a cycle increment during cycle jumps and to a load increment during static ramp up and control cycles. If convergence is not reached within a specified maximum number of iterations $n_{\text{iter}}^{\text{max}}$, the step is cancelled and restarted with a reduced time step increment $\Delta t^{(n)} \leftarrow c_{\text{red}} \Delta t^{(n)}$.

At the start of the first cycle jump, the step size ΔN_{init} is initialized and used to compute fatigue damage. This step size is adapted during the subsequent cycle jumps according to Eq. (3.22). After the cycle jump phase and before a new control-

phase is entered, the new cycle increment ΔN is computed and stored as the initial cycle increment for the next cycle jump phase. This ensures that the control cycle increments and the cycle jumps are separately adapted.

When control cycles are entered, it is first tried to find the solution at the minimum load at once. Since fatigue damage is de-activated during control cycles and the analysis reduces to a linear problem, only two steps, corresponding to the minimum and maximum load, are sufficient in most cases. Sometimes, more steps during control cycles are necessary, in which case the time step is adapted as described above.

3.2.7. MODELING THERMAL RESIDUAL STRESSES

Multidirectional laminates develop residual stresses after curing due to a mismatch in thermal constants between plies. The effect of a temperature change ΔT is taken into account in the ply constitutive model. The orthotropic linear elastic stress-strain relation in 2D is:

$$\boldsymbol{\sigma} = \mathbf{D}(\boldsymbol{\varepsilon} - \boldsymbol{\varepsilon}^{\text{th}}) \tag{3.23}$$

where

$$\boldsymbol{\varepsilon}^{\text{th}} = \left[\alpha_1 \Delta T, \alpha_2 \Delta T, 0\right]^T \tag{3.24}$$

is the thermal strain, with α_i the coefficients of thermal expansion in longitudinal (fiber) direction (α_1) and in transverse direction (α_2).

3.3. QUASI-ISOTROPIC OPEN-HOLE LAMINATE SIMULATIONS

Two quasi-isotropic open-hole laminates, experimentally tested in Refs. [15, 16], have been simulated and results are presented in this section. The laminates have the same number of plies and thicknesses but different lay-ups, leading to distinct failure modes and fatigue lives. The first laminate has lay-up $\left[45_2/90_2/-45_2/0_2\right]_s$ and is *ply-level scaled*, where two plies with the same fiber direction are stacked, effectively increasing the ply thickness. The second laminate has lay-up $\left[45/90/-45/0\right]_{2s}$ and is *sub-laminate scaled*, in which the laminate is created by repeating *sub-laminates*. In the following, the first laminate is denoted as *ply-level scaled specimen* and the second as *sub-laminate scaled specimen*.

3.3.1. MODEL PRELIMINARIES

The open-hole laminates are made of carbon fiber/epoxy plies (prepreg system IM7/8552). The dimensions of the specimens are 64 mm × 16 mm × 2 mm with a hole diameter of 3.175 mm (see Fig. 3.5). The thickness of each ply is 0.125 mm. Thermal residual stresses arise by accounting for the temperature change ΔT from

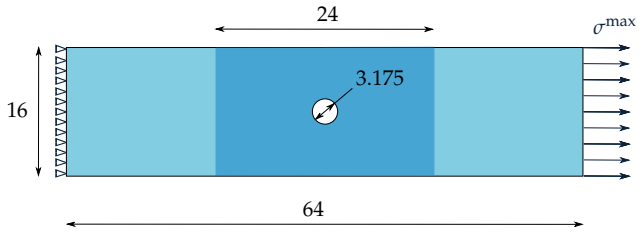

Figure 3.5 Specimen dimensions (in mm) of the quasi-isotropic open-hole laminates. The fine mesh region is indicated in dark blue.

processing temperature (180 °C) to room temperature (20 °C) in the linear elastic constitutive relation (Sec. 3.2.7), while deformations are freely allowed to occur.

The static versions of these cases, experimentally tested in Ref. [52], were previously simulated with the same XFEM progressive failure framework for static loading [53], where the interface strength was reduced to 45 MPa, while the ply fracture energy in mode-I was increased to the value of mode-II, resulting in larger cohesive zone lengths and improved robustness while retaining a good fit with experimental measurements. In the present fatigue simulations, unadapted values for these parameters again gave rise to convergence problems and therefore the same set of static material properties as in Ref. [53] is used here (see Tab. 3.1). For the fatigue-related parameters of CF20, recommended values are used from Ref. [27], which predicted excellent results with IM7/8552 carbon fiber/epoxy in a *double cantilever beam* test [26], *mixed-mode bending* test [33, 34], *double notch shear* test [34], *clamped tapered beam* specimen [33] and $[0_2/90_4]_s$-laminate [34].

The dummy stiffness between the plies is related to the in-plane shear modulus and ply thickness t_p through $K_d = {}^{G_{12}}/_{\frac{1}{2}t_p}$ [37]. Furthermore, the crack-spacing parameter (see Sec. 3.2.2) is set to $l_c = 0.75$ mm. Since the lay-ups are symmetric, only half of each laminate is modelled. The computational domain is discretized with an unstructured mesh and each ply is represented by a layer of plane stress, constant

Table 3.1 Ply material properties used in the simulations.

elastic [54]		**fracture** [53]		**fatigue** [27]		**thermal** [54]	
E_1	161.0 GPa	f_n	95 MPa	η	0.95	α_1	$0\,°C^{-1}$
E_2	11.38 GPa	f_{sh}	107 MPa	ϵ	0.2	α_2	$3.0 \times 10^{-5}\,°C^{-1}$
G_{12}	5.17 GPa	G_{Ic}	$1.0\,N\,mm^{-1}$	p	β		
ν_{12}	0.32	G_{IIc}	$1.0\,N\,mm^{-1}$				
		η_{BK}	2.1				

strain, triangular elements. A rectangular region around the hole is defined where delamination is allowed by inserting zero-thickness interface elements between the plies (shown in Fig. 3.5). This region has a fine-mesh with a typical element size of 0.4 mm. The typical element size outside this region is 1.6 mm, where the plies are rigidly tied. A Newton-Cotes integration scheme is used for the interface elements for superior interaction with the neighboring elements containing the transverse matrix cracks [37]. For the transverse matrix cracks in the plies, as well as for the plies themselves, Gauss integration schemes are used (see Fig. 3.3).

The adaptive stepping scheme in Sec. 3.2.6 allows for efficiently adapting the time steps in the static, control cycle, and cycle jump phases. Three cycle jumps are simulated in each cycle jump phase, after which a control phase is entered to update the *local* stress ratio in every integration point. The stepping parameters in Eq. (3.22) are set to $n_{\text{iter}}^{\text{opt}} = 4$, $c = 2$ and $\xi = 1$. The maximum number of iterations is set to $n_{\text{iter}}^{\text{max}} = 20$. If no convergence is obtained within $n_{\text{iter}}^{\text{max}}$, the step is restarted with a 40% reduction of the previous increment.

3.3.2. PLY-LEVEL SCALED SPECIMEN

The *ply-level scaled specimen* is simulated with four different maximum applied stress levels $\sigma^{\text{max}}(\text{MPa}) = \{334.4, 292.6, 254.0, 209.0\}$, corresponding to 80, 70, 60 and 50% severity levels, respectively. Global severity is defined as the ratio of the maximum load over the static strength [15]. The *global* load ratio R_{glob} is 0.1.

FATIGUE LIFE AND DAMAGE EVOLUTION

S-N curves from experiments and simulations are shown in Fig. 3.6, where the fatigue life corresponds to a 15% loss in normalized effective stiffness $E_{\text{eff}}/E_{\text{eff},0}$, associated with a steep drop in stiffness. The effective stiffness is computed consistently with the experiments as described in Ref. [16]. It can be observed that a good

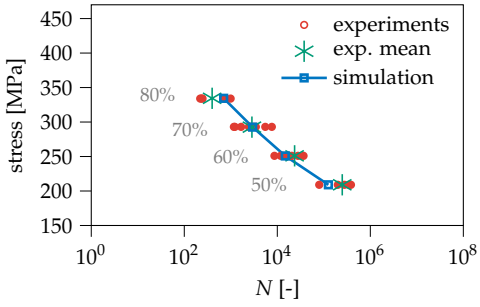

Figure 3.6 S-N curve of the ply-level scaled specimen. Experimental values are extracted from [16].

match is obtained with the experimental fatigue lives. The stiffness reduction and evolution of fatigue damage in the interfaces for four different time instances are shown in Fig. 3.7. First, matrix cracks develop with a limited amount of stiffness loss, accompanied by delamination of small triangular areas near the hole (N_1 - N_2). A significant stiffness drop occurs due to delamination in the 45/90 interface, starting from the transverse matrix cracks (N_2 - N_3). When the matrix cracks have fully developed in the 90° and $-45°$ plies, rapid delamination growth takes place in the 90/-45 and -45/0 interface, growing from the hole to the outer edges. This delamination corresponds to an almost vertical drop in the stiffness (N_3 - N_4). The final damage patterns at 15% stiffness reduction match well with the experimental damage patterns [15].

EFFICIENCY AND ACCURACY

The efficiency and accuracy of the simulations have been investigated. An implicit time integration scheme of the damage variable is used which allows for larger cycle increments. The combination of the implicit scheme and the consistent tangent enables the use of an adaptive time stepping strategy where the number of global iterations to reach a converged solution is a good measure to determine the cycle increment for the next *pseudo* time step [35].

The time-step dependence (see **Remark 3.1** in Sec. 3.2.3) and performance of the adaptive cycle jump scheme is assessed by repeating the 60% severity analysis with a small step size. This limits the amount of stress redistribution between steps and increases the number of control cycles with more regular updates of the *local* stress ratios. The maximum allowed cycle increment is set to $\Delta N = 10$ cycles.

The stiffness reduction curve is shown in Fig. 3.8 with markers for every individual time step, from which it can be observed that the global response in terms of stiffness degradation as function of number of cycles is very similar for the two simulations with 154 and 2746 time steps, respectively. The accumulation of the cycle number N with every time step is depicted in Fig. 3.9, which shows that the adaptive stepping strategy effectively adapts the cycle increments throughout the simulation.

It can be concluded that the adaptive stepping strategy, in combination with the implicit fatigue damage update and consistent tangent, results in efficient and accurate analyses resulting in relatively short run times (5834 s on a laptop computer[1]).

EFFECT OF LOCAL STRESS RATIO

In order to investigate the effect of accounting for the *local* stress ratio R, the analyses are repeated but this time with the *local* stress ratio in Eq. (3.8) set equal to the *global*

[1] Dell laptop with Intel Core i7 processor, 16 GB of RAM and operating system Linux Ubuntu 20.04.

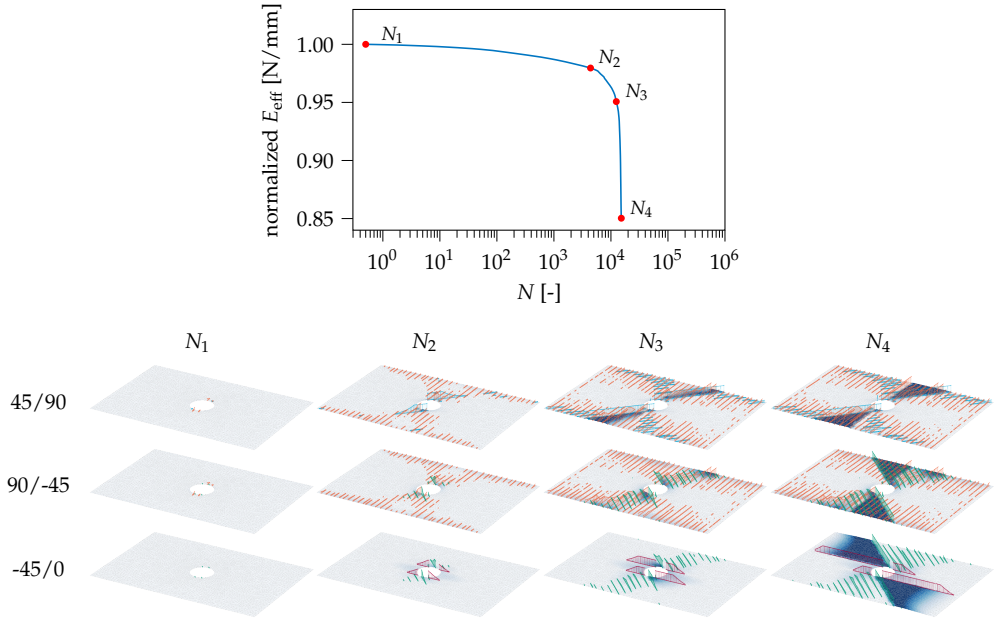

Figure 3.7 Stiffness reduction as a function of number of cycles N (*top*) and damage evolution at indicated time instances in the interfaces (in *dark blue*) and XFEM matrix cracks in 45°-ply (in *light blue*), 90°-ply (in *orange*), -45°-ply (in *green*) and 0°-ply (in *red*).

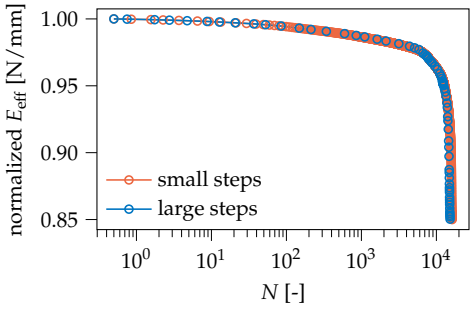

Figure 3.8 Stiffness reduction with number of cycles.

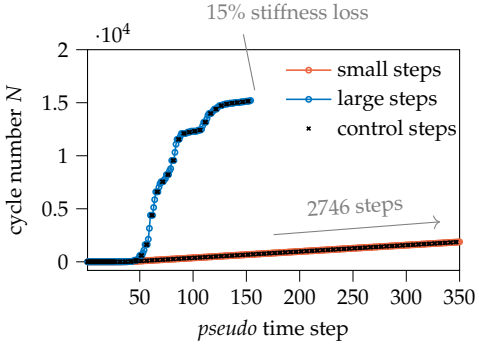

Figure 3.9 Accumulation of cycles with time steps.

load ratio $R_{\text{glob}} = {}^{F^{\min}}/_{F^{\max}} = 0.1$.

The stiffness reduction curves with *global* and *local* R are shown in Fig. 3.10. It can be observed that accounting for *local* stress ratio results in a significantly slower development of fatigue damage. Furthermore, the use of the *local* stress ratio affects the slope of the laminate S-N curve, as shown in Fig. 3.11. The fatigue life prediction with the *global* load ratio shows a mismatch with the experimental values for the lower load levels, whereas with the highest load level, the response is almost independent of the use of *global* or *local* R.

In Fig. 3.12, the *local* R values in the cohesive zone (where $\mathcal{D} \in (0,1)$) are plotted as a field for the lowest (50%) and highest load level (80%) in every interface at approximately 7% stiffness loss. It can be observed that the *local* stress ratio is generally higher for the lowest load level, while for the highest load level the *local* stress ratio is close to the *global* load ratio. This can be explained by looking at Fig. 3.4, where the stress in a point is the superposition of the thermal residual stress and the stress due to the mechanical load. With an increased maximum load and equal *global* load ratio, the *local* stress ratio reduces due to the diminishing relative magnitude of the residual stresses.

With an overall larger stress ratio, fatigue damage accumulates slower compared to simulations in which a *global* load ratio is used in every integration point, leading to an increased discrepancy between the simulation results with decreasing maximum load level (Fig. 3.11).

SENSITIVITY STUDY OF STATIC MATERIAL PROPERTIES

The fatigue cohesive zone model requires the quasi-static fracture properties and a few fatigue-related parameters. However, strength measurements of IM7/8552 carbon fiber/epoxy vary with different testing methods [55, 56]. Moreover, the

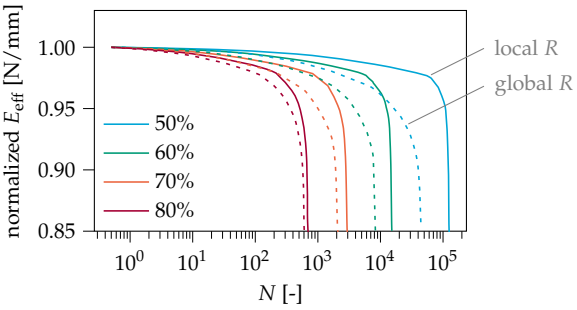

Figure 3.10 Stiffness reduction with number of cycles for four different severity levels. Dashed and solid lines correspond to the response with *global* and *local* stress ratio, respectively.

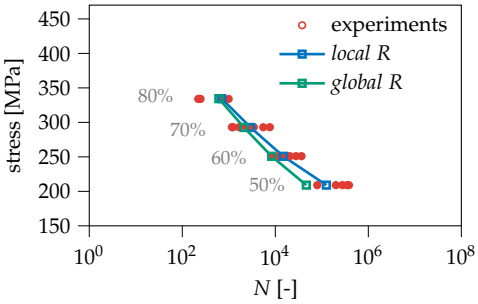

Figure 3.11 S-N curve of the ply-level scaled specimen. *Local* stress ratio vs *global* load ratio.

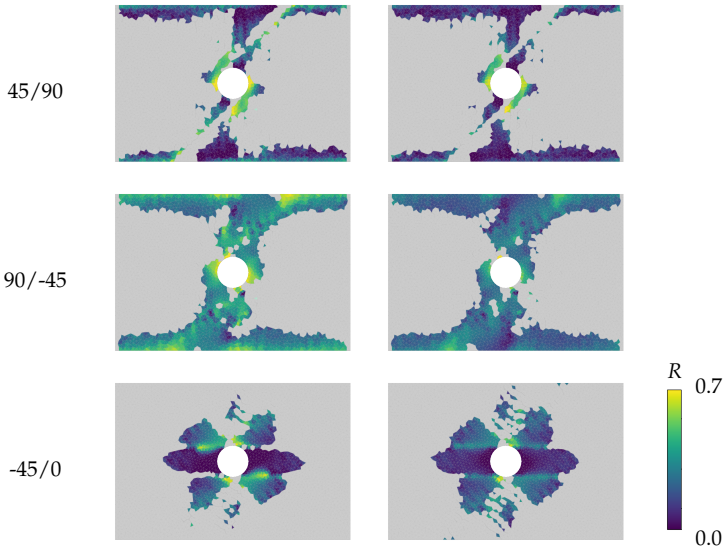

(a) 50% severity **(b)** 80% severity

Figure 3.12 Local stress ratio field in the cohesive zone for each interface at approximately 7% stiffness loss.

strength measured with unidirectional laminates is smaller than the in-situ strength of embedded plies in a multidirectional laminate and depends on the fiber direction in the constraining plies, the ply thickness and the location of the ply in the laminate [57–60].

The effect of the static fracture properties on the quasi-isotropic laminate simulations is investigated by repeating the simulation of the *base* case with properties tabulated in Tab. 3.1, changing one material property at a time. The effect of varying each static property on the laminate S-N curve is shown in Fig. 3.13.[2] The curve corresponding to the *base* case is indicated with the black line. It can be observed that the response is only slightly affected by varying the intra-laminar fracture properties. The tensile strength seems to have the largest influence, where increasing the strength results in a shorter fatigue life. Decreasing the intra-laminar strength shifts the underlying *local* S-N curve downwards and consequently leads to more accumulated fatigue damage in the transverse matrix cracks. With more distributed intra-laminar cracking, tractions in the interface decrease and therefore less inter-laminar fatigue damage accumulates [35]. Since the largest stiffness drops are associated with interface delamination (see Fig. 3.7), the fatigue life of the laminate is longer. The interface shear strength shows the most influence on the *global* S-N curve, where an increase in shear strength results in a longer fatigue life. The slope of the underlying *local* S-N curve remains the same with increasing strength, while the curve is shifted upwards, thus resulting in less fatigue damage at the same stress level compared to a lower interfacial strength. Finally, decreasing the interfacial mode-II fracture energy results in a shorter fatigue life, although the effect is minimal in the range of typical values for the mode-II fracture energy (0.75 - 1.0 $\mathrm{N\,mm^{-1}}$).

Previously, the static version of the open-hole simulation [53] indicated that fracture energy is a more important parameter than strength, since laminate failure is governed by delamination propagation. In elementary static crack propagation tests, Turon's static mixed-mode cohesive zone model, which is the basis of the fatigue formulation by Dávila [26], ensures correct energy dissipation, independent of strength [39, 40]. However, with the fatigue damage extension, it has been shown that crack propagation rates do in fact depend on the static strength values [29, 61]. The results of the present study confirm these previous findings.

[2] Some simulations did not reach a 15% reduction in effective stiffness due to convergence issues, resulting in incomplete S-N plots.

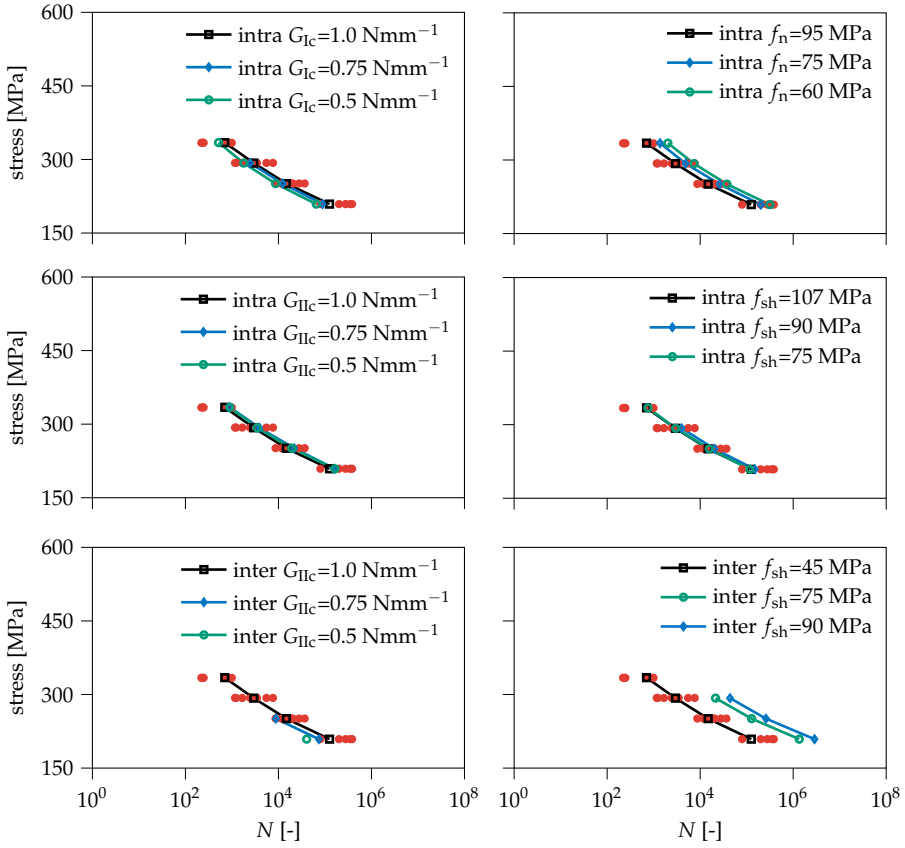

Figure 3.13 Sensitivity study of static material properties.

3.3.3. SUB-LAMINATE SCALED SPECIMEN

The *sub-laminate scaled specimen* is simulated with five maximum *global* stress levels $\sigma^{\max}(\text{MPa}) = \{523.3, 494.2, 465.1, 407.0, 377.9\}$, corresponding to 90, 85, 80, 70 and 65% severity levels, respectively. The *global* load ratio R_{glob} is 0.1.

The S-N curve is shown in Fig. 3.14, where fatigue life is again defined as the number of cycles to reach a 15% reduction of the initial effective stiffness. It can be observed that a good match is obtained in terms of fatigue life, except for the experimental specimens with the highest peak load. It is reported in Ref. [16] that the highest load level (90% severity) resulted in a pull-out failure mode (which cannot be captured with the present numerical framework where fiber failure is not considered), while the second highest load level (85% severity) showed both delamination and pull-out failures. However, the three lowest load levels resulted in all cases in a delamination-type failure mode in the experiments. For the specimens with a delamination-type failure mode, the simulation results are in excellent accordance with the experiments.

The simulation damage patterns are compared to the experimental patterns under severity 80%, at approximately 9% stiffness loss (see Fig. 3.15). The patterns are in good agreement for the outer 45/90, 90/−45 and inner 45/90 interfaces. Similar to the experimental observations [16, 20], damage grows from the free edge towards the hole in the inner 45/90 interface. Also a more dispersed damage pattern compared to the *ply-level scaled specimen*, with increased free-edge delamination, can be observed. For the outer −45/0 and 0/45 interfaces, slightly underdeveloped delamination is predicted, while the inner −45/0 interface shows overdeveloped delamination. Given the scatter in experimental damage patterns [16, 20], the simulated patterns are overall in good correspondence with the experimental ones.

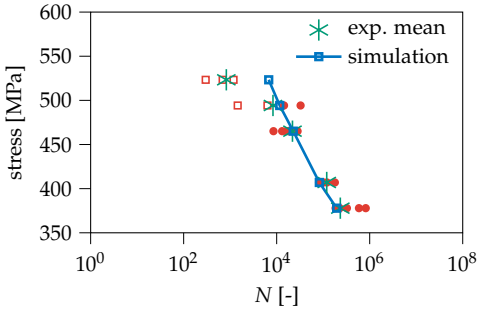

Figure 3.14 S-N curve of the sub-laminate scaled specimen. Experimental values are extracted from [16]. The symbols □ and ● indicate experimental specimens with pull-out and delamination-type failure modes, respectively.

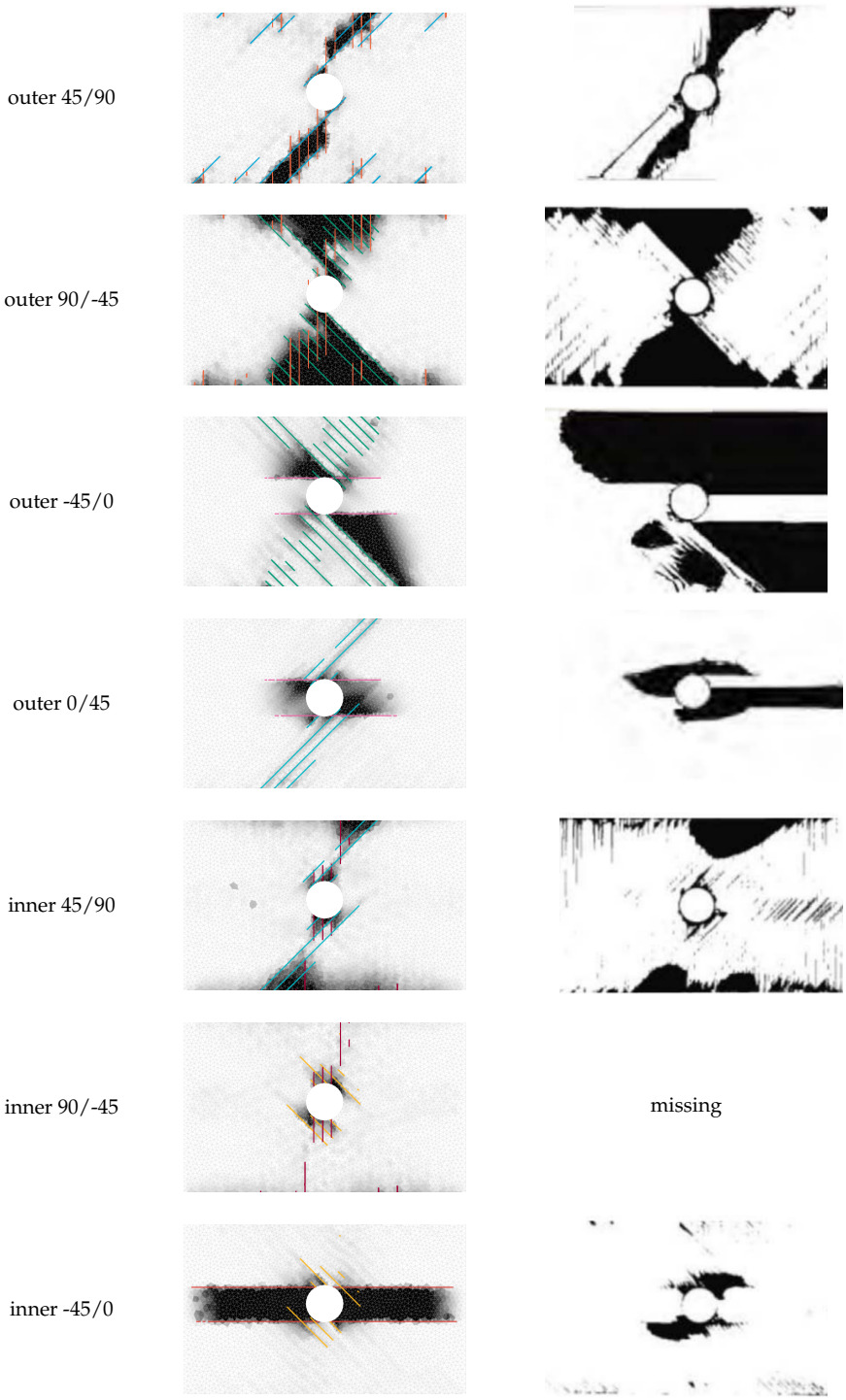

Figure 3.15 Sub-laminate scaled specimen: damage in XFEM matrix cracks and interface delamination vs experimental CT scans (taken from [20]) at 9% stiffness loss. Only fully damaged matrix cracks ($\mathcal{D} = 1$) are depicted.

3.4. CONCLUSION

A previously developed progressive fatigue failure framework has been extended with an adaptive cycle jump approach to capture non-uniform local stress ratios in multidirectional laminates with thermal residual stresses. The local stress ratio is regularly computed by explicitly applying a load cycle to assess the minimum and maximum stress in every integration point, before cycle jumps take place.

The progressive fatigue failure framework is applied to the simulation of two open-hole quasi-isotropic laminates. The model is capable of predicting the fatigue life as a consequence of interacting intra- and inter-laminar damage with excellent agreement. Furthermore, the experimentally observed damage evolution and final failure modes are accurately captured. Moreover, the implicit fatigue damage update, together with the adaptive stepping scheme, allows for simulating a large amount of fatigue cycles while accounting for local stress ratios in an efficient manner. In addition, it is demonstrated that computing the local stress ratios, instead of just using the global load ratio, is relevant for this type of problems.

The numerical model requires only static material properties and a few fatigue-related parameters, calibrated on elementary fracture tests. Static parameters were taken from earlier simulations of static open-hole experiments, including adaptations for improved robustness. The effect of local stress ratio and mode-mixity is internally accounted for in the constitutive relations of the fatigue cohesive zone model, which poses a significant advantage over Paris-type models that require Paris data for different mode-mixities and stress ratios and separate S-N curves for crack initiation. However, the progressive fatigue failure model shows sensitivity to the static material properties, in particular to the inter-laminar strength. Previously it has been shown, with the static version of the open-hole tests, that fracture energy is a more important parameter than strength. Conversely, the present investigation indicates that static strength is an important parameter in the fatigue simulations with the embedded fatigue cohesive zone model.

The progressive fatigue failure framework has been validated for the case of multidirectional laminates with complex failure processes and thermal residual stresses, demonstrating an important step towards efficient virtual testing of composite structural elements under high-cycle fatigue loading.

REFERENCES

[1] R. H. J. Peerlings, W. A. M. Brekelmans, R. de Borst, M. G. D. Geers, Gradient-enhanced damage modelling of high-cycle fatigue, *International Journal for Numerical Methods in Engineering* 49 (2000) 1547–1569.

[2] A. Turon, J. Costa, P. Camanho, C. Dávila, Simulation of delamination in composites under high-cycle fatigue, *Composites Part A: Applied Science and Manufacturing* 38 (11) (2007) 2270–2282.

[3] P. W. Harper, S. R. Hallett, A fatigue degradation law for cohesive interface elements – Development and application to composite materials, *International Journal of Fatigue* 32 (11) (2010) 1774–1787.

[4] L. F. Kawashita, S. R. Hallett, A crack tip tracking algorithm for cohesive interface element analysis of fatigue delamination propagation in composite materials, *International Journal of Solids and Structures* 49 (21) (2012) 2898–2913.

[5] M. Latifi, F. P. van der Meer, L. J. Sluys, A level set model for simulating fatigue-driven delamination in composites, *International Journal of Fatigue* 80 (2015) 434–442.

[6] B. L. V. Bak, A. Turon, E. Lindgaard, E. Lund, A simulation method for high-cycle fatigue-driven delamination using a cohesive zone model, *International Journal for Numerical Methods in Engineering* 106 (3) (2016) 163–191.

[7] M. Latifi, F. P. van der Meer, L. J. Sluys, Fatigue modeling in composites with the thick level set interface method, *Composites Part A: Applied Science and Manufacturing* 101 (2017) 72–80.

[8] M. Latifi, F. P. van der Meer, L. J. Sluys, An interface thick level set model for simulating delamination in composites, *International Journal for Numerical Methods in Engineering* 111 (4) (2017) 303–324.

[9] A. Amiri-Rad, M. Mashayekhi, A Cohesive Zone Approach for Fatigue-Driven Delamination Analysis in Composite Materials, *Applied Composite Materials* 24 (4) (2017) 751–769.

[10] A. Amiri-Rad, M. Mashayekhi, F. P. van der Meer, Cohesive zone and level set method for simulation of high cycle fatigue delamination in composite materials, *Composite Structures* 160 (2017) 61–69.

[11] M. Latifi, M. A. Kouchakzadeh, Modeling the R-curve effects in laminate composites using the interface thick level set method, *Theoretical and Applied Fracture Mechanics* 108 (2020).

[12] L. Carreras, A. Turon, B. L. Bak, E. Lindgaard, J. Renart, F. Martin de la Escalera, Y. Essa, A simulation method for fatigue-driven delamination in layered structures involving non-negligible fracture process zones and arbitrarily shaped

crack fronts, *Composites Part A: Applied Science and Manufacturing* 122 (2019) 107–119.

[13] G. G. Trabal, B. L. V. Bak, B. Chen, L. Carreras, E. Lindgaard, An adaptive floating node based formulation for the analysis of multiple delaminations under high cycle fatigue loading, *Composites Part A: Applied Science and Manufacturing* 160 (2022) 107036.

[14] S. M. Spearing, P. W. Beaumont, Fatigue damage mechanics of composite materials. I: Experimental measurement of damage and post-fatigue properties, *Composites Science and Technology* 44 (2) (1992) 159–168.

[15] O. J. Nixon-Pearson, S. R. Hallett, P. J. Withers, J. Rouse, Damage development in open-hole composite specimens in fatigue. Part 1: Experimental investigation, *Composite Structures* 106 (2013) 882–889.

[16] O. J. Nixon-Pearson, S. R. Hallett, An investigation into the damage development and residual strengths of open-hole specimens in fatigue, *Composites Part A: Applied Science and Manufacturing* 69 (2015) 266–278.

[17] F. Aymerich, M. S. Found, Response of notched carbon/PEEK and carbon/epoxy laminates subjected to tension fatigue loading, *Fatigue and Fracture of Engineering Materials and Structures* 23 (8) (2000) 675–683.

[18] O. J. Nixon-Pearson, S. R. Hallett, P. W. Harper, L. F. Kawashita, Damage development in open-hole composite specimens in fatigue. Part 2: Numerical modelling, *Composite Structures* 106 (2013) 890–898.

[19] E. V. Iarve, K. Hoos, M. Braginsky, E. Zhou, D. H. Mollenhauer, Progressive failure simulation in laminated composites under fatigue loading by using discrete damage modeling, *Journal of Composite Materials* 51 (15) (2016) 2143–2161.

[20] C. Tao, S. Mukhopadhyay, B. Zhang, L. F. Kawashita, J. Qiu, S. R. Hallett, An improved delamination fatigue cohesive interface model for complex three-dimensional multi-interface cases, *Composites Part A: Applied Science and Manufacturing* 107 (2018) 633–646.

[21] T. Zheng, L. Guo, Z. Wang, R. Benedictus, J.-A. Pascoe, A reliable progressive fatigue damage model for life prediction of composite laminates incorporating an adaptive cyclic jump algorithm, *Composites Science and Technology* 227 (2022) 109587.

[22] W.-T. Lu, Z. Gao, H. K. Adluru, K. H. Hoos, W. P. Seneviratne, D. H. Mollenhauer, E. V. Iarve, Fatigue damage modeling in laminated composite by using Rx-FEM and strength tracking method, *Composites Part A: Applied Science and Manufacturing* 163 (2022) 107199.

[23] C. Tao, C. Zhang, H. Ji, J. Qiu, A Paris-law-informed neural fatigue cohesive model and its application to open-hole composite laminates, *International Journal of Solids and Structures* 267 (2023) 112158.

[24] J. Llobet, P. Maimí, A. Turon, B. Bak, E. Lindgaard, L. Carreras, Y. Essa, F. Martin de la Escalera, A continuum damage model for composite laminates: Part IV-Experimental and numerical tests, *Mechanics of Materials* 154 (2021) 103686.

[25] V. Maneval, N.-P. Vedvik, A. T. Echtermeyer, Progressive Fatigue Modelling of Open-Hole Glass-Fibre Epoxy Laminates, *Journal of Composites Science* 7 (12) (2023) 516.

[26] C. G. Dávila, From S-N to the Paris law with a new mixed-mode cohesive fatigue model for delamination in composites, *Theoretical and Applied Fracture Mechanics* 106 (2020) 102499.

[27] C. G. Dávila, C. A. Rose, G. B. Murri, W. C. Jackson, W. M. Johnston, Evaluation of fatigue damage accumulation functions for delamination initiation and propagation, *Nasa/Tp–2020-220584* (2020).

[28] C. G. Dávila, From S-N to the Paris Law with a New Mixed-Mode Cohesive Fatigue Model, *NASA/TP–2018-219838* (2018).

[29] I. Leciñana, J. Zurbitu, J. Renart, A. Turon, A robust fatigue parameter determination method for a local fatigue Cohesive Zone Model, *International Journal of Fatigue* (2023) 107582.

[30] C. G. Dávila, M. W. Joosten, A cohesive fatigue model for composite delamination based on a new material characterization procedure for the Paris law, *Engineering Fracture Mechanics* 284 (2023) 109232.

[31] I. Leciñana, J. Renart, A. Turon, J. Zurbitu, B. Tijs, Characterization and analysis of the mode I interlaminar fatigue behaviour of thermoplastic composites considering R -curve effects, *Engineering Fracture Mechanics* (2023) 109273.

[32] A. Raimondo, C. G. Dávila, C. Bisagni, Cohesive analysis of a 3D benchmark for delamination growth under quasi-static and fatigue loading conditions, *Fatigue and Fracture of Engineering Materials and Structures* (2022).

[33] Y. J. Liang, C. G. Dávila, E. V. Iarve, A reduced-input cohesive zone model with regularized extended finite element method for fatigue analysis of laminated composites in Abaqus, *Composite Structures* 275 (2021) 114494.

[34] M. W. Joosten, C. G. Dávila, Q. Yang, Predicting fatigue damage in composites subjected to general loading conditions, *Composites Part A: Applied Science and Manufacturing* 156 (2022) 106862.

[35] P. Hofman, F. P. van der Meer, L. J. Sluys, A numerical framework for simulating progressive failure in composite laminates under high-cycle fatigue loading, *Engineering Fracture Mechanics* 295 (2024) 109786.

[36] F. P. van der Meer, L. J. Sluys, A phantom node formulation with mixed mode cohesive law for splitting in laminates, *International Journal of Fracture* 158 (2) (2009) 107–124.

[37] F. P. van der Meer, L. J. Sluys, Mesh-independent modeling of both distributed and discrete matrix cracking in interaction with delamination in composites, *Engineering Fracture Mechanics* 77 (4) (2010) 719–735.

[38] A. Turon, P. P. Camanho, J. Costa, C. G. Dávila, A damage model for the simulation of delamination in advanced composites under variable-mode loading, *Mechanics of Materials* 38 (11) (2006) 1072–1089.

[39] A. Turon, P. P. Camanho, J. Costa, J. Renart, Accurate simulation of delamination growth under mixed-mode loading using cohesive elements: Definition of interlaminar strengths and elastic stiffness, *Composite Structures* 92 (8) (2010) 1857–1864.

[40] A. Turon, E. V. González, C. Sarrado, G. Guillamet, P. Maimí, Accurate simulation of delamination under mixed-mode loading using a cohesive model with a mode-dependent penalty stiffness, *Composite Structures* 184 (2018) 506–511.

[41] R. C. Juvinall, K. M. Marshek, Fundamentals of Machine Component Design, 5th Edition, John Wiley & Sons, Hoboken, NJ, 2012.

[42] A. Hansbo, P. Hansbo, A finite element method for the simulation of strong and weak discontinuities in solid mechanics, *Computer Methods in Applied Mechanics and Engineering* 193 (33-35) (2004) 3523–3540.

[43] F. P. van der Meer, Mesolevel Modeling of Failure in Composite Laminates: Constitutive, Kinematic and Algorithmic Aspects, *Archives of Computational Methods in Engineering* 19 (3) (2012) 381–425.

[44] M. May, S. R. Hallett, A combined model for initiation and propagation of damage under fatigue loading for cohesive interface elements, *Composites Part A: Applied Science and Manufacturing* 41 (12) (2010) 1787–1796.

[45] M. May, R. Pullin, M. Eaton, C. Featherston, S. R. Hallett, An advanced model for initiation and propagation of damage under fatigue loading - part II: Matrix cracking validation cases, *Composite Structures* 93 (9) (2011) 2350–2357.

[46] A. Raimondo, C. Bisagni, Analysis of local stress ratio for delamination in composites under fatigue loads, *AIAA Journal* 58 (1) (2020) 455–463.

[47] W. van Paepegem, J. Degrieck, P. de Baets, Finite element approach for modelling fatigue damage in fibre-reinforced composite materials, *Composites Part B: Engineering* 32 (7) (2001) 575–588.

[48] S. Nojavan, D. Schesser, Q. D. Yang, A two-dimensional in situ fatigue cohesive zone model for crack propagation in composites under cyclic loading, *International Journal of Fatigue* 82 (2016) 449–461.

[49] S. Nojavan, D. Schesser, Q. D. Yang, An in situ fatigue-CZM for unified crack initiation and propagation in composites under cyclic loading, *Composite Structures* 146 (2016) 34–49.

[50] O. Sally, F. Laurin, C. Julien, R. Desmorat, F. Bouillon, An efficient computational strategy of cycle-jumps dedicated to fatigue of composite structures, *International Journal of Fatigue* 135 (2020) 105500.

[51] G. N. Wells, L. J. Sluys, A new method for modelling cohesive cracks using finite elements, *International Journal for Numerical Methods in Engineering* 50 (12) (2001) 2667–2682.

[52] B. G. Green, M. R. Wisnom, S. R. Hallett, An experimental investigation into the tensile strength scaling of notched composites, *Composites Part A: Applied Science and Manufacturing* 38 (3) (2007) 867–878.

[53] F. P. van der Meer, L. J. Sluys, S. R. Hallett, M. R. Wisnom, Computational modeling of complex failure mechanisms in laminates, *Journal of Composite Materials* 46 (5) (2012) 603–623.

[54] W.-G. Jiang, S. R. Hallett, B. G. Green, M. R. Wisnom, A concise interface constitutive law for analysis of delamination and splitting in composite materials and its application to scaled notched tensile specimens, *International Journal for Numerical Methods in Engineering* 69 (9) (2007) 1982–1995.

[55] C. M. Arndt, N. V. de Carvalho, M. W. Czabaj, Experimental reexamination of transverse tensile strength for IM7/8552 tape-laminate composites, *Journal of Composite Materials* 54 (23) (2020) 3297–3312.

[56] M. May, S. R. Hallett, An assessment of through-thickness shear tests for initiation of fatigue failure, *Composites Part A: Applied Science and Manufacturing* 41 (11) (2010) 1570–1578.

[57] G. J. Dvorak, N. Laws, Analysis of Progressive Matrix Cracking In Composite Laminates II. First Ply Failure, *Journal of Composite Materials* 21 (4) (1987) 309–329.

[58] A. Arteiro, G. Catalanotti, A. Melro, P. Linde, P. Camanho, Micro-mechanical analysis of the in situ effect in polymer composite laminates, *Composite Structures* 116 (2014) 827–840.

[59] T. Laux, K. W. Gan, J. M. Dulieu-Barton, O. T. Thomsen, Ply thickness and fibre orientation effects in multidirectional composite laminates subjected to combined tension/compression and shear, *Composites Part A: Applied Science and Manufacturing* 133 (2020) 105864.

[60] Q. Sun, G. Zhou, H. Tang, Z. Meng, M. Jain, X. Su, W. Han, In-situ effect in cross-ply laminates under various loading conditions analyzed with hybrid macro/micro-scale computational models, *Composite Structures* 261 (2021) 113592.

[61] I. Lecinana, J. Zurbitu, J. Renart, A. Turon, L. Carreras, Global sensitivity analysis of an SN curve-based fatigue cohesive zone model and validation through a benchmark test, 20th Eur, in: Conf. Compos. Mater. ECCM20, 2022.

4

A MESOSCOPIC VISCOPLASTICITY MODEL FOR THERMOPLASTIC COMPOSITES

With the exception of minor textual adjustments, this chapter is reproduced from: P. Hofman, D. Kovačević, F. P. van der Meer, L. J. Sluys, A viscoplasticity model with an invariant-based non-Newtonian flow rule for unidirectional thermoplastic composites, *Mechanics of Materials* 211 (2025) 105507. **doi:10.1016/j.mechmat.2025.105507.**

ABSTRACT

A three-dimensional mesoscopic viscoplasticity model for simulating rate-dependent plasticity and creep in unidirectional thermoplastic composites is presented. The constitutive model is a transversely isotropic extension of an isotropic finite strain viscoplasticity model for neat polymers. Rate-dependent plasticity and creep are described by a non-Newtonian flow rule where the viscosity of the material depends on an equivalent stress measure through an Eyring-type relation. In the present formulation, transverse isotropy is incorporated by defining the equivalent stress measure and flow rule as functions of transversely isotropic stress invariants. In addition, the Eyring-type viscosity function is extended with anisotropic pressure dependence. As a result of the formulation, plastic flow in fiber direction is effectively excluded and pressure dependence of the polymer matrix is accounted for. The reorientation of the transversely isotropic plane during plastic deformations is incorporated in the constitutive equations, allowing for an accurate large deformation response. The formulation is fully implicit and a consistent linearization of the algorithmic constitutive equations is performed to derive the consistent tangent modulus. The performance of the mesoscopic constitutive model is assessed through a comparison with a micromechanical model for carbon/PEEK, with the original isotropic viscoplastic version for the polymer matrix and with hyperelastic fibers. The micromodel is first used to determine the material parameters of the mesoscale model with a few stress-strain curves. It is demonstrated that the mesoscale model gives a similar response to the micromodel under various loading conditions. Finally, the mesoscale model is validated against off-axis experiments on unidirectional thermoplastic composite plies.

4.1. INTRODUCTION

Unidirectional fiber-reinforced polymer composites are increasingly used in the aerospace and automotive industry because of their appealing properties. These materials, with superior stiffness and strength compared to more traditional metallic materials, allow for lighter structural components, resulting in significant weight-savings in airplanes and automobiles and therefore less fuel consumption and environmental impact [1].

In recent years, there has been a growing interest in the use of thermoplastics in fiber-reinforced polymer composites. Structural elements made of thermoplastic composites can be fusion bonded, without the need of additional materials such as adhesives or bolts, resulting in more weight-savings, faster processing cycles and the possibility to manufacture composite parts with more complex geometries. However, the mechanical performance of these fusion bonded thermoplastic composites strongly depends on the processing conditions [2–5]. At present, the understanding of processing effects on the mechanical response is not fully matured and the lack of sophisticated performance prediction tools forms an obstacle to the wide-spread use of fusion bonded thermoplastic composites. To improve the prediction abilities, it is essential to develop accurate, efficient and robust constitutive models, capable of simulating the material response under short- and long-term loadings.

A constitutive model that unifies stain-rate dependent yielding and creep in glassy polymers is the Eindhoven Glassy Polymer (EGP) model [6–11]. This is an isotropic viscoplastic model and is part of a family of models for polymers without an explicit yield function [12–14]. Instead of a separation in an elastic and plastic response, it is assumed that an applied stress always produces plastic flow and that the rate of plastic flow depends on the stress level. The rate of plastic deformation is then described with a non-Newtonian flow rule following an Eyring-type relation [15].

The isotropic EGP model has been successfully applied to micromechanical analyses of polymer composites with representative volume elements [16–18], where fibers and matrix are explicitly modeled. A representative volume element is sufficient for studying the composites' behavior under homogeneous deformations at the mesocale level—that is, the level at which the composite can be considered a homogeneous medium. For more complex structural analyses of composites with inhomogeneous deformations, a multiscale approach can be used. This requires a coupling between the microscale and mesoscale, where two finite element analyses are performed simultaneously and information is exchanged in between. However, such approaches remain computationally infeasible and are still subject of ongoing research in the case of localization [19, 20]. To overcome the computational burden of

multiscale analyses, either surrogate models [21, 22], homogenized micromechanics-based models [23, 24] or mesoscopic phenomenological constitutive models are required.

Extensions of the EGP model for simulating anisotropic rate-dependent plasticity and creep have previously been proposed [25–28]. The key element in these works is the incorporation of anisotropy in the (hyper-)elasticity and rate-dependent plasticity relations. Van Erp et al. [25] proposed an anisotropic flow rule based on the classical Hill yield criterion [29]. Senden et al. [26] used this flow rule in the EGP model for predicting anisotropic yielding in injection molded polyethylene and Amiri-Rad et al. further developed it for *short* fiber [27] and *long* fiber-reinforced polymer composites [28]. However, a suitable version for *continuous* fiber-reinforced polymer composites does not yet exist.

In continuous fiber-reinforced polymers, fibers behave elastically until fracture, while the polymer matrix is responsible for the viscoelastic/viscoplastic response. Combined in a composite, this results in a mostly elastic response when loaded in fiber direction and in a viscoplastic response under off-axis loads. In a constitutive model, strong transverse isotropy can be achieved through the use of transversely isotropic stress invariants [30, 31] for describing yield criteria, as previously done with Perzyna-type viscoplastic models [32–34]. These models have been successfully applied to the simulation of rate-dependent anisotropic plasticity in *thermosetting* polymer composites under short term loadings. As opposed to *thermosets*, *thermoplastics* lack primary (chemical) bonds between polymer chains [35]. When subjected to stress, the polymer response transitions from solid-like to fluid-like, which is described in the EGP model with an Eyring-type non-Newtonian flow rule. With the non-Newtonian flow rule, creep and rate-dependent plasticity are treated in a unified manner. In addition, the effects of temperature can be taken into account through the Eyring relation, as well as the effects of pressure [8, 36] and aging [9].

In this chapter, we combine the use of transversely isotropic invariants and non-Newtonian flow, and propose an invariant-based mesoscopic extension of the EGP model for simulating rate-dependent plasticity and creep in continuous fiber-reinforced thermoplastic composites. For assessing the accuracy of the mesoscopic constitutive model, a detailed micromodel of a carbon/PEEK composite [16, 37] is used with fibers and matrix explicitly modeled. The micromodel first serves to identify the parameters of the mesoscopic constitutive model through numerical homogenization [38–40] with a parameter identification procedure based on a few stress-strain curves. Subsequently, the response of the mesoscale model under off-axis constant strain rates and creep loads is assessed. Finally, unidirectional plies subjected to off-axis strain rates are simulated and compared against experiments.

Scalars are represented by italic symbols (*e.g.* a), while vectors are denoted using italic bold lower case symbols (*e.g.* $\boldsymbol{a}$). Second-order tensors are expressed with bold upper case Roman symbols (*e.g.* $\mathbf{A}$), and fourth-order tensors are indicated by bold blackboard symbols (*e.g.* $\mathbb{A}$). The symmetric and skew-symmetric parts of a second order tensor $\mathbf{A}$ are given by $\mathbf{A}^{\mathrm{sym}} = 1/2\left(\mathbf{A} + \mathbf{A}^{\mathrm{T}}\right)$ and $\mathbf{A}^{\mathrm{skw}} = 1/2\left(\mathbf{A} - \mathbf{A}^{\mathrm{T}}\right)$. The product of two second-order tensors $\mathbf{A}$ and $\mathbf{B}$ is expressed as $\mathbf{A} \cdot \mathbf{B} = A_{ik}B_{kj}$, while the double contraction is given by $\mathbf{A} : \mathbf{B} = A_{ij}B_{ij}$. Finally, the dyadic product of two vectors $\boldsymbol{a}$ and $\boldsymbol{b}$ is written as $\boldsymbol{a} \otimes \boldsymbol{b} = a_i b_j$.

4.2. FORMULATION OF THE CONSTITUTIVE MODEL

The mesoscopic constitutive model for the composite material is based on the EGP model for neat polymers [6, 7, 10], which assumes two contributions to the stress, a driving stress $\boldsymbol{\sigma}^{\mathrm{d}}$ and a hardening stress $\boldsymbol{\sigma}^{\mathrm{h}}$:

$$\boldsymbol{\sigma} = \boldsymbol{\sigma}^{\mathrm{d}} + \boldsymbol{\sigma}^{\mathrm{h}} \tag{4.1}$$

The driving stress is described by a spectrum of relaxation times, which is incorporated in the model by adding N_{m} nonlinear spring-dashpots (denoted as *modes*) in parallel. The driving stress is the sum of the driving stresses $\boldsymbol{\sigma}_i^{\mathrm{d}}$ in each mode i:

$$\boldsymbol{\sigma}^{\mathrm{d}} = \sum_{i}^{N_{\mathrm{m}}} \boldsymbol{\sigma}_i^{\mathrm{d}} \tag{4.2}$$

For thermorheologically simple materials, it can be assumed that the viscosity of each mode η_i has the same functional dependence on the *total* driving stress $\boldsymbol{\sigma}^{\mathrm{d}}$ [6]. The rheological model of the driving stress contribution is shown in Fig. 4.1.

In this work, the focus is on the driving stress contribution for describing anisotropic rate-dependent plasticity in the pre-yield and yield regime. There-

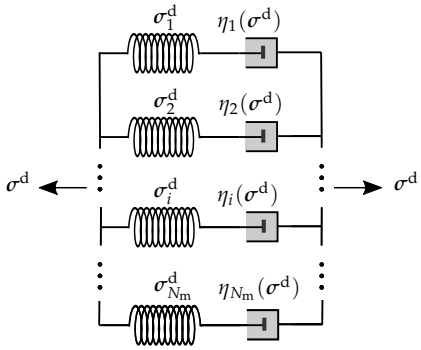

Figure 4.1 Rheological model of the driving stress.

fore, the hardening contribution is not taken into account ($\sigma^{\mathrm{h}} = 0$). To improve readability, the superscript (d) in the driving stress is dropped in the remainder of the text.

4.2.1. KINEMATICS

In each mode i, a multiplicative decomposition of the total deformation gradient $\mathbf{F}$ into an elastic $\mathbf{F}_{ei}$ and a plastic $\mathbf{F}_{pi}$ deformation gradient is assumed [41, 42]:

$$\mathbf{F} = \mathbf{F}_{ei} \cdot \mathbf{F}_{pi} \tag{4.3}$$

The plastic deformation gradient maps the neighborhood of a mesoscopic material point from the *initial* configuration Ω_0 to a fictitious, locally stress-free, *intermediate* configuration $\hat{\Omega}_i$. Subsequently, the elastic deformation maps it from the *intermediate* configuration to the *current* configuration Ω (see Fig. 4.2). The plastic velocity gradient in the *intermediate* configuration reads

$$\hat{\mathbf{L}}_{pi} = \dot{\mathbf{F}}_{pi} \cdot \mathbf{F}_{pi}^{-1} = \underbrace{\left(\dot{\mathbf{F}}_{pi} \cdot \mathbf{F}_{pi}^{-1}\right)^{\mathrm{sym}}}_{\hat{\mathbf{D}}_{pi}} + \underbrace{\left(\dot{\mathbf{F}}_{pi} \cdot \mathbf{F}_{pi}^{-1}\right)^{\mathrm{skw}}}_{\hat{\mathbf{W}}_{pi}} \tag{4.4}$$

where $\hat{\mathbf{D}}_{pi}$ is the *rate of plastic deformation* and $\hat{\mathbf{W}}_{p}$ is the *plastic material spin* [43]. To overcome the non-uniqueness of the multiplicative decomposition regarding the orientation of the *intermediate* configuration, we choose $\hat{\mathbf{W}}_{pi} = \mathbf{0}$ [14, 44]. Therefore, the evolution of $\mathbf{F}_{pi}$ is described with the following differential equation:

$$\dot{\mathbf{F}}_{pi} = \hat{\mathbf{D}}_{pi} \cdot \mathbf{F}_{pi} \tag{4.5}$$

The transverse isotropy that originates from the microstructure of the unidirectional polymer composite is characterized by fiber direction vectors $\boldsymbol{a}_0$, $\hat{\boldsymbol{a}}_i$ and $\boldsymbol{a}$ in the *initial*, *intermediate* and *current* configurations, respectively. In the present mesoscopic

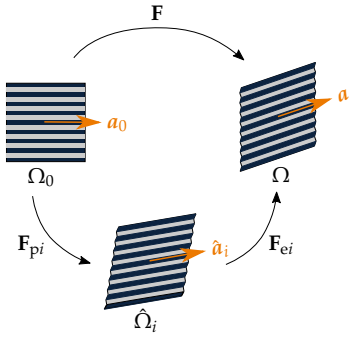

Figure 4.2 Decomposition of total deformation in elastic and plastic deformation for *each* mode i, with the corresponding *initial* Ω_0, *intermediate* $\hat{\Omega}_i$ and *current* configuration Ω.

constitutive model, the fiber vector represents *continuous* fibers in the composite and is assumed to remain affinely attached to the material during deformation,[1] which is described by the following transformations using the multiplicative decomposition in Eq. (4.3):

$$\boldsymbol{a} = \mathbf{F}_{\mathrm{e}i} \cdot \hat{\boldsymbol{a}}_i = \mathbf{F}_{\mathrm{e}i} \cdot \mathbf{F}_{\mathrm{p}i} \cdot \boldsymbol{a}_0 = \mathbf{F} \cdot \boldsymbol{a}_0 \tag{4.6}$$

Furthermore, plastic deformation is assumed to be isochoric:

$$\det\left(\mathbf{F}_{\mathrm{p}i}\right) = 1 \tag{4.7}$$

4.2.2. VISCOPLASTICITY RELATIONS

The rate of plastic deformation in the intermediate configuration in each mode i follows a non-Newtonian flow rule:

$$\hat{\mathbf{D}}_{\mathrm{p}i} = \dot{\gamma}_{\mathrm{p}i} \hat{\mathbf{N}}_{\mathrm{p}i} \tag{4.8}$$

where $\dot{\gamma}_{\mathrm{p}i}$ is the (scalar) equivalent plastic strain rate and $\hat{\mathbf{N}}_{\mathrm{p}i}$ is the direction of plastic flow. The equivalent plastic strain rate is given by

$$\dot{\gamma}_{\mathrm{p}i} = \frac{\bar{\Sigma}_i}{\eta_i} \tag{4.9}$$

where $\bar{\Sigma}_i$ is the equivalent stress in mode i. The viscosity η_i is determined as

$$\eta_i = \eta_{0i}\, a_\sigma \tag{4.10}$$

where a_σ is the *stress shift factor*[2] and η_{0i} is the initial viscosity of mode i. The *stress shift factor* follows an Eyring relation and is a function of the *total* driving stress σ through a *total* equivalent stress $\bar{\sigma}$ and may depend on the temperature, pressure and aging [8, 36, 45]. Neglecting these influences, the *stress shift factor* reads

$$a_\sigma = \frac{\bar{\sigma}/\sigma_0}{\sinh\left(\bar{\sigma}/\sigma_0\right)} \tag{4.11}$$

where σ_0 is a parameter that controls the stress-induced exponential decrease of the viscosity. Note that the viscosity in each mode is different because of the different initial viscosities $\{\eta_{0i}\}$. However, a_σ is the same across all modes, representing a thermorheologically simple material [6].

[1] For short fiber composites, this assumption is debatable as pointed out in Ref. [43], where short fibers may evolve differently from the mesoscopic kinematics.

[2] The name *stress shift factor* refers to its effect of reducing the initial viscosity with increasing stress, resulting in horizontal shifts at different stress levels in creep-compliance curves on logarithmic time scales [7].

For describing plastic flow, a Mandel-like stress tensor [46] is introduced as

$$\boldsymbol{\Sigma}_i = \mathbf{F}_{\mathrm{e}i}^{\mathrm{T}} \cdot \boldsymbol{\sigma}_i \cdot \mathbf{F}_{\mathrm{e}i}^{-\mathrm{T}} \tag{4.12}$$

which is work-conjugate to $\hat{\mathbf{D}}_{\mathrm{p}i}$ and is in general not symmetric for anisotropic materials [47]. To ensure a symmetric $\hat{\mathbf{D}}_{\mathrm{p}i}$ and to remain consistent with the choice of a vanishing $\hat{\mathbf{W}}_{\mathrm{p}i}$ (see Sec. 4.2.1), it is assumed that *only* the symmetric part of $\boldsymbol{\Sigma}_i$ determines the plastic flow direction [31, 34, 48]:

$$\hat{\mathbf{N}}_{\mathrm{p}i} = \frac{\partial \bar{\Sigma}_i}{\partial \boldsymbol{\Sigma}_i^{\mathrm{sym}}} \tag{4.13}$$

In the (original) isotropic EGP model, the equivalent stress(es) are proportional to the Von Mises stress [6–10]. For *short* and *long* fiber-reinforced polymer composites, they can be proportional to the Hill effective stress [27, 28]. In this work, strong transverse isotropy of *continuous* fiber-reinforced polymer composites is taken into account by defining the equivalent stresses $\bar{\sigma}$ and $\bar{\Sigma}_i$ as functions of transversely isotropic stress invariants. In addition, anisotropic pressure dependency is incorporated by modifying the Eyring-type relation Eq. (4.11). The invariant-based formulation is presented in the next section.

4.2.3. INVARIANT FORMULATION

Fiber-reinforced polymer composites can be considered transversely isotropic at the mesoscale. The response of the mesoscopic constitutive model should therefore be invariant with respect to the symmetry transformations for transverse isotropy [49]. For unidirectional fiber-reinforced polymer composites with strong anisotropy, additional requirements can be specified: (*i*) the material should not flow in the direction of the fiber, (*ii*) the plastic deformation should be isochoric (as stated in Eq. (4.7)) and (*iii*) the pressure dependence of the polymer matrix should be taken into account. These requirements can be satisfied by using transversely isotropic invariants [49, 50] for defining the equivalent stresses $\bar{\sigma}$ and $\bar{\Sigma}_i$ and by extending the Eyring relation (Eq. (4.11)) to account for anisotropic pressure dependence.

TOTAL EQUIVALENT STRESS

The material symmetries of the fiber-reinforced polymer composite are represented with fiber direction (unit) vectors $\boldsymbol{a}_0$ and $\bar{\boldsymbol{a}} = \boldsymbol{a}/\|\boldsymbol{a}\|$ in the *initial* and *current* configurations, respectively (see Fig. 4.2). Furthermore, the stress is first split into a plasticity-inducing $\boldsymbol{\sigma}^{\mathrm{pind}}$ and a remaining (elastic) part [30, 50]:

$$\boldsymbol{\sigma}^{\mathrm{pind}} = \boldsymbol{\sigma} - (p\,\mathbf{I} + \sigma_{\mathrm{f}}\,\bar{\mathbf{A}}) \tag{4.14}$$

where p is the pressure, σ_f the part of the stress projection onto the fiber direction that exceeds the pressure and $\bar{\mathbf{A}} = \bar{\boldsymbol{a}} \otimes \bar{\boldsymbol{a}}$. The plasticity-inducing stress can be determined from the total stress $\boldsymbol{\sigma}$ with the mapping

$$\boldsymbol{\sigma}^{\text{pind}} = \mathbb{P} : \boldsymbol{\sigma} \tag{4.15}$$

where $\mathbb{P}$ is a fourth order tensor, given as

$$\mathbb{P} = \mathbb{I} - \frac{1}{2}\mathbf{I} \otimes \mathbf{I} - \frac{3}{2}\bar{\mathbf{A}} \otimes \bar{\mathbf{A}} + \frac{1}{2}\left(\bar{\mathbf{A}} \otimes \mathbf{I} - \mathbf{I} \otimes \bar{\mathbf{A}}\right) \tag{4.16}$$

with $\mathbb{I}_{ijkl} = \delta_{ik}\delta_{jl}$. The following three transversely isotropic invariants are introduced [51]:

$$I_1 = \frac{1}{2}\,\text{tr}\left[\boldsymbol{\sigma}^{\text{pind}} \cdot \boldsymbol{\sigma}^{\text{pind}}\right] - \bar{\boldsymbol{a}} \cdot \left[\boldsymbol{\sigma}^{\text{pind}} \cdot \boldsymbol{\sigma}^{\text{pind}}\right] \cdot \bar{\boldsymbol{a}} \tag{4.17}$$

$$I_2 = \bar{\boldsymbol{a}} \cdot \left[\boldsymbol{\sigma}^{\text{pind}} \cdot \boldsymbol{\sigma}^{\text{pind}}\right] \cdot \bar{\boldsymbol{a}} \tag{4.18}$$

$$I_3 = \text{tr}\left[\boldsymbol{\sigma}\right] - \bar{\boldsymbol{a}} \cdot \boldsymbol{\sigma} \cdot \bar{\boldsymbol{a}} \tag{4.19}$$

To inspect the meaning of these invariants, they can be expressed in terms of stress components in a local frame, where $\boldsymbol{e}_1$ is aligned with the fiber direction vector $\boldsymbol{a}$:

$$I_1 = \frac{1}{4}\left(\sigma_{22} - \sigma_{33}\right)^2 + \sigma_{23}^2 \tag{4.20}$$

$$I_2 = \sigma_{12}^2 + \sigma_{13}^2 \tag{4.21}$$

$$I_3 = \sigma_{22} + \sigma_{33} \tag{4.22}$$

From Eqs. (4.20) to (4.22), it can be seen that I_1 is related to transverse shear, I_2 to longitudinal shear and I_3 to biaxial tension or compression in the transverse plane (see Fig. 4.3).[3] With these invariants, an equivalent stress can be constructed that does not induce yielding due to stress projections in the fiber direction. The *total* equivalent stress $\bar{\sigma}$ that drives the evolution of the viscosity through *stress shift factor* a_σ is proposed as

$$\bar{\sigma} = \sqrt{2\left(I_1 + \alpha_2 I_2\right)} \tag{4.23}$$

where α_2 is a model parameter. The equivalent stress $\bar{\sigma}$ is a measure for shear stress in the polymer matrix, reflecting that for continuous fiber-reinforced polymer composites, transverse shear (invariant I_1) and longitudinal shear (invariant I_2) do not lead to the same shear stresses in the polymer matrix, hence demanding the coefficient α_2.

[3] Note that these invariants are not the same as in classical plasticity theory for $\{I_i\}_{i=1,2,3}$. Here we follow the definitions from Refs. [31–34, 48, 51].

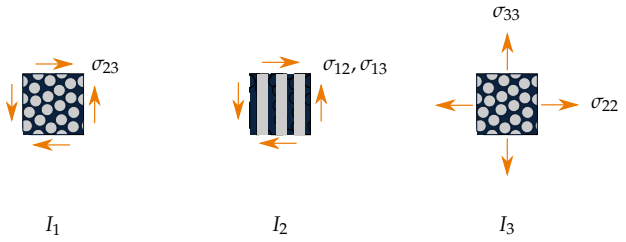

Figure 4.3 The transversely isotropic stress invariants are related to transverse shear (*left*), longitudinal shear (*middle*) and biaxial tension or compression (*right*).

The third invariant I_3 is used to describe pressure dependence of the polymer matrix, by extending the Eyring relation Eq. (4.11) as

$$a_\sigma = \frac{\bar{\sigma}/\sigma_0}{\sinh\left(\bar{\sigma}/\sigma_0\right)} \exp\left(-\mu_\mathrm{p} \frac{I_3}{\sigma_0}\right) \tag{4.24}$$

where μ_p is a pressure dependency parameter. This relation is similar to previous modifications of the Eyring relation for isotropic polymers [8, 9, 36], where instead of I_3, the hydrostatic pressure $p = -1/3 \operatorname{tr} \boldsymbol{\sigma}$ was used in the argument of the exponential function. Note that through I_3 (which is a measure for pressure in the polymer matrix), anisotropic pressure dependence of the composite is taken into account with Eq. (4.24).

EQUIVALENT STRESS OF EACH MODE

As mentioned in Sec. 4.2.2, the equivalent stress of each mode $\bar{\Sigma}_i$ is a function of the symmetric part of $\boldsymbol{\Sigma}_i$ and the fiber direction vector in the *intermediate* configuration $\hat{\boldsymbol{a}}_i$. Replacing in Eq. (4.15) and Eq. (4.16) quantities referring to the *current* configuration $\{\boldsymbol{\sigma}, \boldsymbol{a}\}$ by quantities referring to the *intermediate* configuration $\{\boldsymbol{\Sigma}_i^{\mathrm{sym}}, \hat{\boldsymbol{a}}_i\}$, gives the plasticity-inducing part of $\boldsymbol{\Sigma}_i^{\mathrm{sym}}$:

$$\boldsymbol{\Sigma}_i^{\mathrm{pind}} = \hat{\mathbb{P}}_i : \boldsymbol{\Sigma}_i^{\mathrm{sym}} \tag{4.25}$$

with corresponding fourth order tensor $\hat{\mathbb{P}}_i$:

$$\hat{\mathbb{P}}_i = \mathbb{I} - \frac{1}{2}\mathbf{I} \otimes \mathbf{I} - \frac{3}{2}\hat{\mathbf{A}}_i \otimes \hat{\mathbf{A}}_i + \frac{1}{2}\left(\hat{\mathbf{A}}_i \otimes \mathbf{I} - \mathbf{I} \otimes \hat{\mathbf{A}}_i\right) \tag{4.26}$$

and invariants for each mode i:

$$\hat{I}_{1i} = \frac{1}{2} \operatorname{tr}\left[\boldsymbol{\Sigma}_i^{\mathrm{pind}} \cdot \boldsymbol{\Sigma}_i^{\mathrm{pind}}\right] - \hat{\boldsymbol{a}}_i \cdot \left[\boldsymbol{\Sigma}_i^{\mathrm{pind}} \cdot \boldsymbol{\Sigma}_i^{\mathrm{pind}}\right] \cdot \hat{\boldsymbol{a}}_i \tag{4.27}$$

$$\hat{I}_{2i} = \hat{\boldsymbol{a}}_i \cdot \left[\boldsymbol{\Sigma}_i^{\mathrm{pind}} \cdot \boldsymbol{\Sigma}_i^{\mathrm{pind}}\right] \cdot \hat{\boldsymbol{a}}_i \tag{4.28}$$

To prevent plastic flow in fiber direction and account for plastic incompressibility, only invariants $\hat{I}_{1i}$ and $\hat{I}_{2i}$, which are functions of $\boldsymbol{\Sigma}_i^{\text{pind}}$, are used to describe the direction of plastic flow through Eq. (4.13). Similar to the *total* equivalent stress $\bar{\sigma}$, the equivalent stress of mode i is defined as

$$\bar{\Sigma}_i = \sqrt{2\left(\hat{I}_{1i} + \alpha_2 \hat{I}_{2i}\right)} \tag{4.29}$$

with plastic normal direction

$$\mathbf{N}_{\text{p}i} = \frac{\partial \bar{\Sigma}_i}{\partial \boldsymbol{\Sigma}_i^{\text{sym}}} = \frac{1}{\bar{\Sigma}_i}\left[\frac{\partial \hat{I}_{1i}}{\partial \boldsymbol{\Sigma}_i^{\text{sym}}} + \alpha_2 \frac{\partial \hat{I}_{2i}}{\partial \boldsymbol{\Sigma}_i^{\text{sym}}}\right] \tag{4.30}$$

where α_2 is the same model parameter as in Eq. (4.23), to limit the number of parameters and aid their identification procedure. The derivatives of the invariants read

$$\frac{\partial \hat{I}_{1i}}{\partial \boldsymbol{\Sigma}_i^{\text{sym}}} = \left[\left(\mathbf{I} - \hat{\mathbf{A}}_i\right) \cdot \boldsymbol{\Sigma}_i^{\text{pind}} - \boldsymbol{\Sigma}_i^{\text{pind}} \cdot \hat{\mathbf{A}}_i\right] : \hat{\mathbb{P}}_i \tag{4.31}$$

$$\frac{\partial \hat{I}_{2i}}{\partial \boldsymbol{\Sigma}_i^{\text{sym}}} = \left[\hat{\mathbf{A}}_i \cdot \boldsymbol{\Sigma}_i^{\text{pind}} + \boldsymbol{\Sigma}_i^{\text{pind}} \cdot \hat{\mathbf{A}}_i\right] : \hat{\mathbb{P}}_i \tag{4.32}$$

Remark 4.1 The *total* equivalent stress $\bar{\sigma}$ is a function of $\boldsymbol{\sigma}$ and $\bar{\boldsymbol{a}}$, instead of $\boldsymbol{\Sigma}_i$ and $\hat{\boldsymbol{a}}_i$. The reason for this is that the latter quantities refer to an *intermediate* configuration, which is different for each mode (see Fig. 4.2). Therefore, 'total versions' of $\boldsymbol{\Sigma}$ and $\hat{\boldsymbol{a}}$ do not exist.

Remark 4.2 In the present contribution, thermorheologically simple material behavior is assumed. The model can be extended to simulate thermorheologically complex behavior with several relaxation processes. A multiprocess model can be obtained by adding multiple driving stress contributions in parallel, where each contribution obeys an Eyring relation with a different parameter σ_0 [45] and a different relaxation spectrum.

Remark 4.3 As pointed out by [38], the difference between stress combinations $\sigma_{12} - \sigma_{22}$ and $\sigma_{12} - \sigma_{33}$ is not considered in the invariant formulation. Furthermore, the effect on the yielding of a stress in fiber direction is removed. Although the material should not flow in the fiber direction, the stress in the fiber direction should contribute to the yielding of the polymer matrix under combined loading, for example longitudinal shear and stress in fiber direction. These assumptions remain limitations of the present mesoscale model.

Remark 4.4 In the equivalent stress definitions, only α_2 is used as a coefficient of invariant I_2. The fact that α_2 is cancelled in a transverse uniaxial tension and compression test simplifies the parameter identification procedure as will be shown in Sec. 4.3.

4.2.4. EMBEDDED HYPERELASTIC CONSTITUTIVE RELATIONS

A hyperelastic transversely isotropic constitutive model [52] is used in this work to compute the stress in the composite material. The second Piola Kirchhoff stress $\mathbf{S}$ is decomposed in an isotropic (iso) and a transversely isotropic part (trn) as

$$\mathbf{S} = \mathbf{S}_{\text{iso}} + \mathbf{S}_{\text{trn}} \tag{4.33}$$

Without plastic deformations, these contributions are given as

$$\begin{aligned}
\mathbf{S}_{\text{iso}} &= \mu(\mathbf{I} - \mathbf{C}^{-1}) + \lambda J(J-1)\mathbf{C}^{-1} \\
\mathbf{S}_{\text{trn}} &= 2\beta(\xi_2 - 1)\mathbf{I} + 2\left[\alpha + \beta(\xi_1 - 3) + 2\gamma(\xi_2 - 1)\right] \boldsymbol{a}_0 \otimes \boldsymbol{a}_0 \\
&\quad - \alpha\left(\mathbf{C}\cdot\boldsymbol{a}_0 \otimes \boldsymbol{a}_0 + \boldsymbol{a}_0 \otimes \mathbf{C}\cdot\boldsymbol{a}_0\right)
\end{aligned} \tag{4.34}$$

where $\mathbf{C} = \mathbf{F}^{\mathrm{T}} \cdot \mathbf{F}$ is the right Cauchy-Green deformation tensor and $J = \det(\mathbf{F})$. The parameters $\lambda, \mu, \alpha, \beta$ and γ are material constants that can be computed from the Young moduli and the Poisson ratios:

$$\begin{aligned}
n &= \frac{E_2}{E_1} \\
m &= 1 - \nu_{21} - 2n\nu_{21}^2 \\
\lambda &= E_2 \frac{\nu_{21} + n\,\nu_{21}^2}{m(1+\nu_{21})} \\
\mu &= \frac{E_2}{2(1+\nu_{21})} \\
\alpha &= \mu - G_{12} \\
\beta &= \frac{E_2\,\nu_{21}^2(1-n)}{4m(1+\nu_{21})} \\
\gamma &= \frac{E_1(1-\nu_{21})}{8m} - \frac{\lambda + 2\mu}{8} + \frac{\alpha}{2} - \beta
\end{aligned} \tag{4.35}$$

where the Young moduli E_1 and E_2, the shear modulus G_{12} and the Poisson ratio ν_{21} refer to a local coordinate frame with $\boldsymbol{e}_1$ aligned with the fiber direction. Furthermore, ξ_1 and ξ_2 are defined as

$$\xi_1 = \operatorname{tr}(\mathbf{C}) \tag{4.36}$$

$$\xi_2 = \boldsymbol{a} \cdot \boldsymbol{a} \tag{4.37}$$

In the present contribution, we use this hyperelastic transversely isotropic constitutive model to compute the stress in each mode i when the material is mapped from its *intermediate* configuration to the *current* configuration (see Fig. 4.2). To this end, the following quantities are replaced by quantities that refer to the *intermediate* configurations: $\{\mathbf{S}, \boldsymbol{a}_0, \mathbf{C}, \xi_1, J\} \rightarrow \{\hat{\mathbf{S}}_i, \hat{\boldsymbol{a}}_i, \mathbf{C}_{ei}, \xi_{1ei}, J_{ei}\}$. The relations for the hyperelastic model of each mode i become

$$\begin{aligned}\hat{\mathbf{S}}_{\text{iso},i} &= \mu_i(\mathbf{I} - \mathbf{C}_{ei}^{-1}) + \lambda_i J_{ei}(J_{ei} - 1)\mathbf{C}_{ei}^{-1} \\ \hat{\mathbf{S}}_{\text{trn},i} &= 2\beta_i(\xi_2 - 1)\mathbf{I} + 2\left[\alpha_i + \beta_i(\xi_{1ei} - 3) + 2\gamma_i(\xi_2 - 1)\right]\hat{\boldsymbol{a}}_i \otimes \hat{\boldsymbol{a}}_i \\ &\quad - \alpha_i\left(\mathbf{C}_{ei} \cdot \hat{\boldsymbol{a}}_i \otimes \hat{\boldsymbol{a}}_i + \hat{\boldsymbol{a}}_i \otimes \mathbf{C}_{ei} \cdot \hat{\boldsymbol{a}}_i\right)\end{aligned} \tag{4.38}$$

Note that each mode has a different set of elastic constants. Furthermore, the vector $\hat{\boldsymbol{a}}_i$ is a unit vector since plastic flow is excluded in fiber direction. Pushing forward Eq. (4.38) from the *intermediate* to the *current* configuration gives the Cauchy stress contributions

$$\begin{aligned}\boldsymbol{\sigma}_{\text{iso},i} &= \frac{\mu_i}{J_{ei}}\left(\mathbf{B}_{ei} - \mathbf{I}\right) + \lambda_i(J_{ei} - 1)\mathbf{I} \\ J_{ei}\boldsymbol{\sigma}_{\text{trn},i} &= 2\beta_i(\xi_2 - 1)\mathbf{B}_{ei} + 2\left[\alpha_i + \beta_i(\xi_{1ei} - 3) + 2\gamma_i(\xi_2 - 1)\right]\boldsymbol{a} \otimes \boldsymbol{a} \\ &\quad - \alpha_i\left(\mathbf{B}_{ei} \cdot \boldsymbol{a} \otimes \boldsymbol{a} + \boldsymbol{a} \otimes \mathbf{B}_{ei} \cdot \boldsymbol{a}\right)\end{aligned} \tag{4.39}$$

where $\mathbf{B}_{ei} = \mathbf{F}_{ei} \cdot \mathbf{F}_{ei}^{\mathrm{T}}$ is the elastic left Cauchy-Green deformation tensor. Note that the kinematics in Fig. 4.2, with re-orienting fiber direction vector(s) in the *intermediate* configuration(s), are taken into account in the embedded hyperelastic model.

4.2.5. MULTIMODE MODEL

Direction-, pressure- and rate-dependent yielding can be described by a single mode (see Fig. 4.4), requiring four parameters: α_2, μ_{p}, σ_0 and η_0. However, for polymers and polymer composites, a single viscosity is not sufficient to describe the nonlinear response prior to yielding [6, 10]. A more accurate representation of the time-dependent pre-yield (and creep) response is obtained by including multiple modes (see Fig. 4.4). With N_{m} modes, the yield stress is then determined by the mode with the highest initial viscosity $\eta_0 = \max\{\eta_{0i}\}$.

A relaxation spectrum can be determined from a single stress-strain curve, obtained from a test under a constant strain rate as described in Ref. [10]. This procedure was originally developed for isotropic polymers and recently extended to anisotropic yielding in *short*- and *long*-fiber composites [27]. The same procedure is applied to the present model for *continuous* fiber-reinforced polymer composites

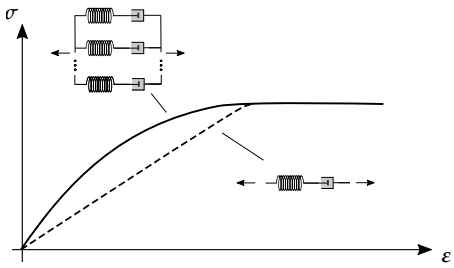

Figure 4.4 Stress-strain response with a single mode and with multiple modes.

and is briefly outlined here for completeness. For more details, the reader is referred to the Refs. [10, 27].

The method makes use of a Boltzmann integral with N_m unknown relaxation times to fit a 1D equivalent stress-strain curve from a constant strain rate test under off-axis angle θ. The result of the procedure is a spectrum of moduli $\{E_{\theta i}\}$ and initial viscosities $\{\eta_{0i}\}$. It is then assumed that the ratio

$$m_i = \frac{E_{\theta i}}{\sum_i^{N_\mathrm{m}} E_{\theta i}} \tag{4.40}$$

is the same for E_1, E_2 and G_{12}. With the set of ratios $\{m_i\}$, the elastic constants are obtained for each mode:

$$\begin{aligned} E_{1i} &= m_i E_1 \\ E_{2i} &= m_i E_2 \\ G_{12i} &= m_i G_{12} \\ \nu_{21i} &= \nu_{21} \end{aligned} \tag{4.41}$$

The hyperelastic parameters for each mode are obtained with Eq. (4.35), replacing constants $\{E_1, E_2, G_{12}\}$ by $\{E_{1i}, E_{2i}, G_{12i}\}$.

4.2.6. INTEGRATION OF THE CONSTITUTIVE RELATIONS

To compute the stress in each mode from the elastic deformation, the plastic deformation must be known, which in turn depends, through the non-Newtonian flow rule, on the stress in each mode and on the *total* stress through the stress-dependent shift factor. This renders a nonlinear relation between the total stress and deformation gradient, that must be solved with an iterative scheme.

NESTED SCHEME

Following Ref. [53], a nested scheme with an *external* and *internal* solution process is used (see Fig. 4.5). In the *external* scheme, the *stress shift factor* a_σ is iteratively solved with Newton iterations. For every *external* iteration, the viscosities $\{\eta_i\}$ of the modes are known, which allows for computing the stress in each mode $\boldsymbol{\sigma}_i$ separately with an *internal* Newton-Raphson scheme.

EXTERNAL NEWTON-RAPHSON SCHEME

For solving the *stress shift factor* a_σ, Eq. (4.24) is cast in residual form:

$$R_{a_\sigma} = a_\sigma - \frac{\bar{\sigma}/\sigma_0}{\sinh\left(\bar{\sigma}/\sigma_0\right)} \exp\left(-\mu_\mathrm{p}\frac{I_3}{\sigma_0}\right) \tag{4.42}$$

The root of this equation is found with Newton iterations $j = 1 \dots N_\mathrm{iter}$ by updating a_σ as follows:

$$a_\sigma^{(j+1)} = a_\sigma^{(j)} - \frac{R_{a_\sigma}^{(j)}}{\left.\frac{\partial R_{a_\sigma}}{\partial a_\sigma}\right|_{\mathbf{F}}^{(j)}} \tag{4.43}$$

where $\partial R_{a_\sigma}/\partial a_\sigma|_{\mathbf{F}}$ is the Jacobian for the *external* scheme, which is derived in Sec. 4.2.7. For each *external* Newton iteration j, the stress in each mode $\boldsymbol{\sigma}_i$ is found with the *internal* Newton-Raphson scheme, with viscosity $\eta_i^{(j)} = \eta_{0i} {a_\sigma}^{(j)}$. Subsequently, the *total equivalent stress* $\bar{\sigma}$ is computed and the residual R_{a_σ} and the Jacobian $\partial R_{a_\sigma}/\partial a_\sigma|_{\mathbf{F}}$ are evaluated to update the stress shift factor $a_\sigma^{(j+1)}$ for the next iteration with Eq. (4.43).

INTERNAL NEWTON-RAPHSON SCHEME

In the *internal* scheme, the plastic deformation $\mathbf{F}_{\mathrm{p}i}$ is chosen as primary unknown. The time integration of Eq. (4.5) is performed with an implicit exponential map [54, 55] to retain plastic incompressibility (Eq. (4.7)) [56]. The plastic deformation at the current time step $\mathbf{F}_{\mathrm{p}i}$ is computed from the rate of plastic deformation at the current time step $\hat{\mathbf{D}}_{\mathrm{p}i}$ and the plastic deformation at the previous time step $\mathbf{F}_{\mathrm{p}i}^0$:

$$\mathbf{F}_{\mathrm{p}i} = \exp\left(\hat{\mathbf{D}}_{\mathrm{p}i}\Delta t\right) \cdot \mathbf{F}_{\mathrm{p}i}^0 \tag{4.44}$$

where the tensor exponential function is replaced by a Padé approximation [57]:

$$\exp\left(\hat{\mathbf{D}}_{\mathrm{p}i}\Delta t\right) \approx \boldsymbol{\Pi}\left(\hat{\mathbf{D}}_{\mathrm{p}i}, \Delta t\right) = \left(\mathbf{I} - \frac{\Delta t}{2}\hat{\mathbf{D}}_{\mathrm{p}i}\right)^{-1} \cdot \left(\mathbf{I} + \frac{\Delta t}{2}\hat{\mathbf{D}}_{\mathrm{p}i}\right) \tag{4.45}$$

Casting this equation in residual form yields

$$\mathbf{R}_{\mathbf{F}_{\mathrm{p},i}} = \mathbf{F}_{\mathrm{p}i} - \boldsymbol{\Pi}\left(\Delta t, \hat{\mathbf{D}}_{\mathrm{p}i}\right) \cdot \mathbf{F}_{\mathrm{p}i}^0 \tag{4.46}$$

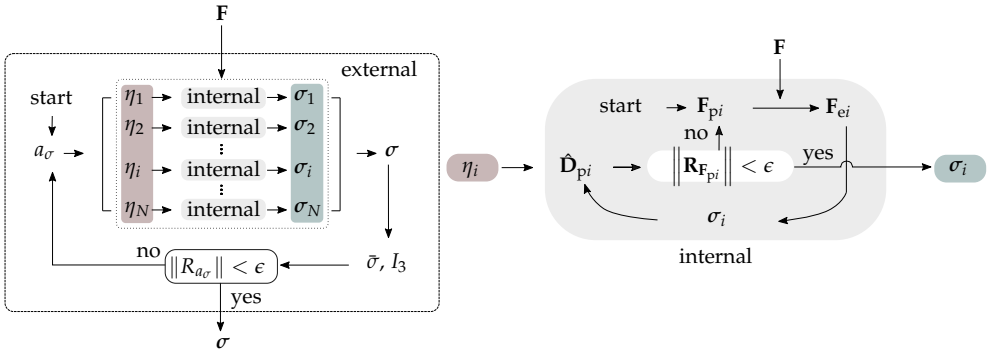

Figure 4.5 Nested external-internal solution scheme. At every external iteration (*left*), N internal schemes are solved, one for each mode i (*right*).

The root of this equation is solved by updating the plastic deformation for each *internal* iteration $k = 1 \dots N_{\text{iter}}$ as follows

$$\mathbf{F}_{pi}^{(k+1)} = \mathbf{F}_{pi}^{(k)} - \left[\frac{\partial \mathbf{R}_{\mathbf{F}_{pi}}}{\partial \mathbf{F}_{pi}}^{(k)} \right]^{-1} : \mathbf{R}_{\mathbf{F}_{pi}}^{(k)} \tag{4.47}$$

where $\partial \mathbf{R}_{\mathbf{F}_{pi}} / \partial \mathbf{F}_{pi}$, is the Jacobian for the *internal* Newton-Raphson scheme, which is given in Sec. 4.2.7. With the plastic deformation $\mathbf{F}_{pi}$, the elastic deformation in each mode $\mathbf{F}_{ei}$ is computed with Eq. (4.3) and the stress $\boldsymbol{\sigma}_i$ with Eq. (4.39). Subsequently, the total equivalent stress $\bar{\sigma}$ is computed with Eq. (4.23), after which the *internal* residual $\mathbf{R}_{\mathbf{F}_{pi}}$ and Jacobian $\partial \mathbf{R}_{\mathbf{F}_{pi}} / \partial \mathbf{F}_{pi}$, are evaluated to update the plastic deformation for the next iteration with Eq. (4.47).

Remark 4.5 The time-step dependence from the time integration scheme with Padé approximation, Eq. (4.46), is assessed in Sec. 4.5. For a better approximation of the exponential map, a higher-order Padé approximation [57] could be used.

4.2.7. JACOBIANS

The Jacobians for the *internal* and *external* Newton-Raphson schemes and the consistent tangent modulus for the *global* implicit solution scheme are derived in this section.

JACOBIAN OF THE INTERNAL SCHEME

The Jacobian of the *internal* residual (Eq. (4.46)) reads

$$\frac{\partial \mathbf{R}_{\mathbf{F}_{pi}}}{\partial \mathbf{F}_{pi}} = \mathbb{I} + \frac{\partial \mathbf{R}_{\mathbf{F}_{pi}}}{\partial \boldsymbol{\Pi}_i} : \frac{\partial \boldsymbol{\Pi}_i}{\partial \hat{\mathbf{D}}_{pi}} : \left[\frac{\partial \hat{\mathbf{D}}_{pi}}{\partial \boldsymbol{\Sigma}_i^{\text{sym}}} : \frac{\partial \boldsymbol{\Sigma}_i^{\text{sym}}}{\partial \mathbf{F}_{ei}} : \frac{\partial \mathbf{F}_{ei}}{\partial \mathbf{F}_{pi}} + \frac{\partial \hat{\mathbf{D}}_{pi}}{\partial \hat{\boldsymbol{a}}_i} \cdot \frac{\partial \hat{\boldsymbol{a}}_i}{\partial \mathbf{F}_{pi}} \right] \tag{4.48}$$

The derivatives in this expression are given in Sec. 4.A.1.

JACOBIAN OF THE EXTERNAL SCHEME

The Jacobian of the *external* residual (Eq. (4.42)) reads

$$\frac{\partial R_{a_\sigma}}{\partial a_\sigma} = 1 + \left[\frac{\partial R_{a_\sigma}}{\partial \bar{\sigma}}\frac{\partial \bar{\sigma}}{\partial \boldsymbol{\sigma}} + \frac{\partial R_{a_\sigma}}{\partial I_3}\frac{\partial I_3}{\partial \boldsymbol{\sigma}}\right] : \left[\sum_{i=1}^{N_\mathrm{m}} \frac{\partial \boldsymbol{\sigma}_i}{\partial \mathbf{F}_{\mathrm{e}i}} : \frac{\partial \mathbf{F}_{\mathrm{e}i}}{\partial \mathbf{F}_{\mathrm{p}i}} : \frac{\partial \mathbf{F}_{\mathrm{p}i}}{\partial a_\sigma}\right] \tag{4.49}$$

where $\partial\bar{\sigma}/\partial\boldsymbol{\sigma}$ follows from Eq. (4.30) by replacing *intermediate* quantities $\{\bar{\Sigma}_i, \boldsymbol{\Sigma}^{\mathrm{sym}}, \hat{I}_{1i}, \hat{I}_{2i}\}$ with *current* quantities $\{\bar{\sigma}, \boldsymbol{\sigma}, I_1, I_2\}$. The first and second terms in the sum on the RHS are given by Eq. (A.19) and Eq. (A.12), respectively. The other terms are given in Sec. 4.A.2. The terms $\{\partial\mathbf{F}_{\mathrm{p}i}/\partial a_\sigma\}$ are obtained as follows. The *internal* residual for mode i is a function of independent variables a_σ and $\mathbf{F}_{\mathrm{p}i}$. Therefore, the variation of the residual reads

$$\delta\mathbf{R}_{\mathbf{F}_{\mathrm{p}i}} = \frac{\partial \mathbf{R}_{\mathbf{F}_{\mathrm{p}i}}}{\partial a_\sigma}\delta a_\sigma + \frac{\partial \mathbf{R}_{\mathbf{F}_{\mathrm{p}i}}}{\partial \mathbf{F}_{\mathrm{p}i}} : \delta\mathbf{F}_{\mathrm{p}i} \tag{4.50}$$

Since we solve iteratively for the root of $\mathbf{R}_{\mathbf{F}_{\mathrm{p}i}}$ with the *internal* scheme, its variation between *external* iterations j vanishes, *i.e.* $\delta\mathbf{R}_{\mathbf{F}_{\mathrm{p}i}} = \mathbf{0}$. This is a *consistency condition* that can be used for finding $\partial\mathbf{F}_{\mathrm{p}i}/\partial a_\sigma$, similar to what is done in deriving consistent tangent moduli in classical plasticity models with return mapping schemes.

The *consistency condition* $\delta\mathbf{R}_{\mathbf{F}_{\mathrm{p}i}} = \mathbf{0}$ gives, after rewriting, the sought-after derivative $\partial\mathbf{F}_{\mathrm{p}i}/\partial a_\sigma$:

$$\delta\mathbf{F}_{\mathrm{p}i} = \underbrace{-\left[\frac{\partial \mathbf{R}_{\mathbf{F}_{\mathrm{p}i}}}{\partial \mathbf{F}_{\mathrm{p}i}}\right]^{-1} : \frac{\partial \mathbf{R}_{\mathbf{F}_{\mathrm{p}i}}}{\partial a_\sigma}}_{\frac{\partial \mathbf{F}_{\mathrm{p}i}}{\partial a_\sigma}}\delta a_\sigma \tag{4.51}$$

where the first term on the RHS is the Jacobian for the *internal* scheme (Eq. (4.48)). The second term on the RHS is given in Sec. 4.A.2.

CONSISTENT TANGENT MODULUS

The derivative of the Cauchy stress with respect to the deformation gradient reads

$$\frac{\partial \boldsymbol{\sigma}}{\partial \mathbf{F}} = \sum_i^{N_\mathrm{m}} \left[\frac{\partial \boldsymbol{\sigma}_i}{\partial \mathbf{F}_{\mathrm{e}i}} : \left(\frac{\partial \mathbf{F}_{\mathrm{e}i}}{\partial \mathbf{F}} + \frac{\partial \mathbf{F}_{\mathrm{e}i}}{\partial \mathbf{F}_{\mathrm{p}i}} : \frac{\partial \mathbf{F}_{\mathrm{p}i}}{\partial \mathbf{F}}\right) + \frac{\partial \boldsymbol{\sigma}_i}{\partial \boldsymbol{a}} \cdot \frac{\partial \boldsymbol{a}}{\partial \mathbf{F}}\right] \tag{4.52}$$

where $\partial\mathbf{F}_{\mathrm{e}i}/\partial\mathbf{F}_{\mathrm{p}i}$, $\partial\boldsymbol{\sigma}_i/\partial\mathbf{F}_{\mathrm{e}}$ and $\partial\boldsymbol{\sigma}_i/\partial\boldsymbol{a}$ are given by Eqs. (A.12), (A.19) and (A.48). The derivatives $\partial\mathbf{F}_{\mathrm{e}i}/\partial\mathbf{F}$ and $\partial\boldsymbol{a}/\partial\mathbf{F}$ can be found by differentiating Eqs. (4.3) and (4.6). Furthermore, $\partial\mathbf{F}_{\mathrm{p}i}/\partial\mathbf{F}$ in Eq. (4.52) reads

$$\frac{\partial \mathbf{F}_{\mathrm{p}i}}{\partial \mathbf{F}} = \left.\frac{\partial \mathbf{F}_{\mathrm{p}i}}{\partial \mathbf{F}}\right|_{a_\sigma} + \frac{\partial \mathbf{F}_{\mathrm{p}i}}{\partial a_\sigma} \otimes \frac{\partial a_\sigma}{\partial \mathbf{F}} \tag{4.53}$$

where $\partial \mathbf{F}_{\mathrm{p}i}/\partial a_\sigma$ is already given by Eq. (4.51). Furthermore, $\partial \mathbf{F}_{\mathrm{p}i}/\partial \mathbf{F}\big|_{a_\sigma}$ is derived through an additional consistency condition of the *internal* scheme. For every fixed a_σ and varying $\mathbf{F}$, the internal residual for mode i vanishes between *global* iterations. Therefore

$$\delta \mathbf{R}_{\mathbf{F}_{\mathrm{p}i}} = \frac{\partial \mathbf{R}_{\mathbf{F}_{\mathrm{p}i}}}{\partial \mathbf{F}_{\mathrm{p}i}} : \delta \mathbf{F}_{\mathrm{p}i} + \frac{\partial \mathbf{R}_{\mathbf{F}_{\mathrm{p}i}}}{\partial \mathbf{F}} : \delta \mathbf{F} = 0 \tag{4.54}$$

The derivative $\partial \mathbf{F}_{\mathrm{p}i}/\partial \mathbf{F}\big|_{a_\sigma}$ can be found by rewriting this expression:

$$\delta \mathbf{F}_{\mathrm{p}i} = \underbrace{-\left[\frac{\partial \mathbf{R}_{\mathbf{F}_{\mathrm{p}i}}}{\partial \mathbf{F}_{\mathrm{p}i}}\right]^{-1} : \frac{\partial \mathbf{R}_{\mathbf{F}_{\mathrm{p}i}}}{\partial \mathbf{F}}}_{\frac{\partial \mathbf{F}_{\mathrm{p}i}}{\partial \mathbf{F}}\Big|_{a_\sigma}} : \delta \mathbf{F} = 0 \tag{4.55}$$

where the first term on the RHS is again the Jacobian of the *internal* residual (see Eq. (4.48)) and the second term on the RHS is given in Sec. 4.A.3.

The third derivative $\partial a/\partial \mathbf{F}$ on the RHS of Eq. (4.53), which is the same for each mode, is obtained with a single *consistency condition* of the *external* scheme. At every *global* iteration, the *external* residual vanishes. Therefore

$$\delta R_{a_\sigma} = \frac{\partial R_{a_\sigma}}{\partial \mathbf{F}} : \delta \mathbf{F} + \frac{\partial R_{a_\sigma}}{\partial a_\sigma} \delta a_\sigma = 0 \tag{4.56}$$

Rewriting this equation yields

$$\delta a_\sigma = \underbrace{-\left[\frac{\partial R_{a\sigma}}{\partial a_\sigma}\right]^{-1} \frac{\partial R_{a_\sigma}}{\partial \mathbf{F}}}_{\frac{\partial a}{\partial \mathbf{F}}} : \delta \mathbf{F} \tag{4.57}$$

where the derivative $\partial a/\partial \mathbf{F}$ is identified. Note that $\partial R_{a_\sigma}/\partial a_\sigma$ is the Jacobian of the *external* scheme (Eq. (4.49)). The second term is given in Sec. 4.A.3.

Remark 4.6 In total, $2N_{\mathrm{m}} + 1$ *consistency conditions* are used to derive the tangent modulus.

4.3. PARAMETER IDENTIFICATION

To determine the (single-mode) yield parameters of the mesoscopic constitutive model, we consider a material point under uniaxial tension and compression with off-axis angle θ_0 at constant strain rate $\dot{\varepsilon}$ (see Fig. 4.6). In addition, we assume small deformations at the moment of yielding, such that: $\hat{\boldsymbol{a}} = \boldsymbol{a}_0$, $\boldsymbol{\sigma} = \boldsymbol{\Sigma} = \boldsymbol{\Sigma}^{\mathrm{sym}}$, and $\bar{\sigma} = \bar{\Sigma}$. Furthermore, we choose an orthonormal basis $\{\boldsymbol{e}_i\}_{i=1,2,3}$ where unit vector

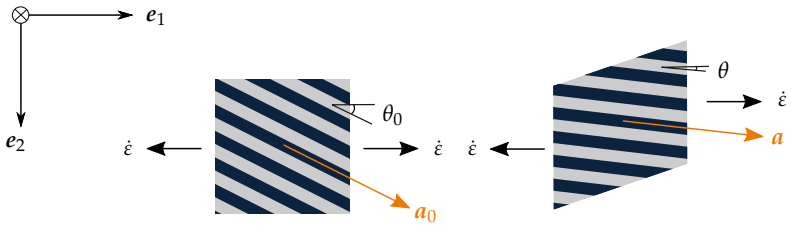

Figure 4.6 Fiber-reinforced polymer composite under off-axis tensile loading.

$\boldsymbol{e}_1$ is aligned with the load direction. The flow rule (Eq. (4.8)) gives the rate of plastic deformation in the load direction:

$$D_{11}^{\mathrm{p}} = \frac{\sigma_0}{\eta_0} \sinh\left(\frac{\bar{\sigma}}{\sigma_0}\right) \exp\left(-\mu_{\mathrm{p}} \frac{I_3}{\sigma_0}\right) \frac{\partial \bar{\sigma}}{\partial \sigma_{11}} \tag{4.58}$$

Plastic and elastic deformations develop simultaneously until the rate of plastic deformation is equal to the applied strain rate ($D_{11}^{\mathrm{p}} = \dot{\varepsilon}$) upon which the stress reaches a plateau,[4] which marks the moment of yielding. When the material yields, $\bar{\sigma} \gg \sigma_0$ and the hyperbolic sine function can be approximated with an exponential function:

$$\dot{\varepsilon} \approx \frac{\sigma_0}{2\eta_0} \exp\left(\frac{\bar{\sigma} - \mu_{\mathrm{p}} I_3}{\sigma_0}\right) \frac{\partial \bar{\sigma}}{\partial \sigma_{11}} \tag{4.59}$$

This equation provides an analytical relation between the applied strain rate $\dot{\varepsilon}$ and the equivalent stress $\bar{\sigma}$ at the moment of yielding.

4.3.1. TRANSVERSE TENSION AND COMPRESSION

The parameters μ_{p}, σ_0 and η_0 can be determined from stress-strain curves of uniaxial tension and compression under off-axis angle $\theta_0 = 90°$ at equal strain rates. For this angle, I_2 is zero and α_2 is eliminated from the equations. The transversely isotropic stress invariants at the moment of yielding read

$$I_1 = \frac{\sigma_{\mathrm{y,90}}^2}{4}, \quad I_2 = 0, \quad I_3 = \begin{cases} \sigma_{\mathrm{y,90t}} & \text{in tension} \\ -\sigma_{\mathrm{y,90c}} & \text{in compression} \end{cases} \tag{4.60}$$

where $\sigma_{\mathrm{y,90}}$ is the yield stress at $\theta = 90°$. Substitution into Eqs. (4.23) and (4.30) and rewriting Eq. (4.59) provides the following expressions of the yield stresses in

[4] Under large deformations, a geometric hardening or softening response may occur due to reorientation of the fibers.

tension $\sigma_{y,90t}$ and compression $\sigma_{y,90c}$:

$$\sigma_{y,90t} = \frac{\sigma_0}{\frac{1}{\sqrt{2}} + \mu_p} \ln\left(2\sqrt{2}\frac{\eta_0}{\sigma_0}\dot{\varepsilon}\right) \tag{4.61}$$

$$\sigma_{y,90c} = \frac{\sigma_0}{\frac{1}{\sqrt{2}} - \mu_p} \ln\left(2\sqrt{2}\frac{\eta_0}{\sigma_0}|\dot{\varepsilon}|\right) \tag{4.62}$$

When the yield stresses $\sigma_{y,90t}$ and $\sigma_{y,90c}$ are known, μ_p is solved for, which gives the following closed-form relation:

$$\mu_p = \frac{1}{\sqrt{2}}\left(\frac{\sigma_{y,90c} - \sigma_{y,90t}}{\sigma_{y,90c} + \sigma_{y,90t}}\right) \tag{4.63}$$

With μ_p known, σ_0 and η_0 are determined from an Eyring plot for uniaxial compression. This requires at least two compression curves at different strain rates. Eq. (4.62) is rearranged as

$$\sigma_{y,90c} = \underbrace{\frac{\sigma_0 \ln(10)}{\frac{1}{\sqrt{2}} - \mu_p}}_{\text{slope } m}\left[\log_{10}(|\dot{\varepsilon}|) + \log_{10}\left(2\sqrt{2}\frac{\eta_0}{\sigma_0}\right)\right] \tag{4.64}$$

where m is the slope in a semi-log plot of yield stress $\sigma_{y,90c}$ *vs* strain rate $\dot{\varepsilon}$. From the slope, σ_0 and η_0 are given by

$$\sigma_0 = m\left(\frac{\frac{1}{\sqrt{2}} - \mu_p}{\ln(10)}\right) \tag{4.65}$$

$$\eta_0 = \frac{\sigma_0\, 10^{\frac{\sigma_{y,90c}}{m}}}{2\sqrt{2}\,\dot{\varepsilon}} \tag{4.66}$$

4.3.2. OFF-AXIS LOADING IN TENSION

Parameter α_2 can be obtained from any other test where I_2 is non-zero, for example the $\theta_0 = 30^\circ$ case. By following the same steps as before, the analytical yield stress for this angle reads

$$\sigma_{y,30t} = \frac{4\sigma_0}{\mu_p + \sqrt{\frac{1}{2} + 6\alpha_2}} \ln\left(\frac{8}{\sqrt{\frac{1}{2} + 6\alpha_2}}\frac{\eta_0}{\sigma_0}\dot{\varepsilon}\right) \tag{4.67}$$

which is a nonlinear equation in its argument α_2 that can be solved numerically, given $\eta_0, \sigma_0, \mu_p, \sigma_{y,30t}$ and corresponding strain rate $\dot{\varepsilon}$.

4.3.3. SUMMARY OF MODEL PARAMETERS

The parameters of the mesomodel are determined in the next section with a micromodel for carbon/PEEK under uniaxial off-axis strain rates. Alternatively, experimental off-axis coupon tests with oblique ends may be used [58]. An overview of all model parameters, the required tests to obtain their values and the corresponding formulas presented in this section, is given in Tab. 4.1.

4.4. NUMERICAL HOMOGENIZATION OF A MICROMODEL

The parameters of the mesoscopic material model are determined by homogenizing a previously calibrated micromodel, with periodic boundary conditions, for carbon/PEEK [16]. The micromodel comprises of hyperelastic transversely isotropic fibers and viscoplastic polymer matrix, where the latter is modeled with the original isotropic EGP model [6, 10]. The micromodel and mesomodel are schematically depicted in Fig. 4.7.

4.4.1. BOUNDARY CONDITIONS FOR OFF-AXIS LOADING

Applying off-axis loads to the micromodel (as shown in Fig. 4.6) is not straightforward. Since periodic boundary conditions are applied, it is not possible to vary the fiber angle inside the micromodel, which would violate the assumption of continuous fibers as imposed by the periodicity. Instead, off-axis loading is achieved by aligning the micromodel with the fibers, while a global deformation is applied in the local frame of the micromodel. Since the local frame changes under off-axis loading due to reorientation of the fibers (see Fig. 4.6), a special constraint equation is used that accounts for these reorientations [18, 37].

In contrast, global deformations can straightforwardly be applied on a single element with the mesoscopic model. Off-axis loading is then achieved by varying the initial fiber direction vector $\boldsymbol{a}_0$, while applying the load in the $\boldsymbol{e}_1$-direction. Although the methods to apply boundary conditions on the micromodel and the mesomodel are different, the resulting (global) deformations are the same.

Table 4.1 Overview of all model parameters and required tests.

Parameters	Tests	Identification
$E_1, E_2, G_{12}, \nu_{21}$	Basic tests to identify elastic properties	-
μ_P	Transverse tension and compression tests †	Eq. (4.63)
σ_0, η_0	Two transverse tests ‡	Eqs. (4.65) and (4.66)
α_2	Single off-axis test under tension/compression	Eq. (4.67)
$\{m_i\}_{i=1}^{N_\mathrm{m}}, \{\eta_{0i}\}_{i=1}^{N_\mathrm{m}}$	Single off-axis test under tension/compression	Sec. 4.2.5

† same strain rate; ‡ at least two different strain rates

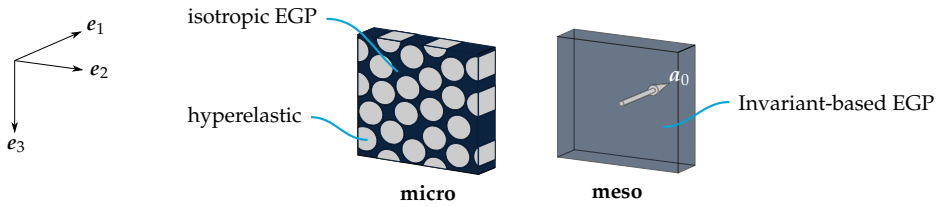

Figure 4.7 Micromodel with hyperelastic fibers and isotropic EGP model for the matrix *vs* mesomodel with proposed invariant-based EGP model and fiber direction vector $\boldsymbol{a}_0$.

4.4.2. ELASTICITY PARAMETERS

The elasticity parameters of the mesoscopic material model are determined by subjecting the micromodel to three basic load cases: longitudinal tension, longitudinal shear and transverse shear. The transversely isotropic elasticity constants are given in Tab. 4.2.

4.4.3. PLASTICITY PARAMETERS

The mesoscopic yield parameters are obtained with the analytical expressions derived in Sec. 4.3. To obtain the pressure-dependency parameter μ_p, the micromodel is subjected to uniaxial transverse compression and tension under true strain rate $\dot{\varepsilon} = 10^{-3}\,\mathrm{s}^{-1}$. For finding η_0 and σ_0, the micromodel is subjected to three strain rates under transverse compression. The stress-strain curves are shown in Fig. 4.8. Note that these curves do not reach a plateau due to hardening, which obscures a clear yield point. In this work, the point at which the stress starts to increase almost linearly is chosen as the 'yield' stress. The resulting mesoscopic parameters are tabulated in Tab. 4.3. The fit of the Eyring curve (Eq. (4.64)) with the transverse compression yield data is shown in Fig. 4.9.

The micromodel is subjected to uniaxial tension under off-axis angle $\theta_0 = 30°$ and true strain rate $\dot{\varepsilon} = 10^{-3}\,\mathrm{s}^{-1}$. The parameter α_2 is first determined by solving Eq. (4.67). With all single-mode parameters known, a multimode relaxation spectrum, with 24 modes is determined by following the procedure as outlined in Sec. 4.2.5. This number of modes follows from the recommendation in Ref. [10, 27], to include one mode per decade in the relaxation spectrum, ensuring an accurate

Table 4.2 Elasticity constants.

E_1 [GPa]	E_2 [GPa]	G_{12} [GPa]	ν_{21}
55.5	7.4	4.8	0.016

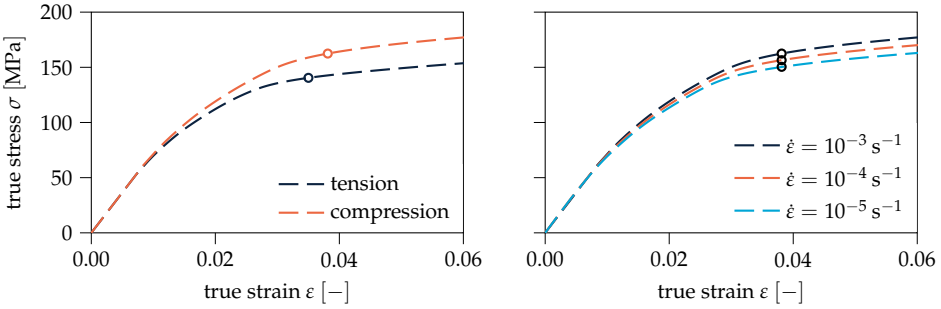

Figure 4.8 Input curves generated with micromodel at $\theta_0 = 90°$: (*left*) transverse tension and compression under strain rate $\dot{\varepsilon} = 10^{-3}\,\mathrm{s}^{-1}$ and (*right*) transverse compression under three different strain rates. The yield stresses are indicated with a dot.

Table 4.3 Plasticity parameters.

μ_p	σ_0 [MPa]	η_0 [MPa s]	α_2
0.053	1.71	5.90×10^{29}	1.147

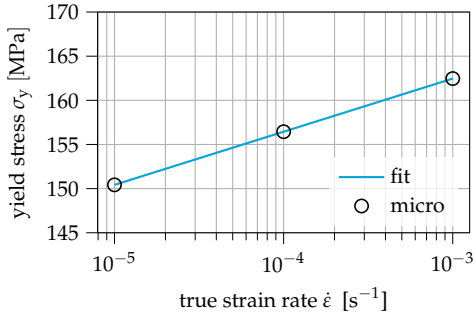

Figure 4.9 Eyring fit (Eq. (4.64)) of yield stress versus strain rate for $\theta_0 = 90°$ in compression.

pre-yield and creep response. A smaller number of modes may introduce spurious oscillations in the stress-strain curve [10].

Applying the method by Refs. [10, 27] (as outlined in Sec. 4.2.5) to the present mesoscopic model, resulted in a slight mismatch between the input and output results. Therefore, the input curve is iteratively adjusted such that the output curve matched with the original input curve. The relaxation spectrum is tabulated in Tab. 4.4. With the ratios $\{m_i\}$, the elasticity parameters are obtained for each mode with Eq. (4.41) and Tab. 4.2. The resulting stress-strain curve is shown in Fig. 4.10.

Remark 4.7 Other invariant-based (Perzyna-type) viscoplasticity models [32–34], more suitable for unidirectional *thermosetting* polymer composites, require six hardening functions as inputs (obtained from bi-axial tension/compression, longitudinal shear, transverse shear and uniaxial tension/compression tests) to describe the nonlinear rate-dependent plastic response. However, obtaining transverse shear and biaxial test data through experiments is not straightforward. Therefore, these hardening functions are usually deduced from other tests, engineering assumptions or micromechanical models [51]. With the present invariant-based non-Newtonian flow model for *thermoplastic* polymer composites, the yield stress is determined by the mode with the highest initial viscosity (see Fig. 4.4), and thus, only four parameters are required. These parameters can be determined from a small number of off-axis constant strain-rate tests as shown in this section with a micromodel, or from off-axis coupon tests with oblique ends under (almost) uniform stress states [58]. Subsequently, the pre-yield nonlinearity is described by a relaxation spectrum, which can be determined from a *single* stress-strain curve under off-axis loading. Therefore, a significant reduction in the amount of necessary inputs is achieved with the present invariant-based constitutive model.

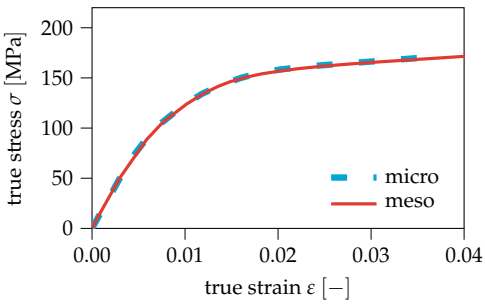

Figure 4.10 Multimode calibration under uniaxial tension with $\theta_0 = 30°$ and $\dot{\varepsilon} = 10^{-3}\,\mathrm{s}^{-1}$: output curve with mesomodel (*meso*) *vs* input curve with micromodel (*micro*).

Table 4.4 Relaxation spectrum.

mode i	m_i [-]	η_{0i} [MPa s]	mode i	m_i [-]	η_{0i} [MPa s]
1	0.020	1.002×10^{6}	13	0.014	2.453×10^{24}
2	0.033	1.486×10^{9}	14	0.023	1.131×10^{25}
3	0.040	1.025×10^{12}	15	0.014	1.654×10^{25}
4	0.053	1.963×10^{14}	16	0.016	3.367×10^{25}
5	0.051	2.726×10^{16}	17	0.018	7.969×10^{25}
6	0.054	1.089×10^{18}	18	0.021	1.920×10^{26}
7	0.056	6.664×10^{19}	19	0.006	9.983×10^{25}
8	0.034	3.867×10^{20}	20	0.029	7.309×10^{26}
9	0.037	6.447×10^{21}	21	0.052	4.257×10^{27}
10	0.031	4.479×10^{22}	22	0.011	1.396×10^{27}
11	0.034	2.799×10^{23}	23	0.029	6.464×10^{27}
12	0.032	2.048×10^{24}	24	0.292	5.920×10^{29}

4.5. RESULTS

The material parameters of the mesomodel are determined in the previous section through calibration against a micromodel for carbon/PEEK [16]. For this purpose, no more than five stress-strain curves were used. The performance of the mesoscopic constitutive model in simulating rate-dependent plasticity and creep is studied in this section. First, its capability in representing a material point of a composite under various off-axis angles, strain-rates and creep loads is assessed with a single element, under the assumption of a uniform deformation (see Fig. 4.6). Subsequently, the model is applied to the simulation of ply-level off-axis specimens and compared against experiments [59].

4.5.1. CONSTANT STRAIN RATE

The microscale and mesoscale model are subjected to constant true strain rates $\dot{\varepsilon}\,(\mathrm{s}^{-1}) \in \{10^{-5}, 10^{-4}, 10^{-3}\}$ under off-axis angles $\theta\,(^\circ) \in \{90, 45, 30, 15, 0\}$ in tension and compression.

Direction-dependence Fig. 4.11 shows the stress-strain curves with $\dot{\varepsilon} = 10^{-3}\,\mathrm{s}^{-1}$ and various off-axis angles θ_0. It is observed that the strongly anisotropic response of the micromodel is well represented with the mesoscale model: under $\theta_0 = 0^\circ$, the response is elastic, whereas under off-axis loading, it is viscoplastic. It is worth noting that the rather simple approach, as described in Sec. 4.2.5, of finding a relaxation spectrum with a single stress-strain curve, gives a good pre-yield response for all off-axis angles and strain rates.

With both the micromodel and the mesomodel under off-axis angle $\theta_0 = 15^\circ$

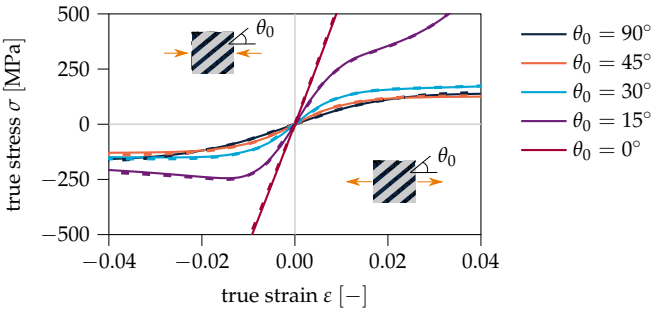

Figure 4.11 Stress-strain curves under various initial off-axis angles θ_0 and constant strain rate $\dot{\varepsilon} = 10^{-3}\,\mathrm{s}^{-1}$ in tension and compression: micromodel (*dashed* line) *vs* mesomodel (*solid* line).

in tension, an increasing stiffness (hardening) is observed in the post-yield regime, whereas under compression, a softening response is obtained. When off-axis tensile loads are applied to the composite material, the fibers progressively align with the load direction (see Fig. 4.6). This reorientation of the fibers is captured by the mesoscale model and is numerically depicted in Fig. 4.12. In contrast, under compression, the opposite effect takes place where the off-axis angle increases, leading to a softening response. The agreement between the two models indicates that the reorientation of the fibers is captured just as well in the mesoscopic constitutive model as in the micromodel where the fibers are explicitly modeled.

Rate-dependence The stress-strain curves with off-axis angles $\theta_0\,(^\circ) \in \{15,30,45,90\}$ and constant strain rates $\dot{\varepsilon}\,(\mathrm{s}^{-1}) \in \{10^{-5}, 10^{-4}, 10^{-3}\}$ in tension are shown in Fig. 4.13. It can be observed that the rate-dependence, which describes an increasing

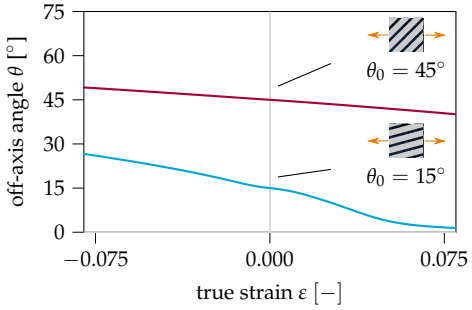

Figure 4.12 Evolution of the off-axis angle θ with the mesoscale model for two *initial* off-axis angles $\theta_0\,(^\circ) \in \{15,30\}$.

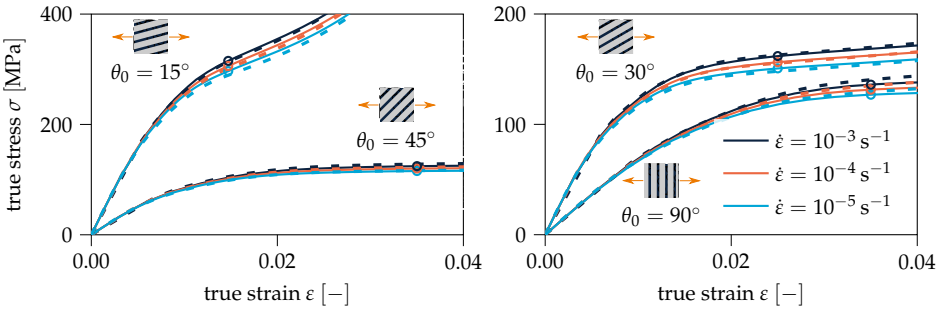

Figure 4.13 Rate-dependence under uniaxial tension with various initial off-axis angles θ_0 and strain rates $\dot{\varepsilon}$: micromodel (*dashed* line) vs mesomodel (*solid* line). The yield stresses are indicated with a dot.

yield stress with increasing strain rate, is accurately reflected by the mesoscale model. The yield stresses from the mesoscale model are indicated in Fig. 4.13 and plotted against strain rates $\dot{\varepsilon}$ on a double logarithmic scale for each off-axis angle θ_0 in Fig. 4.14. In line with experimental observations for unidirectional polymer composites [60], the curves are parallel, indicating a factorizable dependence of yield stress on strain rate $\dot{\varepsilon}$ and off-axis angle θ_0.

Pressure-dependence The stress-strain curves of the micromodel and the mesomodel under transverse tension and compression with $\dot{\varepsilon} = 10^{-3}\,\mathrm{s}^{-1}$ are shown in Fig. 4.15. It can be observed that the response is accurate until the yield point. However, after yielding, a hardening response is observed with the micromodel. In the isotropic EGP for the matrix material of the micromodel, an (elastic) hardening contribution is present [18], representing polymer chain reorientation, which is currently not included in the mesoscale model. In contrast, under off-axis loading, the post-yield hardening response is captured by the mesoscale model (see Fig. 4.13). This type of hardening is due to reorientation of fibers and is of geometric nature (see Figs. 4.6 and 4.12). Under pure transverse loading, reorientation of the fibers does not occur while polymer chain reorientation of the matrix does take place.

Under transverse tensile loading, Carbon/PEEK fractures before a fully developed plastic response is reached due to large hydrostatic stresses in the polymer matrix. The post-yield hardening response is therefore less relevant under tensile loading. However, for a more accurate post-yield response under transverse compression, an (anisotropic) hardening contribution can be included to account for this effect.

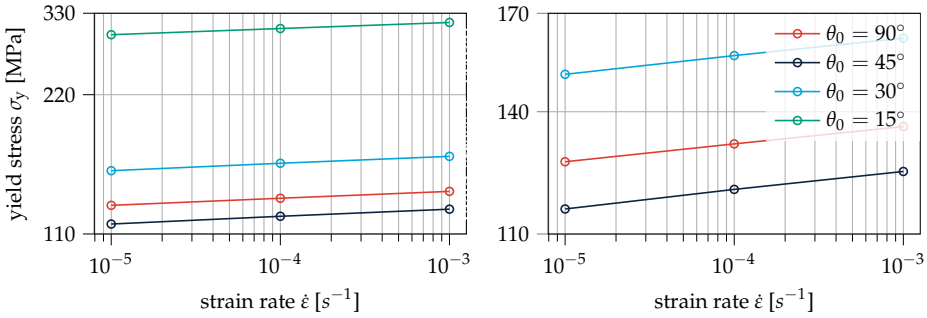

Figure 4.14 Yield stress as function of strain rate for various off-axis angles θ_0 with mesoscale model. The figure on the left contains the curves of all off-axis angles, whereas the figure on the right omits the curve for $\theta_0 = 15°$ to show the rate-dependence on a smaller range of y-axis values.

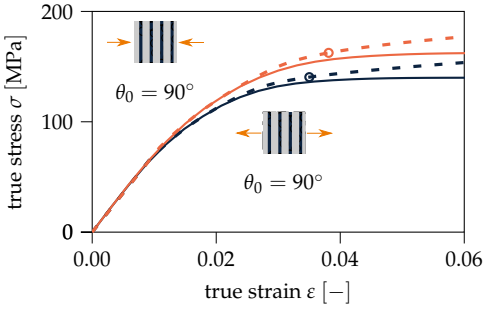

Figure 4.15 Transverse tension and compression under off-axis angle $\theta_0 = 90°$: micromodel (*dashed* line) with yield stresses (indicated with a dot) vs mesomodel (*solid* line).

Time-step dependence The time-step dependence of the time integration scheme, with the Padé approximation (Eq. (4.45)), is assessed by comparing the response obtained with adaptive stepping based on global iterations [61], to the response with fixed time increments. For this purpose, simulations with off-axis constant strain rates $\dot{\varepsilon} = 10^{-3}\,\mathrm{s}^{-1}$ under $\theta_0 = 15°$ and $90°$ are used for the comparison. The simulations with fixed time steps are performed with $\Delta t = 1.0\,\mathrm{s}$ and $0.25\,\mathrm{s}$, resulting in strain increments $\Delta\varepsilon = 10^{-3}$ and 2.5×10^{-4}, respectively. Fig. 4.16 shows the stress-strain curves, from which it is concluded that time-step dependence of the time integration scheme is negligible. In combination with the fully consistent tangent stiffness, adaptive stepping based on global iterations is possible for efficient simulations with high accuracy.

4.5.2. CREEP

An important feature of the EGP model is the capability to simulate not only rate-dependent plasticity but also creep in polymers. This also holds for the present mesoscopic version for polymer composites. To assess the performance under creep, the micro- and meso-scale models are subjected to a constant tensile *engineering* stress rate until a specified stress level is reached in 10 s. After this phase, the engineering stress is kept constant.

The engineering strain as a function of time is shown in Fig. 4.17 for four off-axis angles $\theta\,(°) \in \{90, 45, 30, 15\}$. For each angle, three different engineering stress levels are applied, as indicated in the figures. It can be observed that for all off-axis angles, the strains of the mesomodel during the ramp-up to the maximum engineering stress are in close agreement with those of the micromodel. This is expected since the mesoscale model parameters were determined with (short-term)

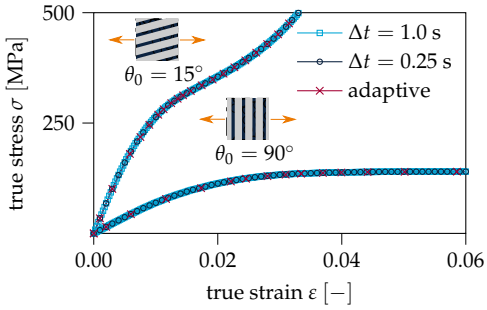

Figure 4.16 Time-step dependence: stress-strain curves with two different fixed time steps and adaptive steps. The markers denote the time steps.

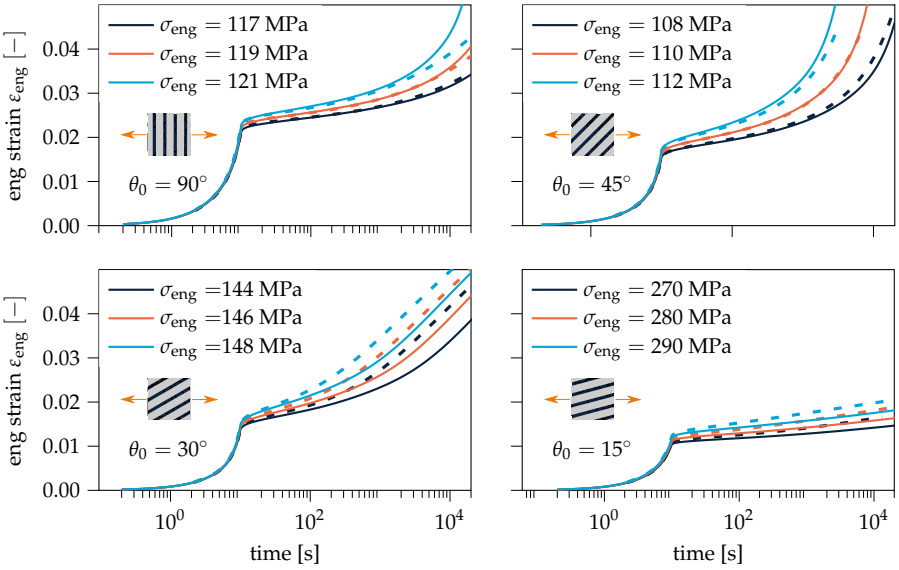

Figure 4.17 Creep response under various off-axis angles θ_0 and engineering stress levels σ_{eng}: micromodel (*dashed* line) vs mesomodel (*solid* line).

constant-strain rate data (Sec. 4.4). After reaching the maximum applied stress level, the creep response with $\theta_0 = 45°$ is very similar to that of the micromodel. However, for the other angles, the match is adequate but not as good as with $\theta_0 = 45°$. It is somewhat surprising that, although the $\theta_0 = 30°$ off-axis angle has been used for determining the multi-mode relaxation spectrum (see Fig. 4.10), the match in creep is worse than with the other off-axis angles. A parameter identification procedure which includes creep data, *e.g.* through a compliance-time master curve from a series of creep tests at different stress levels [6], may improve the creep response.

4.5.3. UNIDIRECTIONAL PLY UNDER OFF-AXIS TENSILE LOADING

So far, material point analyses have been carried out with the mesoscale model. In this section, the mesoscale model is used for the simulation of a unidirectional ply with dimensions $120 \times 15 \times 1.8\,\text{mm}$. The three-dimensional mesh, consisting of 240 trilinear finite elements, is shown in Fig. 4.18. On each end of the specimen, the displacements in the $\boldsymbol{e}_2$- and $\boldsymbol{e}_3$-direction are fixed, mimicking the constraining effect of the grips in the experimental test [59]. In the $\boldsymbol{e}_1$-direction, a constant *engineering* strain rate of $\dot{\varepsilon}_{eng} = 10^{-4}\,\text{s}^{-1}$ is enforced. This is achieved by applying a displacement rate $\dot{u} = 120\,\dot{\varepsilon}_{eng}$ at one end, while at the other end, the displacement is fixed. The engineering stress σ_{eng} is computed from the resulting force in $\boldsymbol{e}_1$-

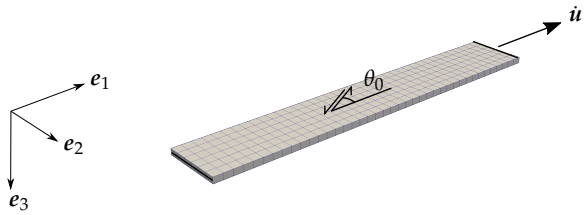

Figure 4.18 Ply simulation: mesh and initial off-axis angle θ_0 of the fiber with respect to the load.

direction, divided by the undeformed area of the surface at the end. Simulations are performed with four initial off-axis angles $\theta_0\,(^\circ) \in \{15, 30, 45, 90\}$.

The engineering stress-strain curves are shown in Fig. 4.19. The ply simulations give an excellent match with the experiments for $\theta_0 = 30^\circ$, 45° and 90°. For $\theta_0 = 15^\circ$, although the pre-yield stiffness is slightly overpredicted and the post-yield hardening response is slightly underpredicted, the overall agreement is satisfactory. It has been observed in Sec. 4.5.1 that the mesomodel and micromodel under uniform tension with $\theta_0 = 15^\circ$ showed a pronounced upswing of the stress after yielding (see Fig. 4.11), due to an increasing alignment of the fibers with the load direction. The same type of reorientation is prevented by the grips in the coupon test and this constraining effect is captured by simulating the ply with the mesomodel. This can be illustrated by plotting the evolution of off-axis angle (θ) and plastic deformation component in $\boldsymbol{e}_1$-direction (F^{p}_{11}), for the mode with the highest initial viscosity (mode 24 in Tab. 4.4), at three different time steps (see Fig. 4.20). As the fibers tend to align with the load direction near the ends ($\theta < \theta_0$), the off-axis angles increase in the middle of the specimen ($\theta > \theta_0$), which is opposite to the direction of reorientation as was previously seen with the single element test under tension (see Fig. 4.12).

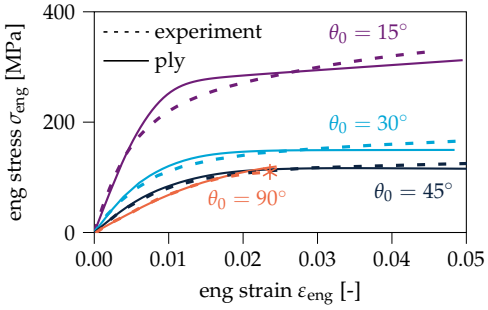

Figure 4.19 Ply simulations *vs* experiments with $\theta_0\,(^\circ) = \{15, 30, 45, 90\}$. The experiment with $\theta_0 = 90^\circ$ fractured (indicated with $*$) before plasticity fully developed.

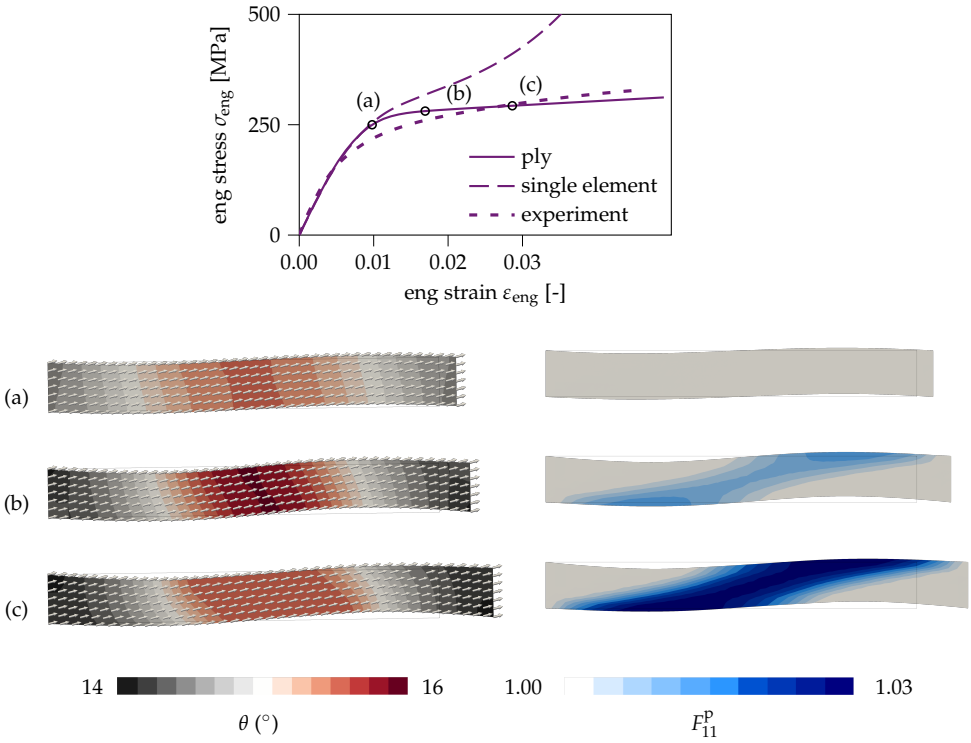

Figure 4.20 Ply simulation with $\theta_0 = 15°$: evolution of fiber angle θ (*left*) and plastic deformation F_{11}^{P} in load direction for the mode with highest initial viscosity (*right*) at indicated time instances on the stress-strain plot (*top*). For comparison, the response of a single element test with $\dot{\varepsilon}_{eng} = 10^{-4}\,s^{-1}$ and the experimental curve are added to the stress-strain diagram. Deformed mesh is magnified (×5).

This increase of matrix-dominated loading, combined with the presence of stress concentrations in the ply specimen, results in an earlier development of plasticity with respect to the single element and a better match with the experiments (see Fig. 4.20, *top*).

The deformations in the coupon test are inhomogeneous and cannot be used directly as material input. To obtain a more homogeneous deformation state, off-axis specimens with oblique tabs may be used [58]. The analytical parameter identification procedure outlined in Sec. 4.3 may then be directly applied to experimental data of off-axis constant strain rates, without requiring a pre-calibrated micromodel to generate inputs for the mesoscopic constitutive model.

4.6. CONCLUSION

A mesoscopic constitutive model for simulating rate-dependent plasticity and creep in unidirectional thermoplastic composites has been presented. The model is an extension of a viscoplastic material model for isotropic polymers with an Eyring-type non-Newtonian flow rule. Strong anisotropy is incorporated through the use of three transversely isotropic stress invariants in the flow rule. As a result, plastic flow in fiber direction is removed and pressure-dependency of the polymer matrix is taken into account by extending the Eyring relation with anisotropic pressure dependence. An important feature of the present invariant-based anisotropic viscoplasticity model is that it can describe both rate-dependent plasticity and creep in thermoplastic polymer composites with non-Newtonian flow.

The constitutive equations are implicitly integrated, which allows for the use of relatively large time steps. Furthermore, a consistent tangent stiffness modulus has been derived by linearizing the stress update algorithm. The model requires four viscoplasticity-related input parameters to describe direction-, rate- and pressure-dependent plasticity and creep, obtained from a few stress-strain curves under off-axis loading. For an accurate pre-yield and creep response, multiple modes can be used with a relaxation spectrum determined from a *single* stress-strain curve. In this work, a micromodel for unidirectional carbon/PEEK is used to determine the mesocale model parameters. However, off-axis coupon tests with oblique ends may also be used.

The mesoscopic constitutive model has been compared to a previously developed micromodel for unidirectional carbon/PEEK. It has been shown that the mesoscale model gives a response similar to the micromodel under various strain rates and off-axis angles. However, under transverse compression, a hardening contribution can be included for an improved post-yield response. The model gives satisfactory results under creep, although not as good as under constant strain

rates. This may indicate that the parameter identification procedure, solely based on (short-term) constant strain rate data, requires further improvements.

Finally, the mesoscale model has been applied to the simulation of unidirectional composite coupon tests under off-axis strain rates and shows a good agreement with experiments. The development of the mesoscopic constitutive model, with a few model parameters, while retaining a high degree of the accuracy of a detailed micromodel, is an important step towards virtual testing of thermoplastic composite laminates. Further extensions can be made to cover multiple relaxation processes and to include temperature dependence.

Summary of contributions The EGP model has been extended for unidirectional thermoplastic composites. Compared to other anisotropic versions of the EGP model for *short* and *long* fiber composites [27, 28], new features of the present model are:

- Strong anisotropy is described by transversely isotropic stress invariants.
- Plastic flow in fiber direction is removed.
- The Eyring-type viscosity function is extended with anisotropic pressure dependence.
- The constitutive equations are implicitly integrated and consistently linearized.
- The model is formulated in global frame and does not require rotations to local frame.

Compared to previous invariant-based Perzyna-type viscoplasticity models for unidirectional composites [32–34]:

- An Eyring-type non-Newtonian flow rule, suitable for *thermoplastic* composites, is used to describe both rate-dependent plasticity and creep.
- Only four parameters and a relaxation spectrum are required, which can be obtained from a small number of off-axis tests (either with a micromodel or with off-axis coupon tests with oblique ends).
- The present anisotropic model allows for future extensions regarding the effects of aging [9], temperature dependence [7] and to cover multiple relaxation processes [45] through the Eyring relation.

4.A. APPENDIX

4.A.1. JACOBIAN INTERNAL NEWTON-RAPHSON SCHEME

The Jacobian for solving the plastic deformation gradient $\mathbf{F}_{\mathrm{p}i}$ with the internal scheme of each mode i is determined in this appendix. To improve readability, subscript i is dropped and index notation is used. The residual for *each* mode reads

$$R_{ij}^{\mathbf{F}_{\mathrm{p}i}} = F_{ij}^{\mathrm{p}} - f_{ij} \tag{A.1}$$

where

$$f_{ij} = \Pi_{ik} F_{kj}^{\mathrm{p},0} \tag{A.2}$$

with

$$\Pi_{ik} = \left(\underbrace{\delta_{il} - \frac{\Delta t}{2} \hat{D}_{il}^{\mathrm{p}}}_{Z_{il}} \right)^{-1} \left(\underbrace{\delta_{lk} + \frac{\Delta t}{2} \hat{D}_{lk}^{\mathrm{p}}}_{Y_{lk}} \right) \tag{A.3}$$

Taking the derivative of Eq. (A.1) with respect to the plastic deformation gradient gives the Jacobian

$$\frac{\partial R_{ij}^{\mathbf{F}_{\mathrm{p}i}}}{\partial F_{mn}^{\mathrm{p}}} = \delta_{im}\delta_{jn} - \frac{\partial f_{ij}}{\partial \Pi_{kl}} \frac{\partial \Pi_{kl}}{\partial \hat{D}_{uv}^{\mathrm{p}}} \left[\frac{\partial \hat{D}_{uv}^{\mathrm{p}}}{\partial \Sigma_{qp}^{\mathrm{sym}}} \frac{\partial \Sigma_{qp}^{\mathrm{sym}}}{\partial F_{rs}^{\mathrm{e}}} \frac{\partial F_{rs}^{\mathrm{e}}}{\partial F_{mn}^{\mathrm{p}}} + \frac{\partial \hat{D}_{uv}^{\mathrm{p}}}{\partial \hat{a}_w} \frac{\partial \hat{a}_w}{\partial F_{mn}^{\mathrm{p}}} \right] \tag{A.4}$$

where

$$\frac{\partial f_{ij}}{\partial \Pi_{mn}} = \delta_{im} F_{nj}^{\mathrm{p},0} \tag{A.5}$$

$$\frac{\partial \Pi_{ij}}{\partial \hat{D}_{mn}^{\mathrm{p}}} = \frac{\partial Z_{ik}^{-1}}{\partial \hat{D}_{mn}^{\mathrm{p}}} Y_{kj} + Z_{ik} \frac{\partial Y_{kj}}{\partial \hat{D}_{mn}^{\mathrm{p}}} \tag{A.6}$$

with

$$\frac{\partial {Z_{kj}}^{-1}}{\partial \hat{D}_{mn}^{\mathrm{p}}} = -{Z_{ik}}^{-1} \frac{\partial Z_{ir}}{\partial \hat{D}_{mn}} Z_{rj}^{-1} \tag{A.7}$$

$$\frac{\partial Z_{ij}}{\partial \hat{D}_{mn}^{\mathrm{p}}} = -\frac{\Delta t}{2} \delta_{im}\delta_{jn} \tag{A.8}$$

$$\frac{\partial Y_{ij}}{\partial \hat{D}_{mn}^{\mathrm{p}}} = \frac{\Delta t}{2} \delta_{im}\delta_{jn} \tag{A.9}$$

The other derivatives read

$$\frac{\partial \hat{D}^{\mathrm{p}}_{ij}}{\partial \Sigma^{\mathrm{sym}}_{mn}} = \frac{1}{\eta}\left[\hat{N}^{\mathrm{p}}_{mn}\hat{N}^{\mathrm{p}}_{ij} + \bar{\Sigma}\frac{\partial \hat{N}^{\mathrm{p}}_{ij}}{\partial \Sigma^{\mathrm{sym}}_{mn}}\right] \tag{A.10}$$

$$\frac{\partial \Sigma^{\mathrm{sym}}_{ij}}{\partial F^{\mathrm{e}}_{mn}} = \frac{1}{2}\left(\frac{\partial \Sigma_{ij}}{\partial F^{\mathrm{e}}_{mn}} + \frac{\partial \Sigma_{ji}}{\partial F^{\mathrm{e}}_{mn}}\right) \tag{A.11}$$

$$\frac{\partial F^{\mathrm{e}}_{rs}}{\partial F^{\mathrm{p}}_{mn}} = -F_{rk}\left(F^{\mathrm{p}}_{km}\right)^{-1}\left(F^{\mathrm{p}}_{ns}\right)^{-1} \tag{A.12}$$

$$\frac{\partial \hat{D}^{\mathrm{p}}_{ij}}{\partial \hat{a}_q} = \frac{1}{\eta}\left[\frac{\partial \bar{\Sigma}}{\partial \hat{a}_q}\hat{N}^{\mathrm{p}}_{ij} + \bar{\Sigma}\frac{\partial \hat{N}^{\mathrm{p}}_{ij}}{\partial \hat{a}_q}\right] \tag{A.13}$$

$$\frac{\partial \hat{a}_q}{\partial F^{\mathrm{p}}_{mn}} = \frac{1}{\|\hat{a}\|}\left[\delta_{qm} - \frac{1}{\|\hat{a}\|^2}\hat{A}_{qm}\right]a^0_n \tag{A.14}$$

with

$$\frac{\partial \Sigma_{ij}}{\partial F^{\mathrm{e}}_{mn}} = \mathbb{I}_{kmin}\,\sigma_{kl}\left(F^{\mathrm{e}}_{jl}\right)^{-1} + F^{\mathrm{e}}_{ki}\frac{\partial \sigma_{kl}}{\partial F^{\mathrm{e}}_{mn}}\left(F^{\mathrm{e}}_{jl}\right)^{-1} - F^{\mathrm{e}}_{ki}\,\sigma_{kl}\left(F^{\mathrm{e}}_{jm}\right)^{-1}(F^{\mathrm{e}}_{nl})^{-1} \tag{A.15}$$

$$\frac{\partial \hat{N}^{p}_{ij}}{\partial \Sigma^{\mathrm{sym}}_{kl}} = \frac{1}{\bar{\Sigma}}\left(\frac{\partial^2 \hat{I}_1}{\partial \Sigma^{\mathrm{sym}}_{kl}\partial \Sigma^{\mathrm{sym}}_{ij}} + \alpha_2\frac{\partial^2 \hat{I}_2}{\partial \Sigma^{\mathrm{sym}}_{kl}\partial \Sigma^{\mathrm{sym}}_{ij}} - \hat{N}^{p}_{kl}\hat{N}^{p}_{ij}\right) \tag{A.16}$$

$$\frac{\partial \bar{\Sigma}}{\partial \hat{a}_m} = \frac{1}{\bar{\Sigma}}\left(\frac{\partial \hat{I}_1}{\partial \hat{a}_m} + \alpha_2\frac{\partial \hat{I}_2}{\partial \hat{a}_m}\right) \tag{A.17}$$

$$\frac{\partial \hat{N}^{\mathrm{p}}_{ij}}{\partial \hat{a}_m} = \frac{1}{\bar{\Sigma}}\left(\frac{\partial^2 \hat{I}_1}{\partial \hat{a}_m\partial \Sigma^{\mathrm{sym}}_{ij}} + \alpha_2\frac{\partial^2 \hat{I}_2}{\partial \hat{a}_m\partial \Sigma^{\mathrm{sym}}_{ij}} - \hat{N}^{\mathrm{p}}_{ij}\frac{\partial \bar{\Sigma}}{\partial \hat{a}_m}\right) \tag{A.18}$$

The derivative of the Cauchy stress with respect to the elastic deformation in Eq. (A.15) is given as

$$\frac{\partial \sigma_{ij}}{\partial F^{\mathrm{e}}_{kl}} = \frac{\partial \sigma^{\mathrm{iso}}_{ij}}{\partial F^{\mathrm{e}}_{kl}} + \frac{\partial \sigma^{\mathrm{trn}}_{ij}}{\partial F^{\mathrm{e}}_{kl}} \tag{A.19}$$

$$\frac{\partial \sigma^{\mathrm{iso}}_{ij}}{\partial F^{\mathrm{e}}_{kl}} = \frac{\mu}{J^{\mathrm{e}}}\left(\frac{\partial B^{\mathrm{e}}_{ij}}{\partial F^{\mathrm{e}}_{kl}} - (B^{\mathrm{e}}_{ij} - \delta_{ij})(F^{\mathrm{e}}_{kl})^{-\mathrm{T}}\right) + \lambda J^{\mathrm{e}} \delta_{ij}(F^{\mathrm{e}}_{kl})^{-\mathrm{T}} \tag{A.20}$$

$$\frac{\partial \sigma^{\mathrm{trn}}_{ij}}{\partial F^{\mathrm{e}}_{kl}} = \frac{1}{J^{\mathrm{e}}}\left(\Phi^1_{ijkl} + \Phi^2_{ijkl} + \Phi^3_{ijkl}\right) - \frac{1}{J^{\mathrm{e}}}\sigma^{\mathrm{trn}}_{ij}(F^{\mathrm{e}}_{kl})^{-\mathrm{T}} \tag{A.21}$$

$$\Phi^1_{ijkl} = 2\beta(\xi_2 - 1)\frac{\partial B^{\mathrm{e}}_{ij}}{\partial F^{\mathrm{e}}_{kl}} \tag{A.22}$$

$$\Phi^2_{ijkl} = 4\beta A_{ij} F^{\mathrm{e}}_{kl} \tag{A.23}$$

$$\Phi^3_{ijkl} = -\alpha\left(\frac{\partial B^{\mathrm{e}}_{im}}{\partial F^{\mathrm{e}}_{kl}} A_{mj} + \frac{\partial B^{\mathrm{e}}_{jm}}{\partial F^{\mathrm{e}}_{kl}} A_{im}\right) \tag{A.24}$$

$$\frac{\partial B^{\mathrm{e}}_{ij}}{\partial F^{\mathrm{e}}_{kl}} = F^{\mathrm{e}}_{jl}\delta_{ik} + F^{\mathrm{e}}_{il}\delta_{jk} \tag{A.25}$$

The other terms in Eqs. (A.16) to (A.18) can be expanded as

$$\frac{\partial \hat{I}_1}{\partial \hat{a}_m} = \Sigma^{\mathrm{pind}}_{rs}\frac{\partial \Sigma^{\mathrm{pind}}_{rs}}{\partial \hat{a}_m} - \frac{\partial \hat{I}_2}{\partial \hat{a}_m} \tag{A.26}$$

$$\frac{\partial \hat{I}_2}{\partial \hat{a}_m} = \Sigma^{\mathrm{pind}}_{mj}\Sigma^{\mathrm{pind}}_{jk}\hat{a}_k + \hat{a}_q\Sigma^{\mathrm{pind}}_{qp}\Sigma^{\mathrm{pind}}_{pm} + \frac{\partial \hat{I}_2}{\partial \Sigma^{\mathrm{pind}}_{rs}}\frac{\partial \Sigma^{\mathrm{pind}}_{rs}}{\partial \hat{a}_m} \tag{A.27}$$

$$\frac{\partial^2 \hat{I}_1}{\partial \Sigma^{\mathrm{sym}}_{rs}\partial \Sigma^{\mathrm{sym}}_{kl}} = \left(\mathbb{\hat{P}}_{ijrs} - \frac{\partial^2 \hat{I}_2}{\partial \Sigma^{\mathrm{sym}}_{rs}\partial \Sigma^{\mathrm{pind}}_{ij}}\right)\mathbb{\hat{P}}_{ijkl} \tag{A.28}$$

$$\frac{\partial^2 \hat{I}_1}{\partial \Sigma^{\mathrm{sym}}_{rs}\partial \Sigma^{\mathrm{sym}}_{kl}} = \left(\mathbb{\hat{P}}_{ijrs} - \frac{\partial^2 \hat{I}_2}{\partial \Sigma^{\mathrm{sym}}_{rs}\partial \Sigma^{\mathrm{pind}}_{ij}}\right)\mathbb{\hat{P}}_{ijkl} \tag{A.29}$$

$$\frac{\partial^2 \hat{I}_2}{\partial \Sigma^{\mathrm{sym}}_{rs}\partial \Sigma^{\mathrm{sym}}_{kl}} = \frac{\partial^2 \hat{I}_2}{\partial \Sigma^{\mathrm{sym}}_{rs}\partial \Sigma^{\mathrm{pind}}_{ij}}\mathbb{\hat{P}}_{ijkl} \tag{A.30}$$

$$\frac{\partial^2 \hat{I}_1}{\partial \hat{a}_m \partial \Sigma^{\mathrm{sym}}_{kl}} = \frac{\partial \hat{I}_1}{\partial \Sigma^{\mathrm{pind}}_{ij}}\frac{\partial \mathbb{\hat{P}}_{ijkl}}{\partial \hat{a}_m} + \left(\frac{\partial \Sigma^{\mathrm{pind}}_{ij}}{\partial \hat{a}_m} - \frac{\partial^2 \hat{I}_2}{\partial \hat{a}_m \partial \Sigma^{\mathrm{pind}}_{ij}}\right)\mathbb{\hat{P}}_{ijkl} \tag{A.31}$$

$$\frac{\partial^2 \hat{I}_2}{\partial \hat{a}_m \partial \Sigma^{\mathrm{sym}}_{kl}} = \frac{\partial \hat{I}_2}{\partial \Sigma^{\mathrm{pind}}_{ij}}\frac{\partial \mathbb{\hat{P}}_{ijkl}}{\partial \hat{a}_m} + \frac{\partial^2 \hat{I}_2}{\partial \hat{a}_m \partial \Sigma^{\mathrm{pind}}_{ij}}\mathbb{\hat{P}}_{ijkl} \tag{A.32}$$

where

$$\frac{\partial \Sigma^{\text{pind}}_{rs}}{\partial \hat{a}_m} = \frac{\partial \Sigma^{\text{pind}}_{rs}}{\partial \hat{\mathbb{P}}_{ijkl}} \frac{\partial \hat{\mathbb{P}}_{ijkl}}{\partial \hat{a}_m} \tag{A.33}$$

$$\frac{\partial \hat{\mathbb{P}}_{ijkl}}{\partial \hat{a}_m} = \frac{\partial \hat{\mathbb{P}}_{ijkl}}{\partial \hat{A}_{rs}} \frac{\partial \hat{A}_{rs}}{\partial \hat{a}_m} \tag{A.34}$$

$$\frac{\partial^2 \hat{I}_2}{\partial \hat{a}_m \partial \Sigma^{\text{pind}}_{ij}} = \left(\frac{\partial \hat{A}_{ir}}{\partial \hat{a}_m} \Sigma^{\text{pind}}_{rj} + \hat{A}_{ir} \frac{\partial \Sigma^{\text{pind}}_{rj}}{\partial \hat{a}_m} + \frac{\partial \Sigma^{\text{pind}}_{ir}}{\partial \hat{a}_m} \hat{A}_{rj} + \Sigma^{\text{pind}}_{ir} \frac{\partial \hat{A}_{rj}}{\partial \hat{a}_m} \right) \tag{A.35}$$

The remaining derivatives can be computed at each *internal* iteration:

$$\frac{\partial^2 \hat{I}_2}{\partial \Sigma^{\text{sym}}_{rs} \partial \Sigma^{\text{pind}}_{ij}} = \left(\hat{A}_{im} \hat{\mathbb{P}}_{mjrs} + \hat{\mathbb{P}}_{imrs} \hat{A}_{mj} \right) \tag{A.36}$$

$$\frac{\partial \hat{I}_1}{\partial \Sigma^{\text{pind}}_{rs}} = 2\Sigma^{\text{pind}}_{rs} \tag{A.37}$$

$$\frac{\partial \hat{I}_2}{\partial \Sigma^{\text{pind}}_{rs}} = \hat{A}_{rk}\, \Sigma^{\text{pind}}_{ks} + \Sigma^{\text{pind}}_{rj}\, \hat{A}_{js} \tag{A.38}$$

$$\frac{\partial \Sigma^{\text{pind}}_{rs}}{\partial \hat{\mathbb{P}}_{ijkl}} = \delta_{ir}\delta_{js}\Sigma_{kl} \tag{A.39}$$

$$\frac{\partial \hat{\mathbb{P}}_{ijkl}}{\partial \hat{A}_{rs}} = -\frac{3}{2}\left(\delta_{ir}\delta_{js}\hat{A}_{kl} + \hat{A}_{ij}\delta_{kr}\delta_{ls} \right) + \frac{1}{2}\left(\delta_{kl}\delta_{ir}\delta_{js} + \delta_{ij}\delta_{kr}\delta_{ls} \right) \tag{A.40}$$

$$\frac{\partial \hat{A}_{rs}}{\partial \hat{a}_m} = \delta_{rm}\hat{a}_s + \hat{a}_r\delta_{sm} \tag{A.41}$$

4.A.2. DERIVATIVES EXTERNAL SCHEME

• The derivatives in Eq. (4.49) are given as

$$\frac{\partial R_{a_\sigma}}{\partial \bar{\sigma}} = -\frac{1}{\sigma_0}\left[\sinh^{-1}\left(\bar{\sigma}/\sigma_0\right) - \frac{\bar{\sigma}}{\sigma_0} \frac{\cosh\left(\bar{\sigma}/\sigma_0\right)}{\sinh^2\left(\bar{\sigma}/\sigma_0\right)} \right] \exp\left(-\mu \frac{I_3}{\sigma_0} \right) \tag{A.42}$$

$$\frac{\partial R_{a_\sigma}}{\partial I_3} = \frac{\bar{\sigma}/\sigma_0}{\sinh\left(\bar{\sigma}/\sigma_0\right)} \exp\left(-\mu \frac{I_3}{\sigma_0} \right) \frac{\mu}{\sigma_0} \tag{A.43}$$

$$\frac{\partial I_3}{\partial \boldsymbol{\sigma}} = (\mathbf{I} - \bar{\mathbf{A}}) \tag{A.44}$$

• Applying the chain rule to the second term on the RHS of Eq. (4.51) yields

$$\frac{\partial \mathbf{R}_{\mathbf{F}_{\text{p}i}}}{\partial a_\sigma} = -\frac{\partial f_i}{\partial \boldsymbol{\Pi}_i} : \frac{\partial \boldsymbol{\Pi}_i}{\partial \hat{\mathbf{D}}_{\text{p}i}} : \frac{\partial \hat{\mathbf{D}}_{\text{p}i}}{\partial a_\sigma} \tag{A.45}$$

where $\partial \hat{\mathbf{D}}_{\text{p},i}/\partial a_\sigma = -\bar{\sigma}/\left(\eta_{0i} a_\sigma^2\right) \hat{\mathbf{N}}_{\text{p},i} = -1/a_\sigma \hat{\mathbf{D}}_{\text{p},i}$ The expressions for $\partial f_i/\partial \boldsymbol{\Pi}_i$ and $\partial \boldsymbol{\Pi}_i/\partial \hat{\mathbf{D}}_{\text{p}i}$ are given by Eqs. (A.5) and (A.6), respectively.

4.A.3. DERIVATIVES FOR CONSISTENT TANGENT MODULUS

• The derivative $\partial \mathbf{R}_{\mathbf{F}_{\mathrm{p}i}} / \partial \mathbf{F}$ in Eq. (4.55) reads

$$\frac{\partial \mathbf{R}_{\mathbf{F}_{\mathrm{p}i}}}{\partial \mathbf{F}} = -\frac{\partial f}{\partial \mathbf{\Pi}} : \frac{\partial \mathbf{\Pi}}{\partial \hat{\mathbf{D}}_{\mathrm{p}i}} : \frac{\partial \hat{\mathbf{D}}_{\mathrm{p}i}}{\partial \mathbf{\Sigma}_i^{\mathrm{sym}}} : \frac{\partial \mathbf{\Sigma}_i^{\mathrm{sym}}}{\partial \mathbf{\Sigma}_i} : \left[\frac{\partial \mathbf{\Sigma}_i}{\partial \mathbf{F}_{\mathrm{e}i}} : \frac{\partial \mathbf{F}_{\mathrm{e}i}}{\partial \mathbf{F}} + \frac{\partial \mathbf{\Sigma}_i}{\partial \sigma_i} : \frac{\partial \sigma_i}{\partial \boldsymbol{a}} \cdot \frac{\partial \boldsymbol{a}}{\partial \mathbf{F}} \right] \tag{A.46}$$

The derivatives $\partial f / \partial \mathbf{\Pi}$, $\partial \mathbf{\Pi} / \partial \hat{\mathbf{D}}_{\mathrm{p}i}$, $\partial \mathbf{\Sigma}_i / \partial \mathbf{F}_{\mathrm{e}i}$ and $\partial \sigma_i / \partial \boldsymbol{a}$, are given by Eqs. (A.5), (A.6), (A.15) and (A.48), respectively. The other terms can be derived by differentiating Eqs. (4.3), (4.6) and (4.12). Applying the chain rule to $\partial \hat{\mathbf{D}}_{\mathrm{p}i} / \partial \mathbf{\Sigma}^{\mathrm{sym}}$ gives

$$\frac{\partial \hat{\mathbf{D}}_{\mathrm{p}i}}{\partial \mathbf{\Sigma}^{\mathrm{sym}}} = \frac{1}{\eta_i} \left[\hat{\mathbf{N}}_{\mathrm{p}i} \otimes \frac{\partial \bar{\Sigma}_i}{\partial \mathbf{\Sigma}_i^{\mathrm{sym}}} + \bar{\Sigma}^i \frac{\partial \hat{\mathbf{N}}_{\mathrm{p}i}}{\partial \mathbf{\Sigma}_i^{\mathrm{sym}}} \right] \tag{A.47}$$

where $\partial \bar{\Sigma}_i / \partial \mathbf{\Sigma}_i^{\mathrm{sym}} = \hat{\mathbf{N}}_{\mathrm{p}i}$ and $\partial \hat{\mathbf{N}}_{\mathrm{p}i} / \partial \mathbf{\Sigma}_i^{\mathrm{sym}}$ is given by Eq. (A.16). The derivative $\partial \sigma_i / \partial \boldsymbol{a}$ in Eq. (A.46) reads

$$\frac{\partial \sigma_i}{\partial \boldsymbol{a}} = \frac{1}{J_{\mathrm{e}i}} \left[\mathbf{\Lambda}_1 + \mathbf{\Lambda}_2 + \mathbf{\Lambda}_3 + \mathbf{\Lambda}_4 \right] \tag{A.48}$$

$$\mathbf{\Lambda}_1 = 4\beta_i \left(\mathbf{B}_{\mathrm{e}i} \otimes \boldsymbol{a} \right) \tag{A.49}$$

$$\mathbf{\Lambda}_2 = 2 \left[\alpha_i + \beta_i \left(\xi_{1i} - 3 \right) + 2\gamma \left(\xi_{2i} - 1 \right) \right] \frac{\partial \mathbf{A}}{\partial \boldsymbol{a}} \tag{A.50}$$

$$\mathbf{\Lambda}_3 = 8\gamma_i \left(\mathbf{A} \otimes \boldsymbol{a} \right) \tag{A.51}$$

$$\mathbf{\Lambda}_4 = -\alpha_i \left(\mathbf{B}_{\mathrm{e}i} \cdot \frac{\partial \mathbf{A}}{\partial \boldsymbol{a}} + \frac{\partial \mathbf{A}}{\partial \boldsymbol{a}} \cdot \mathbf{B}_{\mathrm{e}i} \right) \tag{A.52}$$

where derivative $\partial \mathbf{A} / \partial \boldsymbol{a}$ is given in Eq. (A.41), by replacing $\hat{\mathbf{A}}$ and $\hat{\boldsymbol{a}}$ with $\mathbf{A}$ and $\boldsymbol{a}$.

• The derivative $\partial R_{a_\sigma} / \partial \mathbf{F}$ in equation Eq. (4.57) reads

$$\frac{\partial R_{a_\sigma}}{\partial \mathbf{F}} = \left[\frac{\partial R_{a_\sigma}}{\partial \bar{\sigma}} \frac{\partial \bar{\sigma}}{\partial \sigma} + \frac{\partial R_{a_\sigma}}{\partial I_3} \frac{\partial I_3}{\partial \sigma} \right] : \sum_i^{N_{\mathrm{m}}} \frac{\partial \sigma_i}{\partial \mathbf{F}} + \left[\frac{\partial R_{a_\sigma}}{\partial \bar{\sigma}} \frac{\partial \bar{\sigma}}{\partial \bar{\boldsymbol{a}}} + \frac{\partial R_{a_\sigma}}{\partial I_3} \frac{\partial I_3}{\partial \bar{\boldsymbol{a}}} \right] \cdot \frac{\partial \bar{\boldsymbol{a}}}{\partial \mathbf{F}} \tag{A.53}$$

where the $\partial R_{a_\sigma} / \partial \bar{\sigma}$, $\partial R_{a_\sigma} / \partial I_3$, $\partial I_3 / \partial \sigma$ are given by Eqs. (A.42) to (A.44), respectively. Derivative $\partial \bar{\boldsymbol{a}} / \partial \mathbf{F}$ is given by Eq. (A.14), replacing $\hat{\boldsymbol{a}}$ by $\boldsymbol{a}$. The other derivatives

read

$$\frac{\partial I_3}{\partial \bar{\boldsymbol{a}}} = -2\boldsymbol{\sigma} \cdot \bar{\boldsymbol{a}} \tag{A.54}$$

$$\frac{\partial \bar{\sigma}}{\partial \bar{\boldsymbol{a}}} = \frac{1}{\bar{\sigma}} \left(\frac{\partial I_1}{\partial \bar{\boldsymbol{a}}} + \alpha_2 \frac{\partial I_2}{\partial \bar{\boldsymbol{a}}} \right) \tag{A.55}$$

$$\frac{\partial \bar{\sigma}}{\partial \boldsymbol{\sigma}} = \frac{1}{\bar{\sigma}} \left(\frac{\partial I_1}{\partial \boldsymbol{\sigma}} + \alpha_2 \frac{\partial I_2}{\partial \boldsymbol{\sigma}} \right) \tag{A.56}$$

$$\frac{\partial \boldsymbol{\sigma}_i}{\partial \mathbf{F}} = \frac{\partial \boldsymbol{\sigma}_i}{\partial \mathbf{F}_{\mathrm{e}i}} : \left[\frac{\partial \mathbf{F}_{\mathrm{e}i}}{\partial \mathbf{F}} + \frac{\partial \mathbf{F}_{\mathrm{e}i}}{\partial \mathbf{F}_{\mathrm{p}i}} : \frac{\partial \mathbf{F}_{\mathrm{p}i}}{\partial \mathbf{F}} \right] + \frac{\partial \boldsymbol{\sigma}_i}{\partial \boldsymbol{a}} \cdot \frac{\partial \boldsymbol{a}}{\partial \mathbf{F}} \tag{A.57}$$

where $\{\partial I_j / \partial \bar{\boldsymbol{a}}\}_{j=1,2}$ and $\{\partial I_j / \partial \boldsymbol{\sigma}\}_{j=1,2}$ are derived in Sec. 4.2.3 and can be found by replacing *intermediate* configuration quantities $\boldsymbol{\Sigma}_i^{\mathrm{pind}}$ and $\hat{\boldsymbol{a}}_i$ for each mode i by *total current* configuration quantities $\boldsymbol{\sigma}$ and $\boldsymbol{a}$. The derivative $\partial \mathbf{F}_{\mathrm{p}i} / \partial \mathbf{F}$ in Eq. (A.57) is found by solving the first consistency condition (see Eq. (4.55)).

REFERENCES

[1] A. J. Timmis, A. Hodzic, L. Koh, M. Bonner, C. Soutis, A. W. Schäfer, L. Dray, Environmental impact assessment of aviation emission reduction through the implementation of composite materials, *The International Journal of Life Cycle Assessment* 20 (2) (2015) 233–243.

[2] M. A. Valverde, R. Kupfer, L. F. Kawashita, M. Gude, S. R. Hallett, Effect of processing parameters on quality and strength in thermoplastic composite injection overmoulded components, in: 18th European Conference on Composite Materials, Applied Mechanics Laboratory, 2018.

[3] M. A. Valverde, R. Kupfer, T. Wollmann, L. F. Kawashita, M. Gude, S. R. Hallett, Influence of component design on features and properties in thermoplastic overmoulded composites, *Composites Part A: Applied Science and Manufacturing* 132 (2020) 105823.

[4] R. Akkerman, M. Bouwman, S. Wijskamp, Analysis of the thermoplastic composite overmolding process: Interface strength, *Frontiers in Materials* 7 (2020).

[5] F. Neveu, C. Cornu, P. Olivier, B. Castanié, Manufacturing and impact behaviour of aeronautic overmolded grid-stiffened thermoplastic carbon plates, *Composite Structures* 284 (2022) 115228.

[6] T. A. Tervoort, E. T. J. Klompen, L. E. Govaert, A multi-mode approach to finite, three-dimensional, nonlinear viscoelastic behavior of polymer glasses, *Journal of Rheology* 40 (5) (1996) 779–797.

[7] T. A. Tervoort, R. J. M. Smit, W. A. M. Brekelmans, L. E. Govaert, A Constitutive Equation for the Elasto-Viscoplastic Deformation of Glassy Polymers, *Mechanics of Time-Dependent Materials 1: 269–291, 1998.* 1 (1998) 269–291.

[8] L. E. Govaert, P. H. M. Timmermans, W. A. M. Brekelmans, The Influence of Intrinsic Strain Softening on Strain Localization in Polycarbonate: Modeling and Experimental Validation, *Journal of Engineering Materials and Technology* 122 (2) (2000) 177–185.

[9] E. T. J. Klompen, T. A. P. Engels, L. E. Govaert, H. E. H. Meijer, Modeling of the Postyield Response of Glassy Polymers: Influence of Thermomechanical History, *Macromolecules* 38 (16) (2005) 6997–7008.

[10] L. C. A. van Breemen, E. T. J. Klompen, L. E. Govaert, H. E. H. Meijer, Extending the EGP constitutive model for polymer glasses to multiple relaxation times, *Journal of the Mechanics and Physics of Solids* 59 (10) (2011) 2191–2207.

[11] T. Lenders, J. J. C. Remmers, T. Pini, P. Veenstra, L. E. Govaert, M. G. D. Geers, An elasto-viscoplastic constitutive model for the rate-dependent behavior of polyvinylidene fluoride, *Journal of Polymer Science* 61 (14) (2023) 1439–1456.

[12] R. N. Haward, G. Thackray, The use of a mathematical model to describe isothermal stress-strain curves in glassy thermoplastics, *Proceedings of the Royal Society of London. Series A. Mathematical and Physical Sciences* 302 (1471) (1968) 453–472.

[13] M. C. Boyce, D. M. Parks, A. S. Argon, Large inelastic deformation of glassy polymers. part I: Rate dependent constitutive model, *Mechanics of Materials* 7 (1) (1988) 15–33.

[14] M. C. Boyce, E. L. Montagut, A. S. Argon, The effects of thermomechanical coupling on the cold drawing process of glassy polymers, *Polymer Engineering & Science* 32 (16) (1992) 1073–1085.

[15] H. Eyring, Viscosity, Plasticity, and Diffusion as Examples of Absolute Reaction Rates, *The Journal of Chemical Physics* 4 (4) (1936) 283–291.

[16] D. Kovačević, B. K. Sundararajan, F. P. van der Meer, Microscale modeling of rate-dependent failure in thermoplastic composites under off-axis loading, *Engineering Fracture Mechanics* 276 (2022).

[17] T. Lenders, J. J. Remmers, T. Pini, P. Veenstra, L. E. Govaert, M. G. Geers, A periodic micromechanical model for the rate- and temperature-dependent

behavior of unidirectional carbon fiber-reinforced PVDF, *Journal of Reinforced Plastics and Composites* (2024) 07316844241266012.

[18] D. Kovačević, B. K. Sundararajan, F. P. van der Meer, Micromechanical model for off-axis creep rupture in unidirectional composites undergoing finite strains, *Composites Part A: Applied Science and Manufacturing* 176 (2024) 107860.

[19] J. Oliver, M. Caicedo, E. Roubin, A. Huespe, J. Hernández, Continuum approach to computational multiscale modeling of propagating fracture, *Computer Methods in Applied Mechanics and Engineering* 294 (2015) 384–427.

[20] L. Ke, F. P. van der Meer, A computational homogenization framework with enhanced localization criterion for macroscopic cohesive failure in heterogeneous materials, *Journal of Theoretical, Computational and Applied Mechanics* (2022) 7707.

[21] M. A. Maia, I. B. C. M. Rocha, P. Kerfriden, F. P. van der Meer, Physically recurrent neural networks for path-dependent heterogeneous materials: Embedding constitutive models in a data-driven surrogate, *Computer Methods in Applied Mechanics and Engineering* 407 (2023) 115934.

[22] M. A. Maia, I. B. C. M. Rocha, D. Kovačević, F. P. van der Meer, Surrogate-based multiscale analysis of experiments on thermoplastic composites under off-axis loading (2025). arXiv:2501.10193.

[23] R. Larsson, V. Singh, R. Olsson, E. Marklund, A micromechanically based model for strain rate effects in unidirectional composites, *Mechanics of Materials* 148 (2020) 103491.

[24] V. Singh, R. Larsson, R. Olsson, E. Marklund, A micromechanics based model for rate dependent compression loaded unidirectional composites, *Composites Science and Technology* 232 (2023) 109821.

[25] T. B. van Erp, C. T. Reynolds, T. Peijs, J. A. W. van Dommelen, L. E. Govaert, Prediction of yield and long-term failure of oriented polypropylene: Kinetics and anisotropy, *Journal of Polymer Science Part B: Polymer Physics* 47 (20) (2009) 2026–2035.

[26] D. J. A. Senden, G. W. M. Peters, L. E. Govaert, J. A. W. van Dommelen, Anisotropic yielding of injection molded polyethylene: Experiments and modeling, *Polymer* 54 (21) (2013) 5899–5908.

[27] A. Amiri-Rad, L. V. Pastukhov, L. E. Govaert, J. A. W. van Dommelen, An anisotropic viscoelastic-viscoplastic model for short-fiber composites, *Mechanics of Materials* 137 (2019) 103141.

[28] A. Amiri-Rad, M. Hütter, L. E. Govaert, J. A. W. van Dommelen, Improved associated flow rule for anisotropic viscoplasticity in thermoplastic polymer systems, *Mechanics of Materials* 163 (2021) 104087.

[29] R. Hill, A theory of the yielding and plastic flow of anisotropic metals, *Proceedings of the Royal Society of London. Series A. Mathematical and Physical Sciences* 193 (1033) (1948) 281–297.

[30] A. J. M. Spencer, Kinematic Constraints, Constitutive Equations and Failure Rules for Anisotropic Materials, in: J. P. Boehler (Ed.), Applications of Tensor Functions in Solid Mechanics, Springer, Vienna, 1987, pp. 187–201.

[31] B. Eidel, Anisotropic Inelasticity Modelling, Simulation, Validation, Ph.D. thesis, Technical University Darmstadt (2004).

[32] H. Koerber, P. Kuhn, M. Ploeckl, F. Otero, P.-W. Gerbaud, R. Rolfes, P. P. Camanho, Experimental characterization and constitutive modeling of the nonlinear stress–strain behavior of unidirectional carbon–epoxy under high strain rate loading, *Advanced Modeling and Simulation in Engineering Sciences* 5 (1) (2018) 17.

[33] P.-W. Gerbaud, F. Otero, P. Bussetta, P. Camanho, An invariant based transversely-isotropic constitutive model for unidirectional fibre reinforced composites considering the matrix viscous effects, *Mechanics of Materials* 138 (2019) 103146.

[34] I. A. Rodrigues Lopes, P. P. Camanho, F. M. Andrade Pires, A. Arteiro, An invariant-based elasto-visco-plastic model for unidirectional polymer composites at finite strains, *International Journal of Solids and Structures* 236–237 (2022) 111292.

[35] H. F. Brinson, L. C. Brinson, Polymer Engineering Science and Viscoelasticity: An Introduction, Springer US, Boston, MA, 2015.

[36] L. E. Govaert, H. J. Schellens, H. J. M. Thomassen, R. J. M. Smit, L. Terzoli, T. Peijs, A micromechanical approach to time-dependent failure in off-axis loaded polymer composites, *Composites Part A: Applied Science and Manufacturing* 32 (12) (2001) 1697–1711.

[37] D. Kovačević, F. P. van der Meer, Strain-rate based arclength model for nonlinear microscale analysis of unidirectional composites under off-axis loading, *International Journal of Solids and Structures* 250 (2022) 111697.

[38] F. P. van der Meer, Micromechanical validation of a mesomodel for plasticity in composites, *European Journal of Mechanics - A/Solids* 60 (2016) 58–69.

[39] F. Daghia, A. Lagache, L. Di Gennaro, Validation of a new viscoelastic model for unidirectional polymer matrix composites by analytical and numerical homogenisation, *European Journal of Mechanics - A/Solids* 100 (2023) 104975.

[40] Y. Liu, F. P. van der Meer, L. J. Sluys, J. T. Fan, A numerical homogenization scheme used for derivation of a homogenized viscoelastic-viscoplastic model for the transverse response of fiber-reinforced polymer composites, *Composite Structures* 252 (2020) 112690.

[41] E. Kröner, Allgemeine Kontinuumstheorie der Versetzungen und Eigenspannungen, *Archive for Rational Mechanics and Analysis* 4 (1) (1959) 273–334.

[42] E. H. Lee, Elastic-Plastic Deformation at Finite Strains, *ASMEJ. Appl. Mech. March* 36 (1) (1969) 1–6.

[43] Y. F. Dafalias, Plastic spin: Necessity or redundancy?, *International Journal of Plasticity* 14 (9) (1998) 909–931.

[44] M. Boyce, G. Weber, D. Parks, On the kinematics of finite strain plasticity, *Journal of the Mechanics and Physics of Solids* 37 (5) (1989) 647–665.

[45] E. T. J. Klompen, L. E. Govaert, Nonlinear Viscoelastic Behaviour of Thermorheologically Complex Materials, *Mechanics of Time-Dependent Materials* 3 (1999) 49–69.

[46] J. Mandel, Plasticite Classique et Viscoplasticite:, CISM International Centre for Mechanical Sciences, Springer, 1972.

[47] J. Lubliner, Plasticity Theory, Courier Corporation, 2008.

[48] A. Dean, S. Sahraee, J. Reinoso, R. Rolfes, Finite deformation model for short fiber reinforced composites: Application to hybrid metal-composite clinching joints, *Composite Structures* 151 (2016) 162–171.

[49] J. P. Boehler (Ed.), Applications of Tensor Functions in Solid Mechanics, Springer Vienna, Vienna, 1987.

[50] A. Spencer, Deformations of Fibre-Reinforced Materials, Oxford Science Research Papers, Clarendon Press, 1972.

[51] M. Vogler, R. Rolfes, P. Camanho, Modeling the inelastic deformation and fracture of polymer composites – Part I: Plasticity model, *Mechanics of Materials* 59 (2013) 50–64.

[52] J. Bonet, A. Burton, A simple orthotropic, transversely isotropic hyperelastic constitutive equation for large strain computations, *Computer Methods in Applied Mechanics and Engineering* 162 (1-4) (1998) 151–164.

[53] H. Khaleghi, A. Amiri-Rad, M. Mashayekhi, A thermodynamically consistent continuum damage model for time-dependent failure of thermoplastic polymers, *International Journal of Plasticity* 154 (2022) 103278.

[54] A. L. Eterovic, K.-J. Bathe, A hyperelastic-based large strain elasto-plastic constitutive formulation with combined isotropic-kinematic hardening using the logarithmic stress and strain measures, *International Journal for Numerical Methods in Engineering* 30 (6) (1990) 1099–1114.

[55] G. Weber, L. Anand, Finite deformation constitutive equations and a time integration procedure for isotropic, hyperelastic-viscoplastic solids, *Computer Methods in Applied Mechanics and Engineering* 79 (2) (1990) 173–202.

[56] C. Sansour, F. G. Kollmann, Large viscoplastic deformations of shells. Theory and finite element formulation, *Computational Mechanics* 21 (6) (1998) 512–525.

[57] H. Baaser, The Padé-approximation for matrix exponentials applied to an integration algorithm preserving plastic incompressibility, *Computational Mechanics* 34 (3) (2004).

[58] C. Sun, I. Chung, An oblique end-tab design for testing off-axis composite specimens, *Composites* 24 (8) (1993) 619–623.

[59] B. K. Sundararajan, Matrix dominated failure in continuous carbon fibre reinforced poly(ether ether ketone), Ph.D. thesis, University of Twente, Enschede, The Netherlands (2024).

[60] O. Erartsin, A. Amiri-Rad, M. Van Drongelen, L. E. Govaert, Time-dependent failure of off-axis loaded unidirectional glass/ iPP composites, *Journal of Applied Polymer Science* 139 (23) (2022) 52293.

[61] P. Hofman, F. P. van der Meer, L. J. Sluys, A numerical framework for simulating progressive failure in composite laminates under high-cycle fatigue loading, *Engineering Fracture Mechanics* 295 (2024) 109786.

5

Analysis of fracture and fatigue in an overmolded T-section

With the exception of minor textual adjustments, this chapter is reproduced from: P. Hofman, F. P. van der Meer, L.J. Sluys, Computational analysis of fracture and fatigue in overmolded thermoplastic composites: time-homogenized viscoplasticity, cohesive fracture and processing effects, (2025), Under Review.

ABSTRACT

A numerical framework is presented for simulating fracture and fatigue in a T-section, cut from an overmolded thermoplastic composite panel. The framework combines a cohesive zone model for the overmolded interface with an anisotropic viscoplasticity model for the laminate and accounts for processing effects. For high-cycle fatigue analyses, a two-scale time-homogenized version of the viscoplasticity model is derived. The numerical framework is applied to the analysis of a rib pull-off test and is used to gain insights into the influence on the short- and long-term response of two typical processing effects: out-of-plane deformations of the laminate that occur during thermoforming and non-uniform healing profiles resulting from spatially varying thermal histories. Furthermore, the effects of various modeling assumptions are studied, such as modeling the local fiber orientations of each ply in the laminate with a mesoscopic ply-by-ply approach, the effect of viscoplastic deformations in the laminate, the influence of non-uniform local stress ratios, and the effect of the boundary conditions. The analyses demonstrate that the framework is capable of efficiently simulating a large number of cycles. The simulation results show that the local wrinkles in the laminate as a result of thermoforming have a significant effect on the mechanical response, especially under cyclic loading. Moreover, accounting for viscoplastic deformations appears more important when high degrees of bonding of the overmolded interface are achieved. Finally, it is shown that changes to the boundary conditions have a significant effect on the short and long-term response of the T-section, challenging the validity of the test for characterizing fracture and fatigue properties of the overmolded interface.

5.1. INTRODUCTION

Thermoplastic overmolding is a manufacturing technique that combines thermoforming with injection molding. During this process, a thermoplastic laminate, made of unidirectional or long-fiber woven plies, is heated above the melt temperature and subsequently formed into the desired shape (thermoforming). After thermoforming, a reinforcing rib, often made of the same polymer matrix and optionally reinforced with short fibers, is overinjected onto the laminate.

This manufacturing technique is gaining more interest in recent years since it has the potential to significantly contribute to lightweighting in the automotive and aerospace sectors. In particular, overmolding enables near net shape manufacturing of composite parts with fast processing cycles and complex geometries without additional fasteners that add weight. However, a challenging aspect is that the mechanical performance of the final product depends on the processing parameters [1–6]. The understanding of the relation between processing and performance is currently not at a mature level, which is preventing the wide-spread use of overmolded thermoplastic composite parts in transportation industries.

There are two main processing effects that influence the mechanical performance of the final product. Firstly, the laminate deforms locally out of plane during thermoforming, leading to fibers and polymer resin that enter the mold cavity [2]. After thermoforming, this results in wrinkles in the laminate and after injection molding, these plies protrude into the rib structure (see Fig. 5.1). Secondly, during overmolding, the temperature distribution is non-uniform due to different temperatures of the overmolding compound, the laminate and the mold tool. To obtain a strong interface, a high temperature for a sufficient duration is necessary to allow polymer chains to move across the interface (a process known as *interdifussion*). The difference in thermal histories leads to varying levels of healing and consequently non-uniform fracture properties along the overmolded interface.

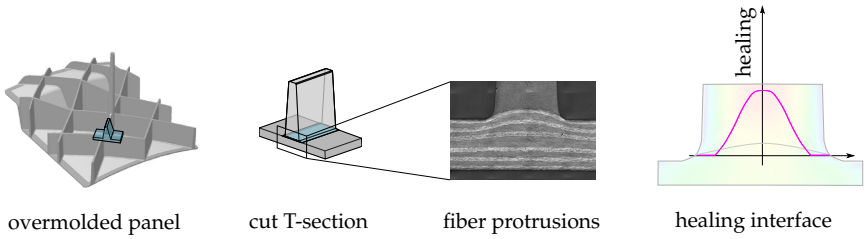

Figure 5.1 Processing effects in an overmolded panel. First and third picture are adapted from [2] and [7], respectively.

Since the processing parameters have a large influence on the mechanical response of thermoplastic overmolded composite parts, optimizing manufacturing procedures and part performance is not straightforward, resulting in time-consuming and costly trial-and-error experimental campaigns. An important factor for performance assessment is determining the quality of the overmolded interface, *e.g.* in terms of strength. At present, there is no standardized test to determine the strength of the interface. Often, a T-section is cut from an overmolded panel (see Fig. 5.1) and tested under tensile loads [6–11]. However, specimen dimensions and boundary conditions influence the measured strength of the specimen [11, 12], questioning the validity of the test for its use in determining the strength of the interface. In contrast to time-consuming and costly experimental testing procedures, numerical models allow for a large number of virtual experiments to predict the effects of processing on the performance and to provide insights into the consequences of certain test set-ups. Therefore, for reaching the full potential of overmolded thermoplastic composites in aerospace and automotive industries, it is crucial to develop accurate, efficient and robust simulation tools.

So far, only a small number of studies have focused on numerically simulating failure in overmolded T-sections [7, 11, 13]. In these works, several assumptions have been made: the numerical models consider the laminate as a single homogenized material and do not take into account the non-uniformly distributed local fiber orientations. Furthermore, all material nonlinearities are lumped at the overmolded interface and the effects of viscoplastic deformations are not taken into account. Moreover, studies have focused on short-term (static) performance assessments, while long-term performance (fatigue and creep) of overmolded thermoplastic composites has not been investigated.

In this work, we set aside the aforementioned simplifying assumptions and present a modeling framework for simulating fracture and fatigue in overmolded thermoplastic composites. The framework builds on previous works [14, 15] (Chapters 2 and 3), where a progressive fatigue framework for multidirectional composites was presented. In this chapter, we extend the previous framework for simulating failure in overmolded composites, taking into account viscoplastic deformations and processing effects. For this purpose, a recently developed anisotropic viscoplasticity model [16] (Chapter 4) is included in the framework and a two-scale time-homogenized version is derived for efficient high-cycle fatigue analyses. In comparison to earlier numerical analyses on overmolded T-sections [7, 11] for static loading, new features of the present framework are:

- A fatigue mixed-mode cohesive zone model [17, 18] is employed for simulat-

ing cohesive fracture and fatigue at the overmolded interface.

- A recently developed transversely isotropic viscoplasticity model for thermoplastic composites [16] is used to account for the effects of viscoplastic deformations in the laminate.

- A two-scale version of the viscoplasticity model is developed with temporal homogenization to efficiently simulate a large number of cycles under high-cycle fatigue.

- A ply-by-ply modeling approach is used for the laminate and the process-induced mesoscopic geometry, including the effect on the fiber orientation, is taken into account. With this approach, the effect of wrinkles due to thermoforming is studied.

With the numerical framework, overmolded T-sections are simulated under quasi-static and cyclic loading to gain insight into the processing effects on both the short- and long-term performance of overmolded composites. In the numerical analyses, special attention is given to the effects of varying healing profiles at the overmolded interface and process-induced deformations on the mechanical response of the specimen. In addition, the effects of modeling assumptions, such as process-induced wrinkles and the importance of viscoplastic deformations in the laminate are investigated. Finally, the effects of the boundary conditions are discussed.

This chapter is outlined as follows. Firstly, the constitutive models for the overmolded interface, the laminate and the rib are discussed in Sec. 5.2. Subsequently, a two-scale version of the viscoplasticity model is derived in Sec. 5.3. In Sec. 5.4, the computational modeling approach of the overmolded T-section is outlined and the results are discussed in Sec. 5.5. Finally, conclusions are presented at the end of the chapter.

5.2. CONSTITUTIVE MODELS

The constitutive models for the T-section are presented in this section. In Sec. 5.2.1, the cohesive zone model [17, 18] for simulating fracture and fatigue at the overmolded interface is outlined. In Sec. 5.2.2, a recently developed transversely isotropic viscoplasticity model for the continuous fiber-reinforced laminate [16] (Chapter 4) is summarized. Furthermore, the rib is considered transversely isotropic elastic and follows the same constitutive relations of the laminate (Sec. 5.2.2), albeit without viscoplastic deformations.

5.2.1. FATIGUE COHESIVE ZONE MODEL

The overmolded interface is modeled with a cycle-dependent cohesive zone model [17, 18]. The model is formulated in a local coordinate frame aligned with the crack plane. The traction vector $\mathbf{t} = [t_n, t_{s1}, t_{s2}]^T$ is computed from the displacement jump $[\![\mathbf{u}]\!] = [[\![u]\!]_n, [\![u]\!]_{s1}, [\![u]\!]_{s2}]^T$ as

$$\mathbf{t} = (\mathbf{I} - d\,\mathbf{P})\mathbf{K}[\![\mathbf{u}]\!] \tag{5.1}$$

where $d \in (0,1)$ is a scalar damage variable, $\mathbf{K}$ is the dummy stiffness matrix and $\mathbf{P}$ is a selection matrix. The matrices $\mathbf{K}$ and $\mathbf{P}$ are given as

$$\mathbf{K} = \begin{bmatrix} K_n & 0 & 0 \\ 0 & K_{sh} & 0 \\ 0 & 0 & K_{sh} \end{bmatrix} \quad \text{and} \quad \mathbf{P} = \begin{bmatrix} \frac{\langle [\![u]\!]_n \rangle}{[\![u]\!]_n} & 0 & 0 \\ 0 & 1 & 0 \\ 0 & 0 & 1 \end{bmatrix} \tag{5.2}$$

Furthermore, K_n is the normal dummy stiffness and K_{sh} is the shear dummy stiffness. The Macaulay operator $\langle \bullet \rangle = \max(0, \bullet)$ in the selection matrix $\mathbf{P}$ prevents interfacial penetration. The model is formulated in terms of a 1D-equivalent traction-separation relation:

$$\sigma = (1-d)K_{\mathcal{B}}\Delta \tag{5.3}$$

which is illustrated in Fig. 5.2. In Eq. (5.3), σ is the equivalent traction, $K_{\mathcal{B}}$ is the mode-dependent dummy stiffness and Δ is the equivalent displacement jump:

$$\sigma = \sqrt{\langle t_n \rangle^2 + t_{s1}^2 + t_{s2}^2} \tag{5.4}$$

$$K_{\mathcal{B}} = K_n(1-\mathcal{B}) + \mathcal{B}K_{sh} \tag{5.5}$$

$$\Delta = \frac{K_n \langle [\![u]\!]_n \rangle^2 + K_{sh}[\![u]\!]_{sh}^2}{\sqrt{K_n^2 \langle [\![u]\!]_n \rangle^2 + K_{sh}^2 [\![u]\!]_{sh}^2}} \tag{5.6}$$

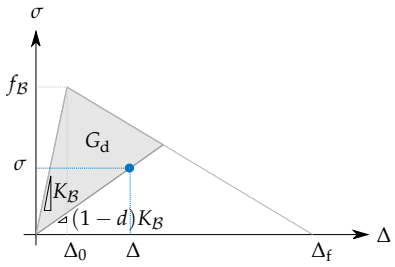

Figure 5.2 1D-equivalent traction-separation relation: the cyclic response (•) is inside the quasi-static envelope.

where $[\![u]\!]_{sh}^2 = [\![u]\!]_{s1}^2 + [\![u]\!]_{s2}^2$. Furthermore, $\mathcal{B}$ is defined as

$$\mathcal{B} = \frac{K_{sh}[\![u]\!]_{sh}^2}{K_n \langle [\![u]\!]_n \rangle^2 + K_{sh}[\![u]\!]_{sh}^2} \tag{5.7}$$

and is a measure of mode-mixity. An energy-based damage variable $\mathcal{D}$ is introduced as state variable which can only increase in time, *i.e.* $\mathcal{D}(t) = \max_{0 \le \tau \le t} \big(\mathcal{D}(\tau)\big)$. The damage variable $\mathcal{D}$ is defined as

$$\mathcal{D} \equiv \frac{G_d}{G_c} \tag{5.8}$$

where G_d is the dissipated energy and G_c is the mixed-mode fracture energy. Furthermore, $f_{\mathcal{B}}$ in Fig. 5.2 is the 1D-equivalent mixed-mode static strength, which is computed as

$$f_{\mathcal{B}} = \sqrt{(K_n(1-\mathcal{B}) + \mathcal{B}K_{sh})\left[f_n^2/K_n + (f_{sh}^2/K_{sh} - f_n^2/K_n)\mathcal{B}^{\eta_{BK}}\right]} \tag{5.9}$$

where f_n, f_{sh} are the tensile strength and shear strength, respectively, and η_{BK} is the Benzeggagh-Kenane mixed-mode interaction parameter [19].

QUASI-STATIC DAMAGE EVOLUTION

Under quasi-static loading, $\mathcal{D}$ is computed as

$$\mathcal{D} = \frac{\Delta - \Delta_0}{\Delta_f - \Delta_0} \tag{5.10}$$

where Δ_0 and Δ_f are the equivalent displacement jumps at fracture initiation and full decohesion:

$$\Delta_0 = \sqrt{\frac{K_n([\![u]\!]_n^0)^2 + \Big(K_{sh}([\![u]\!]_{sh}^0)^2 - K_n([\![u]\!]_n^0)^2\Big)\mathcal{B}^{\eta_{BK}}}{K_{\mathcal{B}}}} \tag{5.11}$$

$$\Delta_f = \frac{K_n[\![u]\!]_n^0[\![u]\!]_n^f + \Big(K_{sh}[\![u]\!]_{sh}^0[\![u]\!]_{sh}^f - K_n[\![u]\!]_n^0[\![u]\!]_n^f\Big)\mathcal{B}^{\eta_{BK}}}{K_{\mathcal{B}}\Delta_0} \tag{5.12}$$

The corresponding jump components are given by

$$[\![u]\!]_n^0 = \frac{f_n}{K_n}, \qquad [\![u]\!]_n^f = \frac{2G_{Ic}}{f_n} \tag{5.13}$$

$$[\![u]\!]_{sh}^0 = \frac{f_{sh}}{K_{sh}}, \qquad [\![u]\!]_{sh}^f = \frac{2G_{IIc}}{f_{sh}} \tag{5.14}$$

where G_{Ic} and G_{IIc} are mode-I and mode-II fracture energies, respectively. Furthermore, the damage variable d is computed as

$$d = 1 - \frac{(1-\mathcal{D})\Delta_0}{\mathcal{D}\Delta_f + (1-\mathcal{D})\Delta_0} \tag{5.15}$$

FATIGUE DAMAGE EVOLUTION

Under cyclic loading, $\mathcal{D}$ evolves with number of cycles N. The damage rate $\mathrm{d}\mathcal{D}/\mathrm{d}N$ is described by the following differential equation [18]:

$$\frac{\mathrm{d}\mathcal{D}}{\mathrm{d}N} = \frac{1}{\gamma}\frac{(1-\mathcal{D})^{\beta-p}}{E^{\beta}(p+1)}\left(\frac{\Delta}{\Delta^*}\right)^{\beta} \tag{5.16}$$

where Δ^* is the displacement jump at which quasi-static damage develops, given as

$$\Delta^* = \mathcal{D}(\Delta_\mathrm{f} - \Delta_0) + \Delta_0 \tag{5.17}$$

The parameters in Eq. (5.16) can be fitted to ensure that the evolution of $\mathcal{D}$ at constant stress level leads to failure after N cycles, as described by an S-N curve (see Fig. 5.3) [17]. In Eq. (5.16), γ and p are model parameters and β is given as

$$\beta = \frac{-7\eta}{\log E} \tag{5.18}$$

where η is a parameter that controls the curved shape of the S-N curve in the low-cycle regime. Furthermore, E is the relative endurance limit, defined as the ratio of the endurance limit σ_end to the static mixed-mode strength $f_\mathcal{B}$ and is given as

$$E = \frac{2C\epsilon}{C\epsilon + 1 + R(C\epsilon - 1)} \tag{5.19}$$

where R is the local stress ratio and ϵ is the endurance limit at $R = -1$. Furthermore, C takes into account the mode-mixity and follows an empirical relation [20]:

$$C = 1 - 0.42\mathcal{B} \tag{5.20}$$

Under cyclic loading, $\mathcal{D}$ is computed with an implicit time integration scheme, using the trapezoidal rule [14] (Chapter 2, Sec. 2.2.2):

$$\mathcal{D}^{(n)} = \mathcal{D}^{(n-1)} + \frac{\Delta N}{2}\left(\frac{\mathrm{d}\mathcal{D}}{\mathrm{d}N}^{(n-1)} + \frac{\mathrm{d}\mathcal{D}}{\mathrm{d}N}^{(n)}\right) \tag{5.21}$$

where the damage rates $\mathrm{d}\mathcal{D}/\mathrm{d}N^{(n-1)}$ and $\mathrm{d}\mathcal{D}/\mathrm{d}N^{(n)}$ correspond to the previous and the current time step, respectively. Eq. (5.21) is a nonlinear equation, which is iteratively solved with Newton's method.

Furthermore, to ensure that the traction-separation response is inside the quasi-static envelope, $\mathcal{D}$ is determined as the maximum of the damage computed with Eq. (5.21) and quasi-static damage with Eq. (5.10):

$$\mathcal{D} = \max\left(\frac{\Delta - \Delta_0}{\Delta_\mathrm{f} - \Delta_0}, \mathcal{D}\right) \tag{5.22}$$

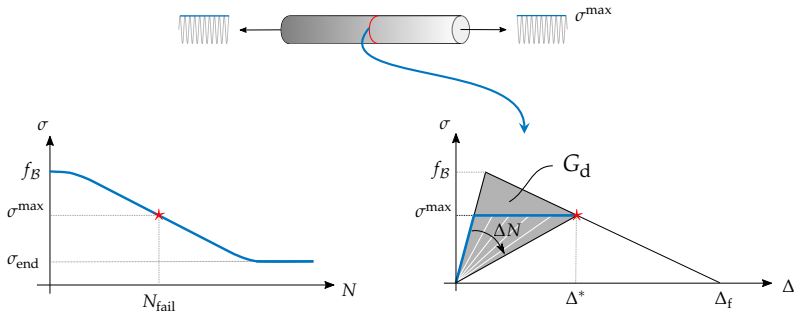

Figure 5.3 Failure with the cohesive zone model is described by an S-N curve: at maximum stress level $\sigma^{\max}$, stiffness degrades with each cycle increment ΔN until the traction-separation response reaches the quasi-static softening line after N cycles $(\Delta^\star, \sigma^{\max})$. Upon further increase in cycles, the material cannot sustain the load anymore and is considered to have failed (indicated with $\star$).

With $\mathcal{D}$ known, the damage variable d in Eq. (5.3) is computed through Eq. (5.15). The consistent tangent stiffness matrix for implicit finite element analysis is presented in [14] (Chapter 2, Sec. 2.2.3).

5.2.2. TRANSVERSELY ISOTROPIC VISCOPLASTICITY MODEL

The laminate is modeled with a transversely isotropic viscoplasticity model for thermoplastic composites [16] (Chapter 4), a recently developed constitutive model based on the Eindhoven Glassy Polymer model [21–23]. To account for a spectrum of relaxation times, the stress is composed of N_{m} nonlinear spring-dashpots, denoted as *modes*:

$$\boldsymbol{\sigma} = \sum_{i}^{N_{\text{m}}} \boldsymbol{\sigma}_i \tag{5.23}$$

where $\boldsymbol{\sigma}_i$ is the stress in mode i. The rheological model is shown in Fig. 5.4. The

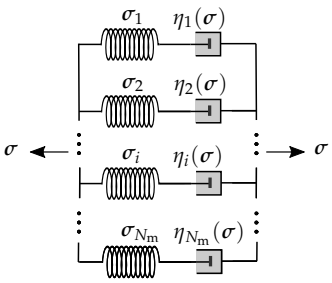

Figure 5.4 Rheological model of the transversely isotropic viscoplasticity model.

total deformation gradient $\mathbf{F}$ is multiplicatively decomposed [24, 25] into an elastic $\mathbf{F}_{ei}$ and a plastic $\mathbf{F}_{pi}$ deformation gradient:

$$\mathbf{F} = \mathbf{F}_{ei} \cdot \mathbf{F}_{pi} \tag{5.24}$$

The decomposition and corresponding configurations are depicted in Fig. 5.5. The plastic velocity gradient is additively decomposed into the rate of plastic deformation tensor $\hat{\mathbf{D}}_{pi}$ and the plastic material spin $\hat{\mathbf{W}}_{p}$:

$$\hat{\mathbf{L}}_{pi} = \dot{\mathbf{F}}_{pi} \cdot \mathbf{F}_{pi}^{-1} = \underbrace{\left(\dot{\mathbf{F}}_{pi} \cdot \mathbf{F}_{pi}^{-1}\right)^{\text{sym}}}_{\hat{\mathbf{D}}_{pi}} + \underbrace{\left(\dot{\mathbf{F}}_{pi} \cdot \mathbf{F}_{pi}^{-1}\right)^{\text{skw}}}_{\hat{\mathbf{W}}_{pi}} \tag{5.25}$$

where the plastic material spin $\hat{\mathbf{W}}_{pi}$ is set to zero to remove the issue of non-uniqueness of Eq. (5.24). As a result, the evolution of $\mathbf{F}_{pi}$ reads

$$\dot{\mathbf{F}}_{pi} = \hat{\mathbf{D}}_{pi} \cdot \mathbf{F}_{pi} \tag{5.26}$$

where $\hat{\mathbf{D}}_{pi}$ is described by the following flow rule:

$$\hat{\mathbf{D}}_{pi} = \dot{\gamma}_{pi} \hat{\mathbf{N}}_{pi} \tag{5.27}$$

In this equation, $\dot{\gamma}_{pi}$ is the equivalent plastic strain rate and $\hat{\mathbf{N}}_{pi}$ is the direction of plastic flow. The equivalent plastic strain rate reads

$$\dot{\gamma}_{pi} = \frac{\bar{\Sigma}_i}{\eta_i} \tag{5.28}$$

where $\bar{\Sigma}_i$ is the equivalent stress in mode i and the viscosity η_i in each mode is given as

$$\eta_i = \eta_{0i}\, a_\sigma \tag{5.29}$$

where a_σ is the so-called *stress shift factor* and η_{0i} is the initial viscosity of mode i. The stress shift factor depends on the total equivalent stress $\bar{\sigma}$ through a transverse pressure-extended Eyring relation:

$$a_\sigma = \frac{\bar{\sigma}/\sigma_0}{\sinh\left(\bar{\sigma}/\sigma_0\right)} \exp\left(-\mu_p \frac{p_m}{\sigma_0}\right) \tag{5.30}$$

where σ_0 is a model parameter that determines the exponential decrease of the viscosity, μ_p is the pressure dependency parameter and p_m is a measure of pressure in the polymer matrix. The quantities $\bar{\Sigma}_i$, $\bar{\sigma}$ and p_m take into account the transverse isotropy in the plasticity relations and are defined below.

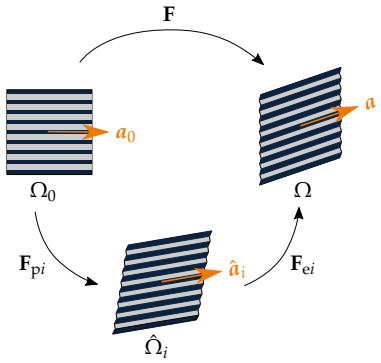

Figure 5.5 Schematic of the multiplicative decomposition of the total deformation into an elastic and plastic deformation with the corresponding configurations: *initial* (Ω_0), *intermediate* ($\hat{\Omega}_i$) and *current* configuration (Ω).

TOTAL EQUIVALENT STRESS

An initial fiber vector $\boldsymbol{a}_0$ (see Fig. 5.5) is introduced to represent transverse isotropy and its evolution is described by Eq. (5.24):

$$\boldsymbol{a} = \mathbf{F}_{ei} \cdot \hat{\boldsymbol{a}}_i = \mathbf{F}_{ei} \cdot \mathbf{F}_{pi} \cdot \boldsymbol{a}_0 = \mathbf{F} \cdot \boldsymbol{a}_0 \tag{5.31}$$

where $\boldsymbol{a}_0$, $\hat{\boldsymbol{a}}_i$ and $\boldsymbol{a}$ are the fiber vectors in the *initial*, *intermediate* and *current* configurations, respectively. Furthermore, the stress is decomposed into a plasticity-inducing $\boldsymbol{\sigma}^{\text{pind}}$ and a remaining part [26, 27]:

$$\boldsymbol{\sigma}^{\text{pind}} = \boldsymbol{\sigma} - (p\,\mathbf{I} + \sigma_f\,\bar{\mathbf{A}}) \tag{5.32}$$

where p is the pressure and σ_f is the part of the stress projected onto the fiber direction that exceeds the pressure. Furthermore, $\bar{\mathbf{A}} = \bar{\boldsymbol{a}} \otimes \bar{\boldsymbol{a}}$ is a structural tensor, with $\bar{\boldsymbol{a}} = \boldsymbol{a}/\|\boldsymbol{a}\|$ being the unit vector in the current configuration. The plasticity-inducing stress is determined as

$$\boldsymbol{\sigma}^{\text{pind}} = \mathbb{P} : \boldsymbol{\sigma} \tag{5.33}$$

where fourth-order tensor $\mathbb{P}$ is defined as

$$\mathbb{P} = \mathbb{I} - \frac{1}{2}\mathbf{I} \otimes \mathbf{I} - \frac{3}{2}\bar{\mathbf{A}} \otimes \bar{\mathbf{A}} + \frac{1}{2}\left(\bar{\mathbf{A}} \otimes \mathbf{I} - \mathbf{I} \otimes \bar{\mathbf{A}}\right) \tag{5.34}$$

with $\mathbb{I}$ the fourth-order identity tensor. The following three invariants for transverse isotropy are introduced [28]:

$$I_1 = \frac{1}{2}\,\mathrm{tr}\left[\boldsymbol{\sigma}^{\mathrm{pind}} \cdot \boldsymbol{\sigma}^{\mathrm{pind}}\right] - \bar{\boldsymbol{a}} \cdot \left[\boldsymbol{\sigma}^{\mathrm{pind}} \cdot \boldsymbol{\sigma}^{\mathrm{pind}}\right] \cdot \bar{\boldsymbol{a}} \tag{5.35}$$

$$I_2 = \bar{\boldsymbol{a}} \cdot \left[\boldsymbol{\sigma}^{\mathrm{pind}} \cdot \boldsymbol{\sigma}^{\mathrm{pind}}\right] \cdot \bar{\boldsymbol{a}} \tag{5.36}$$

$$I_3 = \mathrm{tr}\left[\boldsymbol{\sigma}\right] - \bar{\boldsymbol{a}} \cdot \boldsymbol{\sigma} \cdot \bar{\boldsymbol{a}} \tag{5.37}$$

where I_1 is associated with transverse shear, I_2 with longitudinal shear and I_3 with transverse biaxial tension/compression. The equivalent stress is defined as a function of invariants I_1 and I_2:

$$\bar{\sigma} = \sqrt{2\left(I_1 + \alpha_2 I_2\right)} \tag{5.38}$$

where α_2 is a model parameter. The third invariant is used to define p_{m} in Eq. (5.30):

$$p_{\mathrm{m}} = I_3 \tag{5.39}$$

EQUIVALENT STRESS IN EACH MODE

For defining the equivalent stress in each mode $\bar{\Sigma}_i$, a Mandel-like stress tensor [29] is introduced:

$$\boldsymbol{\Sigma}_i = \mathbf{F}_{\mathrm{e}i}^{\mathrm{T}} \cdot \boldsymbol{\sigma}_i \cdot \mathbf{F}_{\mathrm{e}i}^{-\mathrm{T}} \tag{5.40}$$

The plasticity-inducing part $\boldsymbol{\Sigma}_i^{\mathrm{pind}}$ is determined from the symmetric part of $\boldsymbol{\Sigma}_i$ through [16, 30]:

$$\boldsymbol{\Sigma}_i^{\mathrm{pind}} = \hat{\mathbb{P}}_i : \boldsymbol{\Sigma}_i^{\mathrm{sym}} \tag{5.41}$$

with fourth-order tensor $\hat{\mathbb{P}}_i$:

$$\hat{\mathbb{P}}_i = \mathbb{I} - \frac{1}{2}\mathbf{I} \otimes \mathbf{I} - \frac{3}{2}\hat{\mathbf{A}}_i \otimes \hat{\mathbf{A}}_i + \frac{1}{2}\left(\hat{\mathbf{A}}_i \otimes \mathbf{I} - \mathbf{I} \otimes \hat{\mathbf{A}}_i\right) \tag{5.42}$$

The invariants for each mode read

$$\hat{I}_{1i} = \frac{1}{2}\,\mathrm{tr}\left[\boldsymbol{\Sigma}_i^{\mathrm{pind}} \cdot \boldsymbol{\Sigma}_i^{\mathrm{pind}}\right] - \hat{\boldsymbol{a}}_i \cdot \left[\boldsymbol{\Sigma}_i^{\mathrm{pind}} \cdot \boldsymbol{\Sigma}_i^{\mathrm{pind}}\right] \cdot \hat{\boldsymbol{a}}_i \tag{5.43}$$

$$\hat{I}_{2i} = \hat{\boldsymbol{a}}_i \cdot \left[\boldsymbol{\Sigma}_i^{\mathrm{pind}} \cdot \boldsymbol{\Sigma}_i^{\mathrm{pind}}\right] \cdot \hat{\boldsymbol{a}}_i \tag{5.44}$$

and the equivalent stress $\bar{\Sigma}_i$ is defined as

$$\bar{\Sigma}_i = \sqrt{2\left(\hat{I}_{1i} + \alpha_2 \hat{I}_{2i}\right)} \tag{5.45}$$

The direction of plastic flow is described through an associated flow rule:

$$\mathbf{N}_{\mathrm{p}i} = \frac{\partial \bar{\Sigma}_i}{\partial \boldsymbol{\Sigma}_i^{\mathrm{sym}}} = \frac{1}{\bar{\Sigma}_i}\left[\frac{\partial \hat{I}_{1i}}{\partial \boldsymbol{\Sigma}_i^{\mathrm{sym}}} + \alpha_2 \frac{\partial \hat{I}_{2i}}{\partial \boldsymbol{\Sigma}_i^{\mathrm{sym}}}\right] \tag{5.46}$$

where

$$\frac{\partial \hat{I}_{1i}}{\partial \boldsymbol{\Sigma}_i^{\text{sym}}} = \left[(\mathbf{I} - \hat{\mathbf{A}}_i) \cdot \boldsymbol{\Sigma}_i^{\text{pind}} - \boldsymbol{\Sigma}_i^{\text{pind}} \cdot \hat{\mathbf{A}}_i \right] : \hat{\mathbb{P}}_i \tag{5.47}$$

$$\frac{\partial \hat{I}_{2i}}{\partial \boldsymbol{\Sigma}_i^{\text{sym}}} = \left[\hat{\mathbf{A}}_i \cdot \boldsymbol{\Sigma}_i^{\text{pind}} + \boldsymbol{\Sigma}_i^{\text{pind}} \cdot \hat{\mathbf{A}}_i \right] : \hat{\mathbb{P}}_i \tag{5.48}$$

TRANSVERSELY ISOTROPIC HYPERELASTICITY

The stress in each mode is computed with a hyperelastic model based on [31]. The stress $\boldsymbol{\sigma}_i$ is decomposed in an isotropic (iso) and a transversely isotropic part (trn):

$$\boldsymbol{\sigma}_i = \boldsymbol{\sigma}_{\text{iso},i} + \boldsymbol{\sigma}_{\text{trn},i} \tag{5.49}$$

with

$$\begin{aligned} \boldsymbol{\sigma}_{\text{iso},i} &= \frac{\mu_i}{J_{ei}} \left(\mathbf{B}_{ei} - \mathbf{I} \right) + \lambda_i (J_{ei} - 1) \mathbf{I} \\ J_{ei} \boldsymbol{\sigma}_{\text{trn},i} &= 2\beta_i (\xi_2 - 1) \mathbf{B}_{ei} + 2 \left[\alpha_i + \beta_i (\xi_{1i} - 3) + 2\gamma_i (\xi_2 - 1) \right] \boldsymbol{a} \otimes \boldsymbol{a} \\ &\quad - \alpha_i \left(\mathbf{B}_{ei} \cdot \boldsymbol{a} \otimes \boldsymbol{a} + \boldsymbol{a} \otimes \mathbf{B}_{ei} \cdot \boldsymbol{a} \right) \end{aligned} \tag{5.50}$$

where $\mathbf{B}_{ei} = \mathbf{F}_{ei} \cdot \mathbf{F}_{ei}^{\text{T}}$ is the elastic left Cauchy-Green deformation tensor, $J_{ei} = \det(\mathbf{F}_{ei})$ and ξ_{1i} and ξ_2 are given as

$$\xi_{1i} = \text{tr}\left(\mathbf{B}_{ei} \right) \tag{5.51}$$

$$\xi_2 = \boldsymbol{a} \cdot \boldsymbol{a} \tag{5.52}$$

Furthermore, $\lambda_i, \mu_i, \alpha_i, \beta_i$ and γ_i are elasticity constants that are determined from the Young moduli, shear moduli and the Poisson ratios $\{E_{1i}, E_{2i}, G_{12i}, \nu_{12i}, \nu_{23i}\}$ [32]:

$$\begin{aligned} n_i &= \frac{E_{2i}}{E_{1i}} \\ m_i &= 1 - \nu_{23i} - 2n\nu_{12i}^2 \\ \lambda_i &= E_{2i} \frac{\nu_{23i} + n_i \nu_{12i}^2}{m_i (1 + \nu_{23i})} \\ \mu_i &= \frac{E_{2i}}{2(1 + \nu_{23i})} \\ \alpha_i &= \mu_i - G_{12i} \\ \beta_i &= \frac{E_{2i} \left(\nu_{12i} + \nu_{23i}\nu_{12i} - \nu_{23i} - n\nu_{12i}^2 \right)}{4m_i (1 + \nu_{23i})} \\ \gamma_i &= \frac{E_{1i}(1 - \nu_{23i})}{8m_i} - \frac{\lambda_i + 2\mu_i}{8} + \frac{\alpha_i}{2} - \beta_i \end{aligned} \tag{5.53}$$

The implementation details and derivation of the consistent tangent modulus can be found in [16].

5.3. TIME-HOMOGENIZATION OF VISCOPLASTICITY

For accurate fatigue and fracture analyses of thermoplastic composites, it is important to take viscoplastic deformations into account. However, simulating every cycle in high-cycle fatigue, with multiple time steps per cycle, is computationally too expensive. Therefore, the concept of time-homogenization [33–37] is used to simulate a large number of cycles with a small number of time steps.

5.3.1. EFFECTIVE TIME CONCEPT

In the present model, we separate the bulk behavior, which is viscoplastic (time dependent), from the response at the overmolded interface, which is cohesive (cycle dependent). The fatigue life of thermoplastic composites, in the plasticity-controlled regime, is frequency independent [37, 38]. Therefore, the cyclic response in the bulk can be regarded as a special case of creep. When the load is kept constant, the maximum amount of viscoplastic flow develops. On the other hand, during cyclic loading, only a fraction of the period T is spent at high stress levels and therefore less viscoplastic deformations accumulate. This portion of the time can be considered an *effective time* T_{eff}.

The concept of effective time can be used to speed up the computations significantly. To this end, two time scales are introduced: (*i*) a rapidly varying *micro time* t_μ that runs during a load period T and (*ii*) a slowly varying *macro time* t_{M}. For solving the cyclic response, the problem is split into a microchronogical (t_μ) and macrochronological (t_{M}) boundary value problem. For the microchronological problem, the cyclic load is explicitly modeled. During t_μ, it is assumed that there is not enough time for viscoplastic deformations to evolve and therefore, an elastic material update, with *frozen* plastic deformation, suffices. On the other hand, during t_{M} the full viscoplastic update is necessary and the time integration of Eq. (5.26) is performed with the effective time period T_{eff}, instead of the real time T.

The effective time should incorporate the effect of the cyclic load. This can be achieved by choosing a representative state variable that measures the amount of viscoplastic flow. For the present viscoplasticity model, the equivalent plastic strain rate $\dot{\gamma}_{\text{p}}$ is used, following Ref. [37]. Subsequently, the effective time is determined such that

$$\dot{\gamma}_{\text{p,M}}\, T_{\text{eff}} = \int_T \dot{\gamma}_{\text{p},\mu} \mathrm{d}t_\mu \iff T_{\text{eff}} = \frac{\int_T \dot{\gamma}_{\text{p},\mu} \mathrm{d}t_\mu}{\dot{\gamma}_{\text{p,M}}} \tag{5.54}$$

where $\dot{\gamma}_{\text{p,M}}$ is the equivalent plastic strain rate that is computed at the maximum load during macro time steps and $\dot{\gamma}_{\text{p},\mu}$ is the equivalent plastic strain rate computed during micro time steps. Note that $\dot{\gamma}_{\text{p},\mu}$ is stored for computing T_{eff} and is not used to update the material state. For determining T_{eff}, the rate of plastic deformation

in the mode with the highest initial viscosity is computed at the end of each micro time step and integrated over the load period T. The numerical integration of the integral in Eq. (5.54) is performed with the trapezoidal rule.

Remark 5.1 Note that the effective time T_{eff} is computed for each integration point—with a different stress state—and is therefore spatially non-uniform.

5.3.2. ADAPTIVE CYCLE JUMPING

With the time-homogenization scheme, a full viscoplastic update at every micro time step is avoided, which speeds up the simulations of individual load cycles. Computational efficiency can be further improved by simulating multiple cycles at once as will be shown in the following.

The responses of the EGP material model [37] and the transversely isotropic version [16] (Sec. 5.2.2) are mostly frequency independent. This will be demonstrated in Sec. 5.3.3. Therefore, when T_{eff} is known after each micro time cycle, we can compute a ratio

$$r_{\text{eff}} = \frac{T_{\text{eff}}}{T} \tag{5.55}$$

and use this ratio to account for the effective time over multiple cycles

$$\Delta t_{\text{eff}} = r_{\text{eff}} \Delta t \tag{5.56}$$

where Δt is a time increment that spans multiple cycles and can be chosen with an adaptive stepping scheme based on global convergence rates [14] (Chapter 2, Sec. 2.4). The scheme is schematically depicted in Fig. 5.6. Since plasticity does not evolve during t_μ, the response is elastic and the first half of the explicit load cycle can be mirrored to the second half in order to reduce the number of micro time steps and enhance efficiency. Through time-homogenization and adaptive cycle jumping, multiple cycles can be simulated in a cost-efficient manner.

The time integration of Eq. (5.26) is performed with an implicit exponential map [39, 40] to retain plastic incompressibility [41]. By using the effective time increment Δt_{eff}, the deformation gradient $\mathbf{F}_{\text{p}i}$ is computed as

$$\mathbf{F}_{\text{p}i} = \exp\left(\hat{\mathbf{D}}_{\text{p}i} \Delta t_{\text{eff}}\right) \cdot \mathbf{F}^0_{\text{p}i} \tag{5.57}$$

where $\mathbf{F}^0_{\text{p}i}$ is the deformation gradient at the previous time step.

Remark 5.2 As pointed out in Ref. [37], only the magnitude of plastic deformation is homogenized over the cycle. This is accurate when the direction of plastic flow is constant during the cycle. This means that, under load reversal, when the direction

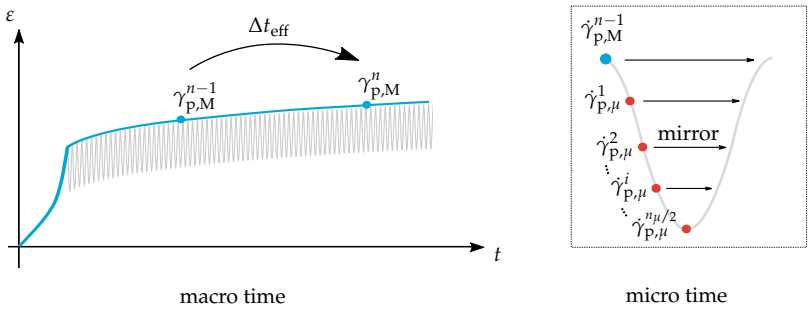

Figure 5.6 Time homogenization scheme. The material is updated at macro time (*blue* curve) with an effective time increment Δt_{eff}. The effective time increment is computed by homogenizing the equivalent plastic strain rate during micro time steps (indicated with ●).

of plastic flow generally changes, inaccuracies may occur with the present scheme. Moreover, since an elastic update is performed during micro time, yielding in the reversed loading direction does not occur, leading to very high equivalent stresses and consequently extremely high equivalent plastic strain rates at the minimum load. As a result, the effective time is unrealistically large and local convergence cannot be achieved. To remedy this, the condition is added that the equivalent plastic strain rate during micro time cannot exceed its value attained at the previous macro time step ($\dot{\gamma}_{\text{p},\mu} \leq \dot{\gamma}^{n-1}_{\text{p,M}}$). This is similar to the condition used in Ref. [37], where instead of the equivalent plastic strain rate, the viscosity was limited. By restricting the value of $\dot{\gamma}_{\text{p},\mu}$, it is ensured that the effective time Δt_{eff} does not reach unrealistic values as a result of load reversals. However, the change in sign of the plastic strain is not accounted for and consequently, the present time-homogenization scheme is only accurate under moderate load reversals.

5.3.3. VERIFICATION WITH A SINGLE ELEMENT TEST

The time-homogenization scheme is verified by comparing the fully resolved cyclic response of a single trilinear hexahedral element to its time-homogenized response. The single element, with dimensions $1 \times 1 \times 1$ mm, is subjected to an off-axis sinusoidal load with externally applied load ratio $R = 0.1$, maximum engineering stress level $\sigma_{\text{max}} = 160$ MPa and off-axis angle $\theta_0 = 30°$ (see Fig. 5.7). The maximum load is reached in 10 s, after which the cyclic loading phase starts. A 24-mode analysis is performed and the material parameters for this analysis are those from Ref. [16] (Chapter 4, Sec. 4.4). Furthermore, $n_\mu = 16$ micro time steps are simulated before each macro time step. The influence of the number of micro and macro time steps

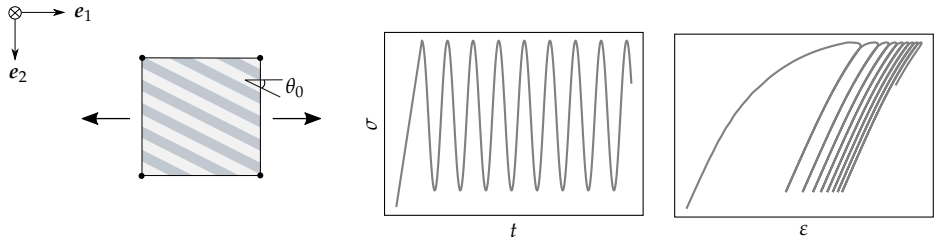

Figure 5.7 Off-axis cyclic load test of single element under $\theta_0 = 30°$. A cyclic stress is applied in the e_1-direction with load ratio $R = 0.1$.

on the response is determined at the end.

FREQUENCY INDEPENDENCE

To assess the assumption that the transversely isotropic viscoplasticity model is mostly frequency independent, three frequencies $f\,(\mathrm{Hz}) = \{0.02, 0.1, 0.5\}$ are simulated. The engineering strain-time histories are depicted in Fig. 5.8. Since the evolution of maximum and minimum strain values over time are very similar across the range of frequencies, it is confirmed that the effect of frequency on the cyclic response can be ignored, which is important because frequency is not represented in the time-homogenized material update.

COMPARISON WITH FULLY RESOLVED RESPONSE

The time-homogenized response is compared to the fully resolved response. The engineering strain-time histories are depicted in Fig. 5.9. For comparison, the creep response under constant stress ($\sigma_{\max} = 160\,\mathrm{MPa}$) is added to the diagram. It can be observed that the strain evolution at the maximum load is well captured by the time-homogenization scheme (T-H). Note that, although the history variables are only

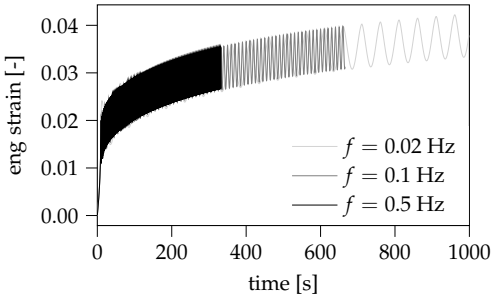

Figure 5.8 Fully resolved response with three different frequencies.

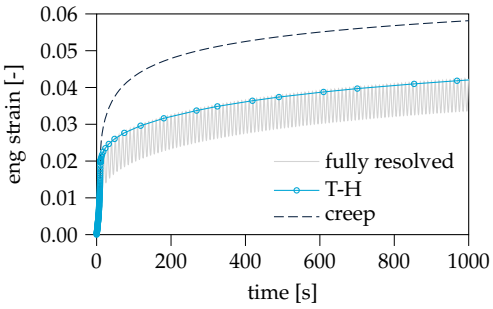

Figure 5.9 Time-homogenized response and comparison with the fully resolved and the creep response under constant engineering stress.

updated at the maximum load level, the time-homogenization scheme accurately accounts for the cyclic variation of the load through the calculation of Δt_{eff} to perform the time integration. Instead, without the time-homogenization scheme (*i.e.* $\Delta t_{\text{eff}} = \Delta t$), a creep response is obtained and the cyclic load is not accounted for. Under creep, more time is spent at high stress levels, hence more viscoplastic deformations develop in comparison to the cyclic loading case. Furthermore, the fully resolved analysis with frequency $f = 0.1$ Hz reached 1000s with a total of 4434 time steps during the cyclic load phase. With the time-homogenization scheme, only 35 macro time steps were required and for each macro time step, 16 micro time steps (with elastic material behavior) were simulated. The present analyses demonstrate that the two-scale time homogenization scheme significantly increases efficiency while retaining high accuracy. This approach enables high-cycle fatigue analysis with the transversely isotropic viscoplasticity model, which was otherwise infeasible in more complex cases with non-uniform stress fields.

MICRO AND MACRO TIME-STEP DEPENDENCE

The influence of the number of micro time steps n_μ on the accuracy of the time-homogenization scheme is assessed by comparing the simulation results obtained with $n_\mu = \{8, 16, 32\}$. The strain-time response is presented in Fig. 5.10. It can be observed that for $n_\mu = 16$ and $n_\mu = 32$ the response does not change, whereas for $n_\mu = 8$ inaccurate results are obtained. Therefore, 16 micro time steps are indeed sufficient to capture the evolution of the maximum strain during the cyclic load.

Next, macro time-step dependence is assessed. The viscoplasticity model with implicit exponential map of the deformation gradient update exhibits negligible time step dependence [16] (Chapter 4, Fig. 4.16). Due to the explicit nature of the time-homogenization scheme under cyclic loads, time-step dependence needs

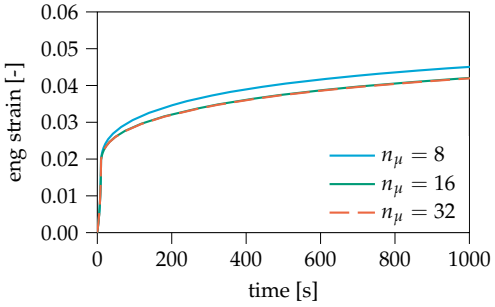

Figure 5.10 Time-homogenized response with three different numbers of micro time steps n_μ.

to be reassessed. For this purpose, the analysis is repeated with the time step size restricted to $\Delta t_{\max}\,(\mathrm{s}) = \{5, 20\}$. The results are shown in Fig. 5.11, along with those obtained with adaptive stepping where the increment was increased up to $\Delta t = 152\,\mathrm{s}$. Since the stress-strain curves overlap, it is concluded that time-step dependence with the two-scale transversely isotropic viscoplasticity model is negligible.

5.4. ANALYSIS OF THE RIB-PULL OFF TEST

The numerical framework is applied to the simulation of a T-section cut from an overmolded rib-stiffened panel. The effect of two typical processing effects on the short- and long-term mechanical performance of the interface are numerically investigated: local fiber protrusions of the laminate into the rib that occur during thermoforming and non-uniform healing as a result of varying thermal histories along the interface. The modeling approach is discussed in this section and the results under static and cyclic loading are presented in Sec. 5.5.

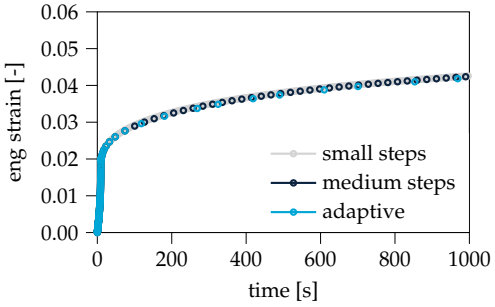

Figure 5.11 Time-homogenized response with three different macro time step sizes.

5.4.1. PROCESSING-INDUCED GEOMETRY

We consider an overmolded specimen, made of carbon fiber thermoplastic (CF/PEEK) composite and with laminate lay-up $\left[90/0\right]_{10s}$. The laminate, with a total of 20 plies, has a width of 20 mm and the thickness is 2.50 mm. The rib has a length of 18 mm. The width of the rib is 3 mm at the base and reduces to 2 mm at the top. Furthermore, the radius of the rib foot is 0.5 mm.

In this work, we model the laminate with a mesoscopic approach, where each ply is modeled and the local orientation of the fiber direction, due to process-induced wrinkles, is taken into account. Manually meshing a processing-induced deformed geometry is a tedious task. In addition, the fiber vector field needs to be conforming with the final mesh. To obtain a representative shape of the geometry after processing, a practical engineering approach is followed. Prior to mechanical simulation, a "pseudo processing step" is performed to obtain a deformed mesh. For the pseudo processing step, special boundary conditions are used in combination with artificial material properties. The boundary conditions, depicted in Fig. 5.12, are applied to obtain a local wrinkle. Furthermore, plane strain conditions are assumed and symmetry is taken into account by modeling only half of the specimen. To drive the deformation, a distributed load q is applied over a width of $x_0 = 0.75$ mm. The load is progressively increased until the protrusion height p is equal to 0.5 mm, measured at the center of the rib (see Fig. 5.13). In addition, the material properties, tabulated in Tab. 5.1, are elastic with artificial values. These values are found by trial and error, with the aim to make sure that the 0° plies do not change thickness and have a smooth curvature, while most of the deformation takes place in the 90° plies, similar to what is observed in experiments [7].

Since a finite strain framework is used, the deformed mesh and fiber vector field at the end of the pseudo processing steps are conforming and can be used in the subsequent mechanical loading step. After the processing step, the mesh and vector field are written to a file and subsequently read prior to the mechanical simulation. The resulting mesh with the pseudo processing step and the initial (undeformed)

Table 5.1 Artificial elasticity parameters for pseudo processing step.

	0°-plies	**90°-plies**	**rib**
E_1	55 GPa	55 GPa	0.55 GPa
E_2	7.4 GPa	0.5 GPa	0.074 GPa
G_{12}	480 GPa	480 GPa	0.048 GPa
ν_{12}	0.016	0.016	0.016
ν_{23}	0.24	0.24	0.24

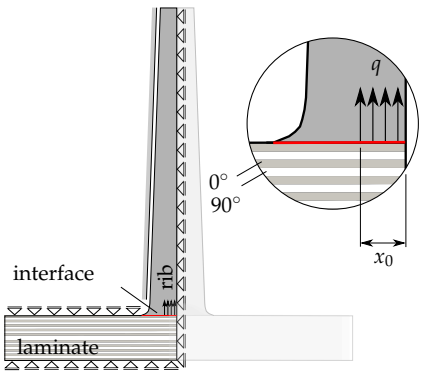

Figure 5.12 Computational model of pseudo processing step.

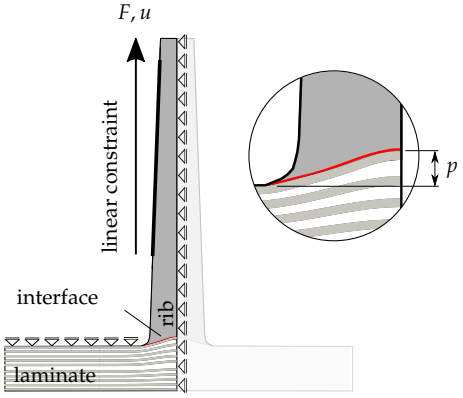

Figure 5.13 Computational model of the mechanical test.

mesh are shown in Fig. 5.14.

Obviously, the pseudo processing step is artificial. In a processing-performance chain of models, it can be replaced by a realistic processing step, where first the laminate is heated, formed and solidified. Simulating these steps requires a sophisticated thermomechanical analysis. Such a processing step has been presented in Ref. [42], where the laminate is simulated in a homogenized sense to improve efficiency. Due to the homogenized assumption, important mesoscopic information for failure analyses (as will be shown later in this chapter), such as the local fiber orientation, is not accounted for. In the absence of a detailed processing step, our approach is a convenient method to obtain a processing-induced deformed mesh and corresponding fiber vector field as a result of thermoforming, enabling the study of the effects of a deformed geometry on the mechanical performance.

5.4.2. COMPUTATIONAL MODEL FOR THE MECHANICAL TEST

The computational model for the mechanical pull-off test is shown in Fig. 5.13. To model the steel tabs that grip the rib during a pull-off test, a linear constraint is applied along the rib edge, starting at a distance of 3 mm above the base of the rib. With the constraint equation, a force-controlled fatigue analysis can be performed. Furthermore, a rib-guard constrains the specimen when the load is applied, which is accounted for by applying homogeneous Dirichlet boundary conditions along the

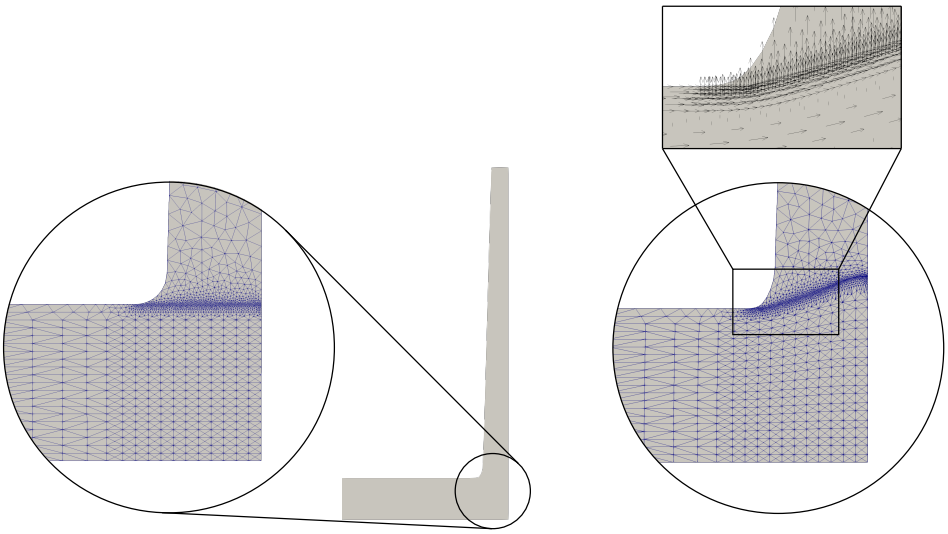

Figure 5.14 Meshes used for studying the effects of processing on the geometry of the T-section. Flat geometry (*left*) vs. processing-induced geometry with ply-aligned fiber direction field (*right*).

top edge of the laminate.

5.4.3. HEALING PROFILE ALONG THE INTERFACE

The degree of healing along the interface is a function of the thermal history [1, 2]. In Ref. [7], it is mentioned that the healing values near the edges of the rib are close to zero, because of the thermal boundary conditions: the temperature of the mold tool is relatively low to allow for rapid manufacturing cycles, which leads to less interdiffusion of polymer chains across the interface and thus lower levels of healing near the edges. The degree of healing, can be represented with a healing index $\mathcal{D}_\mathrm{h}$, ranging from 0 (no healing) to 1 (fully healed).

In this work, two simplified healing profiles, denoted as "healing A" and "healing B" (see Fig. 5.15), are examined for studying the effect of healing on the mechanical response. Following Ref. [7], the fracture properties for the cohesive zone model for mode $X \in \{\mathrm{I}, \mathrm{II}\}$ are adjusted from the pristine properties $(\cdot)^\infty$ with the healing $\mathcal{D}_\mathrm{h}$ as

$$f_X = \mathcal{D}_\mathrm{h} f_X^\infty \tag{5.58}$$

$$G_{X\mathrm{c}} = \mathcal{D}_\mathrm{h}^2 G_{X\mathrm{c}}^\infty \tag{5.59}$$

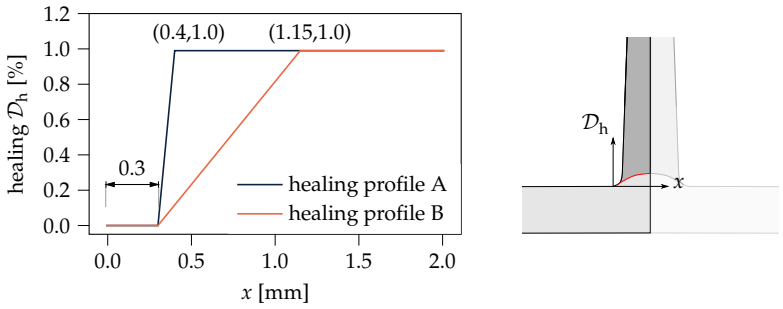

Figure 5.15 Different healing profiles along the overmolded interface. A pre-crack of 0.3 mm is assumed at the edges by assigning zero healing.

5.4.4. LOCAL STRESS RATIO

The fatigue cohesive zone model depends on the number of cycles that elapse and accounts for the local stress ratio through the endurance limit calculation (Eq. (5.19)). When the response is nonlinear, the local stress ratio is not equal to the global load ratio [15, 43]. Therefore, at macro time steps, when fatigue damage is computed, R must be known.

To retrieve the local stress ratio, the maximum and minimum tractions are monitored during micro time steps. The local stress ratio is computed from the *severity vector* $\mathbf{S} = \left[t_n/f_n, t_{sh}/f_{sh}\right]^T$ [44]:

$$R = \frac{\mathbf{S}_{min} \cdot \mathbf{S}_{max}}{\|\mathbf{S}_{max}\|^2} \tag{5.60}$$

where the components of $\mathbf{S}$ are functions of the traction components (t_n and t_{sh}), and the pure-mode strengths (f_n and f_{sh}). After each micro time cycle, the local stress ratio is used to compute fatigue damage at macro time steps through Eq. (5.19).

5.4.5. MATERIAL PARAMETERS

The laminate is modeled with the transversely isotropic viscoplasticity model presented in Sec. 5.2.2 using a single mode for simplicity and more efficient analyses, whereas the rib is considered purely elastic and follows the constitutive equations from Sec. 5.2.2 without plastic deformations ($\mathbf{F} = \mathbf{F}_e$). The overmolded interface is described with the fatigue cohesive zone model outlined in Sec. 5.2.1. The pristine (fully healed) and fatigue cohesive interface properties, the elastic constants of the rib and the laminate viscoplasticity parameters are tabulated in Tab. 5.2.

Table 5.2 Material parameters of the T-section.

rib		laminate				interface			
elastic		elastic		viscoplastic		fracture		fatigue	
E_1	46 GPa [7]	E_1	134 GPa [7]	μ_P	0.053 [16]	f_n^∞	120 MPa [7]	η	0.95 [18]
E_2	9 GPa [7]	E_2	10 GPa [7]	σ_0	1.71 MPa [16]	f_{sh}^∞	95 MPa [7]	ϵ	0.2 [18]
G_{12}	4.3 GPa [7]	G_{12}	5.2 GPa [7]	η_0	5.90×10^{29} MPa s [16]	G_{Ic}^∞	2.0 N mm^{-1} [7]	p	β [18]
ν_{12}	0.086	ν_{12}	0.016	α_2	1.147 [16]	G_{IIc}^∞	4.0 N mm^{-1} [7]		
ν_{23}	0.4	ν_{23}	0.24			η_{BK}	2.284		

5.5. RESULTS

In this section, the pull-off test as described in Sec. 5.4 is simulated. The effect of different healing profiles, processing-induced laminate geometries, viscoplastic deformations and boundary conditions are examined under static and cyclic loading.

5.5.1. ANALYSIS UNDER STATIC LOADING

Firstly, a static analysis is performed. A constant cross-head displacement rate is applied via the grips and the load per unit length is computed from the reaction force.

EFFECTS OF VISCOPLASTIC DEFORMATIONS

The effect of viscoplasticity under static loading is shown in Fig. 5.16, where the force-displacement response is compared to the response without viscoplasticity, with both healing profiles A and B (see Fig. 5.15). The viscoplastic analyses are performed with displacement rates $\dot{u} = 10^{-3}$ mm s^{-1} and 10^{-5} mm s^{-1}. The crosses in the diagrams indicate mechanical instability: the amount of energy that is released

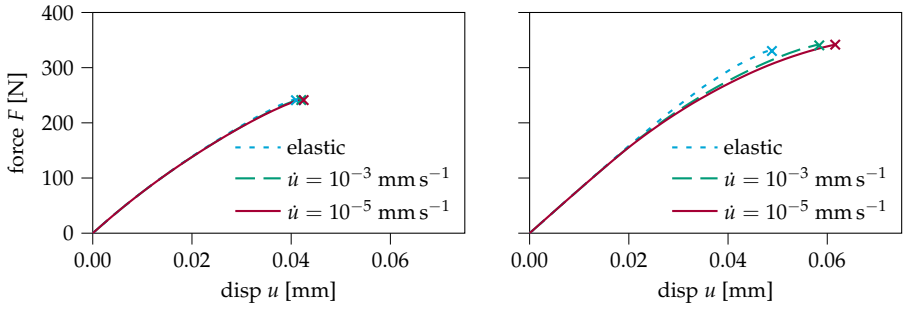

Figure 5.16 Force-displacement curves: effect of viscoplasticity on the static response with healing profile B (*left*) and healing profile A (*right*).

exceeds the amount that is necessary for crack growth, hence the equilibrium path is unstable and cannot be traced in a displacement controlled quasi-static analysis. As can be observed, the effect of viscoplasticity is minimal in the case of healing profile B. However, with improved degrees of healing (healing profile A), the effect of viscoplastic deformations becomes more pronounced. Moreover, when the displacement rate is reduced, there is more time for viscoplastic deformations to accumulate, hence ductility increases and the peak load is delayed.

With a lower degree of healing, the capacity is reduced and fracture in the overmolded interface occurs at lower equivalent stress levels. This is depicted in Fig. 5.17, where the force-displacement diagrams and the equivalent stress contours on deformed meshes are shown with both healing profiles A and B, under displacement rate $\dot{u} = 10^{-3}\,\mathrm{mm\,s^{-1}}$. As expected, with lower degrees of healing, the capacity of the specimen under tensile loading decreases and the equivalent stress is reduced in the laminate and near the crack at the overmolded interface. As a result, viscoplastic deformations play almost no role with low degrees of healing, whereas with improved degrees of healing, stress levels increase and more viscoplastic deformations accumulate.

In the cases studied in Ref. [7], healing was never fully reached. However, recently another material system was studied in Ref. [6] and better degrees of healing were observed, leading to a more progressive fracture process during the pull-off test. As shown in this study, under improved levels of healing, viscoplastic deformations become more important to consider. With the aim of optimizing manufacturing process parameters and performance of overmolded composite parts, it is relevant to account for viscoplastic deformations for establishing processing-performance relations through numerical simulations.

EFFECT OF PROCESSING-INDUCED GEOMETRY

The effect of the processing-induced geometry on the static response is studied with both degrees of healing A and B and displacement rate $\dot{u} = 10^{-3}\,\mathrm{mm\,s^{-1}}$. For this purpose, three modeling assumptions regarding the interface geometry are compared: a flat geometry "geometry F", a deformed geometry with initial fiber vector field "geometry D" and a deformed geometry with updated fiber vector field "geometry D^+" (see Fig. 5.18).

The force-displacement curves, corresponding to the three geometries, are shown in Fig. 5.19. It can be observed that stiffness and capacity of the T-section are larger when the processing-induced geometry is taken into account. As expected and in accordance with Refs. [2, 7], fiber protrusions (geometry D and D^+) improve the strength of the bond due to the curved interface geometry. In addition, the

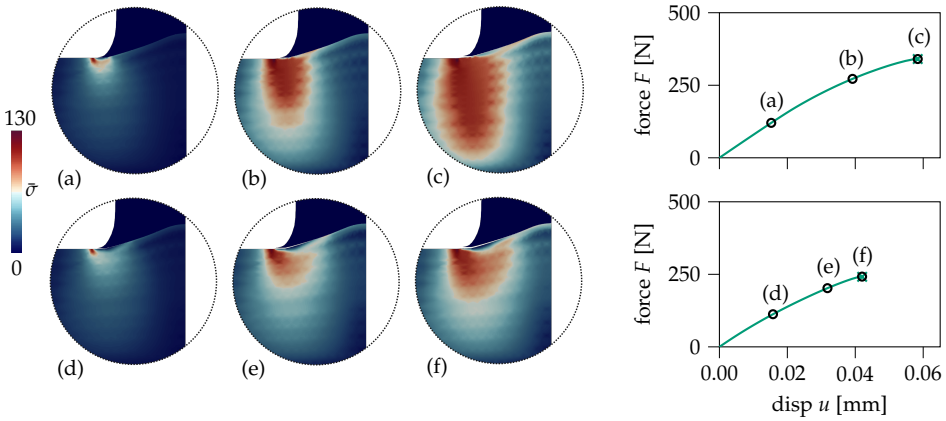

Figure 5.17 Evolution of equivalent stress and corresponding force-displacement curves with healing A (*top*) and healing B (*bottom*) at indicated time steps and with displacement rate $\dot{u} = 10^{-3}\,\mathrm{mm\,s^{-1}}$.

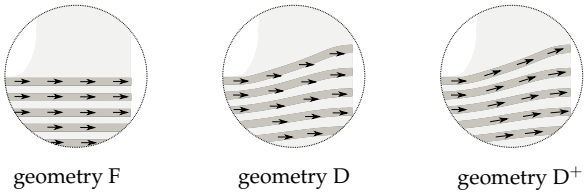

Figure 5.18 Three types of laminate geometries are studied: flat geometry (geometry F), deformed geometry with initial fiber vector field (geometry D) and deformed geometry with updated fiber vector field (geometry D$^+$).

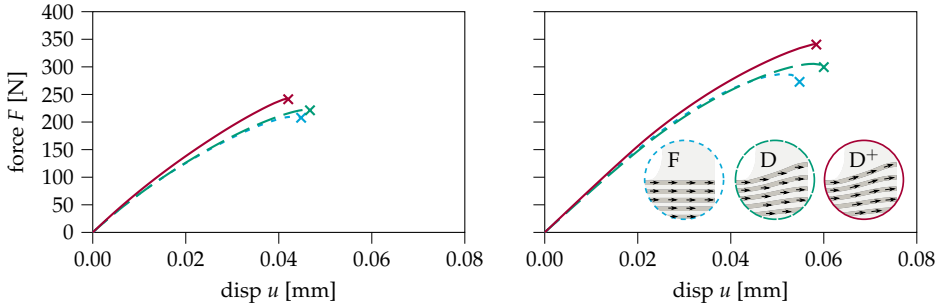

Figure 5.19 Force-displacement curves with displacement rate $\dot{u} = 10^{-3}\,\mathrm{mm\,s^{-1}}$: effect of protruded fibers with healing profile B (*left*) and with healing profile A (*right*).

present analyses demonstrate that accounting for the ply-aligned fiber directions has a significant effect on the strength and stiffness (*cf.* geometry D and geometry D^+).

In previous numerical studies of pull-off testing [7], the laminate was considered a homogeneous medium with a fiber vector field that is aligned with the *undeformed* laminate. This study shows that it is important to take into account the actual fiber direction in the ply, which is captured by the present ply-by-ply mesoscopic analysis.

EFFECT OF BOUNDARY CONDITIONS

Due to the boundary conditions in the test set-up (see Fig. 5.13), the laminate is able to bend. To investigate this effect, the analysis is repeated with different boundary conditions. In addition to the standard test set-up studied until now, the laminate is assumed to be fixed (glued) at the bottom, as previously suggested in [11] to prevent bending to occur (see Fig. 5.20). The force-displacement curves, corresponding to the standard and the glued boundary conditions, are shown in Fig. 5.21. It can be observed that the boundary conditions mainly affect the stiffness, whereas the strength is very similar among the analyses. In addition, the response is less brittle in the glued case since there is less elastic energy stored that is released during fracture.

5.5.2. ANALYSIS UNDER CYCLIC LOADING

For the cyclic load case, a maximum load level $F_{\max}$ is applied in 10 s, after which a sinusoidal cyclic load with frequency $f = 1$ Hz and load ratio $R = {}^{F_{\min}}/_{F_{\max}} = 0.1$ is maintained (see Fig. 5.22). The analysis is performed with the time-homogenization scheme presented in Sec. 5.3. Results from the micro time steps are used to compute not only T_{eff} for the viscoplasticity model, but also the local stress ratio R (Sec. 5.4.4) for the fatigue damage model. For analyzing the cyclic response, the displacement

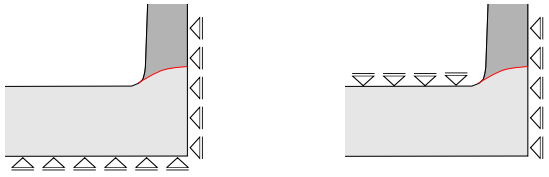

Figure 5.20 Sketch of two types of boundary conditions: glued (*left*) vs standard (*right*) test set-up for characterizing interface performance.

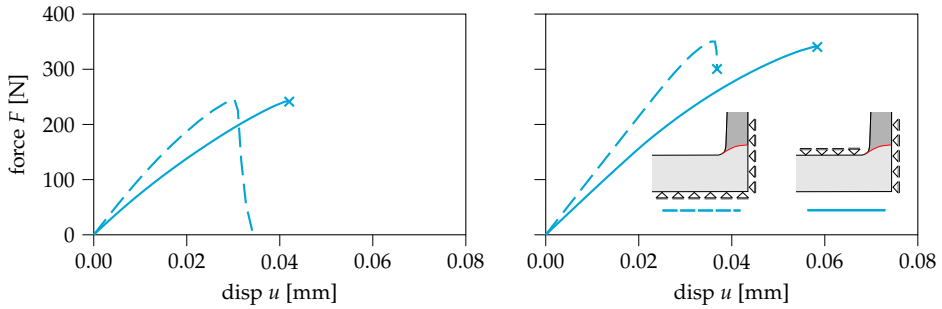

Figure 5.21 Force-displacement curves with displacement rate $\dot{u} = 10^{-3}\,\mathrm{mm\,s^{-1}}$: effect of boundary conditions with healing profile B (*left*) and with healing profile A (*right*).

$u_{\max}$ at the maximum load is recorded. The displacement rate in macro time $\dot{u}_{\max}$ is also analyzed. Even though this time-homogenized rate does not represent the actual displacement rate in the cyclic experiment, inspecting $\dot{u}_{\max}$ gives clear insight in the evolution of deformations during the simulation.

EFFECT OF VISCOPLASTICITY

The effects of viscoplasticity in the laminate on the cyclic response is studied. A force-controlled analysis is first performed with low degree of healing (healing profile B) and with various maximum load levels $F_{\max}\,(\mathrm{N}) \in \{140, 160, 180, 200\}$. The evolutions of the displacement and displacement-rate—at the maximum value of the cyclic load—are shown in Fig. 5.23. Similar to the static analysis, viscoplastic deformations have a minimal effect on the response with healing profile B. With low levels of healing, the capacity under static loading drops significantly (see Fig. 5.16). Since the load level in the cyclic test is below the static capacity, fracture occurs before the stresses are large enough to produce significant viscoplastic deformations.

To investigate the effect of the healing profile, the analysis is repeated with

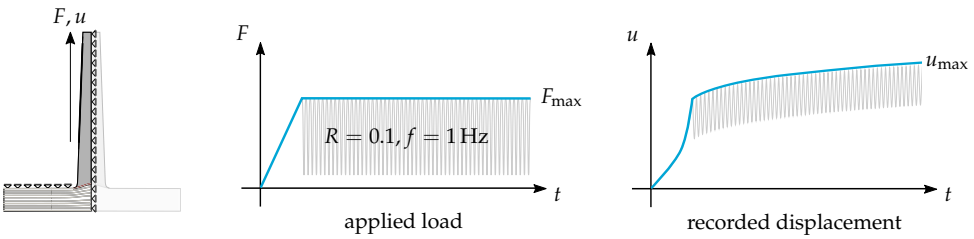

Figure 5.22 Analysis under cyclic loading. The maximum load $F_{\max}$ is applied during macro time and the maximum displacement $u_{\max}$ is recorded.

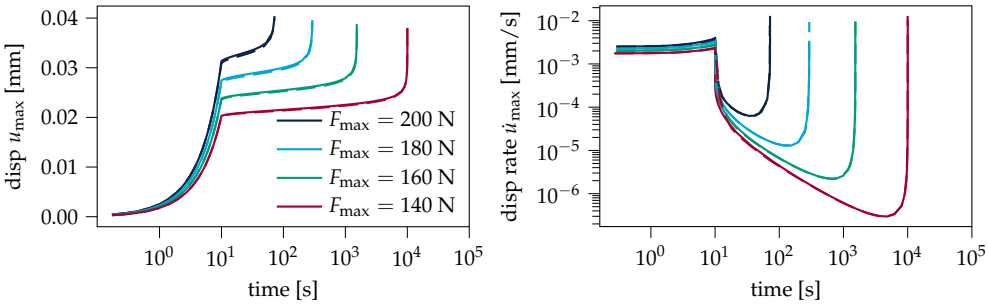

Figure 5.23 Response under cyclic load with viscoplasticity (*solid lines*) and without viscoplasticity (*dashed lines*) with healing profile B: displacement history (*left*) and displacement rate history (*right*) at the maximum values of the load.

improved healing (healing profile A) and maximum stress levels $F_{max}\,(\mathrm{N}) \in \{210, 230, 250, 285\}$, see Fig. 5.24. With the higher degree of healing, there is an effect of the viscoplastic deformations, which increases with the applied load level: at increased load levels, stresses are higher and consequently, more viscoplastic deformations develop. As a result, the time-to-failure, which can be identified as the moment when the displacement-rate sharply increases, is delayed (see Fig. 5.24, *right*).

Apart from the fact that viscoplastic deformations accumulate and interact with crack growth in the overmolded interface, under cyclic loading, viscoplastic deformations also alter the local stress ratio along the interface. To isolate the effects of the local stress ratio, the analysis with $F_{max} = 285\,\mathrm{N}$ is repeated, but this time with the stress ratio in each integration point set equal to the global load ratio. The displacement histories are shown in Fig. 5.25 on the left. It can be observed that the viscoplastic deformations have a pronounced effect on the response, while the effect of the local stress ratio is very limited. The local stress ratio history is shown on the right of Fig. 5.25 for all time steps. Although the local stress ratio is non-uniform, on average it is not much different from the global load ratio, explaining the negligible effect on the fatigue response.

To investigate the effect of the loading type, a displacement controlled analysis is performed, with displacement ratio $R_{disp} = u_{min}/u_{max} = 0.1$, applied maximum displacement $u_{max} = 0.04\,\mathrm{mm}$ and healing profile A. The force histories and local stress ratio along the interface are shown in Fig. 5.26. It can be observed that under displacement control, the corresponding reaction force at the beginning of the cyclic loading phase is slightly lower in the presence of viscoplastic deformations. Consequently under lower stress levels, the time-to-failure is increased. In addition, the

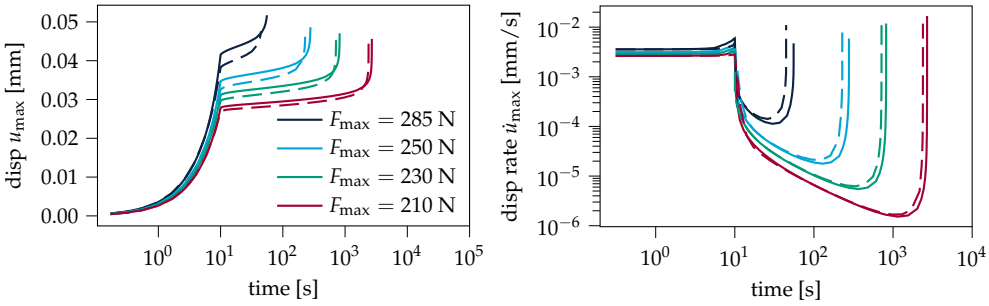

Figure 5.24 Response under cyclic load with viscoplasticity (*solid lines*) and without viscoplasticity (*dashed line*) with healing profile A: displacement history (*left*) and displacement rate history (*right*) at the maximum values of the load.

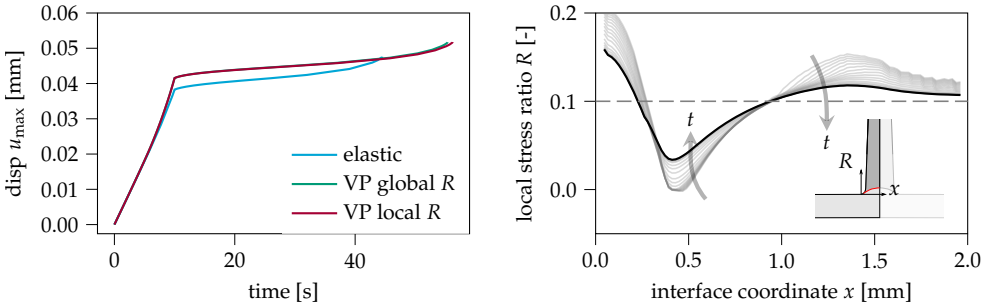

Figure 5.25 Effect of viscoplasticity and local stress ratio under force-control with healing profile A and $F_{max} = 285\,\text{N}$: displacement-time histories (*left*) and corresponding local stress ratio history with viscoplasticity (*right*). The global load ratio is indicated with a dashed line and each gray line corresponds to a different time step. The last time step is indicated with the black line.

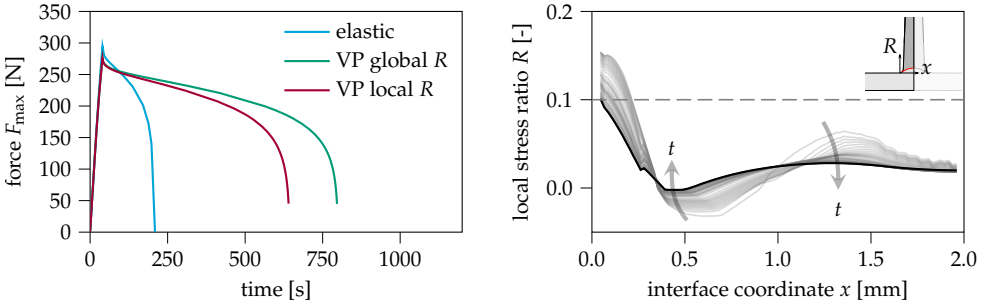

Figure 5.26 Effect of viscoplasticity and local stress ratio under displacement-control with healing profile A and $u_{max} = 0.04\,\text{mm}$: force-time histories (*left*) and corresponding local stress ratio history with viscoplasticity (*right*). The global displacement ratio is indicated with a dashed line and each gray line corresponds to a different time step. The last time step is indicated with the black line.

local stress ratio along the profile of the interface is lower than the global displacement ratio. The lower stress ratio results in faster fatigue damage accumulation and thus a decrease in fatigue life in comparison to the case where the stress ratio is chosen equal to the displacement ratio.

The analysis with healing profile A is repeated with various applied maximum displacements $u_{\max}\,(\mathrm{mm}) \in \{0.025, 0.030, 0.035, 0.040\}$ and the time-to-failure for each applied $u_{\max}$ is shown in Fig. 5.27. From this figure, it is confirmed that viscoplastic deformations are more significant in the low cycle regime and almost negligible in the high-cycle regime. In addition, the time-to-failure curves with the local stress ratio simulations are shifted horizontally towards lower fatigue lives with respect to the curves obtained with a global load ratio.

This study indicates that with lower levels of healing (healing profile B in Fig. 5.15), viscoplastic deformations have a limited effect on the response of the cyclic pull-off test. However, with improved healing of the interface (healing profile A in Fig. 5.15), it is important to consider the effects of viscoplastic deformations, mainly in the low cycle regime where the stresses are higher. Therefore, viscoplasticity may be relevant to consider for establishing processing-performance relations to optimize product designs and processing parameters. In addition, it may be important to consider the local stress ratio in the pull-off analyses, particularly in displacement-controlled settings where the local stress ratio and global displacement ratio are not equal. The framework with time-homogenized viscoplasticity with the ability to capture the local stress ratio is suitable for simulating these effects.

EFFECT OF PROCESSING-INDUCED GEOMETRY

The cyclic response with the three geometries depicted in Fig. 5.18 is assessed. For this purpose, the lower degree of healing (healing profile B) is used with maximum

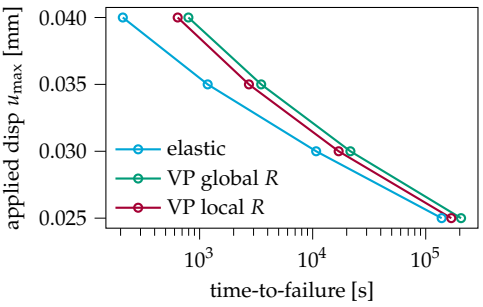

Figure 5.27 Time-to-failure under displacement controlled cyclic loading ($R_{\mathrm{disp}} = 0.1$, $f = 1\,\mathrm{Hz}$) with various applied maximum displacements: effect of viscoplasticity and local stress ratio.

load level $F_{max} = 160\,\text{N}$. The displacement and displacement-rate histories are shown in Fig. 5.28. It can be observed that the effect of modeling the mesoscopic geometry—as a result of processing—on the fatigue life is significant. However, similar to what was observed under static loading (see Fig. 5.19), modeling the protruded interface geometry is not enough, it is also important to account for the alignment of the fibers with the deformed plies, which more than doubles the time-to-failure (*cf.* the response obtained with geometry D and geometry D^+ in Fig. 5.28). The analysis is repeated with various load levels and with both healing profiles A and B. The applied maximum load is plotted against the corresponding time-to-failure in Fig. 5.29. This figure shows that for both healing profiles across all load levels, modeling the ply-aligned fibers is important.

EFFECT OF BOUNDARY CONDITIONS

The effect of the boundary conditions on the cyclic response is studied. The analyses with both healing profiles A and B are repeated, but this time the base plate is glued at the bottom (see Fig. 5.20).

The displacement histories with both types of boundary conditions, healing profile A and maximum load $F_{max} = 250\,\text{N}$, are depicted in Fig. 5.30. It can be observed that the boundary conditions have a strong effect on the cyclic response: the time-to-failure is increased with approximately 71% when bending is prevented. Fig. 5.31 shows the time-to-failure for each load level with both healing profiles, from which it can be observed that the glued test set-up results in a horizontal shift in the time-to-failure across all stress levels. Under lower degrees of healing (healing profile B) the effect is less significant than under improved healing (healing profile A).

This study demonstrates that the time-to-failure obtained from the pull-off test

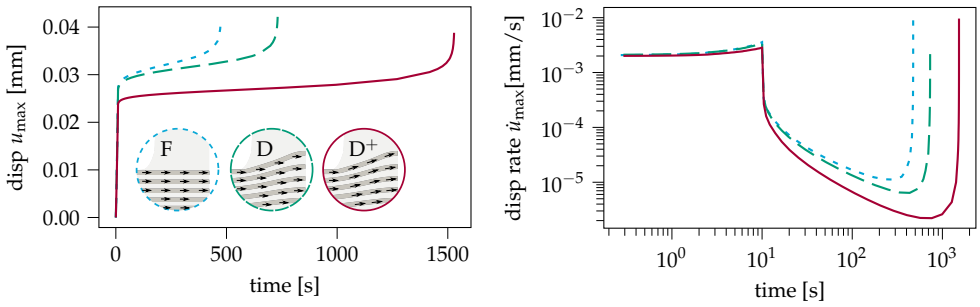

Figure 5.28 Cyclic response with different interface geometries F, D, and D^+: displacement histories (*left*) and displacement-rate histories (*right*) with healing profile B and maximum load $F_{max} = 160\,\text{N}$.

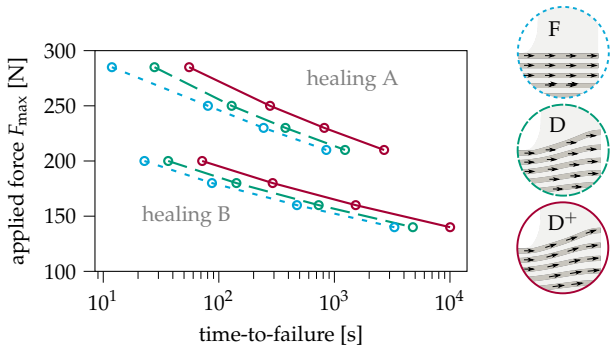

Figure 5.29 Time-to-failure under force controlled cyclic loading ($R = 0.1$, $f = 1\,\text{Hz}$) with various applied maximum load levels: effect of modeling the protruded fibers with healing profiles A and B.

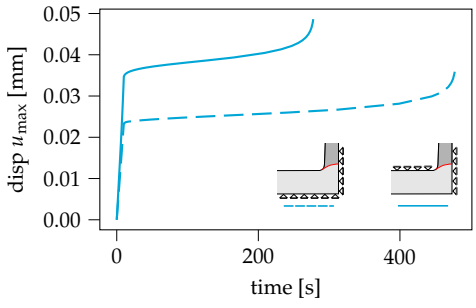

Figure 5.30 Displacement-time history: effect of boundary conditions on the cyclic response with healing profile A and $F_{max} = 250\,\text{N}$.

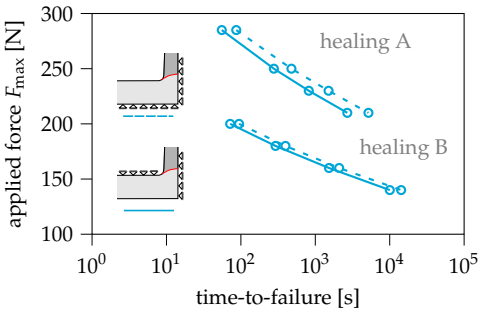

Figure 5.31 Time-to-failure under force controlled cyclic loading ($R = 0.1$, $f = 1\,\text{Hz}$) at various load levels and healing profiles A and B: effect of different boundary conditions.

depends on the test set-up, indicating that S-N curves obtained from pull-off tests do not characterize the interface response under cyclic loads and cannot be used directly as material input in macroscopic failure analyses.

TIME-STEP DEPENDENCE

To assess the time-step dependence of the numerical framework, the analyses with maximum load levels $F_{\max} = 210\,\mathrm{N}$ and $285\,\mathrm{N}$ and healing profile A, are repeated with a very large number of time steps. This is achieved by restricting the maximum allowed time step increment: $\Delta t_{\max} = 1\,\mathrm{s}$. The displacement rate histories are shown in Fig. 5.32 and compared to the ones with the adaptive stepping scheme from Fig. 5.24. It can be observed that time-step dependence is negligible. With the adaptive stepping scheme, the time-homogenized micro-macro analyses with $F_{\max} = 210\,\mathrm{N}$ and $285\,\mathrm{N}$ are performed with only 17 and 36 macro time steps during the cyclic loading phase, corresponding to 45 and 2682 cycles, respectively. Note that simulating every cycle individually, with 16 micro time steps per cycle, would require 720 and 42912 time steps. The present analyses demonstrate that the numerical framework with time-homogenized viscoplasticity and cycle-dependent cohesive fracture allows for efficient simulations of high-cycle fatigue.

5.6. CONCLUSION

A previously developed numerical framework for simulating fracture and fatigue in composite laminates [14, 15] (Chapters 2 and 3) has been extended to numerically investigate the effects of processing on the mechanical performance of overmolded thermoplastic composites. The framework consists of a time-homogenization scheme to efficiently account for the accumulation of viscoplastic deformations during fatigue cycles. A two-scale version of a recently developed transversely isotropic viscoplasticity model for thermoplastic composites [16] (Chapter 4) has been derived. Furthermore, fatigue at the overmolded interface is modeled with a cycle-dependent cohesive zone model that takes into account the local stress ratio, which is computed during the analyses.

The numerical framework is applied to the static and cyclic analysis of a T-section cut from an overmolded panel. Two typical processing effects are studied: mesoscopic deformations as a result of thermoforming and non-uniform healing due to varying local thermal histories along the interface. To obtain a processing-induced deformed mesh, an engineering approach is proposed by applying special boundary conditions in combination with artificial material properties to generate a mesh with local wrinkles in the laminate. The resulting deformed mesh and fiber vector field are subsequently used to study the effect of the processing-induced

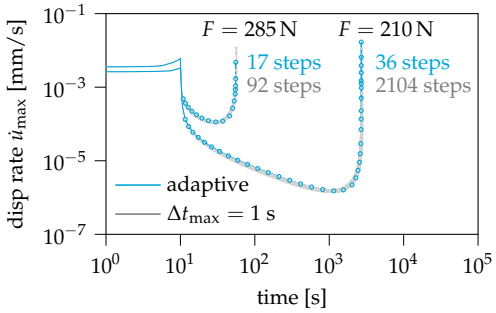

Figure 5.32 Strain-rate histories with two different load levels and step sizes: adaptive stepping vs small time steps ($\Delta t_{\max} = 1\,\mathrm{s}$). The markers in the plot indicate macro time steps during the cyclic loading phase.

geometry on the mechanical performance. The analyses provide the following insights:

- **The process-induced geometry of the interface leads to a better performance**. Besides the curved geometry, it is also important to account for the fiber vector field that is conforming with the plies, which leads to a higher stiffness and capacity under static loading, and longer fatigue life under cyclic loading. This is captured with the presented ply-by-ply modeling approach where the local non-uniform fiber orientation is taken into account. Therefore, for assessing mechanical performance of the overmolded interface, processing simulations should not only predict the macroscopic geometry, but also provide information on the local fiber orientation. A thickness-homogenized approach for predicting processing effects may not be sufficient for accurate performance assessment, since information is lost about the local fiber orientation.

- **Viscoplasticity affects the strength and fatigue life of overmolded specimens**. With poor healing, the viscoplastic effect is minimal, whereas with good healing, the effect becomes more pronounced. Therefore, for establishing processing-performance relations to optimize processing and product designs, accounting for viscoplastic deformations becomes relevant when a high interface performance is reached. The time-homogenized framework with the two-scale viscoplasticity model is able to account for these viscoplastic deformations under cyclic loading.

- **Viscoplastic deformations alter the local stress ratio**. Under force-controlled

loading, the viscoplastic effect is negligible since the local stress ratio on average is close to the global load ratio. However, under displacement-control, the local stress ratio must be accounted for since it cannot be assumed to be equal to the global displacement ratio in the presence of viscoplastic deformations. The macro-micro loading scheme, where the local stress ratio is computed during the analysis, is able to capture this effect.

- **The boundary conditions have a pronounced effect on the response**. Due to the test set-up, the laminate bends, which affects the mechanical response. The effect of gluing the base plate to a support plate on the bottom for characterizing static strength [11], is investigated under both static and cyclic loading. Under static loading, the effect on the strength is negligible. However, under cyclic loading, the fatigue life is strongly affected by the boundary conditions. Therefore, fatigue properties such as global S-N curves, obtained with the rib pull-off test, cannot be regarded as material properties and directly used as input in macroscopic performance predictions of rib-stiffened overmolded panels.

The development of the numerical framework contributes towards a better understanding of processing effects in overmolded composites. The present studies provided relevant insights, although experimental validation is necessary, especially for fatigue loading, which is currently not available in literature. Furthermore, improvements regarding subcritical intra- and inter-laminar damage, viscoplastic deformations in the short-fiber ribs, accounting for the effects of residual stresses and a more accurate description of the healing profile along the interface are recommended as improvements to the current framework.

REFERENCES

[1] M. A. Valverde, R. Kupfer, L. F. Kawashita, M. Gude, S. R. Hallett, Effect of processing parameters on quality and strength in thermoplastic composite injection overmoulded components, in: 18th European Conference on Composite Materials, Applied Mechanics Laboratory, 2018.

[2] R. Akkerman, M. Bouwman, S. Wijskamp, Analysis of the thermoplastic composite overmolding process: Interface strength, *Frontiers in Materials* 7 (2020).

[3] L. Fu, M. Zhang, Z. Zhai, F. Jiang, The influence of preheating temperature on the mechanical properties of injection-overmolded hybrid glass fiber reinforced thermoplastic composites, *Polymer Testing* 105 (2022) 107425.

[4] W. Jiang, C. Chen, T. Deng, X. Wang, Z. Huang, H. Zhou, H. Zhou, Effect of material and processing parameters on fiber pinning effect and resultant interfacial bonding strength of CF/PEEK bilayer parts in overmolding process, *Polymer Testing* 108 (2022) 107509.

[5] F. Neveu, C. Cornu, P. Olivier, B. Castanié, Manufacturing and impact behaviour of aeronautic overmolded grid-stiffened thermoplastic carbon plates, *Composite Structures* 284 (2022) 115228.

[6] A. J. Parsons, J. Molinar-Díaz, A. Koptelov, W. Darby, H. Hooshmand, F. U. Hernandez Ledezma, O. T. Thomsen, J. P. Belnoue, L. T. Harper, Failure modes of CF-PEEK overmoulded onto unidirectionally reinforced CF-LM-PAEK: Multi-scale pull-off testing and microscopy investigation of rib stiffened geometries, *Composites Part B: Engineering* 305 (2025) 112700.

[7] M. A. Valverde, An Improved Description of the Bonding and Consolidation for Overmoulded Thermoplastic Composite Ribbed Plates, Ph.D. thesis (2021).

[8] T. Joppich, A. Menrath, F. Henning, Advanced Molds and Methods for the Fundamental Analysis of Process Induced Interface Bonding Properties of Hybrid, Thermoplastic Composites, *Procedia CIRP* 66 (2017) 137–142.

[9] A. Liebsch, W. Koshukow, J. Gebauer, R. Kupfer, M. Gude, Overmoulding of consolidated fibre-reinforced thermoplastics - increasing the bonding strength by physical surface pre-treatments, *Procedia CIRP* 85 (2019) 212–217.

[10] R. Giusti, G. Lucchetta, Cohesive Zone Modeling of the Interface Fracture in Full-Thermoplastic Hybrid Composites for Lightweight Application, *Polymers* 15 (22) (2023) 4459.

[11] X. Song, F. Daghia, C. Cluzel, Y. Elie, Influence of boundary conditions on the failure behavior of T-joint shaped overmolded composite structures, in: 21st European Conference on Composite Materials, Nantes, France, 2024.

[12] F. Daghia, X. Song, Y. Elie, C. Cluzel, Characterizing Adhesion and Failure in Overmolded T-Joint Composites with Novel Isostatic Fixtures, in: European Solid Mechanics Conference, Lyon, 2025.

[13] R. Giusti, G. Lucchetta, Modeling the Adhesion Bonding Strength in Injection Overmolding of Polypropylene Parts, *Polymers* 12 (9) (2020) 2063.

[14] P. Hofman, F. P. van der Meer, L. J. Sluys, A numerical framework for simulating progressive failure in composite laminates under high-cycle fatigue loading, *Engineering Fracture Mechanics* 295 (2024) 109786.

[15] P. Hofman, F. P. van der Meer, L. J. Sluys, Modeling of progressive high-cycle fatigue in composite laminates accounting for local stress ratios, *Composites Part A: Applied Science and Manufacturing* 183 (2024) 108219.

[16] P. Hofman, D. Kovačević, F. P. van der Meer, L. J. Sluys, A viscoplasticity model with an invariant-based non-Newtonian flow rule for unidirectional thermoplastic composites, *Mechanics of Materials* 211 (2025) 105507.

[17] C. G. Dávila, From S-N to the Paris law with a new mixed-mode cohesive fatigue model for delamination in composites, *Theoretical and Applied Fracture Mechanics* 106 (2020) 102499.

[18] C. G. Dávila, C. A. Rose, G. B. Murri, W. C. Jackson, W. M. Johnston, Evaluation of fatigue damage accumulation functions for delamination initiation and propagation, *Nasa/Tp–2020-220584* (2020).

[19] M. L. Benzeggagh, M. Kenane, Measurement of mixed-mode delamination fracture toughness of unideirctional glass/epoxy composites with mixed-mode bending, *Composites Science and Technology* 56 (1996) 439–449.

[20] R. C. Juvinall, K. M. Marshek, Fundamentals of Machine Component Design, 5th Edition, John Wiley & Sons, Hoboken, NJ, 2012.

[21] T. A. Tervoort, E. T. J. Klompen, L. E. Govaert, A multi-mode approach to finite, three-dimensional, nonlinear viscoelastic behavior of polymer glasses, *Journal of Rheology* 40 (5) (1996) 779–797.

[22] T. A. Tervoort, R. J. M. Smit, W. A. M. Brekelmans, L. E. Govaert, A Constitutive Equation for the Elasto-Viscoplastic Deformation of Glassy Polymers, *Mechanics of Time-Dependent Materials 1: 269–291, 1998.* 1 (1998) 269–291.

[23] L. C. A. van Breemen, E. T. J. Klompen, L. E. Govaert, H. E. H. Meijer, Extending the EGP constitutive model for polymer glasses to multiple relaxation times, *Journal of the Mechanics and Physics of Solids* 59 (10) (2011) 2191–2207.

[24] E. Kröner, Allgemeine Kontinuumstheorie der Versetzungen und Eigenspannungen, *Archive for Rational Mechanics and Analysis* 4 (1) (1959) 273–334.

[25] E. H. Lee, Elastic-Plastic Deformation at Finite Strains, *ASMEJ. Appl. Mech. March* 36 (1) (1969) 1–6.

[26] A. Spencer, Deformations of Fibre-Reinforced Materials, Oxford Science Research Papers, Clarendon Press, 1972.

[27] A. J. M. Spencer, Kinematic Constraints, Constitutive Equations and Failure Rules for Anisotropic Materials, in: J. P. Boehler (Ed.), Applications of Tensor Functions in Solid Mechanics, Springer, Vienna, 1987, pp. 187–201.

[28] M. Vogler, R. Rolfes, P. Camanho, Modeling the inelastic deformation and fracture of polymer composites – Part I: Plasticity model, *Mechanics of Materials* 59 (2013) 50–64.

[29] J. Mandel, Plasticite Classique et Viscoplasticite:, CISM International Centre for Mechanical Sciences, Springer, 1972.

[30] I. A. Rodrigues Lopes, P. P. Camanho, F. M. Andrade Pires, A. Arteiro, An invariant-based elasto-visco-plastic model for unidirectional polymer composites at finite strains, *International Journal of Solids and Structures* 236–237 (2022) 111292.

[31] J. Bonet, A. Burton, A simple orthotropic, transversely isotropic hyperelastic constitutive equation for large strain computations, *Computer Methods in Applied Mechanics and Engineering* 162 (1-4) (1998) 151–164.

[32] D. Kovačević, F. P. van der Meer, Strain-rate based arclength model for nonlinear microscale analysis of unidirectional composites under off-axis loading, *International Journal of Solids and Structures* 250 (2022) 111697.

[33] Q. Yu, J. Fish, Temporal homogenization of viscoelastic and viscoplastic solids subjected to locally periodic loading, *Computational Mechanics* 29 (3) (2002) 199–211.

[34] C. Oskay, J. Fish, Fatigue life prediction using 2-scale temporal asymptotic homogenization, *International Journal for Numerical Methods in Engineering* 61 (3) (2004) 329–359.

[35] S. Haouala, I. Doghri, Modeling and algorithms for two-scale time homogenization of viscoelastic-viscoplastic solids under large numbers of cycles, *International Journal of Plasticity* 70 (2015) 98–125.

[36] I. B. C. M. Rocha, F. P. van der Meer, L. J. Sluys, Efficient micromechanical analysis of fiber-reinforced composites subjected to cyclic loading through time homogenization and reduced-order modeling, *Computer Methods in Applied Mechanics and Engineering* 345 (2019) 644–670.

[37] D. Kovačević, P. Hofman, I. B. C. M. Rocha, F. P. van der Meer, Unifying creep and fatigue modeling of composites: A time-homogenized micromechanical framework with viscoplasticity and cohesive damage, *Journal of the Mechanics and Physics of Solids* 193 (2024) 105904.

[38] M. J. Kanters, T. Kurokawa, L. E. Govaert, Competition between plasticity-controlled and crack-growth controlled failure in static and cyclic fatigue of thermoplastic polymer systems, *Polymer Testing* 50 (2016) 101–110.

[39] A. L. Eterovic, K.-J. Bathe, A hyperelastic-based large strain elasto-plastic constitutive formulation with combined isotropic-kinematic hardening using the logarithmic stress and strain measures, *International Journal for Numerical Methods in Engineering* 30 (6) (1990) 1099–1114.

[40] G. Weber, L. Anand, Finite deformation constitutive equations and a time integration procedure for isotropic, hyperelastic-viscoplastic solids, *Computer Methods in Applied Mechanics and Engineering* 79 (2) (1990) 173–202.

[41] C. Sansour, F. G. Kollmann, Large viscoplastic deformations of shells. Theory and finite element formulation, *Computational Mechanics* 21 (6) (1998) 512–525.

[42] A. Koptelov, X. Wu, W. Darby, A. Parsons, O. T. Thomsen, S. R. Hallett, L. T. Harper, J. P. Belnoue, Modelling compaction-induced defects in overmoulding of thermoplastic composites, in: Material Forming, 2025, pp. 638–645.

[43] A. Raimondo, C. Bisagni, Analysis of local stress ratio for delamination in composites under fatigue loads, *AIAA Journal* 58 (1) (2020) 455–463.

[44] M. W. Joosten, C. G. Dávila, Q. Yang, Predicting fatigue damage in composites subjected to general loading conditions, *Composites Part A: Applied Science and Manufacturing* 156 (2022) 106862.

6

Conclusions and future perspectives

New numerical methods for simulating failure in polymer composites have been developed. High-cycle fatigue has been simulated with a fatigue cohesive zone model that covers initiation and propagation while requiring a relatively small number of inputs. The model has been enhanced with an implicit time integration scheme and a consistent tangent stiffness matrix to efficiently and robustly simulate interacting and competing transverse cracks and delaminations in composite laminates. Furthermore, the model has been combined with XFEM to allow for transverse cracks to initiate at arbitrary locations in multidirectional laminates. For efficient high-cycle fatigue analyses, an adaptive cycle jump approach is employed, which accounts for spatially varying local stress ratios in the presence of thermal residual stresses and plastic deformations. To incorporate rate-dependent plasticity and creep in thermoplastic composites, a new mesoscopic viscoplasticity model has been developed. The model has been extended to a two-scale time-homogenized version to efficiently account for plastic strains in fatigue analyses under a large number of cycles, without simulating each load cycle explicitly. By combining the two-scale viscoplastic model with the fatigue cohesive zone model, the framework allows for simulating fracture and fatigue in overmolded thermoplastic composites.

The numerical methods developed in this thesis enable efficient and robust high-cycle fatigue simulations of polymer composites relevant to practical engineering applications. With these methods, a contribution has been made towards more reliable virtual testing.

6.1. CONTRIBUTIONS

The following contributions have been made to the field of computational mechanics of composites:

1. Dávila's fatigue cohesive zone model [1, 2] has been enhanced with a fully implicit time integration scheme.

2. Dávila's fatigue cohesive zone model [1, 2], including Turon's underlying quasi-static version [3], has been consistently linearized.

3. Dávila's fatigue cohesive zone model [1, 2] is combined with cohesive XFEM for simulating distributed transverse cracking in multidirectional laminates [4, 5].

4. A new fatigue crack insertion criterion for XFEM has been proposed, based on the endurance limit and consistent with the fatigue cohesive zone model.

5. The numerical framework has been combined with an adaptive cycle jumping scheme to account for spatially varying local stress ratios as a result of thermal residual stresses and plastic deformations.

6. A new mesoscopic constitutive model has been developed for simulating viscoplastic deformations and creep in unidirectional thermoplastic composites. Invariants are used to describe transverse isotropy, remove the possibility of plastic flow in fiber direction and include pressure dependency.

7. A two-scale, time-homogenized, version of the mesoscopic viscoplasticity model has been developed, allowing for efficient high-cycle fatigue analyses.

8. An engineering approach is proposed to obtain (qualitatively) a deformed mesh by applying special boundary conditions and using artificial material properties. Through this approach, tedious meshing and defining a conforming fiber vector field is avoided.

6.2. CONCLUSIONS

The progressive fatigue framework has been applied to the simulation of various numerical examples.

General conclusions The following general conclusions regarding the progressive fatigue framework are made:

- Analyses are more robust and efficient by using an implicit time integration scheme for Dávila's fatigue cohesive zone model. In addition, implicit time integration enables the use of an adaptive stepping strategy based on global iterations. By combining implicit time integration, adaptive stepping and a consistent tangent modulus, a large number of load cycles can be simulated in a computationally efficient manner.

- Dávila's fatigue cohesive zone model covers initiation and propagation. The model requires a small number of input parameters and the effect of local stress ratio and mode-mixity is included in the constitutive equations. This is a significant advantage over Paris-type cohesive zone models that require Paris curves to describe propagation, and separate S-N curves to describe crack initiation, each with different mode-mixities and stress ratios.

- For cases where thermal residual stresses and plastic deformations are present, it is important to account for the local stress ratio. With a standard load envelope approach, the local stress ratio is unknown. However, by modeling a complete load cycle before a jump in cycles takes place, local stress ratio can be retrieved and used to compute fatigue damage at each integration point. Dávila's fatigue cohesive zone model internally accounts for a local stress ratio through the constitutive equations, thereby allowing it to vary both spatially and temporally.

Multidirectional laminate simulations Specifically for simulating multidirectional laminates, the following conclusions are made:

- The cohesive XFEM framework is able to simulate a transition from diffuse to localized fatigue failure by modeling the interaction between transverse matrix cracking and delamination. A crack-spacing parameter is used to mitigate the ill-posedness inherent in mesoscale plane-stress analyses and to simplify the implementation of strategies for merging transverse cracks [4–6]. Although the simulation results show a slight sensitivity to this numerical parameter, the range of sensitivity remains acceptable for fatigue life prediction.

- The laminate simulations showed sensitivity to the static interlaminar strength. It has been shown previously, when simulating the same cases under static loading [7], that strength did not affect the response as much as fracture energy. However, for the fatigue simulations performed in this dissertation, static strength appears to be an important parameter.

- The cohesive XFEM-framework is capable of predicting the fatigue lives of multidirectional laminates in good agreement with experiments. Furthermore, the experimentally observed damage evolution and final failure modes are well captured. For some cases where fiber fracture occurred in the experiments, the model was less accurate since fiber fracture is not included as a failure process.

Mesoscopic viscoplasticity model For simulating failure in overmolded thermoplastic composites, a transversely isotropic viscoplasticity model has been developed. The conclusions are:

- The transversely isotropic homogenized response of a micromodel, with viscoplastic matrix and hyperelastic fibers explicitly modeled, is accurately captured with the mesomodel through invariants and proper kinematic descriptions regarding the configurations.

- The development of the mesoscopic viscoplasticity model enabled ply-level coupon simulations, providing a better match with experiments under small off-axis angles than previously could be achieved with micromechanical simulations under mesoscopically uniform deformations [8].

- The mesomodel requires only *four* parameters and a relaxation spectrum, which can be determined from a small number of off-axis tests.

- The response of the micromodel under various constant strain rates and off-axis angles is well captured. However, under creep loading, results are satisfactory, but require further improvements.

- The two-scale time-homogenized version, combined with adaptive cycle jumping, allows for simulating a large number of cycles efficiently.

Overmolded thermoplastic composite simulations With the extended framework, initial steps have been made towards modeling fracture and fatigue in a rib pull-off test of a T-section cut from an overmolded rib-stiffened panel. The conclusions are:

- The geometry of the laminate in an overmolded thermoplastic composite, as a result of processing, has a significant effect on the mechanical bond performance. The local wrinkles result in a higher capacity under quasi-static loading and an increased fatigue life under cyclic loading.

- Modeling the ply-aligned fiber direction through a mesoscopic approach has a significant influence on the failure simulations. A homogenized approach (through the thickness of the laminate), as previously used in literature [9, 10], does not contain this information. Therefore, in a fully virtual testing framework for optimizing processing parameters and performance of the overmolded interface, a mesoscopic approach is preferred.

- In most numerical investigations in literature, viscoplasticity in the laminate is ignored. However, viscoplastic deformations can increase the strength and fatigue life. This is mainly the case with good degrees of healing at the overmolded interface, otherwise fracture occurs before a sufficient amount of viscoplastic deformations in the laminate accumulates.

- The boundary conditions affect the strength and fatigue life of the rib-pull off test. Therefore, strength and fatigue response curves from this type of test may not be directly used to obtain input for macroscopic failure simulations on overmolded rib-stiffened panels.

6.3. FUTURE PERSPECTIVES

Recommendations to further improve the predictive capabilities of the developed numerical framework are listed below.

Multidirectional laminate simulations Regarding the multidirectional laminate simulations, the following recommendations are made for future research:

- **Investigate the strength-dependence on fatigue propagation**. With the multidirectional laminate simulations, it was found that the fatigue response depends on the interfacial strength. In cases with pre-cracks, such as the double cantilever beam test, the underlying cohesive zone model for quasi-static fracture shows a strength-independent response in the propagation regime [3]. However, the fatigue-extended version of the cohesive zone model [1, 2] assumes that propagation (Paris curve) can be described by an S-N curve, thus depending on strength. Since the strength was adjusted to aid convergence of the simulations, it is worth investigating if this strength dependency is physical and how it should be dealt with in fatigue simulations where both initiation and propagation take place.

- **Include fiber fracture as a failure process**. In the sub-laminate scaled specimens, fiber fracture at the higher load levels was observed in the experiments. Since fiber fracture is not considered in the numerical framework, the fatigue

lives obtained with these load levels were overestimated. To cover also the higher load levels, a fiber fracture model needs to be included in the framework.

Mesoscopic viscoplasticity model Possible improvements to the developed constitutive model are:

- **Include material strain hardening**. In the mesoscopic viscoplasticity model, material hardening is not included. Mainly under pure transverse tension and compression, a mismatch with the micromechanical simulations was observed in the post-yield regime. In the micromechanical simulations, the polymeric matrix did include a strain hardening component, physically representing reorientation of polymer chains. Under transverse tension, fracture occurs before full plastification takes place. However, under transverse compression, a hardening component may be included for an improved post-yield hardening response.
- **Account for the effect of stress in fiber direction**. In the mesoscopic viscoplasticity model, stress in fiber direction plays no role in the yield process through the invariant formulation. Although plastic flow in fiber direction is effectively removed, ideally all stress components should contribute to the yield process [11]. It would be interesting to investigate if under other load cases, this shortcoming requires further improvements to the formulation.
- **Improve the creep response**. The mesomodel provided an excellent match under constant strain-rate loading. Under creep, the match was not as good. Possibly, the match under creep can be improved by including creep data in the calibration procedure.
- **Extend to temperature dependence, multiple relaxation process and aging.** Through the Eyring relation, the mesomodel can be extended to include temperature dependence, multiple relaxation processes and the effects of aging, following previous works on the isotropic version of the viscoplastic model for neat polymers [12–14].

Overmolded thermoplastic composite simulations A first step towards a reliable performance prediction tool has been developed for overmolded thermoplastic composites under cyclic loads. The potential improvements are listed below:

- **Validate against experiments**. There are no experimental data available in literature under cyclic loading. The first suggestion is to perform experiments

on T-sections. Relevant data would be: force-time and displacement-time curves under various strain rates, load levels and stress-ratios. In addition, DIC data and pictures of the damage patterns are important for comparison with the numerical results.

- **Include an anisotropic viscoplastic model for the ribs**. Viscoplasticity in the ribs is missing in the numerical framework. It would be interesting to include a viscoplastic material model for the short-fiber composite ribs. A good candidate would be either the model by Amiri-Rad et al. [15], or an extension of the viscoplastic model developed in this thesis, by incorporating another invariant related to stress in fiber direction as in Dean et al. [16].

- **Include a fracture model for the rib**. In some experiments on overmolded thermoplastic composites under static loading [9], fracture in the rib has been reported instead of fracture in the overmolded interface. The XFEM model could be used to account for this, but requires a proper crack direction criterion.

- **Include subcritical damage in the laminate**. In some experiments, significant subcritical damage occurred in the laminate [17]. Since the locations of interfaces between the plies in the laminate are *a priori* known, on the fly insertion of cohesive segments may be suitable to account for this. A multilinear traction-separation relation may be required to account for fiber bridging in thermoplastic composites. This can be achieved by superimposing cohesive segments with bilinear traction-separation relations [18].

- **Account for varying fiber orientations and volume fractions**. In this work, it is assumed that the short fibers in the rib are vertically oriented and the volume fractions are uniformly distributed. Ideally, these fields should be predicted from accurate processing simulations. Subsequently, they can be used to determine average structural tensors that enter the constitutive model at each integration point. In addition, it is assumed that the fiber volume fractions in the laminate are uniform. These too should come from accurate processing simulations. Spatially varying volume fractions result in different kinetic yield parameters at each material point. Therefore, relations between volume fraction and mesoscopic model parameters must be established. These relations could be established through homogenization of micromechanical models with explicit representations of the fibers and matrix. By varying the fiber volume fraction and assuming accurate constitutive descriptions of the

phases, the resulting homogenized response may then be used to determine the mesoscopic model parameters for each material point.

- **Include more detailed healing profiles**. The degree of healing along the overmolded interface may come from thermomechanical analyses for modeling the overmolding process. The thermomechanical history, which determines the interdifussion process, needs to be translated to strength and fracture energies for the cohesive zone model at the overmolded interface. It is yet to be determined if the fatigue parameters in Dávila's cohesive zone model are also affected by various healing degrees.

- **Include process-dependent constitutive models**. Variations in cooling rates and processing temperatures result in different degrees of crystallinity of the thermoplastic polymer. In the numerical model, this means that the yield kinetics parameters of the mesoscopic viscoplasticity model should be process-dependent. Moreover, the effect of cooling rates on crystallinity also influences the bond quality: it affects the interdiffusion process and consequently the healing of the overmolded interface. Therefore, constitutive models should depend on the processing parameters for a full understanding of the effects of processing on the performance of the overmolded part.

- **Macroscopic full-scale analyses.** For macroscopic analyses of full-scale stiffened panels, additional modeling ingredients are required. These include the development of a shell-to-shell cohesive element capable of efficiently simulating delamination and panel-stiffener debonding. Furthermore, such a framework requires constitutive models for describing inelastic deformations and failure in the laminate and in the rib, as well as homogenized interface properties for the overmolded interface, including strength, fracture energy, and fatigue initiation and propagation parameters.

REFERENCES

[1] C. G. Dávila, From S-N to the Paris law with a new mixed-mode cohesive fatigue model for delamination in composites, *Theoretical and Applied Fracture Mechanics* 106 (2020) 102499.

[2] C. G. Dávila, C. A. Rose, G. B. Murri, W. C. Jackson, W. M. Johnston, Evaluation of fatigue damage accumulation functions for delamination initiation and propagation, *Nasa/Tp–2020-220584* (2020).

[3] A. Turon, E. V. González, C. Sarrado, G. Guillamet, P. Maimí, Accurate simula-

tion of delamination under mixed-mode loading using a cohesive model with a mode-dependent penalty stiffness, *Composite Structures* 184 (2018) 506–511.

[4] F. P. van der Meer, L. J. Sluys, A phantom node formulation with mixed mode cohesive law for splitting in laminates, *International Journal of Fracture* 158 (2) (2009) 107–124.

[5] F. P. van der Meer, L. J. Sluys, Mesh-independent modeling of both distributed and discrete matrix cracking in interaction with delamination in composites, *Engineering Fracture Mechanics* 77 (4) (2010) 719–735.

[6] F. P. van der Meer, Mesolevel Modeling of Failure in Composite Laminates: Constitutive, Kinematic and Algorithmic Aspects, *Archives of Computational Methods in Engineering* 19 (3) (2012) 381–425.

[7] F. P. van der Meer, L. J. Sluys, S. R. Hallett, M. R. Wisnom, Computational modeling of complex failure mechanisms in laminates, *Journal of Composite Materials* 46 (5) (2012) 603–623.

[8] D. Kovačević, B. K. Sundararajan, F. P. van der Meer, Microscale modeling of rate-dependent failure in thermoplastic composites under off-axis loading, *Engineering Fracture Mechanics* 276 (2022) 108884.

[9] M. A. Valverde, An Improved Description of the Bonding and Consolidation for Overmoulded Thermoplastic Composite Ribbed Plates, Ph.D. thesis (2021).

[10] X. Song, F. Daghia, C. Cluzel, Y. Elie, Influence of boundary conditions on the failure behavior of T-joint shaped overmolded composite structures, in: 21st European Conference on Composite Materials, Nantes, France, 2024.

[11] F. P. van der Meer, Micromechanical validation of a mesomodel for plasticity in composites, *European Journal of Mechanics - A/Solids* 60 (2016) 58–69.

[12] E. T. J. Klompen, T. A. P. Engels, L. E. Govaert, H. E. H. Meijer, Modeling of the Postyield Response of Glassy Polymers: Influence of Thermomechanical History, *Macromolecules* 38 (16) (2005) 6997–7008.

[13] T. A. Tervoort, R. J. M. Smit, W. A. M. Brekelmans, L. E. Govaert, A Constitutive Equation for the Elasto-Viscoplastic Deformation of Glassy Polymers, *Mechanics of Time-Dependent Materials 1: 269–291, 1998.* 1 (1998) 269–291.

[14] E. T. J. Klompen, L. E. Govaert, Nonlinear Viscoelastic Behaviour of Thermorheologically Complex Materials, *Mechanics of Time-Dependent Materials* 3 (1999) 49–69.

[15] A. Amiri-Rad, L. V. Pastukhov, L. E. Govaert, J. A. W. van Dommelen, An anisotropic viscoelastic-viscoplastic model for short-fiber composites, *Mechanics of Materials* 137 (2019) 103141.

[16] A. Dean, S. Sahraee, J. Reinoso, R. Rolfes, Finite deformation model for short fiber reinforced composites: Application to hybrid metal-composite clinching joints, *Composite Structures* 151 (2016) 162–171.

[17] A. J. Parsons, J. Molinar-Díaz, A. Koptelov, W. Darby, H. Hooshmand, F. U. Hernandez Ledezma, O. T. Thomsen, J. P. Belnoue, L. T. Harper, Failure modes of CF-PEEK overmoulded onto unidirectionally reinforced CF-LM-PAEK: Multi-scale pull-off testing and microscopy investigation of rib stiffened geometries, *Composites Part B: Engineering* 305 (2025) 112700.

[18] I. Leciñana, J. Renart, A. Turon, J. Zurbitu, B. Tijs, Characterization and analysis of the mode I interlaminar fatigue behaviour of thermoplastic composites considering R -curve effects, *Engineering Fracture Mechanics* (2023) 109273.

Curriculum Vitæ

Pieter Hofman

July 17, 1993 Born in Amsterdam, the Netherlands.

Education

Dec. 2021 – Nov. 2025	**Ph.D.** Computational Mechanics Delft University of Technology
Feb. 2018 – Jun. 2021	**M.Sc.** (cum laude) Civil Engineering Delft University of Technology
Sep. 2016 – Feb. 2018	**Pre-master** Civil Engineering Delft University of Technology
Sep. 2012 – Jun. 2016	**B.Sc.** Civil Engineering Amsterdam University of Applied Sciences

Experience

Sep. 2021 – Nov. 2021	**Researcher** Computational Mechanics Delft University of Technology
Feb. 2016 – Jun. 2016	**Bachelor's Thesis student** Iv-Infra
Feb. 2015 – Jul. 2015	**Internship Trainee** Iv-Infra

Research outputs

Journal articles related to this dissertation

4. **P. Hofman**, F. P. van der Meer and L. J. Sluys, Computational analysis of fracture and fatigue in overmolded thermoplastic composites: time-homogenized viscoplasticity, cohesive fracture and processing effects. *Under Review* (2026).

3. **P. Hofman**, D. Kovačević, F. P. van der Meer and L. J. Sluys, A Viscoplasticity Model with an Invariant-Based Non- Newtonian Flow Rule for Unidirectional Thermoplastic Composites. *Mechanics of Materials* **211**, 105507. issn: 01676636. https://linkinghub.elsevier.com/retrieve/pii/S0167663625002698 (2025).

2. **P. Hofman**, F. P. van der Meer and L. J. Sluys, Modeling of Progressive High-Cycle Fatigue in Composite Laminates Accounting for Local Stress Ratios. *Composites Part A: Applied Science and Manufacturing* **183**, 108219. issn: 1359835X. https://linkinghub.elsevier.com/retrieve/pii/S1359835X24002161 (2024).

1. **P. Hofman**, F. P. van der Meer and L. J. Sluys, A Numerical Framework for Simulating Progressive Failure in Composite Laminates under High-Cycle Fatigue Loading. *Engineering Fracture Mechanics* **295**. https://linkinghub.elsevier.com/retrieve/pii/S0013794423007440 (2024).

Other journal articles

2. D. Kovačević, **P. Hofman**, I. B. C. M. Rocha and F. P. van der Meer, Unifying Creep and Fatigue Modeling of Composites: A Time-Homogenized Micromechanical Framework with Viscoplasticity and Cohesive Damage. *Journal of the Mechanics and Physics of Solids* **193**, 105904. issn: 00225096. https://linkinghub.elsevier.com/retrieve/pii/S0022509624003703 (2024).

1. **P. Hofman**, L. Ke and F. P. van der Meer, Circular Representative Volume Elements for Strain Localization Problems. *International Journal for Numerical Methods in Engineering* **124**, 784–807. issn: 0029-5981, 1097-0207. https://onlinelibrary.wiley.com/doi/10.1002/nme.7142 (2023).

AWARDS

2024 Best presentation at the 27th Engineering Mechanics Symposium - Modelling of Interfacial Fracture and Fatigue in Polymer Composites

SUPERVISION OF MSC STUDENTS

2024 MSc thesis Stijn Platzer - Implementation and Evaluation of the Shifted Fracture Method for Crack Propagation in Fiber-Reinforced Polymer Composites

2022 MSc thesis Linda Dupain - Modelling Fatigue Transition Behaviour of FRP in Mode I Block Loading

CONFERENCE TALKS

2025	M2i Conference	Papendal (the Netherlands)
2025	Composites	Vienna (Austria)
2025	European Solid Mechanics Conference	Lyon (France)
2024	Engineering Mechanics Symposium	Papendal (the Netherlands)
2024	ECCOMAS	Lisbon (Portugal)
2024	NewFrac	Porto (Portugal)
2023	Composites	Trapani (Italy)
2023	CompTest	Girona (Spain)
2021	Composites (online)	Gothenburg (Sweden)